Investigating the Stability of Perovskite Light-Emitting Diodes



Jonathan Warby

Wadham College

Department of Physics

University of Oxford

This dissertation is submitted for the degree of Doctor of Philosophy

December 2020

ABSTRACT

Metal halide perovskite semiconductors have recently attracted significant attention as a class of materials with huge potential for a wide array of optoelectronic applications. They have shown great promise as emitters in light-emitting diodes where they demonstrate emission wavelength tunability across the entire visible spectrum, narrow emission spectra and high EQE_{EL} in excess of 20%. Despite this excellent performance they have poor operational stability, resulting in lifetimes of 250 hours in the best case.

In this thesis, I first investigate factors which govern the fabrication of efficient green-emitting perovskite LEDs through the implementation and study of different device structures and passivation strategies for green emitting perovskite LEDs. Following this, I investigate the use of 2D/3D perovskite heterostructures as a strategy for efficient green-emitting perovskite LEDs. I systematically alter composition and examine changes in carrier recombination and device performance. Additionally, I study the effect of different experimental protocols on reproducibility of 2D/3D devices which leads to the development of a novel hole injection layer which affords efficient and highly reproducible devices.

In the final experimental chapter, I study the effect of the composition of 2D/3D perovskite LEDs on stability. I demonstrate that the introduction of the cation phenylethylammonium into the perovskite is highly detrimental to operational stability. This leads to investigations into the drivers behind poor operational stability where I reveal that changes to radiative efficiency and charge injection are the primary factors, which is attributed to increased ionic mobility.

ACKNOWLEDGEMENTS

The work in this thesis was carried out over the course of 4 years of challenging work which would not have been possible without the help and support of many of my fantastic colleagues.

I would like to thank my supervisor Henry Snaith, you have been an excellent mentor over the past four years. Your enthusiasm and passion for science is contagious and your guidance has allowed me to grow into an independent researcher. Your ideas and suggestions have expanded my abilities as a scientist. Your eagerness to push the limits of what is possible in a field have shown me the power of imagination in science. I am very grateful to have done my PhD with you.

Finishing this PhD would not have been possible without the support of many wonderful people in the Snaith group. Foremost, I would like to thank Bernard Wenger who has been an absolute bastion of inspiration, education, support and friendship though the whole process. Bernard, you have taught me so much of the ways of optoelectronics and life, when I started out coming from an entirely different field. You were always there for a chat or to teach me how to do something new or completely crazy. I really admire your selflessness, passion and willingness to teach everyone in the lab and I will miss coming to distract you in your office! Thank you so much for all of your endless help over the past four years and for reading through this manuscript.

To past group members who were gone like a flash in the pan but I still remember and cherish. Nakita, Max, David, Severin, Alba and co. You were there in the beginning and got me started in the lab, it was a whole lot of fun and I won't forget it. I was sad to see you leave early on but know that I have friends for life!

To other scientific mentors who have been of immense help; Alex Ramadan, James Ball, Ashley Marshal, Nobuya Sakai and Jongchul Lim. You have all been directly extremely supportive in my research and in my development as a scientist when it wasn't asked of you. I admire all of your approaches to science and your willingness to educate and it's something that I hope to bring with me into the future. Not only that you are all a hell of a lot of fun and I will miss cups of tea, chats over lunch and also many chats over pints. Keep doing what you're doing you're all great!

To the rest of the Snaith group Robbie, Giulia, Grey, Melissa, Philippe, Derek, Mike, Augustin, Giulio, Kelly, Suhas, Laura, Eli, Emil, Jarla, Manuel, Yen and many more. I could write several pages about how everyone in the group have been such great colleagues and friends. We are truly a unique group where everyone is so supportive and

likeminded and I will really cherish the time that I had with all of you. Clare, thank you for being such a help in getting through this whole process, bringing order where there was chaos in my life, I'll be forever grateful for that.

To everyone in my life outside of the lab who have been so supportive and adept at providing the antidote to the daily grind of PhD life. Rav, Flo, Nick, Sam and Tom I couldn't have made it without you, thanks for picking me up when I was down, the drinks, the chats, the music, all of the sofas crashed on. Gareth, Jacob and Rory thank you for the meals, the laughs, the chats and making life homely in Oxford – good luck in the end of your PhDs! Emma, I couldn't have made it to the end without your undying support and positivity. I'm so lucky to have met you here in Oxford, I love you and can't wait for the next chapter!

Finally, to my family. Mum, Dad, Em, Luce; nothing would have been possible without you. You have instilled in me the feeling that anything is possible if I put my mind to it and here I am doing something that really did seem impossible at times. Thank you all for your love and support. I dedicate this to you.

CONTENTS

1 INTRODUCTION 18
1.1 SEMICONDUCTORS 18
1.1.1 Charge-carrier recombination 18
1.1.2 Photoluminescence quantum yield 22
1.1.3 Junctions 27
1.2 METAL HALIDE PEROVSKITES 33
1.2.1 Overview 33
1.2.2 Dimensionality in metal halide perovskites 35
1.2.3 Perovskite photovoltaics 37
1.3 LIGHT-EMITTING DIODES 38
1.3.1 History of LEDs 38
1.3.2 Quantum wells in LEDs 38
1.3.3 Perovskite thin film LED structure 39
1.3.4 Radiometry and Photometry 40
1.3.5 Efficiency quantification 44
1.4 PEROVSKITE LEDS 45
1.4.1 Methods for High Efficiency 46
1.4.2 Operational stability 52
1.5 SCOPE OF THIS THESIS 55
1.6 REFERENCES 55
2 EXPERIMENTAL TECHNIQUES 61
2.1 FILM AND DEVICE FABRICATION PROCEDURES 61
2.1.1 Substrate Cleaning 61
2.1.2 Fabrication of nip LEDs with ZnO via spray pyrolysis 61
2.1.3 Fabrication of nip LEDs with ZnO nanoparticles 61
2.1.4 Fabrication of pin LEDs 62
2.1.5 Perovskite Deposition 64
2.1.6 Precursor preparation 67
2.2 CHARACTERISATION 68
2.2.1 LED Efficiency 68
2.2.2 PLQY 68
2.2.3 Steady-state PL and EL spectra 69
2.2.4 TRPL 69

2.2.5 UV-Vis *69*
2.2.6 Scanning Electron Microscopy *69*
2.2.7 X Ray Photoelectron Spectroscopy *69*
2.2.8 Fourier Transform Photocurrent Spectroscopy *69*
2.2.9 X Ray Diffraction *70*
2.3 REFERENCES 70
3 EXPLORATION OF DEVICE STRUCTURES AND PASSIVATION STRATEGIES FOR PEROVSKITE LEDS 71
3.1 INTRODUCTION 71
3.2 FABRICATION OF *NIP* F8BT AND GREEN PEROVSKITE LEDS 71
3.2.1 Introduction *71*
3.2.2 nip F8BT LEDs *72*
3.2.3 Improvement of ZnO through nip near-infrared 2D/3D perovskite LEDs *74*
3.2.4 Investigation into $CsPbBr_3$ as an emitter in the nip configuration *76*
3.2.5 Investigation into $MAPbBr_3$ and $FAPbBr_3$ as an emitter in the nip configuration *78*
3.2.6 Discussion and Conclusions *80*
3.3 FABRICATION OF *PIN* F8BT + GREEN-EMITTING PEROVSKITE LEDS AND PASSIVATION OF $APbBr_3$ PEROVSKITES FOR IMPROVED PLQY 81
3.3.1 Introduction *81*
3.3.2 Implementation of a pin device structure and first green perovskite LEDs *82*
3.3.3 Investigation into the effect of benzylamine in the antisolvent *84*
3.3.4 The effect of choline as a passivating agent *89*
3.3.5 Conclusion *97*
3.4 CHAPTER CONCLUSION 97
3.5 REFERENCES 98
4 OPTIMISATION OF HIGH EFFICIENCY 2D/3D PEROVSKITE LEDS 102
4.1 INTRODUCTION 102
4.2 2D/3D LEDS 103
4.2.1 $PEA_2FA_2Pb_3Br_{10}$ LEDs *103*
4.2.2 Further optical properties of $PEA_2FA_{n-1}Pb_nBr_{3n+1}$ films *107*
4.2.3 Addressing reproducibility issues *114*
4.3 PEABR:$CsPbBr_3$ HYBRIDS 115
4.3.1 18-crown-6: $CsPbBr_3$ films and LEDs *116*
4.3.2 Reproducible 2D/3D LEDs (at last) *118*

4.3.3 The effect of PEABr content and testing environment on stability *120*
4.3.4 Characterisation of PEABr:CsPbBr$_3$ hybrids *122*
4.3.5 Investigation into effect of hole injection layer for high EQE$_{EL}$ *123*
4.4 CONCLUSION 127
4.5 REFERENCES 128
5 REVEALING FACTORS INFLUENCING THE OPERATIONAL STABILITY OF PEROVSKITE LIGHT-EMITTING DIODES 130
5.1 INTRODUCTION 130
5.2 FABRICATION AND CHARACTERISATION OF PEABR:CSPBBR$_3$ HYBRIDS 131
5.2.1 Morphological tailoring and characterisation *132*
5.2.2 Optical absorption and emission *133*
5.2.3 Photoluminescent quantum yield *135*
5.2.4 X-Ray Diffraction *137*
5.3 INCORPORATION OF FILMS INTO DEVICES 139
5.3.1 Device Structure *139*
5.3.2 Device Performance *139*
5.3.3 Device Stability *142*
5.4 INVESTIGATION INTO MECHANISM OF EFFICIENCY LOSS 146
5.4.1 Thermal and photo- stability *146*
5.4.2 Changes in structural and electronic properties *147*
5.5 DISCUSSION AND CONCLUSIONS 157
5.6 REFERENCES 159
6 CONCLUSION 164

LIST OF TABLES

Table 1.1 Comparison of equivalent radiometric and photometric units. 40

Table 3.1 PLQY improvement with immediate dispense of ChX solution after antisolvent quench; optical intensity 93 mW cm^{-2} , λ_{exc} = 405 nm. 92

Table 5.1. PL Peak, PLQY, FWHM of PL and PL stability of the different compositions of (PEABr)xCsPbBr3 used in this study. All films were on glass and encapsulated in an N_2 filled glovebox. 137

Table 5.2. Peak assignments for $CsPbBr_3$ peaks in diffractograms presented in Figure 5.5 138

Table 5.3. Max EQE_{EL} achieved and T_{50} at 10 mA cm^{-2} for all $(PEABr)_xCsPbBr_3$ LEDs measured in this study. 144

Table 5.4 Literature review of Stability and efficiency of state of the art $CsPbBr_3$ perovskite LEDs. The results are in three categories: Blue = Bulk $CsPbBr_3$ with polymer or small molecule additives; Yellow = Alkylammonium additives with $CsPbBr_3$ spincoated together; Green = colloidal $CsPbBr_3$ nanocrystals which are coordinated with ammonium salts. 145

List of Figures

Figure 1.1 The variation of carrier density dependent PLQY with different values for $k_{1\text{-}SRH}$. $k_2 = 10^{-10}$ cm^3 s^{-1}; $k_3 = 10^{-28}$ cm^6 s^{-1}. 25

Figure 1.2 The variation of carrier density dependent PLQY with different values for k_2. $k_1 = 10^7$ s^{-1}; $k_3 = 10^{-28}$ cm^6 s^{-1}. 26

Figure 1.3 The variation of carrier density dependent PLQY with different values for k_3. $k_1 = 10^7$ s^{-1}; $k_2 = 10^{-10}$ cm^3 s^{-1}. 27

Figure 1.4 Schematic showing the formation of a *pn* homojunction 28

Figure 1.5 Plot showing saturation of current in reverse bias at a nominal value for J_0 of 1 mA. 29

Figure 1.6 IV characteristics of *pn* homojunctions made from different semiconductor materials showing a clear difference in onset voltage. a) Ge E_g = 0.7 eV; b) Si E_g = 1.1 eV; c) GaAs E_g = 1.4 eV; d) GaAsP E_g = 2.0 eV; e) GaInN E_g = 2.9 eV. Figure credit.[1] 30

Figure 1.7 Schematic showing the formation of a Schottky diode by bringing a metal and an *n* type semiconductor into contact. 31

Figure 1.8 Schematic showing the formation of an Ohmic Junction by bringing a metal and an *n* type semiconductor into contact. 32

Figure 1.9 Schematic showing the relative energetic position of bands to form the 3 types of heterojunctions 32

Figure 1.10 The structure of a cubic perovskite, showing corner sharing octahedra and a central cuboctahedrally coordinated cation. Figure credit[10] 34

Figure 1.11 Schematic showing transition from a 2D perovskite (n = 1), to quasi-2D perovskite (n>1), and, 3D perovskite (n = ∞) Figure credit[16] 36

Figure 1.12 a) emission, and, b) absorption (inferred from reflectance) of a series of quasi-2D perovskite single crystals where A = MA and the spacer cation is butylammonium. Figure Credit[17] 37

Figure 1.13 Schematic of a typical perovskite LED device structure and the relative energetic alignment of the various layers. 39

Figure 1.14 The luminous efficiency function as defined by the CIE. This represents the average sensitivity of the human eye to visible wavelengths. 42

Figure 1.15 The xy CIE chromaticity chart. Figure Credit.[30] 43

Figure 1.16 The CIE colour matching functions X,Y and Z. Figure credit[31] 44

Figure 1.17 Absorbance, PL and photographs of the first reported 3D perovskite LEDs. Figure credit.[29] 46
Figure 1.18 a) Absorbance and PL of a typical 2D/3D perovskite film; b) schematic of 'energy funnelling' process in 2D/3D films. Figure credit.[46] 49
Figure 1.19 a) Carrier density dependent PLQY of 3D and 2D/3D (labelled MQW, for multiple quantum well) films; b) Carrier density vs initial PL intensity for 3D and 2D/3D films. Figure Credit[48] 50
Figure 1.20 PL and absorptance of PEABr:$CsPbBr_3$ 2D/3D film produced by the methodology introduced by Ban et al.[61] 51
Figure 1.21 A typical operational stability curve for a perovskite LED. Operating conditions 10 mA cm^{-2}, T_{50} = 240 s. 53
Figure 3.1 Morphology of ZnO on ITO showing a) flakes at close magnification, and, b) the extent of their distribution at lower magnification. 73
Figure 3.2 Characterisation of *nip* F8BT LED: a) Device structure; b) EL spectrum; c) JVL characteristics; d) EQE_{EL} v Voltage. 74
Figure 3.3 Summary of near infrared *nip* perovskite LEDs: a) Device structure; b) Champion EQE_{EL} vs V; c) EL spectrum; d) JV-Radiance characteristics 75
Figure 3.4 a) Stability study of NIR perovskite LED: a) EQE_{EL} vs T, and, retests after 2 h of recovery; b) Boxplot of EQE_{EL} of pristine substrate and after a retest. 76
Figure 3.5 Morphology of $CsPbBr_3$ thin films made by 'heat-gun method' showing significant pinholes at a) closer magnification, and, long range uniformity at b) lower magnification. 77
Figure 3.6 SEM of films of spincoated $CsPbBr_3$ with; a) 0% BA_2PbBr_4; b) 10% BA_2PbBr_4; c) 20% BA_2PbBr_4. 78
Figure 3.7 a) PLQY (fluence 120 mW cm^{-2}) vs molar percentage of A_2PbBr_4 in $MAPbBr_3$ for A=PEA and A=BA ; b) PLQY vs molar percentage of PEA_2PbBr_4 in $MAPbBr_3$ on PVK and ZnO/PEIE; c) SEM of 33 mol % PEA_2PbBr_4 in $MAPbBr_3$.; d) Photographs of films of PEA_2PbBr_4 in $MAPbBr_3$, substrate size 28 x 28 mm 79
Figure 3.8 a) Device structure of successful green *nip* perovskite LED; b) Photograph of its EL. 80
Figure 3.9 a) Device structure of *pin* F8BT LED; b) JV of first LiF optimisation showing improved electron injection; c) Corresponding EQE_{EL} v V; d) JV of further optimisation of LiF thickness; e) Photograph of optimised LED in operation. 83
Figure 3.10 First measurable visible perovskite LED in the Snaith group: a) Device structure; b) EL spectrum; c) JVL characteristics; d) EQE_{EL} v V. 84

Figure 3.11 Photophysical characterisation of benzylamine modified $MAPbBr_3$ films: a) normalised PL; b) Unnormalised PL; c) Stabilised and unstabilised PLQY; d) UV-Vis absorbance. 85
Figure 3.12 SEM characterisation of benzylamine treated $MAPbBr_3$ 86
Figure 3.13 SEM of 0.5 vol% Benzylamine treated $MAPbBr_3$ film showing unusual cubic morphology. 87
Figure 3.14 Device characterisation of benzylamine modified $MAPbBr_3$ LEDs: a) EQE_{EL} v J; b) JVL characteristics; c) Boxplot of EQE_{EL} as a function of composition; d) Operational stability of 0.25 vol% BzA at 4V and 0.5 vol% BzA at 5V. 88
Figure 3.15 SEM characterisation of $(FA_{0.9}Cs_{0.1})_{1.1}PbBr_3$ films with different vol% additions of formic acid to the precursor solvent. 90
Figure 3.16 PLQY of FACs perovskite as a function of ChX post-treatment; optical intensity 93 mW cm^{-2} , λ_{exc} = 405 nm. 91
Figure 3.17 Integrated PL intensity vs T at a fixed fluence of 93 mW cm^{-2} of; a) unencapsulated, and, b) encapsulated ChBr treated samples of FACs. 93
Figure 3.18 a) EQE_{EL} vs J for $FAPbBr_3$ LEDs on PEDOT:PSS and PEDOT:PSS/NPD hole injection layers; b) Operational stability of PEDOT:PSS/NPD $FAPbBr_3$ LED at 10 mA cm^{-2} 94
Figure 3.19 Integrated PL intensity vs T at a fixed fluence of 93 mW cm^{-2} of; a) unencapsulated, and, b) encapsulated ChBr treated samples of $FAPbBr_3$; c) comparison of encapsulated and unencapsulated ChCl treated $FAPbBr_3$ films. 95
Figure 3.20 Integrated PL intensity vs T at a fixed fluence of 93 mW cm^{-2} of ChCl treated $FAPbBr_3$ films with different treatment times tested on, a) the day of fabrication, and, b) 24 h after fabrication; c) PL spectra of films from b); d) PLQY of optimised films on different hole injection layers. 96
Figure 3.21 a) Powder X-Ray diffraction, and, b) UV-Vis of optimised ChCl treated $FAPbBr_3$ 97
Figure 4.1 a) EQE_{EL} v J for champion device (thick PEDOT device with DMSO soaking, 70 nm TPBi); b) JVL characteristics of champion device; c) Boxplot of efficiencies showing effect of transport layer thickness. 104
Figure 4.2 a) Intensity dependent PLQY of n=3 films on quartz and PEDOT:PSS λ_{exc} = 405 nm; b) EQE_{EL} v T of n=3, 70 nm TPBi device at 10 mA cm^{-2}; c) UV-Vis and PL of n=3 films. 106

Figure 4.3 a) Device structure of PVK HIL, n = 3 LED; b) JVL characteristics of champion device; c) EQE_{EL} v current density of champion device; d) EQE_{EL} v Temperature at 10 mA cm^{-2} of a representative device. 107
Figure 4.4 XRD of 2D/3D films. One can see clear evidence of PEA_2PbBr_4 in the n=2 sample. 108
Figure 4.5 Photostability of 2D/3D films (λ_{exc} = 405 nm, fluence = 97 mW cm^{-2}) encapsulated with; a) poly butyl rubber, and, b) UV-epoxy 109
Figure 4.6 a) UV-Vis (top) and normalised PL (bottom) for 2D/3D films; b) photograph of corresponding films. 110
Figure 4.7 Unnormalised PL of 2D/3D samples showing lack of emission from lower dimensional phases (except for n=2). 111
Figure 4.8 Intensity dependent PLQY of 2D/3D films. (λ_{exc} = 405 nm) 112
Figure 4.9 a) TRPL of 2D/3D films (λ_{exc} = 510 nm, optical intensity 43 mW cm^{-2}); b) Analysis of time for decay to fall to 1/e of its initial value. 113
Figure 4.10 a) Boxplot of EQE_{EL} comparing $PbBr_2$ suppliers and LiF thickness; b) Boxplot of EQE_{EL} comparing different HILs; c) Device stability at 10 mA cm^{-2} corresponding to b); d) Boxplot of EQE_{EL} comparing glovebox environment. 114
Figure 4.11 Schematic showing how 18-crown-6 increases the entropy of a system using the chelate effect. 116
Figure 4.12 SEM of films of $CsPbBr_3$ with various concentrations of 18-crown-6 117
Figure 4.13 a) EQE_{EL} v T for $CsPbBr_3$ LEDs with different concentrations of 18-crown-6; b) Boxplot of EQE_{EL} for those LEDs 118
Figure 4.14 Characterisation of $CsPbBr_3$ LED with 40 mol% PEABr and 4 mg mL^{-1} 18-C-6: a) EQE_{EL} v I; b) JVL characteristics; c) EL spectrum; d) Comparison of operational stability at 10 mA cm^{-2} with previous 2D/3D composition. 119
Figure 4.15 Boxplot of $CsPbBr_3$ LED with 40 mol% PEABr and 4 mg mL^{-1} 18-C-6 control device across a series of experiments, showing improved reproducibility. 120
Figure 4.16 a) operational stability of $CsPbBr_3$ LEDs as a function of PEABr content (measured in integrating sphere); b) Comparison of operational stability measured in integrating sphere (ambient) and glovebox testing rig (pure N_2); c) Schematic showing emission pattern of a Lambertian emitter; d) Schematic showing glovebox testing setup. 122

Figure 4.17 Characterisation of PEABr:$CsPbBr_3$ hybrids: a) Operational stability at 10 mA cm^{-2} measured in glovebox; b) Boxplot of EQE_{EL}; c) PL showing blueshift and broadening; d) PLQY of encapsulated films on glass.....123
Figure 4.18 a) Boxplot of EQE_{EL} comparing PVK with poly-TPD/PEIE HIL; b) Boxplot of EQE_{EL} v J with different thicknesses of poly-TPD and 2 nm LiF wetting layer; c) Operational stability at 10 mA cm^{-2} for devices shown in b); d) Boxplot of EQE_{EL} showing improved performance of devices after retesting. 125
Figure 4.19 Differences in JV characteristics between samples with different thicknesses of poly- TPD. An increase in injected current is observed with decreasing thickness of poly-TPD 125
Figure 4.20 a) Boxplot of EQE_{EL} for different thicknesses of LiF on poly-TPD; b) operation stability for devices presented in a). 126
Figure 4.21 EQE_{EL} v I of champion device showing a maximum value of 12% 127
Figure 5.1. a) The effect of increasing 18-crown-6 concentration on film morphology and its structure. Addition of 18-crown-6 has a marked impact on the film morphology.; b) The effect of PEABr on film morphology and the chemical structure of PEABr, all of the films have 4 mg/mL of 18-crown-6 in the precursor solution. Additon of PEABr has a strong effect on the film morphology causing even further decrease in grain size until we cannot easily resolve it by SEM. 133
Figure 5.2. a) Photograph of films used for characterisation under ambient lighting in glovebox, numbers indicate molar fraction i.e. 0.1 = (PEABr)0.1CsPbBr3, b) photograph of corresponding films under 365 nm UV light in glovebox.....134
Figure 5.3. a) Absorptance data of $CsPbBr_3$ with increasing molar excess of PEABr; b) Normalised photoluminescence spectra of $CsPbBr_3$ with increasing molar excess of PEABr; 135
Figure 5.4. Photoluminescent quantum yield of $CsPbBr_3$ with increasing molar excess of PEABr 136
Figure 5.5. a) Peak fitting of $CsPbBr_3$ sample to $CsPbBr_3$ and ITO peaks; b) Peak fitting of $(PEABr)_{0.4}CsPbBr_3$ sample to $CsPbBr_3$ and ITO peaks 137
Figure 5.6. comparison of the FWHM of $(PEABr)_{0.4}CsPbBr_3$ and $CsPbBr_3$ (101) peaks, $(PEABr)_{0.4}CsPbBr_3$ has a FWHM 3 x larger than $CsPbBr_3$. 138
Figure 5.7 LED device structure used in this study including layer thicknesses.....139
Figure 5.8. Typical J v EQE_{EL} for all $(PEABr)_xCsPbBr_3$ compositions in this study..140
Figure 5.9. Box plots of measured EQE_{EL} for one batch of devices sweeping through all $(PEABr)_xCsPbBr_3$ compositions during this study. 141

Figure 5.10. JVL characterisation of all $(PEABr)_xCsPbBr_3$ compositions in this study. The data here generated from the same sweeps of J v EQE_{EL} in Figure 5.8 141
Figure 5.11 Normalised EQE_{EL} v Time data for perovskite LEDs operated at 10 mA cm^{-2} showing the remarkable drop off in stability with increasing PEABr content ... 142
Figure 5.12 Absolute EQE_{EL} v Time data for perovskite LEDs operated at 10 mA cm^{-2} showing the remarkable drop off in stability with increasing PEABr content. Further our most efficient composition becomes worse than our control after only 2.5 hours 143
Figure 5.13. Graphical plot of T_{50} vs PEABr amount showing the strong decrease in stability when PEABr is added. 144
Figure 5.14. a) EQE_{EL} statistics for all 8 pixels on one $(PEABr)_{0.4}CsPbBr_3$ substrate after annealing for different periods of time at 50 °C; b) Photostability as a function of composition at an irradiance of 93 mW/ cm^2 ; λ_{exc} = 405 nm. All samples were encapsulated to remove the effects of atmosphere on the measurement. 146
Figure 5.15. A 1 cm^2 $(PEABr)_{0.4}CsPbBr_3$ LED in operation such as those used for structural degradation studies..... 147
Figure 5.16. a) UV-Visible absorptance data for pristine and degraded LEDs, typically two 1 cm^2 electrodes were evaporated on a substrate, one was electrically degraded and both the electrodes were delaminated for further characterisation; b) PL spectra for a pristine and degraded $(PEABr)_{0.4}CsPbBr_3$ LED. The degraded samples in this figure were operated for 1 h at 10 mA/cm^2..... 148
Figure 5.17. a) PL of $(PEABr)_{1.0}CsPbBr_3$ LED before and after operation for 1 h at 10 mA/cm^2; b) UV-Vis data of $(PEAr)_{0.9}CsPbBr_3$ LED before and after operation for 1 h at 10 mA/cm^2..... 148
Figure 5.18. a) FTPS spectra for $(PEABr)_{0.4}CsPbBr_3$ LED after operation at 10 mA/cm^2 for various amounts of time; b) The same spectra presented on a normalised scale, showing no significant changes in the low energy tail. 150
Figure 5.19. Overlapped high resolution XPS spectra of Pb 4f, Br 3d and Al 2p for unoperated (unop.) and operated (op.) LED devices. PEABr concentration in the relevant devices is 40% molar excess. The figure shows shows no significant shift in peak positions between control and PEABr devices and those which have been operated vs. unoperated..... 150
Figure 5.20. XRD data for pristine and degraded LEDs, typically 2 x 1 cm^2 electrodes were evaporated on a substrate, one was electrically degraded and both the electrodes were delaminated for further characterization. 151

Figure 5.21. SEM characterisation of our control films and our most efficient composition $(PEABr)_{0.4}CsPbBr_3$ before and after operation. The samples were operated and then the Al electrode was delaminated and the TPBi electron injection layer was washed off with chlorobenzene.....152

Figure 5.22 a) Decay of intensity of EL for $(PEABr)_{0.4}CsPbBr_3$ LEDs operated at 20 mA/cm^2 on an absolute scale (inset: The same data on a normalised scale); b) Normalised EL spectra of $(PEABr)_{0.4}CsPbBr_3$ LEDs operated at 20 mA/cm^2 on a log scale showing the growth of a broad shoulder in the emission; c) Decay of intensity of EL $CsPbBr_3$ LEDs operated at 20 mA/cm^2on an absolute scale (inset: The same data on a normalised scale), note the remarkably superior stability compared with $(PEABr)_{0.4}CsPbBr_3$; b) Normalised EL spectra of $CsPbBr_3$ LEDs operated at 20 mA/cm^2 on a log scale showing the growth of a broad shoulder in the emission, note that the shoulder is present in the pristine device whereas it is not in $(PEABr)_{0.4}CsPbBr_3$. 153

Figure 5.23. a) J v L of pristine and degraded $(PEABr)_{0.4}CsPbBr_3$ LED after 1 h of operation at 10 mA cm^{-2}; b) changes in J-V-L characteristics before and after 1 h of operation at 10 mA cm^{-2} 154

Figure 5.24. Changes in J-V-L characteristics of $CsPbBr_3$ LED before and after 1 h of operation at 10 mA cm^{-2}.....155

Figure 5.25. a) Intensity dependence of PLQY of full LED before and after operation for 1 h at 10 mA cm^{-2} ; b) changes in the PL spectrum of $(PEABr)_{0.4}CsPbBr_3$ LED after operation for 1 hour at 10 mA cm^{-2}.....156

LIST OF ABBREVIATIONS

18-crown-6 (CE) - 1,4,7,10,13,16-hexaoxacyclooctadecane

BA - Butylammonium

ChX – Choline Halide

CIE - Commission Internationale de l'éclairage

DMF – Dimethyl formamide

DMSO – Dimethyl sulfoxide

EIL – Electron injection layer

EL - Electroluminescence

EQE_{EL} – External electroluminescent quantum efficiency

EQE_{PV} – External photovoltaic quantum efficiency

F8BT - Poly(9,9-dioctylfluorene-alt-benzothiadiazole)

FA - Formamidinium

FTPS – Fourier transform photocurrent spectroscopy

FWHM – Full width half maximum

GB - Glovebox

HIL – Hole injection layer

HOMO – Highest occupied molecular orbital

ITO – Indium tin oxide

LED – Light-emitting diode

LUMO – Lowest unoccupied molecular orbital

MA - Methylammonium

NIR – Near-infrared

NMA - 1-Naphthyl methylammonium

NPD – 2,2′-Dimethyl-*N,N′*-di-[(1-naphthyl)-*N,N′*-diphenyl]-1,1′-biphenyl-4,4′-diamine

Ox - Oxide

PD - Photodiode

PEA - Phenylethylammonium

PEDOT:PSS - Poly(3,4-ethylenedioxythiophene)-Poly(Styrenesulfonate)

PEIE - Polyethylenimine Ethoxylated

PFN - Poly(9,9-bis(3'-(N,N-dimethyl)-N-ethylammoinium-propyl-2,7-fluorene)-alt-2,7-(9,9-dioctylfluorene))dibromide

PEO – Poly(ethylene oxide)

PL – Photoluminescence

PLQY – Photoluminescence quantum yield

Poly-TPD - Poly(N,N'-bis-4-butylphenyl-N,N'-bisphenyl)benzidine

PVK – Poly(9-vinylcarbazole)

rpm – Revolutions per minute

SEM – Scanning electron microscopy

T_{50} – Time to reach 50% of initial luminance

TCO – Transparent conducting oxide

TFB - Poly(9,9-dioctylfluorene-alt-N-(4-sec-butylphenyl)-diphenylamine)

TPBi - 2,2',2''-(1,3,5-Benzinetriyl)-tris(1-phenyl-1-H-benzimidazole)

TPPO – Triphenylphosphine oxide

TRPL – Time resolved photoluminescence

UV-Vis – Ultraviolet-Visible

XPS – X-Ray photoelectron spectroscopy

XRD - X-Ray diffraction

1 INTRODUCTION

This chapter is not intended to serve as a reference work on semiconductor physics but rather give an overview of the more specialist knowledge required for understanding this thesis. A basic knowledge of band theory and other classical models will be assumed.

1.1 Semiconductors

1.1.1 Charge-carrier recombination

Upon illumination of a semiconductor with electromagnetic radiation with an energy greater than or equal to the band gap (E_g), the excitation of electrons into the valence band can occur, leaving behind an electron vacancy or 'hole'. The dynamics of these charge carriers and how they eventually recombine is of fundamental importance for the functioning of many electronic devices (including light-emitting diodes). Under illumination, the rate of change of the free carrier density for an intrinsic semiconductor, $n(t)$, can be described by the rate equation

$$\frac{dn}{dt} = G - k_1 n - k_2 n^2 - k_3 n^3$$

Equation 1.1

Where G is the generation rate, k_1 is the monomolecular recombination rate constant, k_2 is the bimolecular recombination rate constant and k_3 is the Auger recombination constant. This expression can be rewritten as

$$\frac{dn}{dt} = G - nR_T$$

Equation 1.2

Where R_T is the total recombination rate

A brief overview of the fundamental processes governing these constants will be given below

1.1.1.1 First order recombination

First order recombination can occur *via* three pathways; i) trap-assisted non-radiative recombination, ii) excitonic radiative recombination, and, iii) radiative recombination from injected minority carriers. Trap assisted recombination occurs when a carrier relaxes from the conduction band to the valence band *via* a localised energetic state which is within the band gap (trap state). The physical origin of the trap state is either: i) an imperfection in the crystal lattice such as an interstitial atom or a vacancy or ii) an impurity atom in the lattice such as a dopant, (iii) a defect at the surface of the crystal (dangling bonds, uncoordinated atoms). The relaxation of electrons through this trap state is mediated through the emission of phonons which causes an increase in the temperature of the semiconductor. As no photons are emitted during this process trap assisted recombination is a non-radiative process

Trap-assisted recombination is also known as Shockley Read Hall (SRH) recombination name as such after the physicists who proposed a model which effectively describes the process. The model is described by four processes:

1. The capture of a free electron in the conduction band by an unoccupied trap state whose energy lies within the band gap
2. The emission of a trapped electron back into the conduction band
3. The capture of a hole in the valence band by the same trap state
4. The emission of a trapped hole back into the valence band

If an electron is captured into a trap state where a trapped hole is already located or vice versa they will recombine. Through consideration of these four processes one can derive an expression for the total recombination rate *U*:

$$U = V_{th}\sigma N_T \frac{(np - n_i^2)}{n + p + 2n_i \cosh(\frac{E_T - E_i}{kT})}$$

Equation 1.3

Where V_{th} is the thermal velocity of electrons and holes, σ is the capture cross section of electrons and holes, N_T is the trap concentration, n and p are the concentrations of electrons and holes respectively, n_i is the intrinsic carrier concentration and E_i is the intrinsic Fermi level. We will define the rate constant of SRH recombination as $k_{1\text{-}SRH}$.

The important take away from this equation is the dependence of the non-radiative recombination rate on the relative energy of the trap state to the intrinsic Fermi level. When $E_T = E_i$ the hyperbolic cosine function will reach a minimum and enumerate to 1 resulting in a smaller value for the denominator. Thus, it follows that recombination rate U will be maximum when the trap state energy is exactly in the middle of the gap.

Qualitatively the conclusions from this expression are intuitive, the rate of capture of the carriers into this trap state depends on the energy difference between the band and the trap state. Namely, the smaller the gap the higher the rate of capture, thus if the trap state is close to the conduction band the rate of capture of electrons will be high but the rate of capture of holes will be low. Further these trapped electrons are more likely to be reemitted into the band (de-trapping). Bringing the trap state energy to the middle of the band balances the rate of these two processes resulting in a higher overall recombination rate.

A further conclusion that we can draw from Equation 1.3 is that $k_{1\text{-}SRH}$ is heavily dependent on the number of traps. As previously mentioned, traps are due to imperfections in the crystal lattice and as such are extrinsic properties of the sample.

The second type of monomolecular recombination which can occur is excitonic. Excitonic recombination is a form of radiative recombination. An exciton is a quasiparticle, a concept used in condensed matter physics to describe the bound state of an electron-hole pair which are attracted to each other by the Coulombic force. This force can be described by the equation:

$$F = \frac{1}{4\pi\varepsilon_0\varepsilon_r}\frac{q^2}{r^2}$$

Equation 1.4

Where ε_0 is the permittivity of free space, ε_r is the relative permittivity of the medium, q is the elementary charge and r is the distance between the two charges. The attractive force is described by the exciton binding energy E_b.

Under steady state conditions, there is an equilibrium between excitons and free carriers. If we only consider the 1s state of the exciton and an unbound electron-hole pair state, the ratio of number of electron-hole pairs ($n_{e\text{-}h}$) to excitons (n_{ex}), α can be described by the Saha equation;

$$\frac{\alpha^2}{1-\alpha} = \frac{1}{n_{tot}\,\lambda_T^3}\exp\left(\frac{-E_b}{k_B T}\right)$$

Equation 1.5

Where, explicitly; $\alpha = n_{e\text{-}h} / n_{tot}$, and $n_{tot} = n_{e\text{-}h} + n_{ex}$. λ_T is the thermal de Broglie wavelength ($\lambda_T = \mathrm{h}/\sqrt{2\pi\mu k_B \mathrm{T}}$), and, the *e-h* reduced mass is $\mu = m_e m_h / m_{ex}$ where m_e , m_h and m_{ex} are the masses of the electrons, holes and excitons respectively. Therefore, depending on the temperature of the system and the exciton binding energy E_b the relative contribution of free carriers and excitons to the radiative recombination current varies. In light-emitting diodes it is beneficial to have a high exciton binding energy as this will encourage the localisation of electron-hole pairs which can then recombine radiatively. However, it is not the only consideration one must make as other factors such as electron and hole mobilities, and trap state densities are also important. We will define the rate constant of excitonic radiative recombination as $k_{1\text{-}Ex}$.

A further class of first-order recombination is radiative recombination of carriers in an electronically doped semiconductor. As there is an excess of one type of carrier at equilibrium, the recombination is dependent on the concentration of the minority carrier. As such, one will observe a linear increase in photoluminescence with the concentration of the minority carrier, leading to first order kinetics. We will define the rate constant of minority carrier radiative recombination as $k_{1\text{-}MC}$.

1.1.1.2 Bimolecular

Bimolecular recombination directly relates to the inverse process of absorption of electromagnetic radiation by a semiconductor. It requires the recombination of an electron in the conduction band with a hole in the valence band to produce a photon. As this event requires both particles it is dependent upon both the electron density (n_e) and hole density (n_h) and therefore the rate of its occurrence is dependent on $n_e n_h = n^2$, in the absence of

doping. As such, the rate constant k_2 is a mostly intrinsic property of the material which does not vary with processing conditions. However, the externally measured value for k_2 will vary depending on factors such as film roughness and morphology which will be discussed below. There may be slight variations if the material is of very different crystallite size i.e. single crystal *vs.* nanocrystal, or if the material is distributed in a medium of a differing relative permittivity.

1.1.1.3 Many-Body or Auger

Many- bodied recombination (or Auger) is the recombination process by which an electron in the conduction band recombines with a hole in the valence band and transfers energy and momentum to another electron or hole. Auger recombination is a non-radiative recombination process, and, being dependent on three carriers is thus strongly dependent on carrier density. The Auger recombination constant k_3 is again a more intrinsic property than k_1 and depends strongly on band structure. The process of recombination requires the conservation of energy and momentum and thus is greatly facilitated by available states which often originate from additional bands other than the conduction and valence band.

1.1.2 Photoluminescence quantum yield

The photoluminescence quantum yield (PLQY) is defined as the ratio of photons emitted to photons absorbed by a sample. If we consider the various decay pathways for excited charge carriers we have just discussed we can write different expressions for the internal PLQY depending on the nature of the semiconductor.

For case 1 we consider a heavily doped semiconductor such that all radiative recombination is proportional to minority carriers:

$$\text{(Case 1): internal PLQY} = \frac{k_{1-MC}}{k_{1-SRH} + k_{1-MC}}$$

Equation 1.6

This relation only holds when the background carrier density is significantly larger than the minority carrier density. After this point a transition to bimolecular recombination behaviour (case 3) will be observed.

For case 2 we consider a semiconductor with an $E_b >> k_BT$ such that all radiative recombination is excitonic:

$$\text{(Case 2): internal PLQY} = \frac{k_{1-Ex}}{k_{1-SRH} + k_{1-Ex}}$$

Equation 1.7

For case 3 we consider an undoped semiconductor where all radiative recombination is bimolecular:

$$\text{(Case 3): internal PLQY} = \frac{\text{radiative recombination rate}}{\text{total recombination rate } (R_T)} = \frac{nk_2}{k_{1-SRH} + nk_2 + n^2k_3}$$

Equation 1.8

Where *n* is the free carrier concentration.

For brevity we will only cover these 3 cases, however, there can be systems which have more complex behaviour – for example a moderately doped semiconductor with $E_b \approx k_BT$ – and many more could be imagined.

It is important to distinguish between the *internal* and *external* PLQY – the internal PLQY is described by Equation 1.8. The external PLQY (in the absence of photon recycling) can be defined by:

$$\text{external PLQY} = \text{internal PLQY} \times \text{light extraction efficiency}$$

Equation 1.9

Where the light extraction efficiency (LEE) is the ratio of emitted photons which escape the sample to the total number emitted. The light extraction efficiency depends on i) the refractive index (*n*) of the sample, and, ii) the morphology of the sample. For a smooth, planar film with no photon recycling, the LEE cannot exceed the ray-optical limit (Snell's law);

$$\text{LEE} < \frac{1}{2n^2}$$

Equation 1.10

The thickness of the film will affect the amount of waveguided *vs* outcoupled light so planar films of different thicknesses could have the same internal PLQY but different external PLQY. Morphology and structure of the film will also affect the LEE – a

discontinuous or rough film can have a higher LEE because photons that would be waveguided in the film can be scattered by features which are of a similar length scale and potentially outcoupled.

In the presence of photon recycling the LEE of a smooth, planar film can increase beyond the ray-optical limit. Photon recycling is when a photon is reabsorbed and re-emitted by the active layer. If significant photon recycling is occurring then photons which would have been waveguided can be re-emitted into an outcoupled mode. The LEE in the presence of photon recycling ($\mathrm{LEE_{pr}}$) can be defined by:

$$\mathrm{LEE_{pr}} = \frac{\mathrm{LEE}}{1 - f_{ra} \times \mathrm{PLQY(internal)}}$$

Equation 1.11

Where f_{ra} is the proportion of emitted photons which are reabsorbed by the active layer. In principle it is possible to calculate the internal PLQY however the thin film samples prepared in this thesis often have different degrees of roughness and continuity making its determination very difficult. In this thesis all PLQY measured and reported is the *external* PLQY. Therefore, considerations about the roughness and continuity of the film must be made.

We will now examine how the *internal* PLQY varies as a function of carrier density depending on the i) the different cases of semiconductors which we have discussed, and, ii) the values of $k_{1\text{-}SRH}$, $k_{1\text{-}Ex}$, $k_{1\text{-}MC}$, k_2 and k_3. For case 1 and case 2 we have the simple relation that the PLQY will not vary with carrier density. The absolute value of the PLQY is determined by the value of $k_{1\text{-SRH}}$. Below we will consider the case of an undoped semiconductor where bimolecular recombination is the only contribution to radiative recombination (case 3). We will fix the recombination constants at typical values for the semiconductor methylammonium lead iodide ($MAPbI_3$) and vary them individually. First, we vary $k_{1\text{-}SRH}$ (Figure 1.1) as we have previously stated that this is an extrinsic value which is highly dependent on processing. We observe the two intuitive results by increasing $k_{1\text{-}SRH}$ (which is the physical result of increasing trap state density), which are, i) there is a reduction in the peak value of the PLQY, and, ii) the carrier density required to reach peak PLQY increases.

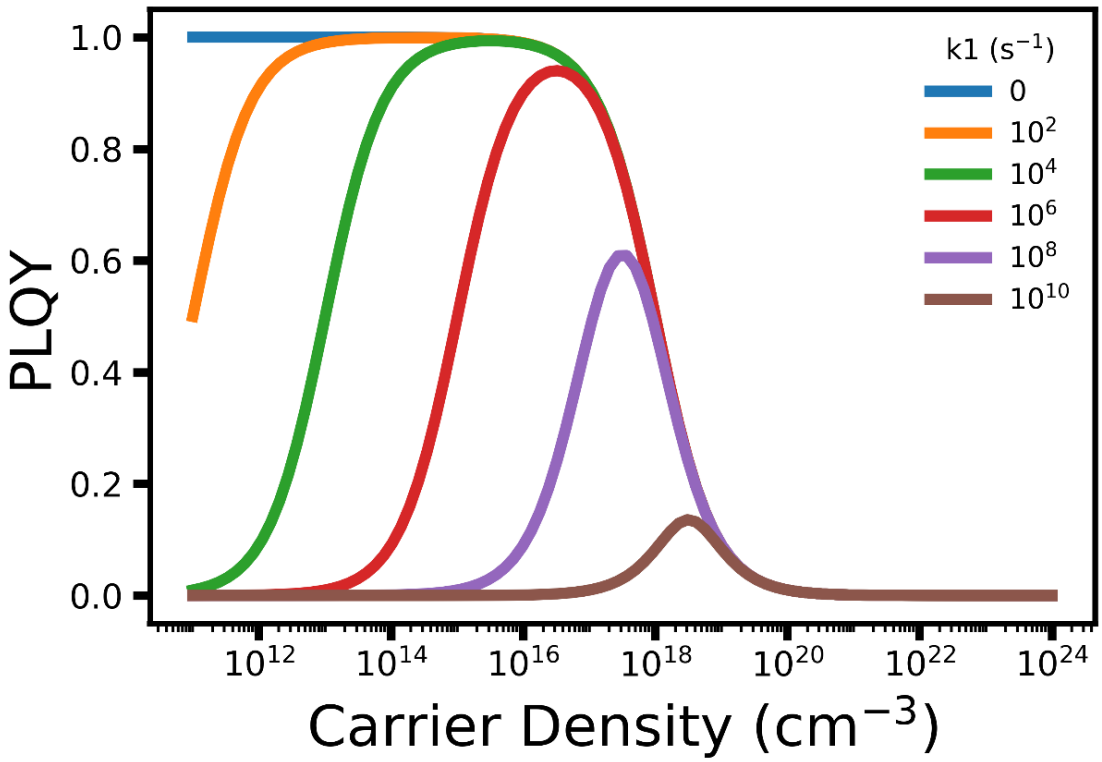


Figure 1.1 The variation of carrier density dependent PLQY with different values for $k_{1\text{-}SRH}$. k_2 = 10^{-10} cm^3 s^{-1}; k_3 = 10^{-28} cm^6 s^{-1}.

From this plot, and, the consideration of case 1 and case 2 above, we can conclude that for devices where radiative recombination is desirable (such as light-emitting diodes) the absolute minimisation of $k_{1\text{-}SRH}$ is a key target of experimentalists.

If we observe Figure 1.2 in which k_2 is varied with fixed values for k_1 and k_3 we can observe that a higher radiative recombination rate is desirable for light emitting applications. Experimentalists are limited in modifying the value of k_2-internal but changes in the dielectric medium and crystallite size are potential routes of modification to improve response characteristics of devices such as light emitting diodes. However, k_2-external can be varied by increasing the fraction of outcoupled light though strategies such as film texturing. This strategy is often adopted by researchers in light emitting diodes to increase the externally measured luminescence efficiency. Interestingly, indirect bandgaps have much smaller values of k_2 (~10^{-13} cm^3 s^{-1}) which means it is much more challenging to make LEDs with these materials.

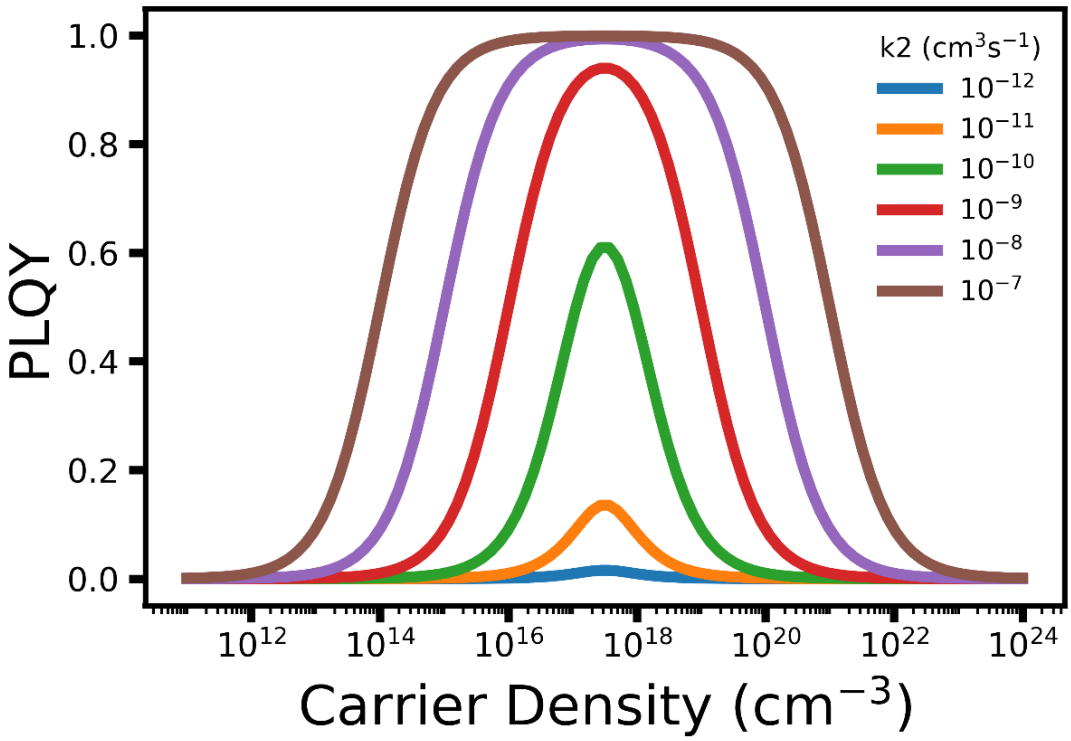


Figure 1.2 The variation of carrier density dependent PLQY with different values for k_2. $k_1 = 10^7$ s^{-1}; $k_3 = 10^{-28}$ cm^6 s^{-1}.

If we observe Figure 1.3 in which k_3 is varied with fixed values for k_1 and k_2 we can observe that a lower Auger recombination rate is desirable. Again, this is an intrinsic property of the material so reducing it is not possible for bulk semiconductors. However, there are examples where the Auger recombination rate can be increased in semiconductors, for example in quantum well structures which are used in gallium nitride LEDs. In this instance spatial confinement of the carriers within a smaller volume of the emissive layer causes an increase in the externally measured Auger recombination constant.

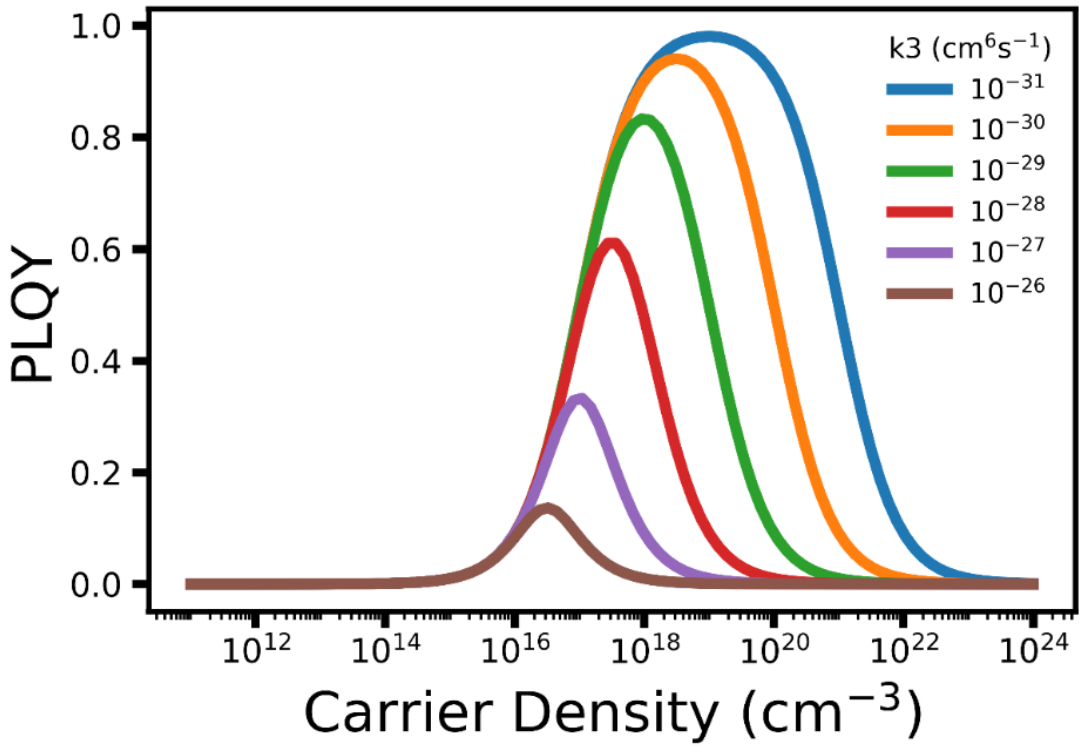


Figure 1.3 The variation of carrier density dependent PLQY with different values for k_3. $k_1 = 10^7$ s^{-1}; $k_2 = 10^{-10}$ cm^3 s^{-1}.

Another key observation is that while reduction of the Auger recombination constant does increase the peak value of the PLQY it moves that peak value to higher carrier densities. This would become important for light emitting applications if the carrier density at which the peak PLQY is achieved is greater than those experienced in the device.

Overall one can see that the most beneficial recombination constant to focus research efforts on is k_1. This can be achieved through a variety of different experimental strategies which be discussed in the ensuing chapters of this thesis.

1.1.3 Junctions

Semiconductor devices involve the formations of junction of both different materials and the same material with differing doping densities. A brief description of these different junctions, their utility and applications will form the following section.

1.1.3.1 *pn* homo junction

The *pn* homojunction is a very useful and important example to understand the formation of many different semiconductor devices. Through understanding of the theory of how a *pn* homojunction is formed we can extend our conceptual understanding to more complicated examples of junctions in semiconductor devices

First, we consider two slabs of semiconductor which are *n* and *p* doped respectively (formation summarised Figure 1.4). These two slabs of semiconductor are made of the same material and have identical positions of their conduction and valence bands. However, due to doping the positions of their Fermi level is shifted towards the valence band for the *p* doped sample and towards the conduction band for the *n* doped material. If we bring these two slabs together so that they are in electronic contact, an equilibration of the Fermi levels will take place. Electrons will diffuse from the *n* doped region into the *p*-doped region and holes will diffuse from the *p*-doped region into the *n*-doped region. This will cause the build-up of a region of space charge in each slab of opposite sign and therefore an electric field. This electric field builds up until it prevents the flow of charges from one slab to another and equilibrium is reached. In this equilibrium state the region of ionised dopants has been 'depleted' of free carriers initially introduced by the dopants and is thus referred to as the depletion region. The potential that has built up can be referred to as the diffusion voltage V_D.

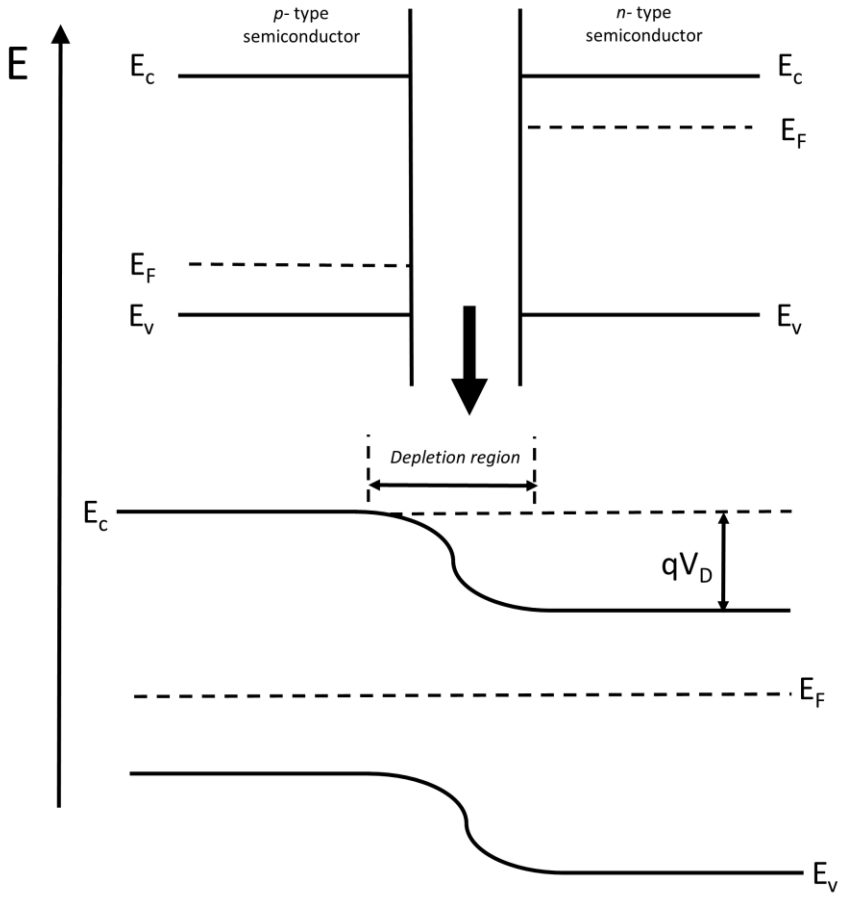


Figure 1.4 Schematic showing the formation of a *pn* homojunction

The current- voltage characteristics of a *pn* diode were first described by Shockley and thus referred to as the Shockley diode equation. In reverse bias the equation can be approximated as:

$$J = J_0\left(\exp\left(\frac{qV}{kT}\right) - 1\right)$$

Equation 1.12

Where J_0 is the saturation current, q is the elementary charge, V is the applied voltage, k is the Boltzmann constant, and T is the temperature. One can see a plot of equation 1.6 for a diode with area 1 cm^2 with an arbitrary value for J_0 = 1 mA in Figure 1.5. Under reverse bias (i.e. a negative voltage) the current will saturate at the value of the J_0

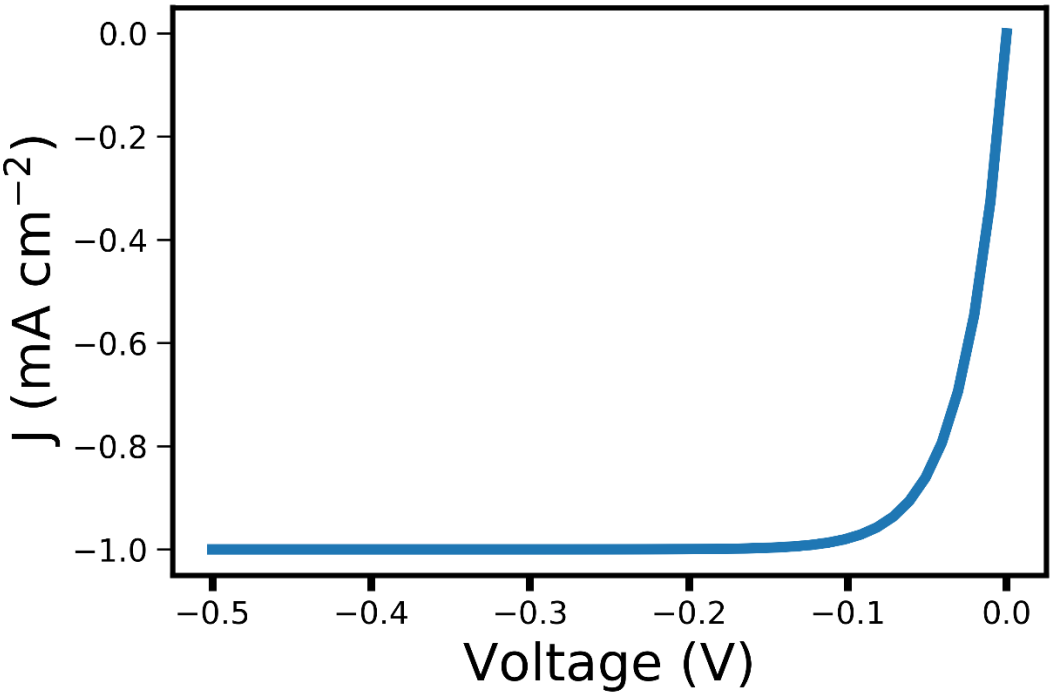


Figure 1.5 Plot showing saturation of current in reverse bias at a nominal value for J_0 of 1 mA.

In forward bias conditions

$$J \propto \exp\left(\frac{q(V - V_D)}{kT}\right)$$

Equation 1.13

Where V_D is the previously mentioned diffusion voltage that has built up at the p-n homojunction. This equation suggests that as the diode voltage approaches the diffusion voltage of the semiconductor the current will exponentially increase. The diffusion

voltage is dependent on the doping and the bandgap of the semiconductor, for a *pn* homojunction in the high *p* and *n* doping regime the diffusion voltage can be approximated as the bandgap divided by the elementary charge *q*. The effect of the diffusion V_D being close to the bandgap of the material is shown clearly in Figure 1.6.

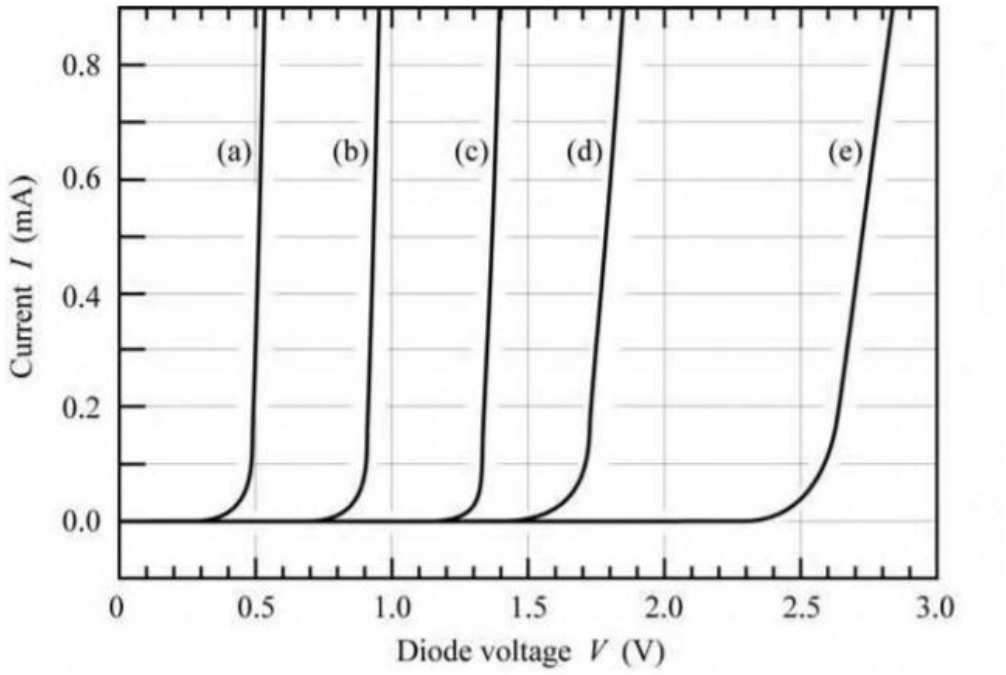


Figure 1.6 IV characteristics of *pn* homojunctions made from different semiconductor materials showing a clear difference in onset voltage. a) Ge E_g = 0.7 eV; b) Si E_g = 1.1 eV; c) GaAs E_g = 1.4 eV; d) GaAsP E_g = 2.0 eV; e) GaInN E_g = 2.9 eV. Figure credit.[1]

pn junctions have been of great use in the fabrication of efficient LEDs as

i) Doping of both the n and p regions means one is able to achieve Ohmic contact with the electrodes. This allows for more efficient injection of carriers with reduced resistive heating.

ii) The carriers that are injected diffuse into the region of opposite conductivity where they will encounter a large concentration of carriers of opposite charge with which they can recombine radiatively with high probability.

1.1.3.2 Metal – semiconductor junctions

Metal semiconductor contacts abound in semiconductor devices and applications. There are two types of electronic junctions which can occur when a metal is contacted with a semiconductor which are the Ohmic junction and the Schottky diode. We will consider

the formation of a junction between two metals of differing Fermi levels with an *n* doped semiconductor, similar behaviour would be observed for a *p* type semiconductor.

1.1.3.2.1 Schottky Diode

If we bring a metal with a Fermi level lower than that of the n-type semiconductor, electrons from the semiconductor will flow into the metal until the Fermi levels equilibrate. This will leave behind a region of positive space charge from the positively ionised dopants in the semiconductor which causes the bands to bend downwards. The deformation of the band structure results in the formation of an energetic barrier for injection of electrons from the semiconductor into the metal (Figure 1.7). The barrier to injection grows in reverse bias and decreases in forward bias until electrons are easily injected from the metal into the semiconductor. This rectifying behaviour is why this junction is called a Schottky diode and its current-voltage characteristics can be described by Equation 1.13.

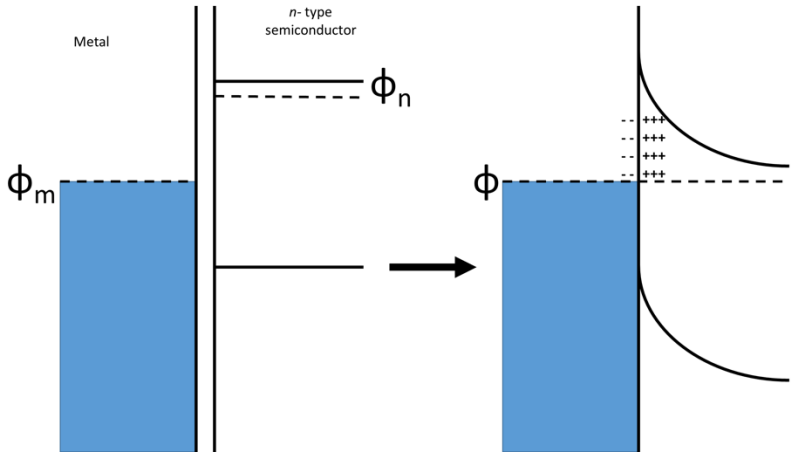


Figure 1.7 Schematic showing the formation of a Schottky diode by bringing a metal and an *n* type semiconductor into contact.

1.1.3.2.2 Ohmic Junction

If we bring a metal which has a Fermi level closer to vacuum than the Fermi level of the semiconductor we have different behaviour. In order to equilibrate the Fermi level and reduce their energy, electrons flow from the metal into semiconductor, which results in an upward band bending of the semiconductor. There exists no potential barrier for the flow of electrons from the semiconductor to the metal, therefore, injection occurs in a linear fashion. This injection obeys Ohm's law thus giving it its name

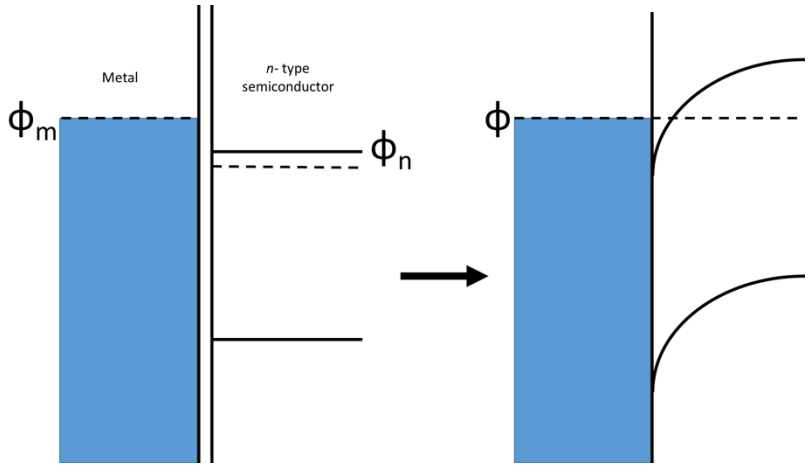


Figure 1.8 Schematic showing the formation of an Ohmic Junction by bringing a metal and an *n* type semiconductor into contact.

1.1.3.3 Heterojunctions

Semiconductor heterojunctions are formed when two different semiconducting materials are in electronic contact with each other. Being entirely different materials with different band structures means that a far more diverse array of junctions can be fabricated in this fashion. There are 3 classes of heterojunction, which are defined by the relative positions of the conduction and valence band of each semiconductor. These are the 'straddling gap' (type I), 'staggered gap' (type II) and 'broken gap' (type III) heterojunctions, shown in Figure 1.9.

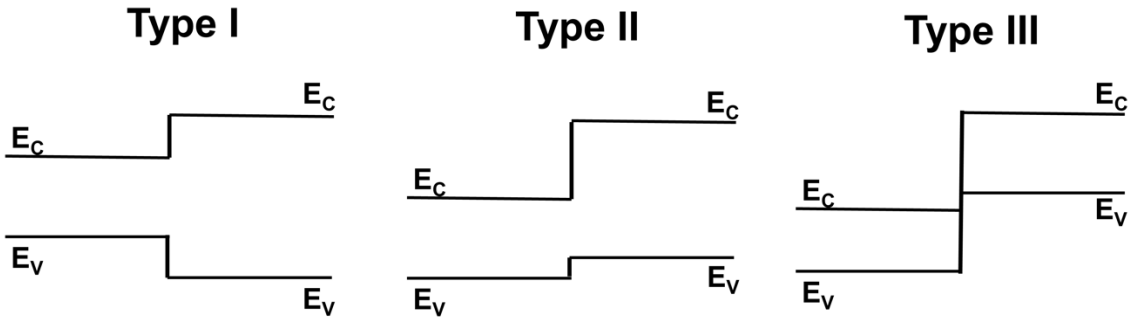


Figure 1.9 Schematic showing the relative energetic position of bands to form the 3 types of heterojunctions

Type I heterojunctions are of particular use for both thin film solar cells and LEDs as they can provide charge selectivity at an interface. Judicious choice of the electron and hole injection layers in a thin film LED can also aid with the confinement of charge carriers within the emissive layer. Looking at the type I heterojunction in Figure 1.9 we consider injection of electrons and holes from opposing interfaces. Once injected, there is an energetic barrier for the charges to escape from the emissive layer. If this barrier is much

greater than the thermal energy, the carriers are confined within the emissive layer whereby they can either recombine radiatively or non-radiatively. This confinement strategy has been widely used in GaN LEDs for the formation of 'quantum wells' which greatly enhance their efficiency.

1.2 Metal Halide Perovskites

Metal halide perovskites are a class of semiconductors which can be processed by techniques such as thermal evaporation[2] or a large variety of solution processing methods including spin coating,[3] spray coating,[4] inkjet printing[5] and slot die coating.[6] Further, they have recently shown great promise as the active layer in solar cells,[3] light emitting diodes,[7] transistors[8] and optically pumped lasers.[9] The focus of this thesis is developing metal halide perovskites as the emitter in light-emitting diodes

1.2.1 Overview

Perovskite as a term describes a class of materials which crystallise with the same periodic arrangement of atoms and stoichiometry as the material calcium titanate ($CaTiO_3$). We can thus state the general formula to be ABX_3 where A and B are cations and X is an anion. They do not necessarily have identical crystal structures as they can crystallise with different symmetries (e.g. cubic, tetragonal or orthorhombic form). The ideal cubic structure is characterised by; i) a network of corner sharing octahedra with B-site cations being coordinated by X-site anions, and, ii) cuboctahedrally coordinated A-site cations which support the network of octahedra through occupation of the voids left by the space between them (Figure 1.10)

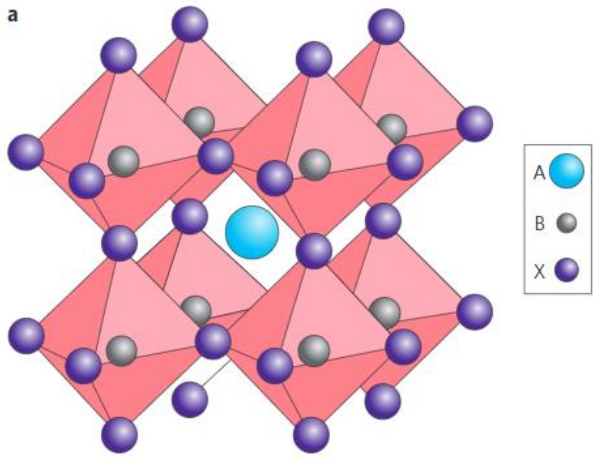


Figure 1.10 The structure of a cubic perovskite, showing corner sharing octahedra and a central cuboctahedrally coordinated cation. Figure credit[10]

The size of the A-site cation must be; i) large enough to stabilise the network of octahedra, and, ii) not too large that it will not 'fit' into the void left by the octahedra. This consideration can be distilled into the Goldschmidt tolerance factor (*t*) which predicts whether a perovskite structure will form based on the relation between the ionic radii (Equation 1.14).

$$t = \frac{r_A + r_X}{\sqrt{2}(r_B + r_X)}$$

Equation 1.14

Where r_A, r_B and r_X are the ionic radii of the A, B and X ions respectively

If:

$t > 1$; the A-site cation is too large to occupy the space between the octahedra and the material will crystallise in a hexagonal or tetragonal structure.

$t = 0.9 – 1$; the ratio of the A-site to B-site cations is ideal and the material should crystallise in a cubic structure.

$t = 0.7 – 0.9$; the A-site cation is not an ideal size to fit into the space between the octahedra, however the perovskite structure may still persist but in a different crystal symmetry (i.e. orthorhombic or tetragonal)

$t < 0.7$; The A-site cation is too small to stabilise the perovskite structure. The material may be in any of the various crystal symmetries.

The Goldschmidt tolerance factor is not perfect as a prediction of whether a compound will crystallise into a perovskite structure as it is only a geometric consideration and does not consider factors such as enthalpy of formation and kinetic trapping[11] which can cause some perovskites to form outside of the predicted region.

Perovskite materials are very compositionally diverse as there are a wide variety of ions which satisfy these conditions. As such, perovskite materials can have many different properties, including superconductivity, ferroelectricity, ionic conductivity and strong photoluminescence. Due to their compositional diversity, it is possible to engineer these materials through substitution to optimise these properties.

A subclass of the family of perovskite materials is *metal halide perovskites*, which are defined by their X-site anions being halide ions and their B-site cation being a metal ion, the A-site cation can be either be a metal or organic cation. In particular the materials which will be studied in this thesis are those where the B-site cation is Pb^{2+}. These materials are synthetic and do not occur naturally in the Earth's crust. The first report of lead halide perovskites were the synthesis of cesium lead halides ($CsPbX_3$) in 1893,[12] although they were not identified as the perovskite structure (X-Ray crystallography was not developed at this time). They remained largely unstudied until a concerted effort was undertaken in the 80s and 90s to study their optoelectronic and magnetic properties, where in particular they were studied for transistors[8] and light-emitting diodes.[13] During this research period, the concept of organic A-site cations into the perovskite structure was introduced, in particular the replacement of cesium with methylammonium (MA or $CH_3NH_3^+$) was discovered to give a perovskite structure.[14] After the period of intensive study, the field went relatively quiet as the organic-inorganic hybrid materials had relatively poor stability and could only achieve electroluminescence at liquid nitrogen temperatures.

1.2.2 Dimensionality in metal halide perovskites

In the previous section, we discussed the geometric constraints upon the A-site cation and the Goldschmidt tolerance factor. In the case of organic- inorganic metal halide perovskites such as $MAPbBr_3$, if we increase the size of our organic A-site cation to a size which can no longer fit into the cavity between the octahedra (i.e. butylammonium) a new two-dimensional phase can form. This phase has a stoichiometry of A_2PbX_4 and consists of layers of lead halide corner sharing octahedra interleaved with 'spacer cations' separating the layers. This change in structure has strong implications on the optical

properties of the material as charge carriers are confined within the perovskite layer. As a result, there is a large increase in exciton binding energy, and a blue shift in the absorption and photoluminescence due to quantum confinement effects.

This class of phase is called the Ruddlesden-Popper phase and was first synthesised and characterised by its namesakes through the materials Sr_2TiO_4 and Ca_2MnO_4 in 1957.[15] Perovskites of the type ABX_3 are referred to as '3D' perovskites owing to their 3 dimensional network of corner sharing octahedra and perovskites of the type A_2BX_4 are referred to as '2D' perovskites and are not perovskite under the strict definition given above.

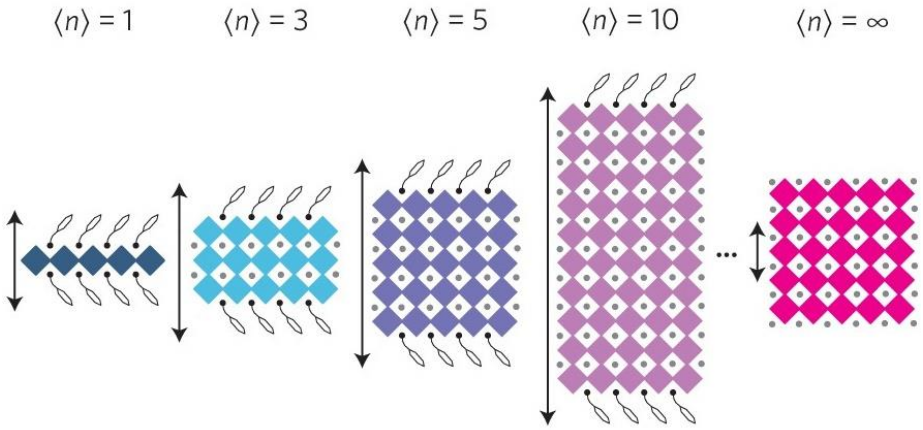


Figure 1.11 Schematic showing transition from a 2D perovskite (n = 1), to quasi-2D perovskite (n>1), and, 3D perovskite (n = ∞) Figure credit[16]

Interestingly it is possible to make intermediate phases where multiple layers of corner sharing octahedra are interleaved by spacer cations. These so called quasi-2D phases are described by the number of layers of octahedra there are between the spacer cations, (i.e. 1 layer → 'n=1', 2 layers → 'n = 2', 3 layers → 'n = 3' …) (Figure 1.11) these materials have the general formula $A_2A`_{n-1}B_nX_{3n+1}$ where A is the spacer cation and A` is a conventional A-site cation like MA. From the standpoint of optical applications this is interesting as the optical properties can be tuned based on the number of layers (Figure 1.12). In 2016, Stoumpos *et al.* synthesised and characterised methylammonium lead iodide and the corresponding n = 1, 2, 3 and 4 phases using butylammonium as a spacer cation.[17] This demonstrated the ability to make a wide range Ruddlesden-Popper perovskite phases in the lead halide perovskite subclass.

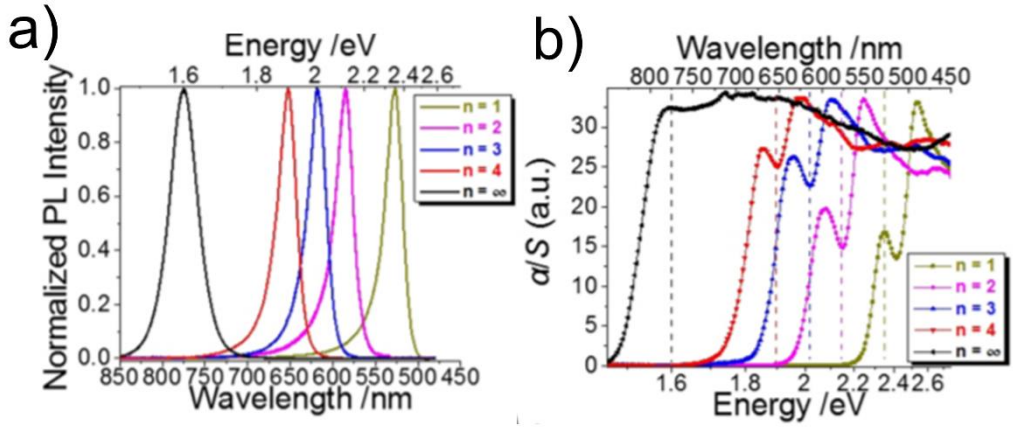


Figure 1.12 a) emission, and, b) absorption (inferred from reflectance) of a series of quasi-2D perovskite single crystals where A = MA and the spacer cation is butylammonium. Figure Credit[17]

1.2.3 Perovskite photovoltaics

A further effort was made to incorporate lead halide perovskite materials into photovoltaic devices from 2009 onwards, which yielded impressive, unprecedented results. Kojima *et al.* incorporated the two metal halide perovskites methylammonium lead iodide ($CH_3NH_3PbI_3$) and methylammonium lead bromide ($CH_3NH_3PbBr_3$) into a photovoltaic device structure which was heavily used in the dye sensitised solar cell community.[18] The researchers achieved high open circuit voltages of 0.96 V, however very poor stability under illumination due to the presence of a liquid electrolyte and an efficiency of 3.1% meant that the publication did not garner much immediate interest. In 2012 Lee *et al.* made two breakthroughs which increased the efficiency up to 10.9% causing an explosion in perovskite research.[3] These were; i) replacing the liquid electrolyte with the solid state hole transport material (HTM) 2,2',7,7'-Tetrakis[N,N-di(4-methoxyphenyl)amino]-9,9'- spirobifluorene (spiro-OMeTAD) which improved the stability greatly, and, ii) replacing the mesoporous TiO_2 with mesoporous Al_2O_3. This final point was surprising as Al_2O_3 is an insulator whereas TiO_2 is an *n*-type semiconductor – demonstrating that $CH_3NH_3PbI_3$ is capable of long range charge transport rather than relying on the mesoscopic TiO_2 reducing the distance that charge needs to travel.

1.3 Light-Emitting Diodes

1.3.1 History of LEDs

Light-emitting diodes (LEDs) are solid state devices which emit light through the phenomenon of electroluminescence (EL) as opposed to incandescence (i.e. visible black body radiation) and show rectifying behaviour. There are some reports of EL from SiC Schottky diodes[19,20] in the early twentieth century which mark the nascence of LEDs though these were of very low efficiency. Infrared LEDs using an amphoterically Si doped GaAs *pn* junction grown through liquid phase epitaxy on a GaAs wafer resulted in external quantum efficiencies of electroluminescence of up to 6% which was a breakthrough for LED technology.[21] Another breakthrough came from the successful *p*-doping of GaN using Mg acceptors activated through electron-beam irradiation[22] which allowed the fabrication of blue emitting GaN *pn* junction LEDs.[23] This breakthrough allowed for the creation of efficient white LEDs for solid state lighting which are ubiquitous in the home and office today and have presented considerable energy savings over conventional incandescent lighting.

The subject of this thesis is not on this class of LEDs but thin film LEDs which came into development through the discovery of electroluminescence from organic materials by Bernanose *et al.* in 1953.[24] This discovery eventually resulted in the implementation of a bilayer thin film structure of evaporated organics by Tang and Slyke[25] in 1987 and subsequently the discovery of EL from solution processed polymeric semiconductors by Burroughes *et al.*[26] in 1990. These two discoveries caused a rapid increase of research into organic EL and the development of the field of organic LEDs (OLEDs). This class of devices consists of multilayer thin film structures which are optimised for EL efficiency through improvement of, i) balanced charge injection, ii) charge confinement, and, iii) light outcoupling. This concerted effort into the field of OLEDs resulted in the thin film LED structure which will be the focus of this thesis.

1.3.2 Quantum wells in LEDs

As mentioned in 1.2.2 metal halide perovskites can form quantum well structures. The use of quantum well structures has been widely exploited in commercial lasers and LEDs. An archetypal example is the GaN/AlGaN system. The advantages of using a quantum well system are:

i) Quantum confinement causes a quantisation of the energy levels and increase the bandgap. This allows the bandgap to be tuned.

ii) There is increased spatial confinement of electrons and holed which increases the probability of radiative recombination

iii) The density of states is independent of energy (as opposed to being dependent on $E^{1/2}$ as with unconfined semiconductors. This increases the probability of radiative recombination because there are many more states available at the band edges.

1.3.3 Perovskite thin film LED structure

The device structures that are used in this thesis are multi-layered thin film structures which are designed to inject a balanced current of electrons and holes into an emitter layer (the metal halide perovskite), where they can recombine radiatively. In order to achieve this we build the device up layer by layer from a glass substrate coated with a transparent conductive electrode (TCO) (Figure 1.13.a.). The TCO (which is either indium tin oxide or fluorine doped tin oxide) allows light generated in the device be emitted normal to the plane of the substrate and into the environment.

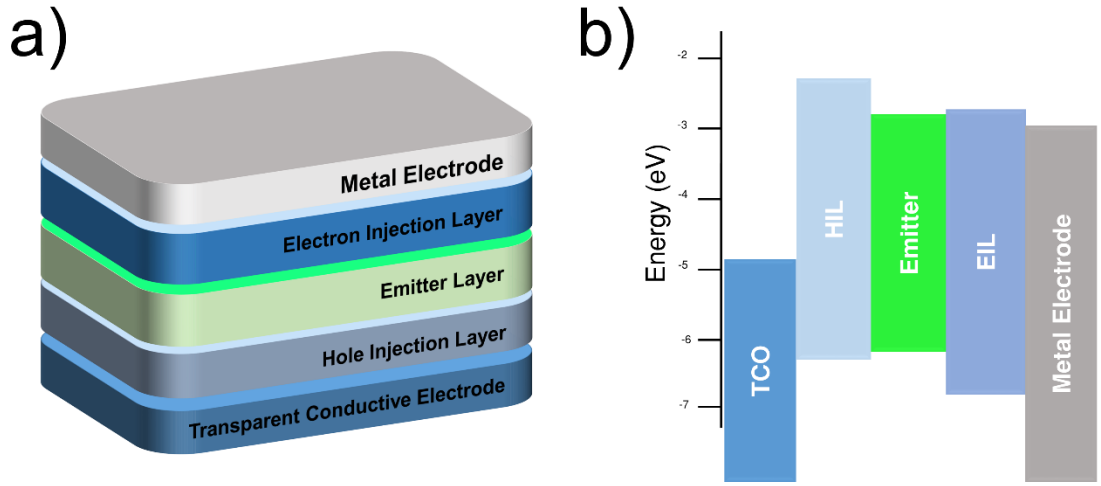


Figure 1.13 Schematic of a typical perovskite LED device structure and the relative energetic alignment of the various layers.

Following the TCO either a hole injection layer (HIL) is deposited – this layer is a p-type semiconductor (typically a polymer) which has been designed to carry a unipolar current of holes and have a good energetic alignment with the valence band of the emitter layer to allow facile injection (Figure 1.13.b.). Ideally this should be a type I heterojunction as shown in Figure 1.13.b. as this will i) have a small barrier for injection of holes, and, ii)

will confine the electrons within the emitter layer as there is a large barrier for them to pass through to the TCO.

The emitter layer can be a variety of materials including polymers[27], colloidal quantum dots[28], and, metal halide perovskites[29] and is optimised to have high PLQY on the injecting contacts while maintaining a high enough mobility to allow injection. Upon this an electron injection layer (EIL) is deposited which is designed to carry a unipolar current of electrons which can be injected easily into the conduction band of the emitter. Finally, a metal electrode is deposited which allows us to make contact and complete our circuit to inject carriers and cause emission in our active layer. The structure described here is called a *pin* device structure (p-type/ intrinsic/ n-type) where the emitter layer is assumed to be an intrinsic semiconductor. Within this thesis there are also *nip* device structures where the order of the p- and n- type are reversed. Both of these devices operate on the same principles and the choice of either order is down to engineering and optimisation concerns as to how to produce the most efficient or stable device.

1.3.4 Radiometry and Photometry

In order to describe the properties of electromagnetic radiation (such as photon energy and photon flux) one can use radiometric units. This allows us to characterise all electromagnetic radiation across the entire spectrum in a standardised way. However, when producing LEDs which emit at visible wavelengths for applications such as displays (as is the subject of this thesis) it is useful to reference the properties with respect to the perception of the human observer.

Electromagnetic Radiation emitted by -	**Radiometric quantity (units)**	**Photometric quantity (units)**
a source in total	Radiant power (W)	Luminous flux (lm)
a source per unit solid angle (i.e. directionally)	Radiant intensity (W sr^{-1})	Luminous intensity (cd)
a location on a surface per unit projected solid angle (i.e. directionally)	Radiance (W sr^{-1} m^{-2})	Luminance (cd m^{-2})

Table 1.1 Comparison of equivalent radiometric and photometric units.

This field is called photometry and its basis is the sensitivity of the human eye to different wavelengths of light. A table of relevant radiometric and equivalent photometric units are

shown above (Table 1.1).This allows us to quantify parameters such as colour purity and brightness using predefined units. We will discuss these two specific parameters below.

1.3.4.1 The Lumen and Candela

The perceived light intensity of LEDs by the human eye can be more technically be described as the *luminous intensity*, this is quantified by the units Candela (cd). The unit of candela has its origins in the emitted intensity of a standard candle but is today now defined as *a monochromatic light source emitting 1/683 of a watt at a wavelength of 555 nm into a solid angle of 1 steradian.*

The Lumen (lm) differs from the cd in that it describes the *luminous flux* which is the *total* amount of visible light which is emitted by a light source. The two quantities are related to each other through units of solid angle steradians (sr); 1 cd = 1 lm / sr. Given that a sphere makes up 4π sr of solid angle one can conclude that a light source which emits 1 cd of luminous intensity in all directions has a luminous flux of 4π (~12.6) lm.

In this thesis the *luminance* of LEDs is discussed as a unit of merit in LEDs. This is defined by the units cd m^{-2} which is the luminous flux per unit *projected* solid angle per unit *source* area. The source area in this case will be our LED which has an area of ~9 mm^2.

1.3.4.2 The Photopic Response of the Human eye

In the previous section the wavelength of 555 nm was chosen for the monochromatic wavelength of light which defined the candela. This wavelength is chosen because it is the peak in the photopic response of the human eye (or the luminous efficiency function). The photopic response curve (Figure 1.14) shows the sensitivity of the eye to a given wavelength when in the photopic regime; this is when the luminance level is relatively high (> 3 cd/ m^2) and signal from the cone cells in the eye is dominating vision. The luminous efficiency function is standardised by the Commission Internationale de l'Éclairage (CIE) and allows us to convert the radiance of any given source of electromagnetic radiation into luminance.

This standard is very useful when fabricating LEDs for displays as it allows us to make practical displays that have equal *perceived* contributions from each of the red, green and blue pixels. Because the luminous efficiency function peaks at green (~550 nm) and is much lower at red (~650 nm) and blue (~450 nm) in order for the red and blue LEDs to have the same luminance as the green LED, they will have to have a higher radiance.

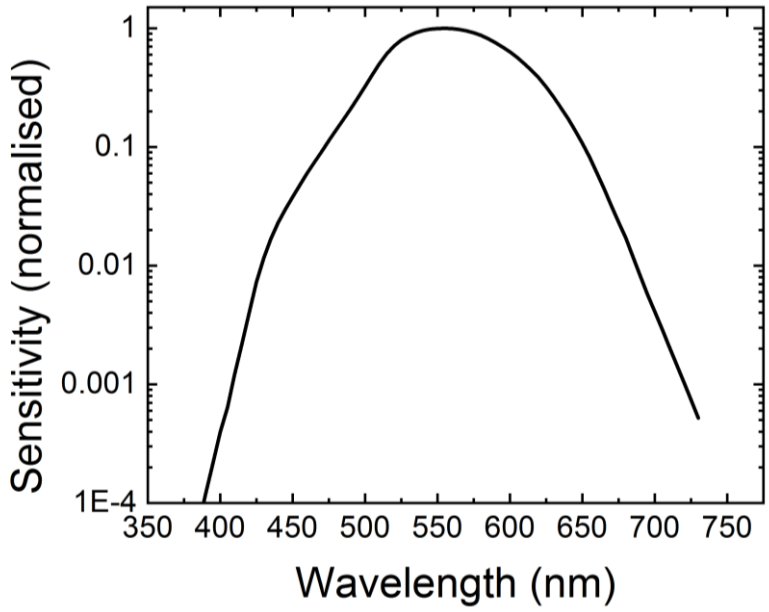


Figure 1.14 The luminous efficiency function as defined by the CIE. This represents the average sensitivity of the human eye to visible wavelengths.

1.3.4.3 Chromaticity

Another important aspect of LEDs for display is their *chromaticity* which describes the colour of the light without regard for its luminance. The CIE chromaticity chart is shown in Figure 1.15, all visible colours to the average human eye can are contained within the horseshoe shape of the graph. Through the use of CIE colour matching functions (Figure 1.16) we can generate an xy coordinate on the CIE colour chart for any spectral power distribution of visible light.

This is done by:

i) integrating the multiple of the spectrum with the 3 functions to generate the parameters X,Y and Z

ii) Normalising the values of X and Y using $x = \frac{X}{X+Y+Z}$ $y = \frac{Y}{X+Y+Z}$

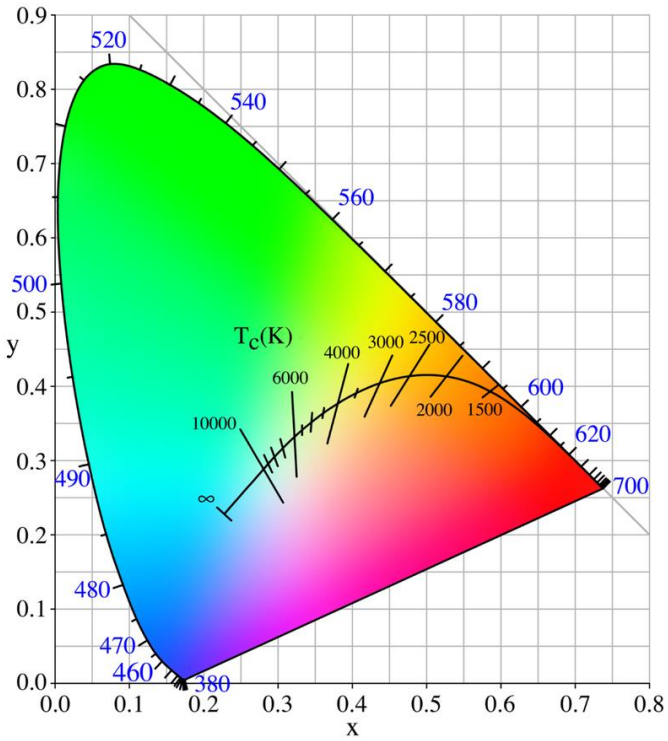


Figure 1.15 The xy CIE chromaticity chart. Figure Credit.[30]

Once we have these coordinates, we can place the colour of our LED on the chromaticity chart. The curved portion of the xy chromaticity diagram is called the *spectral locus* which defines the xy coordinates of monochromatic light. No practical visible light source is truly monochromatic so will lie off of the spectral locus within the visible colour space. The wider the spectral distribution of the light source (within the visible wavelengths), the further off the spectral locus it will lie.

More interestingly, if we have a second light source of different chromaticity and draw a line between the two sets of coordinates, those two light sources will be able to reproduce any colour along this line by using different relative intensities. We can extend this further by introducing a third light source and defining a triangle between the three coordinates. This representation is called a colour space and all colours within the space can be reproduced by mixing the three colours in different intensities. This becomes important when making RGB displays as we can define a larger colour space by: i) judiciously selecting the 3 peak wavelengths, and, ii) making LEDs with a narrower spectrum (higher colour purity). We will then be able to produce a wider range of the colours perceivable to the human eye and create more vibrant displays.

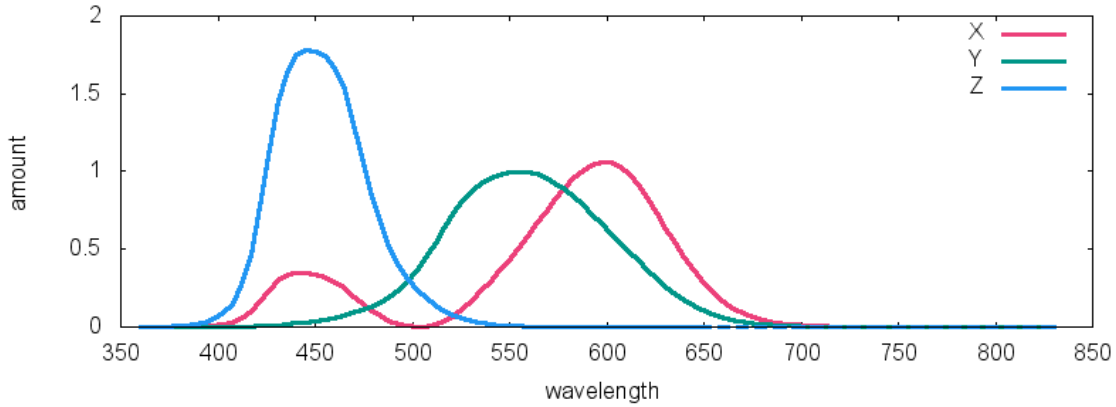


Figure 1.16 The CIE colour matching functions X,Y and Z. Figure credit[31]

1.3.5 Efficiency quantification

In order to compare the relative metrics of LEDs, there are several ways to define the practical efficiency using both radiometric and photometric units.

1.3.5.1 External quantum efficiency of electroluminescence (EQE_{EL})

$$EQE_{EL} = \frac{\text{number of photons emitted}}{\text{number of electrons injected}}$$

Equation 1.15

EQE_{EL} is the equivalent of PLQY with electrical excitation as opposed to photoexcitation. This efficiency metric is used often in this thesis. As metal halide perovskites are a widely tuneable material family, fundamental studies on LEDs occur at a wide variety of emission wavelengths. Photometric efficiency quantification favours LEDs with wavelengths close to the peak in the photopic curve, so is not useful for comparison across wavelengths from this academic standpoint.

1.3.5.2 Current efficiency

$$\text{Current Efficiency} = \frac{\text{Luminous intensity (cd)}}{\text{Injected current (A)}}$$

Equation 1.16

The current efficiency is a photometric measure of efficiency which relays how much brightness is perceived by the observer. It is of use to highlight the lower current efficiency of blue and red LEDs of similar EQE_{EL} to a green LED. It is often used as a

performance metric in academic literature however we do not focus on it as it can obfuscate important information if used on its own.

1.3.5.3 Wall plug efficiency

$$\text{Wall plug efficiency} = \frac{\text{Total Emitted Power (W)}}{\text{Input Electrical Power (W)}} = \frac{\text{number of photons emitted} \times h\nu}{\text{number of electrons injected} \times q \times V}$$
$$= \text{EQE}_{\text{EL}} \times \frac{h\nu}{qV}$$

Equation 1.17

The wall plug efficiency is an important metric for an LED when considering its final application. It is the ratio of the total power of light emitted to the total input electrical power to the system. One can see in Equation 1.17 that this is proportional to the EQE_{EL} but can be decreased by an increase in voltage. Practically, this has obvious implications that reducing the driving voltage required will improve the power efficiency but not necessarily improve the EQE_{EL}. Thus, the power efficiency can be improved by reducing the series resistance of the system, which can be affected not only by the internal series resistance of the LED but also the resistance of connection wires. Although this metric is important, it is not focussed on in this thesis.

1.4 Perovskite LEDs

During the 90s there was some interest in making LEDs from 2D lead halide perovskite semiconductors.[13,32,33] Reported EQE_{EL} of up to 2.8%, were achieved[33] however this was at a temperature of 110 K and EL at room temperature was highly inefficient. After this effort there were no publications on perovskite LEDs until discoveries in perovskite photovoltaics were made. The first publication of 3D lead halide perovskite LEDs was in August 2014,[29] where room temperature EL was demonstrated for near-infrared ($CH_3NH_3PbI_3$), red ($CH_3NH_3PbBr_2I$) and green ($CH_3NH_3PbBr_3$) wavelengths (Figure 1.17) and an EQE_{EL} of 0.76% at room temperature for $CH_3NH_3PbI_3$. The device was in a *nip* configuration with a device structure ITO/TiO_2/Perovskite/poly(9,9′-dioctylfluorene) (F8)/MoO_3/Ag. This report resulted in a resurgence in perovskite LED research which is a buoyant field today.

Perovskite LEDs of this class are highly attractive for a number of reasons. Firstly, metal halide perovskites are inherently tuneable. One can modify the emission wavelength in

the visible almost continuously through substitution on the A and X-site. Currently, it has been conclusively shown that the ions MA, formamidinium (FA)[34] and cesium may occupy the A-site which can offer tuning of the bandgap. One can span the visible spectrum by changing the halide from I→Br→Cl which causes a shift from the near infrared → violet, with intermediate wavelengths possible by alloying the halides.[35] Secondly, they have high mobilities (>1 cm^2 V^{-1} s^{-1}),[36] which allow for lower operating voltages and higher brightness than in OLEDs.[37] Thirdly, they have been shown to have very high PLQY (a prerequisite for efficient LEDs) using relatively simple processing conditions.[38] Finally they have narrow spectra (full width half maxima 20 nm[39]) compared with OLEDs which generally have full width half maxima >50 nm. This means larger colour spaces can be formed using these materials for display applications.

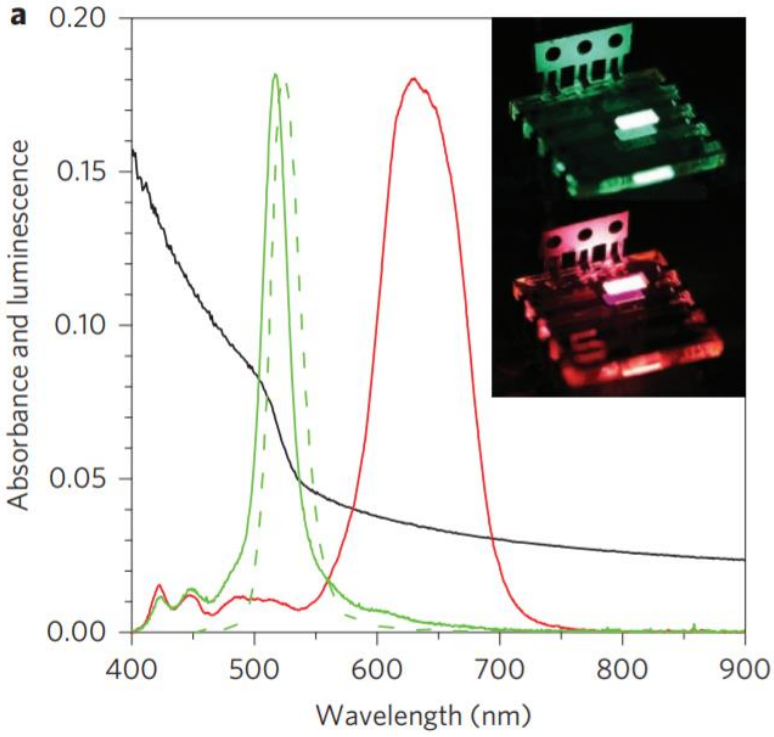


Figure 1.17 Absorbance, PL and photographs of the first reported 3D perovskite LEDs. Figure credit.[29]

1.4.1 Methods for High Efficiency

Once a proof of concept had been demonstrated the first goal of the field was to demonstrate high efficiency perovskite LEDs. The following section is a brief overview of key strategies which have been adopted by different research groups while working to achieve this goal in the past 6 years. The focus is on the composition and crystallisation of the perovskite as opposed to different device structures. On the topic of crystallisation,

the use of antisolvent induced crystallisation which was pioneered in perovskite solar cells in 2014,[40,41] is used for some LEDs and not others, which will be highlighted. This will not be an exhaustive review of the incremental gains made in efficiency by the whole community. Particular attention is paid to state of the art green emitting LEDs as these are the focus of the thesis. Additionally, the use of quasi-2D perovskites versus 3D perovskites will be in focus.

1.4.1.1 Beginnings

In February 2015, Wang *et al.*[42] achieved an EQE_{EL} of 3.5 % with the perovskite emitter $MAPbI_3$ using a modified device structure of ITO/ZnO/polyethyleneimine (PEI)/$MAPbI_3$/poly(9,9-dioctyl-fluorene-*co*-N-(4-butylphenyl)diphenylamine) (TFB)/MoO_3/Au. The PEI interlayer between the ZnO and $MAPbI_3$ prevents interfacial degradation due to the basicity of ZnO.[43] A substantial jump in performance was realised by Cho *et al.* in Dec 2015[44] where an EQE_{EL} of 8.5% was attained for a $MAPbBr_3$ emitter (the first report of $MAPbBr_3$ had an EQE_{EL} of 0.1%[29]). The researchers improved the PLQY of the emitter from 3% to 36% by, i) Adding a ~5% molar excess of MABr which they determine reduces the formation of metallic lead in the resultant film, ii) using antisolvent induced crystallisation, and, iii) the introduction of the small molecule 2,2′,2″-(1,3,5-benzinetriyl)-tris (1-phenyl-1-H-benzimidazole) (TPBi) into the antisolvent. The latter two changes allow complete film coverage and reduce the size of the perovskite grains from >1 μm to <100 nm in size, which the researchers posit improves confinement of charges within grains encouraging bimolecular recombination. Given, that TPBi is a Lewis base (as it contains lone pairs on the imadizole nitrogens) and this has been shown to improve the photoluminescence of perovskites,[45] we posit that it is also acting to passivate traps. This report marks the beginning of strategies to significantly modify the perovskite to improve the PLQY of the emitter itself.

1.4.1.2 2D/3D compositions

One significant strategy which emerged after this report was the use of quasi-2D perovskites as a method to improve the PLQY of the emitter. It should be noted that in all of the following reports the films are made up of a blend of 2D, quasi-2D and 3D perovskite due to the inability to fully control the crystallisation of the perovskite (absorption and PL of an exemplar film, Figure 1.18.a). This complex blend of phases is often referred to as a '2D/3D' system. In June 2016 Yuan *et al.* reported an EQE_{EL} of 8.8% in the near infrared[16] using, i) antisolvent induced crystallisation, and , ii) a

precursor solution with a nominal 'n=5' stoichiometry with phenylethylammonium (PEA) as the spacer cation and MA as the A site cation. This was quickly followed by a reported EQE_{EL} of 11.7% in the near infrared from Wang *et al.*[46] using, i) the ZnO/PEI structure they had previously pioneered,[42] and, ii) a 2D/3D system using 1-napthylmethylammonium as a spacer cation and FA as an A-site cation. These impressive results in the near infrared were not yet matched at green wavelengths. In February 2015 Byun et al.[47] reported a current efficiency of 4.9 cd A^{-1} (approx. 1 % EQE_{EL}) using a 2D/3D blend using PEA as a spacer cation and MA as an A-site cation. It is noted that the researchers did not use antisolvent induced crystallisation.

The improved PLQY and EQE_{EL} of 2D/3D compositions over 3D perovskites has been actively explored by the community. Transient absorption analysis has shown efficient transfer of photoexcited carriers from higher bandgap 2D domains to lower bandgap domains occurs on a ps timescale (Figure 1.18.b).[16,48,49] This so called 'carrier funnelling' increases the carrier concentration in the low gap domains and fills traps so that radiative bimolecular recombination can dominate. However, under electrical injection, efficient devices show high EQE_{EL} at voltages well below the bandgap of the wide gap 2D perovskites;[46,50] this indicates that injection is happening into lower gap regions and energy funnelling is not the entire story.

Figure 1.18.a. shows the absorption and emission spectrum of a 2D/3D film,[46] one can see a large excitonic absorption peak at ~550 nm (quasi-2D, n=2) and a relatively much smaller absorption edge at ~720 nm. The emission spectrum consists of several peaks with one dominant peak at ~750 nm (3D $FAPbI_3$ or high n quasi-2D). This relative distribution of 2D/quasi-2D to 3D causes a significant decrease in the overlap of the absorption and emission spectrum as opposed to a neat 3D perovskite. This is an artificially created Stokes shift and has the benefit of decreasing reabsorption and thereby increasing light outcoupling from the film. However, this is only beneficial up to a certain radiative efficiency of the emitter as reabsorption can lead to a further emission event which in turn increases the proportion of outcoupled light. This phenomenon is known as photon recycling and has been shown for lead halide perovskite systems.[51,52] In fact, recent optical modelling of perovskite LEDs predicts in order to obtain the highest EQE_{EL} the reabsorption coefficient must be maximised.[51] As such, the artificial Stokes shift, can be seen as a 'stopgap' solution while striving to increase the radiative efficiency of emitters with more reabsorption.

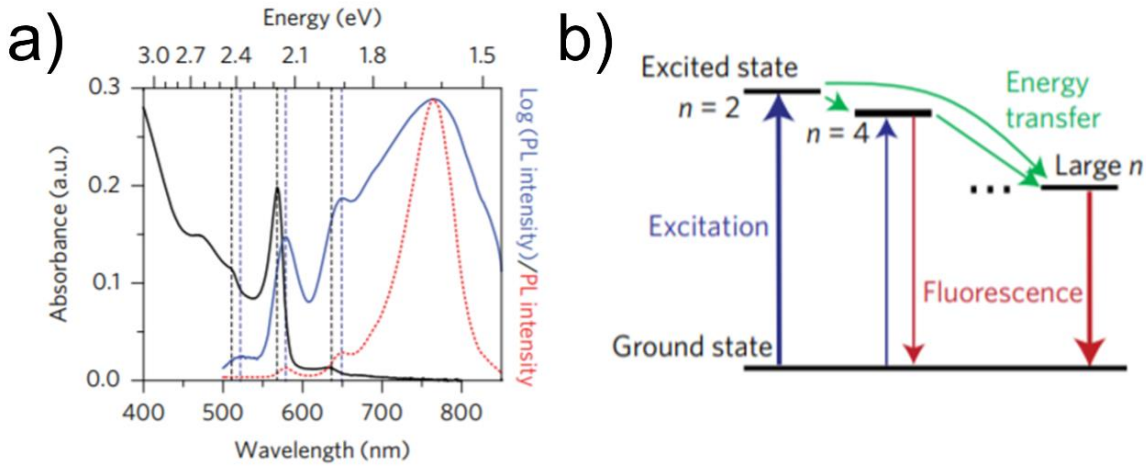


Figure 1.18 a) Absorbance and PL of a typical 2D/3D perovskite film; b) schematic of 'energy funnelling' process in 2D/3D films. Figure credit.[46]

Figure 1.19.a. shows the carrier density dependent PLQY of a 2D/3D film versus a 3D film. One can see trap filling behaviour (*cf.* Figure 1.2) and followed by a roll off due to Auger recombination (*cf.* Figure 1.3) in the PLQY for the 3D film whereas the 2D/3D film does not show any trap filling in the range presented and shows a roll off at lower carrier densities. This is consistent with carrier funnelling increasing carrier concentration in the emissive domains. Further, Figure 1.19.b. shows that the PL intensity is proportional to the carrier density for the 2D/3D film (excitonic, monomolecular) and to the square for the 3D perovskite (free carrier, bimolecular). The transition to excitonic recombination for the 2D/3D film indicates that the emission may be due to the high exciton binding energy of the quasi-2D regions which are excited and fast exciton (ps timescale) transfer to the lower gap regions. Therefore, improved performance of 2D/3D perovskites is likely not only due to carrier funnelling and optical transparency but also improved passivation of emission regions and increased exciton binding energy.

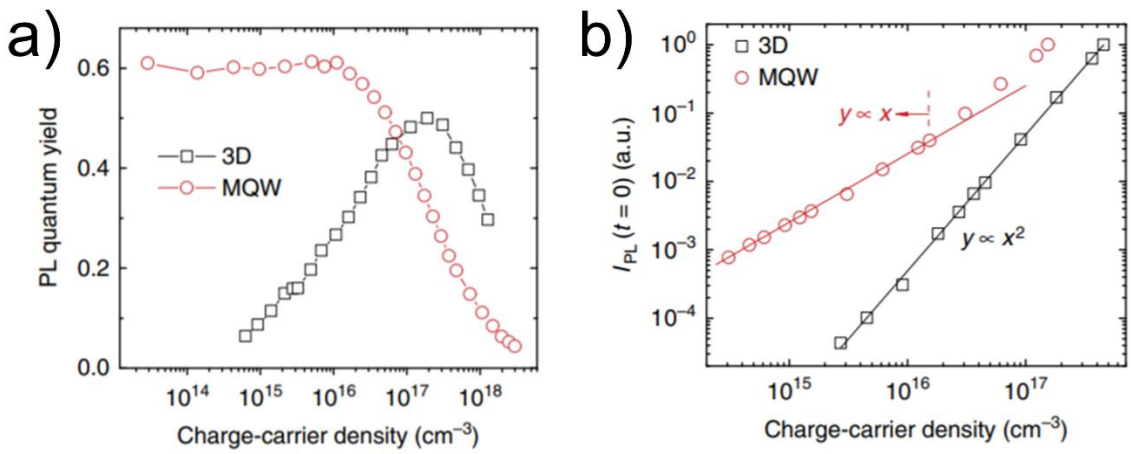


Figure 1.19 a) Carrier density dependent PLQY of 3D and 2D/3D (labelled MQW, for multiple quantum well) films; b) Carrier density vs initial PL intensity for 3D and 2D/3D films. Figure Credit[48]

1.4.1.3 Perovskite polymer hybrids

While high efficiencies were still not attained with 2D/3D compositions, other researchers had success using other methodologies. In February 2015 Li *et al.* attained an EQE_{EL} of 1.2% using $MAPbBr_3$ mixed with a short chained polyimide.[53] The polymer created a dielectric matrix for the perovskite precursor which help prevent parasitic shunts through the device and also improved the PL efficiency. This strategy of using a polymer additive to, i) improve film coverage, and, ii) increase the PLQY of the film via surface passivation, has been widely adopted. In particular we wish to highlight the use of polyethylene oxide (PEO) which has been used with great success in particular with the emitter $CsPbBr_3$. In August 2016, Ling *et al.* attained an EQE_{EL} of 4.3% using a $CsPbBr_3$:PEO blend.[54] This was improved upon by Song *et al.* who reached an EQE_{EL} 5.3% and a PLQY of 30% by further tuning the CsBr:$PbBr_2$ ratio.[55] Another report by Wu *et al.* of 4.8% in May 2017 using $CsPbBr_3$:PEO with an antisolvent vapour induced recrystallisation further corroborates the strategy.[56]

1.4.1.4 Passivation of 3D emitters

Another strategy pursued by researchers was the use of amines to passivate the perovskite. In April 2017, Lee *et al.* demonstrated an EQE_{EL} of 6.2% with $MAPbBr_3$ and an ethylenediamine post treatment.[57] In March 2018 Lee *et al.* improved on this work by incorporating benzylamine as a passivation agent into the antisolvent used to induce crystallisation in $MAPbBr_3$ where they reached an EQE_{EL} of 12.1%.[58]

1.4.1.5 Current state of the art

Meanwhile, efficiencies of green 2D/3D perovskites started to improve rapidly through the use of antisolvent induced crystallisation. In January 2017, Xiao *et al.* demonstrated an EQE_{EL} of 9.3% using PEA as a spacer cation and MA as the A-site cation.[59] This was quickly followed by Quan *et al.* who reached 7.4% using a similar system, [50] and then Yang *et al.* who reached a then record of 14.4% using PEA with FA, and trioctylphosphine oxide passivation of the film.[60] Ban *et al.* broke the record for visible emission again in September 2018 with an EQE_{EL} of 15.5 % using PEA as the spacer and Cs as the A-site cation. [61] Intriguingly the researchers did not use an antisolvent but instead used the small molecule 18-crown-6 to mediate crystallisation, marking the first report of a green perovskite LED above 10 % without antisolvent induced crystallisation. Additionally, they did not use a quasi-2D stoichiometry in the precursor solution but instead used standard $CsPbBr_3$ stoichiometry and added PEABr in excess; the films produced by this methodology have similar absorption and PL to a 3D perovskite, which causes a much more significant overlap and thus increases the possibility of photon recycling (Figure 1.20). Indeed the very high PLQY of 66% they demonstrate is only possible for a planar film with significant photon recycling.[51]

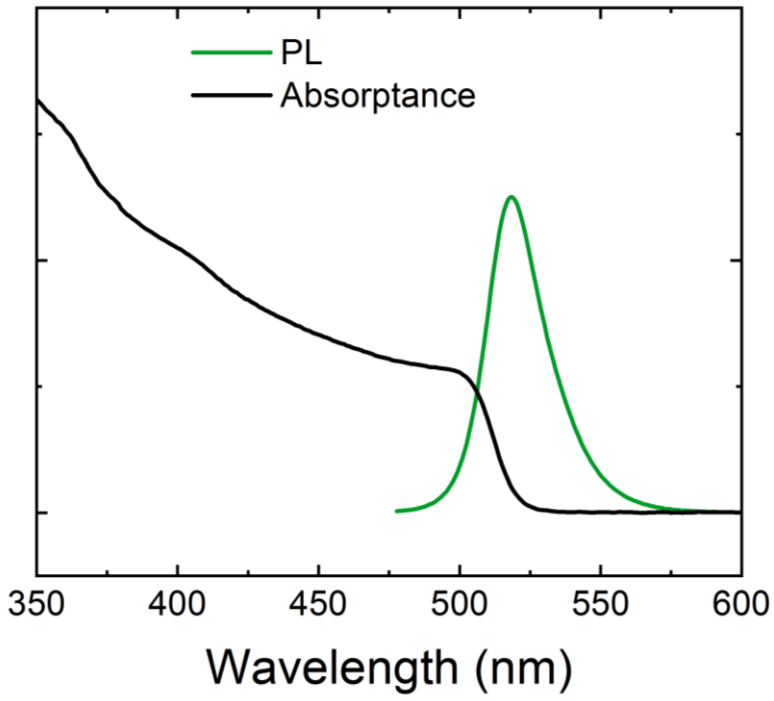


Figure 1.20 PL and absorptance of PEABr:$CsPbBr_3$ 2D/3D film produced by the methodology introduced by Ban et al.[61]

More recently, several groups have started to break the landmark of 20% EQE_{EL} which begins to be competitive with OLEDs used in displays. Interestingly, they all achieved this goal using different strategies. In October 2018, Cao *et al.* reported an EQE_{EL} of 20.7% in the near infrared using a discontinuous film of $FAPbI_3$ (which aids with light outcoupling) passivated by the additive 5-aminovaleric acid.[37] Almost simultaneously Lin *et al.* achieved 20.3% in the visible using a $CsPbBr_3$/MABr quasi-core/shell structure.[62] Very quickly after this, Zhao *et al.* reported 20.1% in the near infrared using a 2D/3D composition blended with a polymer to aid light extraction.[49] Subsequently , Zhou *et al.* pushed the efficiency of near infrared perovskite LEDs to 21.6% using discontinuous $FAPbI_3$ with a 2,2′-(ethylenedioxy)diethylamine passivating agent.[7]

In conclusion, since its nascence in 2014 the field has very rapidly achieved high efficiencies. Currently, there are several different overarching strategies which have been developed which have been outlined here. The use of 2D/3D perovskites is very prevalent but recently a trend to improving the properties of bulk perovskites has emerged.[7,37,62] It is not clear at this moment what strategy will win out in the goal of high efficiency. We will contextualise the efficiency with respect to operational stability in the next section.

1.4.2 Operational stability

Despite their excellent efficiency perovskite LEDs have poor stability which typically have a time for the luminance to decrease to 50% of its initial value (T_{50}) of several minutes to a few hours (typical operational stability, Figure 1.21.) .[7,56,61]

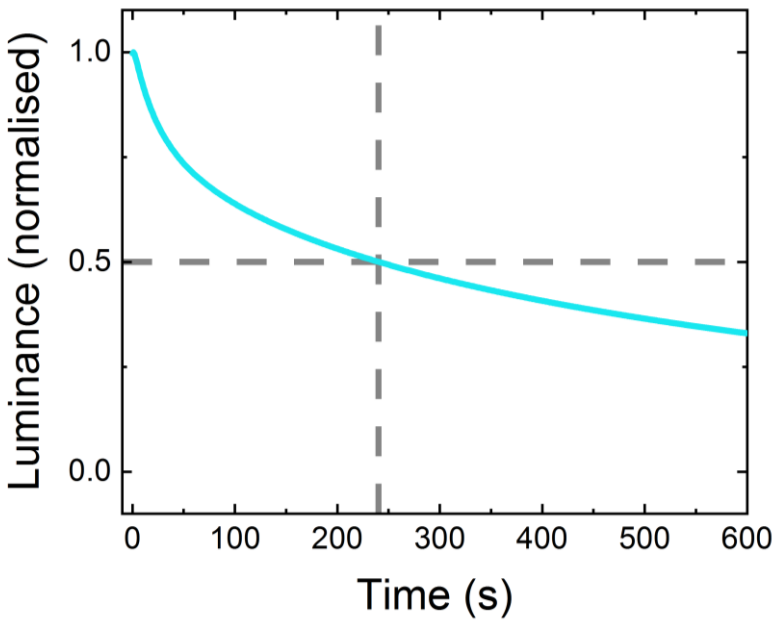


Figure 1.21 A typical operational stability curve for a perovskite LED. Operating conditions 10 mA cm^{-2}, T_{50} = 240 s.

Some research groups have demonstrated much improved stability over the provided example through modifications to the perovskite such as greatly increasing grain size (T_{80} = 80 h),[56] the use of passivation post treatments (T_{50} = 100 h at 100 mA cm^{-2}),[63] and the introduction of an organic/inorganic matrix surrounding the emitter (T_{50} = 250 h at 100 cd m^{-2}).[64] However, these examples of unusually high stability are the exception rather than the norm and there is little understanding in what governs stability.

The most likely source of most of the stability issues in perovskite LEDs is the migration of ions from the perovskite itself. Various research groups have demonstrated and quantified the migration of ions in metal halide perovskites,[65,66] and given the higher bias voltages that are required in perovskite LEDs it can be assumed that ion motion is contributing to the degradation process. This has been corroborated by several groups using time of flight secondary ion mass spectrometry (TOF-SIMS) who show accumulation of ions in both the contact layers and at the electrodes.[67,68] Further, Futscher *et al.* have linked degradation of perovskite LEDs to the diffusion coefficient and activation energy for bromide ions in $CsPbBr_3$ LEDs using transient capacitance measurements.[69]

Birkhold *et al.* showed PL quenching of $MAPbI_3$ moving from the cathode to the anode under bias in a lateral electrode configuration. They inferred ion motion through redistribution of the electrical field using scanning Kelvin probe microscopy and demonstrated that PL quenching does not occur from poling alone but also requires

electrical injection. The requirement of charge indicates that electrochemical processes at the electrode may cause the quenching.

$$\text{Cathode: Pb(II)} + 2\ e^- \rightarrow \text{Pb(0)};\ \text{Anode: } 2\ I^- + 2\ h^+ \rightarrow I_2$$

Equation 1.18

While this is not in a vertical LED type structure it demonstrates the interplay between ion motion and electrical charge which may be occurring in perovskite LEDs. Interestingly, Miao *et al.* measured the simultaneous evolution of the PL of their LED while also measuring the EL, and showed that it decays at a slower rate than the EL indicating that loss in PL is not the sole contributing factor to the degradation process.[63]
One other potential source of degradation is changes in charge injection during operation due to accumulation of ions at interfaces. Bandiello *et al.* showed improved EL characteristics of $MAPbI_3$ diodes using prebiasing,[70] which they demonstrate is correlated to changes in the JV behaviour of the device. This effect was later also reported by Zhao *et al.* where they also saw improvements with repeated JV sweeps and eventually slight degradation which was correlated with changes in the diode characteristics[71]
There has been some study on how composition of the perovskite layer affects stability as well. Prakasam *et al.* recently showed the superior stability of $CsPbBr_3$ compared with $MAPbBr_3$ in LEDs.[72] They show compelling evidence for the deprotonation of MA to form methylamine which leaves the layer as a gas. Watanabe *et al.* showed fast degradation of quasi-2D perovskite LEDs which they show is due to formation of Pb(0) and also loss of organic cations leaving $PbBr_2$.[73] Notably, the best reported stability to date of T_{50} = 100 h at 100 mA cm^{-2} comes from a 3D perovskite ($FAPbI_3$),[63] the best reported stability at green wavelengths comes from bulk $CsPbBr_3$ dispersed in a matrix of cesium trifluoroacetate.[64] Though some reports have shown an improvement over control devices through a change in composition, little work has been done to systematically study the effect. Additionally, there are likely differences in what chemically creates a more stable composition depending on the exact perovskite used (i.e. A = MA vs FA vs Cs; X = I vs Br).
In conclusion, the field of perovskite LEDs is beginning to gain further understanding into the root causes of degradation. However, there is a lack of good systematic studies into the underlying causes in changes in PL, JV characteristics and the effect of composition on stability.

1.5 Scope of this thesis

The scope of this thesis is to implement efficient green-emitting perovskite LEDs through investigations into device structure and passivation strategies. Once this goal has been achieved, a systematic investigation into the composition of a perovskite emitter and its effect on stability is performed. Specifically, the effect of 2D/3D vs 3D compositions are investigated which leads to further investigations into possible origins of degradation. Finally, underlying factors contributing to degradation are unveiled paving the way for more targeted work by the field to address them.

1.6 References

1. Schubert, E. F. *Light-emitting diodes*. *Light-emitting Diodes, Second Edition* (Cambridge University Press, 2006). doi:10.1017/CBO9780511790546
2. Li, J. *et al.* Highly Efficient Thermally Co-evaporated Perovskite Solar Cells and Mini-modules. *Joule* **4,** 1035–1053 (2020).
3. Lee, M. M., Teuscher, J., Miyasaka, T., Murakami, T. N. & Snaith, H. J. Efficient hybrid solar cells based on meso-superstructured organometal halide perovskites. *Science (80-.).* **338,** 643–647 (2012).
4. Bishop, J. E., Read, C. D., Smith, J. A., Routledge, T. J. & Lidzey, D. G. Fully Spray-Coated Triple-Cation Perovskite Solar Cells. *Sci. Rep.* **10,** 1–8 (2020).
5. Mathies, F. *et al.* Inkjet-Printed Triple Cation Perovskite Solar Cells. *ACS Appl. Energy Mater.* **1,** 1834–1839 (2018).
6. Deng, Y. *et al.* Tailoring solvent coordination for high-speed, room-temperature blading of perovskite photovoltaic films. *Sci. Adv.* **5,** eaax7537 (2019).
7. Xu, W. *et al.* Rational molecular passivation for high-performance perovskite light-emitting diodes. *Nat. Photonics* (2019). doi:10.1038/s41566-019-0390-x
8. Kagan, C. R., Mitzi, D. B. & Dimitrakopoulos, C. D. Organic-inorganic hybrid materials as semiconducting channels in thin- film field-effect transistors. *Science (80-.).* **286,** 945–947 (1999).
9. Qin, C. *et al.* Stable room-temperature continuous-wave lasing in quasi-2D perovskite films. *Nature* **585,** 53 (2020).

10. Green, M. A., Ho-Baillie, A. & Snaith, H. J. The emergence of perovskite solar cells. *Nature Photonics* **8,** 506–514 (2014).
11. Eperon, G. E. *et al.* Inorganic caesium lead iodide perovskite solar cells. *J. Mater. Chem. A* **3,** 19688–19695 (2015).
12. Wells, H. L. Über die Cäsium- und Kalium-Bleihalogenide. *Zeitschrift für Anorg. Chemie* **3,** 195–210 (1893).
13. Chondroudis, K. & Mitzi, D. B. Electroluminescence from an organic-inorganic perovskite incorporating a quaterthiophene dye within lead halide perovskite layers. *Chem. Mater.* **11,** 3028–3030 (1999).
14. Weber, D. $CH_3NH_3PbX_3$, ein Pb(II)-System mit kubischer Perowskitstruktur. *Zeitschrift fur Naturforsch. - Sect. B J. Chem. Sci.* **33,** 1443–1445 (1978).
15. Ruddlesden, S. N. & Popper, P. New compounds of the K_2NIF_4 type. *Acta Crystallogr.* **10,** 538–539 (1957).
16. Yuan, M. *et al.* Perovskite energy funnels for efficient light-emitting diodes. *Nat. Nanotechnol.* **11,** 872–877 (2016).
17. Stoumpos, C. C. *et al.* Ruddlesden-Popper Hybrid Lead Iodide Perovskite 2D Homologous Semiconductors. *Chem. Mater.* **28,** 2852–2867 (2016).
18. Kojima, A., Teshima, K., Shirai, Y. & Miyasaka, T. Organometal Halide Perovskites as Visible-Light Sensitizers for Photovoltaic Cells. *J. Am. Chem. Soc.* **131,** 6050–6051 (2009).
19. Round, H. J. A note on carborundum. *Electr. World* **19,** 309 (1907).
20. Lossev, O. V. CII. Luminous carborundum detector and detection effect and oscillations with crystals . *London, Edinburgh, Dublin Philos. Mag. J. Sci.* **6,** 1024–1044 (1928).
21. Rupprecht, H., Woodall, J. M., Konnerth, K. & Pettit, D. G. Efficient electroluminescence from GaAs diodes at 300 K. *Appl. Phys. Lett.* **9,** 221–223 (1966).
22. Amano, H., Kito, M., Hiramatsu, K. & Akasaki, I. P-type conduction in Mg-doped GaN treated with low-energy electron beam irradiation (LEEBI). *Jpn. J. Appl. Phys.* **28,** L2112–L2114 (1989).
23. Nakamura, S., Senoh, M., Iwasa, N. & Nagahama, S. I. High-brightness InGaN blue, green and yellow light-emitting diodes with quantum well structures. *Jpn. J. Appl. Phys.* **34,** L797–L799 (1995).
24. Bernanose, A. & Vouaux, P. Électroluminescence organique : étude du mode d'émission. *J. Chim. Phys.* **50,** 261–263 (1953).

25. Tang, C. W. & Vanslyke, S. A. Organic electroluminescent diodes. *Appl. Phys. Lett.* **51,** 913–915 (1987).
26. Burroughes, J. H. *et al.* Light-emitting diodes based on conjugated polymers. *Nature* **347,** 539–541 (1990).
27. Kabra, D., Lu, L. P., Song, M. H., Snaith, H. J. & Friend, R. H. Efficient Single-Layer Polymer Light-Emitting Diodes. *Adv. Mater.* **22,** 3194–3198 (2010).
28. Caruge, J. M., Halpert, J. E., Wood, V., Buloví, V. & Bawendi, M. G. Colloidal quantum-dot light-emitting diodes with metal-oxide charge transport layers. *Nat. Photonics* **2,** 247–250 (2008).
29. Tan, Z. K. *et al.* Bright light-emitting diodes based on organometal halide perovskite. *Nat. Nanotechnol.* **9,** 687–692 (2014).
30. Chromaticity (Wikipedia). Available at: https://en.wikipedia.org/wiki/Chromaticity. (Accessed: 8th October 2020)
31. Abraham, C. A Beginner's Guide to (CIE) Colorimetry. (2016). Available at: https://medium.com/hipster-color-science/a-beginners-guide-to-colorimetry-401f1830b65a. (Accessed: 8th October 2020)
32. Era, M., Morimoto, S., Tsutsui, T. & Saito, S. Organic-inorganic heterostructure electroluminescent device using a layered perovskite semiconductor $(C_6H_5C_2H_4NH_3)_2PbI_4$. *Appl. Phys. Lett.* **65,** 676–678 (1994).
33. Hattori, T., Taira, T., Era, M., Tsutsui, T. & Saito, S. Highly efficient electroluminescence from a heterostructure device combined with emissive layered-perovskite and an electron-transporting organic compound. *Chem. Phys. Lett.* **254,** 103–108 (1996).
34. Eperon, G. E. *et al.* Formamidinium lead trihalide: A broadly tunable perovskite for efficient planar heterojunction solar cells. *Energy Environ. Sci.* **7,** 982–988 (2014).
35. Protesescu, L. *et al.* Nanocrystals of Cesium Lead Halide Perovskites ($CsPbX_3$, X = Cl, Br, and I): Novel Optoelectronic Materials Showing Bright Emission with Wide Color Gamut. *Nano Lett.* **15,** 3692–3696 (2015).
36. Herz, L. M. Charge-Carrier Mobilities in Metal Halide Perovskites: Fundamental Mechanisms and Limits. *ACS Energy Letters* **2,** 1539–1548 (2017).
37. Cao, Y. *et al.* Perovskite light-emitting diodes based on spontaneously formed submicrometre-scale structures. *Nature* **562,** 249–253 (2018).
38. Na Quan, L. *et al.* Edge stabilization in reduced-dimensional perovskites. *Nat. Commun.* **11,** 1–9 (2020).

39. Si, J. *et al.* Efficient and High-Color-Purity Light-Emitting Diodes Based on in Situ Grown Films of $CsPbX_3$ (X = Br, I) Nanoplates with Controlled Thicknesses. *ACS Nano* **11,** 11100–11107 (2017).
40. Jeon, N. J. *et al.* Solvent engineering for high-performance inorganic-organic hybrid perovskite solar cells. *Nat. Mater.* **13,** 897–903 (2014).
41. Xiao, M. *et al.* A Fast Deposition-Crystallization Procedure for Highly Efficient Lead Iodide Perovskite Thin-Film Solar Cells. *Angew. Chemie* **126,** 10056–10061 (2014).
42. Wang, J. *et al.* Interfacial control toward efficient and low-voltage perovskite light-emitting diodes. *Adv. Mater.* **27,** 2311–2316 (2015).
43. Schutt, K. *et al.* Overcoming Zinc Oxide Interface Instability with a Methylammonium-Free Perovskite for High-Performance Solar Cells. *Adv. Funct. Mater.* **29,** 1900466 (2019).
44. Cho, H. *et al.* Overcoming the electroluminescence efficiency limitations of perovskite light-emitting diodes. *Science (80-.).* **350,** 1222–1225 (2015).
45. Noel, N. K. *et al.* Enhanced photoluminescence and solar cell performance via Lewis base passivation of organic-inorganic lead halide perovskites. *ACS Nano* **8,** 9815–9821 (2014).
46. Wang, N. *et al.* Perovskite light-emitting diodes based on solution-processed self-organized multiple quantum wells. *Nat. Photonics* **10,** 699–704 (2016).
47. Byun, J. *et al.* Efficient Visible Quasi-2D Perovskite Light-Emitting Diodes. *Adv. Mater.* **28,** 7515–7520 (2016).
48. Xing, G. *et al.* Transcending the slow bimolecular recombination in lead-halide perovskites for electroluminescence. *Nat. Commun.* **8,** 14558 (2017).
49. Zhao, B. *et al.* High-efficiency perovskite–polymer bulk heterostructure light-emitting diodes. *Nat. Photonics* **12,** 783–789 (2018).
50. Quan, L. N. *et al.* Tailoring the energy landscape in quasi-2D halide perovskites enables efficient green light emission. *Nano Lett.* acs.nanolett.7b00976 (2017). doi:10.1021/acs.nanolett.7b00976
51. Cho, C. *et al.* The role of photon recycling in perovskite light-emitting diodes. *Nat. Commun.* **11,** 611 (2020).
52. Crothers, T. W. *et al.* Photon Reabsorption Masks Intrinsic Bimolecular Charge-Carrier Recombination in $CH_3NH_3PbI_3$ Perovskite. *Nano Lett.* **17,** 5782–5789 (2017).
53. Li, G. *et al.* Efficient Light-Emitting Diodes Based on Nanocrystalline Perovskite

in a Dielectric Polymer Matrix. *Nano Letters* **15,** 2640–2644 (2015).

54. Ling, Y. *et al.* Enhanced Optical and Electrical Properties of Polymer-Assisted All-Inorganic Perovskites for Light-Emitting Diodes. *Adv. Mater.* **28,** 8983–8989 (2016).
55. Song, L. *et al.* Efficient Inorganic Perovskite Light-Emitting Diodes with Polyethylene Glycol Passivated Ultrathin $CsPbBr_3$ Films. *J. Phys. Chem. Lett.* **8,** 4148–4154 (2017).
56. Wu, C. *et al.* Improved Performance and Stability of All-Inorganic Perovskite Light-Emitting Diodes by Antisolvent Vapor Treatment. *Adv. Funct. Mater.* **27,** 1–7 (2017).
57. Lee, S. *et al.* Amine-Based Passivating Materials for Enhanced Optical Properties and Performance of Organic-Inorganic Perovskites in Light-Emitting Diodes. *J. Phys. Chem. Lett.* **8,** 1784–1792 (2017).
58. Lee, S. *et al.* Growth of Nanosized Single Crystals for Efficient Perovskite Light-Emitting Diodes. *ACS Nano* **12,** 3417–3423 (2018).
59. Xiao, Z. *et al.* Efficient perovskite light-emitting diodes featuring nanometre-sized crystallites. *Nat. Photonics* **11,** 108–115 (2017).
60. Yang, X. *et al.* Efficient green light-emitting diodes based on quasi-two-dimensional composition and phase engineered perovskite with surface passivation. *Nat. Commun.* **9,** 570 (2018).
61. Ban, M. *et al.* Solution-processed perovskite light emitting diodes with efficiency exceeding 15% through additive-controlled nanostructure tailoring. *Nat. Commun.* **9,** 3892 (2018).
62. Lin, K. *et al.* Perovskite light-emitting diodes with external quantum efficiency exceeding 20 per cent. *Nature* **562,** 245–248 (2018).
63. Miao, Y. *et al.* Stable and bright formamidinium-based perovskite light-emitting diodes with high energy conversion efficiency. *Nat. Commun.* **10,** 1–7 (2019).
64. Wang, H. *et al.* Trifluoroacetate induced small-grained $CsPbBr_3$ perovskite films result in efficient and stable light-emitting devices. *Nat. Commun.* **10,** 665 (2019).
65. Kim, G. Y. *et al.* Large tunable photoeffect on ion conduction in halide perovskites and implications for photodecomposition. *Nat. Mater.* **17,** 445–449 (2018).
66. Futscher, M. H. *et al.* Quantification of ion migration in $CH_3NH_3PbI_3$ perovskite solar cells by transient capacitance measurements. *Mater. Horizons* **6,** 1497–1503 (2019).
67. Li, J., Dong, Q., Li, N. & Wang, L. Direct Evidence of Ion Diffusion for the Silver-

Electrode-Induced Thermal Degradation of Inverted Perovskite Solar Cells. *Adv. Energy Mater.* **7,** (2017).

68. Lee, H., Ko, D. & Lee, C. Direct Evidence of Ion-Migration-Induced Degradation of Ultrabright Perovskite Light-Emitting Diodes. *ACS Appl. Mater. Interfaces* **11,** 11667–11673 (2019).
69. Futscher, M. H., Gangishetty, M. K., Congreve, D. N. & Ehrler, B. Manganese Doping Stabilizes Perovskite Light-Emitting Diodes by Reducing Ion Migration. *ACS Appl. Electron. Mater.* **2,** 1522–1528 (2020).
70. Bandiello, E. *et al.* Influence of mobile ions on the electroluminescence characteristics of methylammonium lead iodide perovskite diodes. *J. Mater. Chem. A* **4,** 18614–18620 (2016).
71. Zhao, L. *et al.* Electrical Stress Influences the Efficiency of $CH_3NH_3PbI_3$ Perovskite Light Emitting Devices. *Adv. Mater.* **29,** 1605317 (2017).
72. Prakasam, V., Tordera, D., Bolink, H. J. & Gelinck, G. Degradation Mechanisms in Organic Lead Halide Perovskite Light-Emitting Diodes. *Adv. Opt. Mater.* **7,** 1900902 (2019).
73. Watanabe, S. *et al.* Excited-state stability of quasi-two-dimensional metal halide perovskite films under optical and electrical excitations. *Appl. Phys. Lett.* **115,** 233502 (2019).

2 EXPERIMENTAL TECHNIQUES

All procedures outlined in this section were conducted by the author unless stated explicitly.

2.1 Film and Device Fabrication Procedures

2.1.1 Substrate Cleaning

Pre-etched 28 × 28 mm ITO or FTO substrates were cleaned by sonication in a 2 v/v% Decon 90 detergent solution, deionized water, acetone, and isopropanol for 2 min each. The substrates were dried with a stream of N_2 and cleaned by UV-ozone for 10 min.

2.1.2 Fabrication of *nip* LEDs with ZnO *via* spray pyrolysis

A film of ZnO was deposited onto FTO substrates *via* spray pyrolysis of an 80 mg mL^{-1} solution of $ZnAc_2.2H_2O$ in methanol at 350°C which was then annealed for 60 minutes at 350°C. After cooling, a 5 mg mL^{-1} solution of Cs_2CO_3 in 2-ethoxyethanol was spincoated on the substrate (6000 rpm; 6000 rpm s^{-1}). Subsequently the emitter layer was deposited, details of perovskite deposition are found in Section 0. In the case of polymer LEDs, a 10 mg mL^{-1} solution of F8BT (1-Material) in *p*-xylene was spincoated at 3000 rpm to make the emissive layer and annealed at 100°C for 10 minutes. The substrates were transferred to a vacuum evaporator in a N_2 filled glovebox where 10 nm MoOx was deposited (rate 0.3 A s^{-1}) followed by 100 nm Au (rate 1 A s^{-1}) .

2.1.3 Fabrication of *nip* LEDs with ZnO nanoparticles

A solution of ZnO nanoparticles (detailed preparation, Section 2.1.6.1) was spincoated onto cleaned ITO substrates (2000 rpm; 2000 rpm s^{-1}) and annealed at 150°C for 10 minutes. The substrates were allowed to cool and subsequently a 0.04 wt % solution of PEIE in 2-methoxy ethanol was spincoated (5000 rpm; 5000 rpm s^{-1}). Subsequently the emitter layer was deposited, details of perovskite deposition are found in Section 0. Next the hole injection layer was deposited, a 10 mg mL^{-1} solution of either PVK or TFB in

chlorobenzene was spincoated (4000 rpm; 4000 rpm s^{-1}). The substrates were transferred to a vacuum evaporator in a N_2 filled glovebox where 10 nm MoOx was deposited (rate 0.3 A s^{-1}) followed by 100 nm Au (rate 1 A s^{-1}).

2.1.4 Fabrication of *pin* LEDs

2.1.4.1 Hole injection layer

The hole injection layer was deposited onto cleaned ITO substrates; all hole injection layers used in this device structure are detailed below.

2.1.4.1.1 PEDOT:PSS

A PEDOT:PSS solution (Heraeus AL4083) was spincoated at two different speeds to make 'thick' (3500 rpm; 3500 rpm s^{-1}) or 'thin' (6000 rpm; 6000 rpm s^{-1}) layers.

2.1.4.1.2 PVK – Plasma treated

PVK (Sigma-Aldrich) was dissolved at a concentration of 6 mg mL^{-1} in chlorobenzene at 70^{o}C overnight and filtered by a 0.22 µm PTFE filter. The solution was spincoated (2000 rpm; 2000 rpm s^{-1}) and then annealed at 120^{o}C for 10 minutes. The substrates were then transferred to a vacuum chamber where they were treated for 2 s with O_2 plasma in order to improve wettability.

2.1.4.1.3 PVK –DMSO treated

PVK films were prepared as above. Prior to deposition of the perovskite layer 50 µL of DMSO was dynamically dispensed onto a spinning substrate (3000 rpm) the substrate continued to spin and the perovskite solution was dynamically dispensed 10 s later.

2.1.4.1.4 PVK / TCTA

PVK films were prepared as above. TCTA (Sigma Alrich) was dissolved at a concentration of 3 mg mL^{-1} in chlorobenzene and 50 µL was dynamically spincoated at 4000 rpm onto the PVK film and annealed at 120^{o}C for 10 minutes.

2.1.4.1.5 NiOx

248.9 mg of $Ni(Ac)_2.4H_2O$ (Sigma –Aldrich) and 60.3 µL of ethanolamine was dissolved in 10 mL of ethanol and stirred at 70^{o}C for 4 h, followed by filtration with a 0.45 µm PTFE filter. The solution was spincoated (6000 rpm; 6000 rpm s^{-1}) at approx. 30% RH, 25^{o}C. The film was then annealed at 280^{o}C for 1 h.

2.1.4.1.6 Poly-TPD / PEIE

Poly-TPD (1-Material) was dissolved at a concentration of 10 mg mL^{-1} in chlorobenzene at 70°C overnight and filtered by a 0.22 µm PTFE filter. The solution was spincoated (4000 rpm; 4000 rpm s^{-1}) and then annealed at 150°C for 10 minutes. The substrates were allowed to cool and subsequently a 0.1 wt % solution of PEIE in 2-methoxy ethanol was spincoated (5000 rpm; 5000 rpm s^{-1}).

2.1.4.1.7 Poly-TPD / PFN

Poly-TPD was deposited as above. Following this a 0.5 mg mL^{-1} solution of PFN-P2 (1-Material) in methanol with a 1 vol% addition of acetic acid to improve solubility was spincoated (5000 rpm; 5000 rpm s^{-1}). The perovskite solution was deposited immediately afterwards.

2.1.4.1.8 Poly-TPD / LiF

Poly-TPD was deposited as above except at a concentration of 5 mg mL^{-1}. The substrates were transferred to a vacuum evaporator in a N_2 filled glovebox where 2 nm LiF was deposited (rate 0.1 A s^{-1}). It was ensured that the substrates were not exposed to ambient prior to deposition of the perovskite.

2.1.4.2 Remaining layers of LED

Subsequently the emitter layer was deposited, details of perovskite deposition are found in Section 2.1.5. In the case of polymer LEDs, a 10 mg mL^{-1} solution of F8BT in *p*-xylene was spincoated at 3000 rpm to make the emissive layer and annealed at 100°C for 10 minutes. The substrates were transferred to a vacuum evaporator in a N_2 filled glovebox where the electron injection layer TPBi was deposited. Then 45 nm of TPBi (rate 1 A s^{-1}) was evaporated from an alumina crucible followed by 1 nm of LiF (rate = 0.1 A s^{-1}). These two materials were evaporated over the entire area of the substrate, and the chamber was vented. They were then transferred into a different evaporation mask and placed into the chamber again, where 100 nm Al (rate = 1 A s^{-1}) was evaporated from an alumina-coated molybdenum boat. The mask, which defined the pixel area, creates an overlap area between the patterned ITO and the aluminium of 3 × 3 mm, giving a total pixel area of 9 mm^2.

2.1.5 Perovskite Deposition

2.1.5.1 $CsPbBr_3$ (heat gun)

A 0.5 M solution of $CsPbBr_3$ was prepared by dissolving 106.4 mg CsBr (Sigma Aldrich) and 183.5 mg $PbBr_2$ (Alfa Aesar) in 1 mL DMSO which was stirred for 2 h at 60°C and then filtered with a 0.45 µm PTFE filter. 100 µL of the solution was dispensed onto either a ZnO/Cs_2CO_3 or ZnO/PEIE substrate which was preheated at 100°C which was then immediately spincoated (1500 rpm; 500 rpm s^{-1}). After 3 seconds the still spinning substrate was dried with a heat gun set at a distance of 30 cm with a temperature of 130°C. The films were noted to crystallise after approximately 2-3 seconds of heat gun treatment. They were then annealed at 100°C for 10 minutes.

2.1.5.2 $NMA_2FAPb_2I_7$ – near infrared emitter

A 10 wt % solution of $NMA_2FAPb_2I_7$ in DMF was prepared by dissolving 68.5 mg of napthylmethylammonium iodide (details of preparation section 2.1.6.2), 20.7 mg FAI and 110.8 mg PbI_2 in 1.9 mL of DMF. The solution was stirred overnight at room temperature and filtered with a 0.45 µm PTFE filter. The solution was then dispensed onto a ZnO/ PEIE substrate and spincoated for 30 s (3000 rpm; 3000 rpm s^{-1}) and annealed at 100°C for 10 minutes

2.1.5.3 $CsPbBr_3$ with BA_2PbBr_4

A 0.5 M solution of $CsPbBr_3$ was prepared by dissolving 106.4 mg CsBr (Sigma Aldrich) and 183.5 mg $PbBr_2$ (Alfa Aesar) in 1 mL DMSO; a 0.5 M solution of BA_2PbBr_4 was prepared by dissolving 154.1 mg BABr and 183.5 mg $PbBr_2$ in 1 mL 4:1 v/v DMF:DMSO. The solutions were stirred at 60°C for 2 h and were then mixed in appropriate ratios to have the desired relative ratio. This solution was then filtered with a 0.45 µm PTFE filter. 100 µL of solution was dispensed onto the substrate and spincoated (2000 rpm; 2000 rpm s^{-1}) for 120 s. The substrate had visibly changed colour to yellow by the end of the program. The films were then annealed at 100°C for 10 minutes

2.1.5.4 $MAPbBr_3$ with PEA_2PbBr_4 or BA_2PbBr_4

A 0.5 M solution of $MAPbBr_3$ (56.0 mg MABr and 183.5 mg $PbBr_2$) in 1 mL DMSO and a 0.5 M solution of PEA_2PbBr_4 (202.1 mg PEABr and 183.5 mg $PbBr_2$) or BA_2PbBr_4 (154.1 mg BABr and 183.5 mg $PbBr_2$) in 1 mL 4:1 v/v DMF:DMSO were stirred at 60°C for 2 h and were then mixed in appropriate ratios to have the desired relative ratio. This solution was then filtered with a 0.45 µm PTFE filter. Following this 100 µL of the solution was spincoated in air (3000 rpm; 3000 rpm s^{-1}) for 30 s. 10s into the program

200 µL of chlorobenzene was dispensed onto the spinning substrate over the course of ~1 s to induce crystallisation. The films were then annealed at 100ºC for 10 minutes.

2.1.5.5 $FAPbBr_3$

A 0.66 M solution of $FAPbBr_3$ (82.5 mg FABr and 242.2 g $PbBr_2$) was dissolved in 1 mL 3:2 v/v DMF:DMSO with a 5 vol% addition of formic acid. The solution was stirred at 60ºC for 2 h and then filtered with a 0.45 µm PTFE filter. The solution was dispensed onto a pre-spinning substrate 1 s into a 2 step deposition program, (1000 rpm; 1000 rpm s^{-1}) for 10 s followed by (5000 rpm; 5000 rpm s^{-1}) for 30 s. 26s into the program 200 µL of anisole was dispensed onto the spinning substrate over the course of ~1 s to induce crystallisation. The films were then annealed at 100ºC for 10 minutes.

2.1.5.6 $(FA_{0.9}Cs_{0.1})_{1.1}PbBr_3$ and Choline Halide quench procedure

The procedure is the same as above. The precise masses and volumes used are 173.2 mg FABr, 32.8 mg CsBr, 513.9 mg $PbBr_2$ dissolved in 0.8 mL DMSO, 1.2 mL DMF and 100 µL formic acid. However at different delay periods after the anisole quench 50 µL of choline halide dissolved at varying concentrations in isopropanol was dispensed onto the still spinning substrate. The substrates were annealed at 100ºC for 10 minutes.

2.1.5.7 $MAPbBr_3$ with Benzylamine

A 0.6 M solution of $MAPbBr_3$ (67.2 mg MABr and 220.2 mg $PbBr_2$) was dissolved in 1 mLof 7:3 v/v DMF:DMSO and stirred at 60ºC for 2 h before being filtered with a 0.45 µm PTFE filter. The solution was dispensed onto the substrate which was spincoated in N_2 (3000 rpm; 3000 rpm s^{-1}) for 80 s, after 27 s of the programme 300 µL of chlorobenzene with different vol % of benzylamine was dropped onto the spinning substrate over the course of 1 s. The substrates were annealed at 100ºC for 10 minutes.

2.1.5.8 $PEA_{2n}FA_{n-1}Pb_nBr_{3n+1}$

0.6 M solutions of the different 2D/3D compositions were prepared using the precursors PEABr, FABr and $PbBr_2$, weighing out each vial separately rather than mixing solutions. The solutions were prepared such that there was 0.6 mmol $PbBr_2$ mL^{-1} and all other powders were varied to obtain the correct concentration. The solution was stirred at 50ºC for 2 h and then filtered with a 0.45 µm PTFE filter. The solution was dispensed onto the substrate which was then spincoated in N_2 (3000 rpm; 3000 rpm s^{-1}) for 60 s. 35 s into the program 200 µL of chlorobenzene was dispensed onto the spinning substrate over the course of 1 s to induce crystallisation. The films were then annealed at 90ºC for 30

minutes. If TPPO passivation was applied the solution in chlorobenzene was dynamically spincoated onto the perovskite film at 2000 rpm.

2.1.5.9 $CsPbBr_3$:18-crown-6: PEABr hybrids

Perovskite precursor solutions were prepared to a standard wt % of approximately 12.4%, where our $(PEABr)_{0.4}CsPbBr_3$ samples were at a concentration of 0.2 M. The masses in mg/mL of all of the salts for the solutions can be found below

	$CsPbBr_3$	**$(PEABr)_{0.1}$**	**$(PEABr)_{0.2}$**	**$(PEABr)_{0.4}$**	**$(PEABr)_{0.6}$**	**$(PEABr)_{1.0}$**
CsBr	48.5	46.9	45.3	42.56	38.4	33.8
PbBr2	83.6	80.8	78.2	73.402	66.3	58.3
PEABr	0	4.45	8.6	16.2	27.4	40.1
crown	4	4	4	4	4	4

All of the following procedures were carried out in a N_2- filled glovebox. The solutions were prepared by weighing all of the powders into a single vial, dissolving them in anhydrous DMSO by stirring at 50 °C for 3 h, and then filtering with a 0.45 μM PTFE membrane filter. A spin-coating program of 1000 rpm (1000 rpm s^{-1} ramp) for 5 s followed by 3000 rpm for 55 s (3000 rpm s^{-1} ramp) was used. The spin-coater was set up with a plastic collar (15 cm diameter) lined with a clean room wipe surrounding the chuck and run with the lid open (using a magnet to override the interlock). The 28 × 28 mm substrate was placed on the chuck and spun for approximately 2 s before 50 μL of precursor solution was dynamically dispensed onto the spinning substrate. We periodically checked the substrate while it was spinning with a UV torch to check for luminescence and found the $(PEABr)_{0.4}CsPbBr_3$ samples to begin to luminesce approximately 30 s into the spin program. The film was then annealed for 10 min at 100 °C; we observed that for $(PEABr)_{0.4}CsPbBr_3$ the luminescence is initially quenched but returns visibly to its initial intensity after 5 min. After each film was spincoated the clean room wipe was replaced in order to reduce the amount of DMSO in the immediate vicinity of the film during crystallization. We found this critical for the fabrication of reproducible films and devices.

2.1.6 Precursor preparation

2.1.6.1 ZnO nanoparticle dispersion

329 mg of $Zn(Ac)_2.2H_2O$ was dissolved in 15 mL of DMSO filtered with a 0.22 μM PTFE filter into a round bottomed flask with a stirbar . 459 mg of tetramethylammonium hydroxide ($TMAOH.5H_2O$) was dissolved in 5 mL of ethanol. At a temperature of 26-28^oC and relative humidity of 30-40% the TMAOH solution was added dropwise to the stirring $Zn(Ac)_2$ solution over the course of 3-4 minutes and then left to stir for 2 hours. The solution was split equally into 4 centrifuge tubes and 15 mL of ethyl acetate was added to each one, causing the solution to turn milky. The solution was centrifuged at 3000 rpm for 3 minutes and the supernatant was discarded, the white precipitate in each tube was redissolved in 1 mL of ethanol (4 mL total) to yield a clear solution. The redissolution of the nanoparticles was performed by adding the ethanol to the centrifuge tube and gently vortexing allowing the particles to slowly dissolve. Quickly vortexing or rigorous shaking during the process caused a cloudy solution. Then 5 mL of ethyl acetate was added to each tube causing a white precipitate to form. The solution was centrifuged at 3000 rpm for 3 minutes. The supernatant was discarded and 2 mL of ethanol was added to each tube to yield a clear solution. This solution was filtered with a 0.22 μm filter and used directly for spincoating.

2.1.6.2 Organic ammonium halide salts

PEABr/NMAI was prepared by the following procedure: 5 mL of phenethylamine/ napthylmethylamine and 30 mL of ethanol were mixed and stirred in a 250 mL two-neck flask in an ice−water bath. Then, 7 mL of HBr (48 wt % in water)/ HI (57 wt % in water) was slowly added into the mixture. The mixture was stirred for 2 h at 0 °C, maintained using an ice−water bath. The reacted solution was evaporated by a rotary evaporator at 55−60 °C to remove the solvent (ethanol and water), and a white precipitate was formed. The white precipitate was then washed with diethyl ether and collected by vacuum filtration, a step that was repeated three times. After filtration, the obtained PEABr/NMAI white powder was collected and dried in a vacuum oven at 60 °C overnight. After that, PEABr/NMAI was dissolved into ethanol and diethyl ether to obtain a supersaturated solution. The solution was put into a freezer overnight. The white precipitate was then washed with diethyl ether and collected by vacuum filtration, a step that was repeated three times. After filtration, the obtained PEABr/NMAI white powder was collected and dried in a vacuum oven at 60 °C overnight. It was then transferred to a N_2 glovebox.

2.2 Characterisation

2.2.1 LED Efficiency

Two different methods were used to measure the external quantum efficiency detailed below. In chapter 3 the EQE_{EL} was only measured using the integrating sphere method. During chapter 4 the photodiode method was implemented and the EQE_{EL} obtained by the two methods were compared for the same device and found to be the same.

2.2.1.1 Integrating sphere method

Current density−voltage characteristics (J−V) were measured by a Keithley source-measure unit (2600 series). The LED was placed in a N_2-filled holder that was mounted to the side of an integrating sphere. The electroluminescence spectrum and the photon flux were simultaneously measured using a calibrated grating spectrometer (MayaPro 2000). Using these data all of the relevant performance parameters can be calculated. Calibration was carried out by Bernard Wenger with assistance from me.

2.2.1.2 Photodiode method

Current density−voltage characteristics (J−V) were measured with a Keithley source-measure unit (2400 series). Simultaneously the photon flux was measured by a calibrated photodiode (Thorlabs FDS 1010), which was placed directly above the sample at a distance of 9 mm and held in a reverse bias of 3 V. The total number of photons emitted from the sample was calculated assuming a Lambertian emission profile and calculating the radiation view factor, which corrects for the fact that the LED is not a point source at this distance. The electroluminescence spectrum was measured using a calibrated grating spectrometer (MayaPro 2000). Using these data in addition to the responsivity of the photodiode, all of the relevant performance characteristics can be calculated. All measurements were carried out in a N_2-filled glovebox. I designed, built and calibrated the hardware for this setup. The software used to drive the diodes and collect data was designed in Labview by Bernard Wenger.

2.2.2 PLQY

Photoluminescent quantum efficiency measurements were carried out using a 405 nm laser (Roithner laser MLL-III-405-200 mW), an integrating sphere, and a calibrated grating spectrometer (MayaPro 2000 or Maya QE Pro). This was calibrated at the same time as the . The PLQY was calculated using previously established protocols.[1]

2.2.3 Steady-state PL and EL spectra

PL spectra were collected either using a calibrated MayaPro 2000 or Maya QE Pro grating spectrometer or a Horiba Scientific Fluorolog.

2.2.4 TRPL

Time-resolved photoluminescence (TRPL) measurements were conducted using a time correlated single photon counting protocol. A PicoQuant FluoTime 300 was used with either a 398 nm or 510 nm laser.

2.2.5 UV-Vis

Transmission and reflection measurements were carried out with a PerkinElmer 1050+ UV−vis−NIR spectrophotometer with an integrating sphere accessory.

2.2.6 Scanning Electron Microscopy

The SEM micrographs were measured using a FEI Quanta 600 FEG scanning electron microscope.

2.2.7 X Ray Photoelectron Spectroscopy

A Thermo Scientific Ka X-ray photoelectron spectrometer was used to perform XPS measurements using a monochromated Al Ka Xray source at a takeoff angle of 90°. The core level XPS spectra were recorded using a pass energy of 20 eV (resolution approximately 0.4 eV) from an analysis area of 300 μm × 300 μm. The spectrometer work function and binding energy scale were calibrated using the Fermi edge, and the 3d peak was recorded from a polycrystalline Ag sample prior to the commencement of the experiments. These measurements were carried out by Dr. Alexandra Ramadan

2.2.8 Fourier Transform Photocurrent Spectroscopy

The photovoltaic external quantum efficiency (EQE_{PV}) was measured using a custom-built Fourier transform photocurrent spectrometer (FTPS) based on a Bruker Vertex 80v Fourier transform interferometer. Devices were illuminated with a 0.4 sun (40 mW/ cm^2), AM 1.5G spectrum generated by an Oriel class AAA solar simulator. The LEDs were masked with a metal aperture, with a defined active area of 0.0625 cm^2 . All of the photocurrent measurements were carried out in air. To calculate the EQE_{PV}, the device photocurrent spectrum was divided by a calibrated silicon reference cell spectrum with a

known EQE. The acquisition time for each spectrum was approximately 1 min. These measurements were conducted by Robert D. J. Oliver

2.2.9 X Ray Diffraction

XRD diffractograms were obtained using a Panalytical X'Pert Pro X-ray diffractometer with a Cu-alpha source ($\lambda = 1.54$ Å).

2.3 References

1. de Mello, J. C., Wittmann, H. F. & Friend, R. H. An improved experimental determination of external photoluminescence quantum efficiency. *Adv. Mater.* **9,** 230–232 (1997).

3 Exploration of Device Structures and Passivation Strategies for Perovskite LEDs

3.1 Introduction

The aim set out for this thesis was to investigate and understand what governs stability in metal halide perovskite light emitting diodes (LEDs). In order to undertake this study, we set the target of fabricating perovskite LEDs with state of the art efficiency and emission at a technologically relevant wavelength. We chose to target our efforts at perovskite emitters of the composition $APbBr_3$ (A = methylammonium (MA), formamidinium (FA) or cesium (Cs)) as: i) They have an emission peak of 510 -540 nm are thus ideal for green LEDs, where they are close to the peak of the photopic response of the human eye; ii) They do not require mixing of halides to achieve this wavelength, which removes the possibility of halide segregation.[1]

The achievement of these targets was far from trivial and constituted a large part of the time period of this thesis. The group had never made LEDs before and as such I had to work up both new device structures and new materials for the first time. This chapter contains the initial phase of; i) searching for a suitable device structure for green perovskite LEDs, and, ii) improving the PL efficiency of green perovskite emitters through different passivation methods towards the goal of efficient perovskite LEDs. Subsequent chapters will detail the further optimisation and stability studies on efficient green LEDs once this initial target had been achieved.

3.2 Fabrication of *nip* F8BT and green perovskite LEDs

3.2.1 Introduction

A thin film LED is a complex device structure which must be optimised so as to ensure efficient charge transport, recombination and light outcoupling. In a first phase, we

developed protocols for the deposition of the different layers and use established light emitters such as F8BT and $CsPbBr_3$. At this juncture the most efficient perovskite LEDs used an *nip* configuration and near infrared emitters,[2] we therefore decided to pursue this configuration as it also shows high efficiency in solar cells[3] with which we have expertise in the lab.

3.2.2 *nip* F8BT LEDs

We began by reproducing the work of Kabra *et al.*[4] where a simple device structure is used to achieve efficient emission from F8BT (Figure 3.2). In this paper, ZnO is deposited *via* spray pyrolysis followed by a thin layer of Cs_2CO_3 which they demonstrate enhances electron injection. Following, the emitter layer of F8BT is deposited *via* spincoating, and finally a ~10 nm layer of MoO_x and a 100 nm layer of Au are deposited *via* thermal evaporation. The function of the MoO_x is to significantly enhance hole injection from the Au into the F8BT which has a HOMO of 5.8 eV.[4]

In order to make this device structure, we first optimised the deposition of ZnO via spray pyrolysis. Initially, significant inhomogeneity was observed on a macroscopic scale and different deposition procedures were trialled. A compact layer which appeared homogenous to the eye was achieved by using a pulsed spraying method. Small pulses of the precursor solution were sprayed (~1 s) and allowed to completely dry before proceeding. The films were then analysed by scanning electron microscopy (SEM, Figure 3.1), where it was found the presence of: i) small flakes up to 500 nm in length, and, ii) pinholes on the order of 100 nm in size. Then, we proceeded to build up the rest of the device, which required the implementation of a process for the evaporation of MoO_x in the glovebox. Subsequently, we successfully fabricated a functioning LED with F8BT as the emitter.

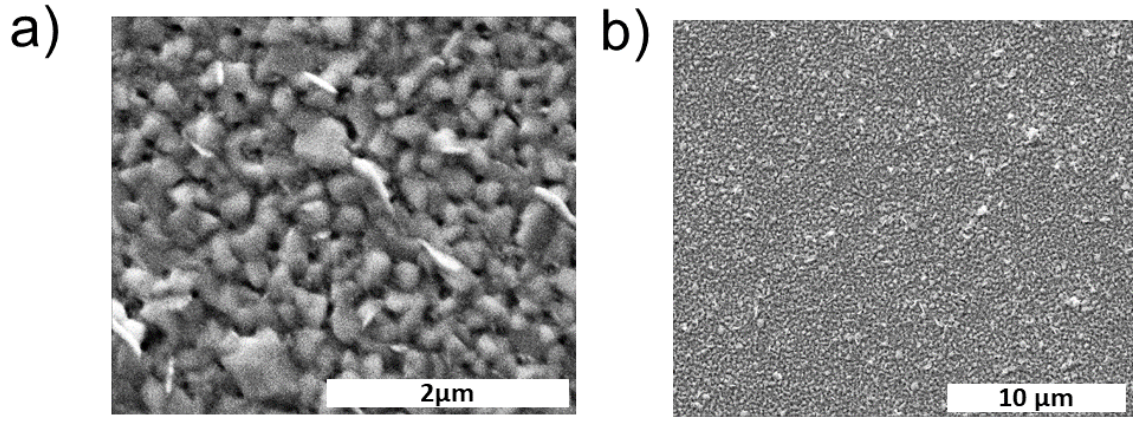


Figure 3.1 Morphology of ZnO on ITO showing a) flakes at close magnification, and, b) the extent of their distribution at lower magnification.

In Figure 3.2.b. one can see the EL spectrum of F8BT from our optimised device. The emission peak is at an ideal wavelength of 550 nm at the peak of the photopic response of the human eye, however the FWHM of the EL is approximately 100 nm which results in a poor colour purity and a yellowish emission is observed. This demonstrates the need for emitters like metal halide perovskites which have easily tuneable emission wavelengths and narrow FWHM (approx. 20 nm)[5]. One can see the performance of the device in Figure 3.2.c. and d. A maximum luminance of 500 cd m^{-2} and a maximum EQE_{EL} of 0.17 % were achieved. This performance is relatively poor compared to the report of Kabra *et al.* where they achieved an EQE_{EL} up to 7%. One can see in Figure 3.2.c. that there is a current density of ~ 2 mA cm^{-2} being injected into the device prior to 2.5 V. This is indicative of shunts in the device which could be due to the previously observed pinholes in the ZnO or a discontinuous F8BT layer creating Au to ZnO contact. In either instance the shunt is a parasitic loss which contributes to the poorer performance. Further, we tested the PLQY of the F8BT that we used in the study to be 28% on glass which is significantly lower than the value of 76% measured by Kabra *et al.* which could be due to a lower quality material. We then focussed our efforts on improving the morphology of the ZnO electron injection layer.

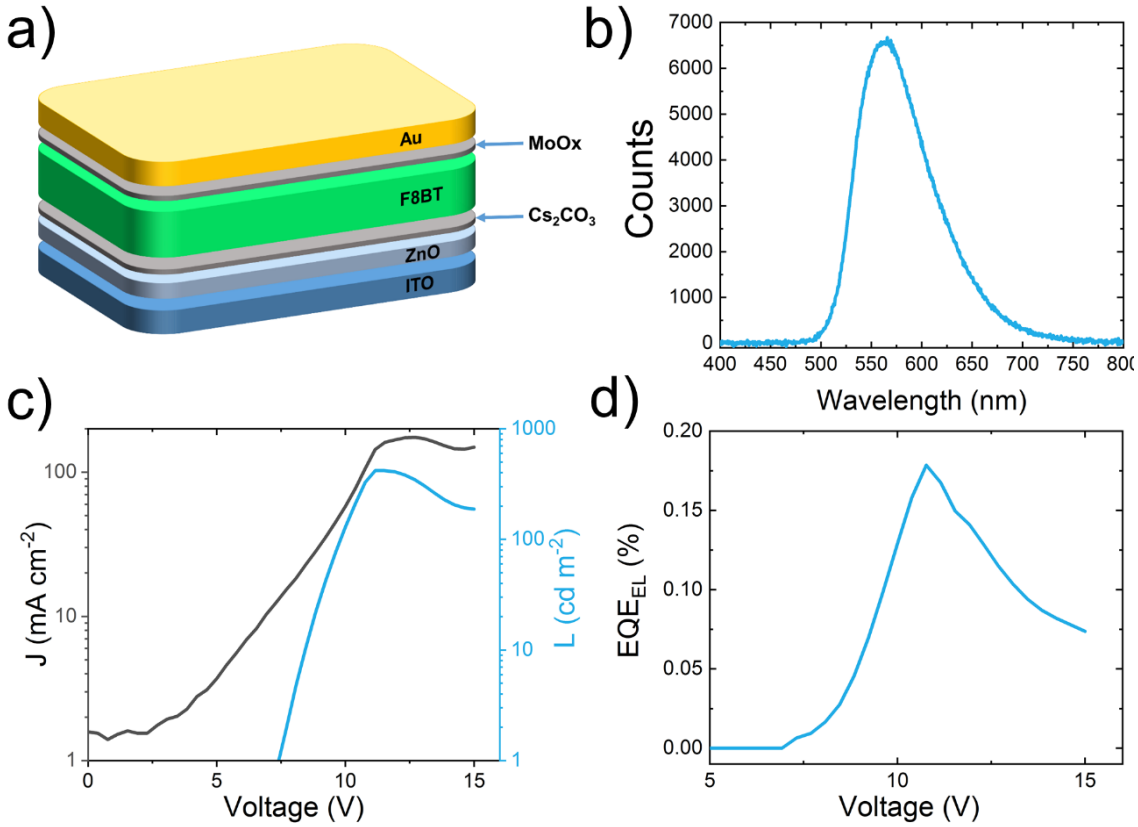


Figure 3.2 Characterisation of *nip* F8BT LED: a) Device structure; b) EL spectrum; c) JVL characteristics; d) EQE_{EL} v Voltage.

3.2.3 Improvement of ZnO through *nip* near-infrared 2D/3D perovskite LEDs

One of the key problems we identified for the fabrication of efficient F8BT LEDs, was the poor morphology of the electron injection layer in the stack. Reports of highly efficient near-infrared (NIR) pure iodide perovskite LEDs had recently emerged which used ZnO nanoparticles as an effective electron injection layer.[6] We sought to synthesise the colloidal dispersion of nanoparticles and reproduce these LEDs to confirm their proper function.

A brief optimisation of the ZnO nanoparticles led to the production of a transparent colloidal dispersion the details of which can be found in the methods section of this thesis. We note the use of a layer of ethoxylated polyethylenimine (PEIE) between the ZnO and perovskite (Figure 3.3.a.). The function of the layer is to prevent degradation of the perovskite due to a reaction with the ZnO. Samples without a PEIE interlayer would quickly turn yellow after annealing (an indication of the formation of lead iodide). This effect has been studied in literature and is attributed to the basicity of ZnO. This causes deprotonation and volatilisation of the organic cations in the emitter layer.[7]

Having successfully fabricated the ZnO/PEIE electron injection layer, we were able to quickly produce functional 2D/3D perovskite LEDs with an EQE_{EL} of up to 4.6 % (Figure 3.3.b.). One can see the emission wavelength peak is in the near infrared (NIR) at approximately 780 nm (Figure 3.3.c.) which is beyond the photopic response of the human eye, as such the electroluminescence of the LED is barely visible due to its small contribution in the red domain (650-700 nm). In Figure 3.3.d. we note that the leakage current (below turn-on voltage), is much smaller than the previously studied F8BT LED (Figure 3.2.c.). This indicates that the quality of the ZnO and/or emitter layer are greatly improved.

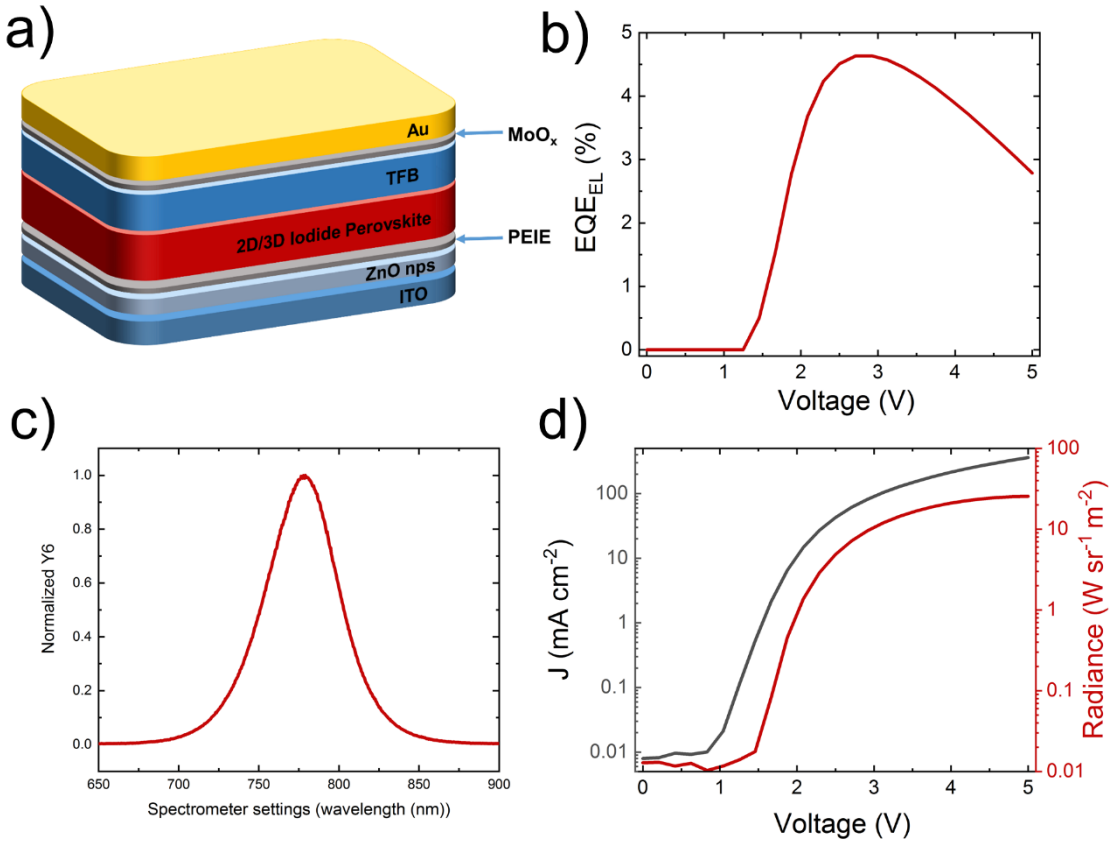


Figure 3.3 Summary of near infrared *nip* perovskite LEDs: a) Device structure; b) Champion EQE_{EL} vs V; c) EL spectrum; d) JV-Radiance characteristics

While operating the LEDs, we observed substantial degradation but also a slight recovery of the efficiency when the devices are left unbiased for minutes or hours. We seek to understand the reversibility of the degradation of the EQE_{EL} as this had not been reported.[6] We operated the LEDs at a constant current density of 4 mA cm^{-2} and track the evolution of the EQE_{EL} over time and retested this pixel twice after a 2 h recovery period

(Figure 3.4.a.). We observe that there is a small degree of reversibility after leaving the LED to recover for 2 h.

Additionally, we performed voltage sweeps for all pixels on a separate substrate from 0-5 V (Figure 3.4.b.), left the substrate to recover for 24 h and repeated the measurement. We observe that the efficiency has significantly decreased, which indicates that the measurement process is causing an irreversible degradation. In Figure 3.3.b. + d. we can see that there is significant 'roll-off' of the EQE_{EL} at 5 V and approximately 400 mA cm^{-2} is being passed through the device. This roll-off in perovskite LEDs of this class has been attributed to Auger recombination,[8] however these results indicate that at least part of the roll-off is due to irreversible degradation.

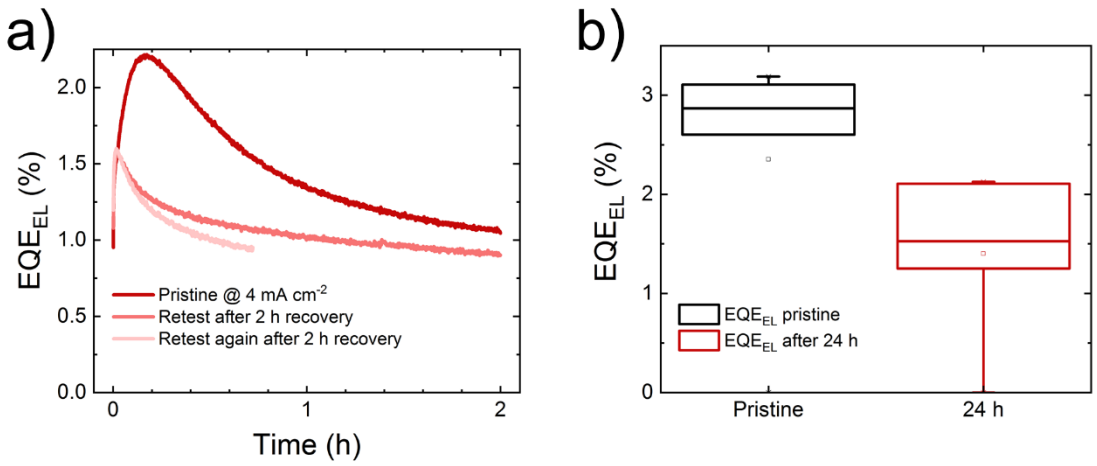


Figure 3.4 a) Stability study of NIR perovskite LED: a) EQE_{EL} vs T, and, retests after 2 h of recovery; b) Boxplot of EQE_{EL} of pristine substrate and after a retest.

3.2.4 Investigation into $CsPbBr_3$ as an emitter in the *nip* configuration

We now proceed to incorporate a green perovskite emitter into the now functioning perovskite LED device stack. We begin with the emitter $CsPbBr_3$ which had been shown to be the most thermally stable green-emitting lead halide perovskite,[9] which we posit may translate to better EL stability.

Various spincoating deposition procedures were trialled for $CsPbBr_3$ including the now ubiquitous antisolvent quench procedure.[10] This was found to give a macroscopically rough morphology so other methods were tried to obtain specular films. Eventually, it was found that hot-casting the $CsPbBr_3$ solution onto the substrate and drying it with a heat gun while spinning gave relatively smooth films to the eye (referred to as $CsPbBr_3$ – heat gun method, in experimental methods). These films were investigated by SEM and it was found that there was a high pinhole density (Figure 3.5. a. + b.). The pinholes encountered here were commonly occurred when working with $CsPbBr_3$ during the

thesis, and are reported often in the literature.[11–13] The root cause of the issue is twofold: i) The precursors for $CsPbBr_3$ (particularly CsBr) have poor solubility in commonly available solvents,[14] the maximum solubility we were able to achieve for a stable solution was 0.4 M in DMSO *cf.* MAPI which can be > 2 M in DMSO, and, ii) The crystallisation of bromide based perovskites is more rapid than iodide perovskites which reduces its controllability.

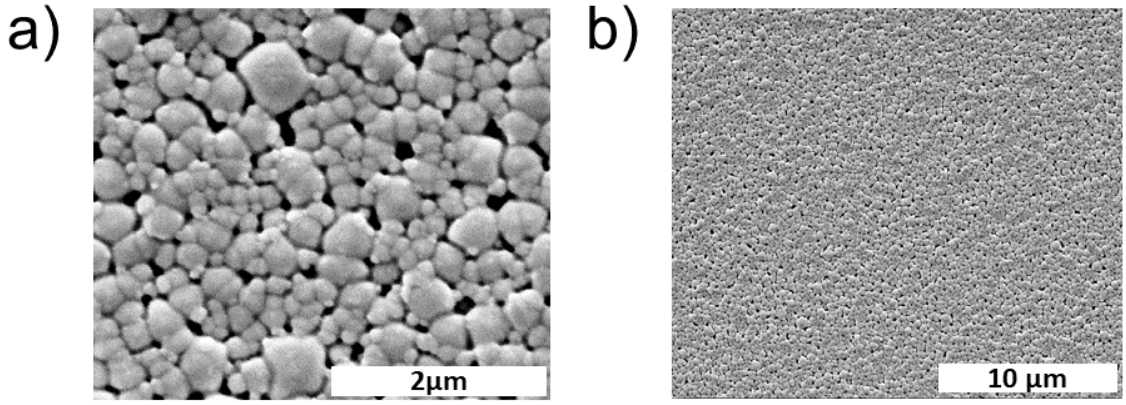


Figure 3.5 Morphology of $CsPbBr_3$ thin films made by 'heat-gun method' showing significant pinholes at a) closer magnification, and, long range uniformity at b) lower magnification.

We were unable to achieve any measurable emission from LEDs using this deposition procedure so we explored different deposition methods to reduce the pinhole density of the thin films. We created a new deposition protocol for $CsPbBr_3$ where the substrate was spincoated at 3000 rpm for 120 s which caused the film to crystallise while spinning. This controlled evaporation of the solvent led to more specular films with a lower pinhole density as can be seen in Figure 3.6.a.. Despite this there was still a high density of pinholes so we decided to intermix a 2D perovskite butylammonium lead iodide (BA_2PbBr_4); the surfactant nature of this perovskite should allow the formation of more continuous films.[15] We found that a 10 mol% addition was optimal to achieve smooth pinhole free films (Figure 3.6.b.), a 20 mol% addition caused pinholes and a clear phase segregation (Figure 3.6.c.).

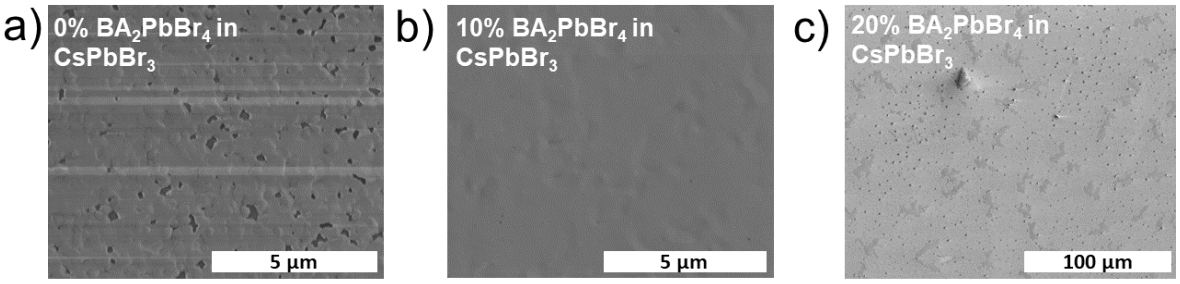


Figure 3.6 SEM of films of spincoated $CsPbBr_3$ with; a) 0% BA_2PbBr_4; b) 10% BA_2PbBr_4; c) 20% BA_2PbBr_4.

Despite the much improved morphology upon incorporation we did not observe visible emission from the devices with 10% BA_2PbBr_4. We measured the PLQY of the 10 mol% sample at a fluence of 120 mW cm^{-2} and found it to be approximately 1% which we deem is too low to afford efficient EL.

3.2.5 Investigation into $MAPbBr_3$ and $FAPbBr_3$ as an emitter in the *nip* configuration

Having established that the PLQY of the 10% BA_2PbBr_4 was too low, we focussed our efforts on improving the PLQY of the perovskite emitter by substituting the A site cation of Cs for methylammonium (MA). Additionally, we used an antisolvent quench procedure successfully for these perovskites which aided in the formation of continuous films. We then compared 2 different 2D forming cations, BA and phenylethylammonium (PEA) and found that PEA gave higher PLQY on glass reaching up to 12% with a 25 mol% addition (Figure 3.7.a.). We then continued the optimisation in a narrower range of compositions and looked at PL quenching on the transport layers which we had selected. We found that; i) the optimal composition was 33% PEABr which gave the highest PLQY (Figure 3.7. b.) and also smooth pinhole free films (Figure 3.7.c.), and, ii) ZnO/PEIE substrate quenched the PL the most giving a PLQY of 7.8% for the 33 mol% composition.

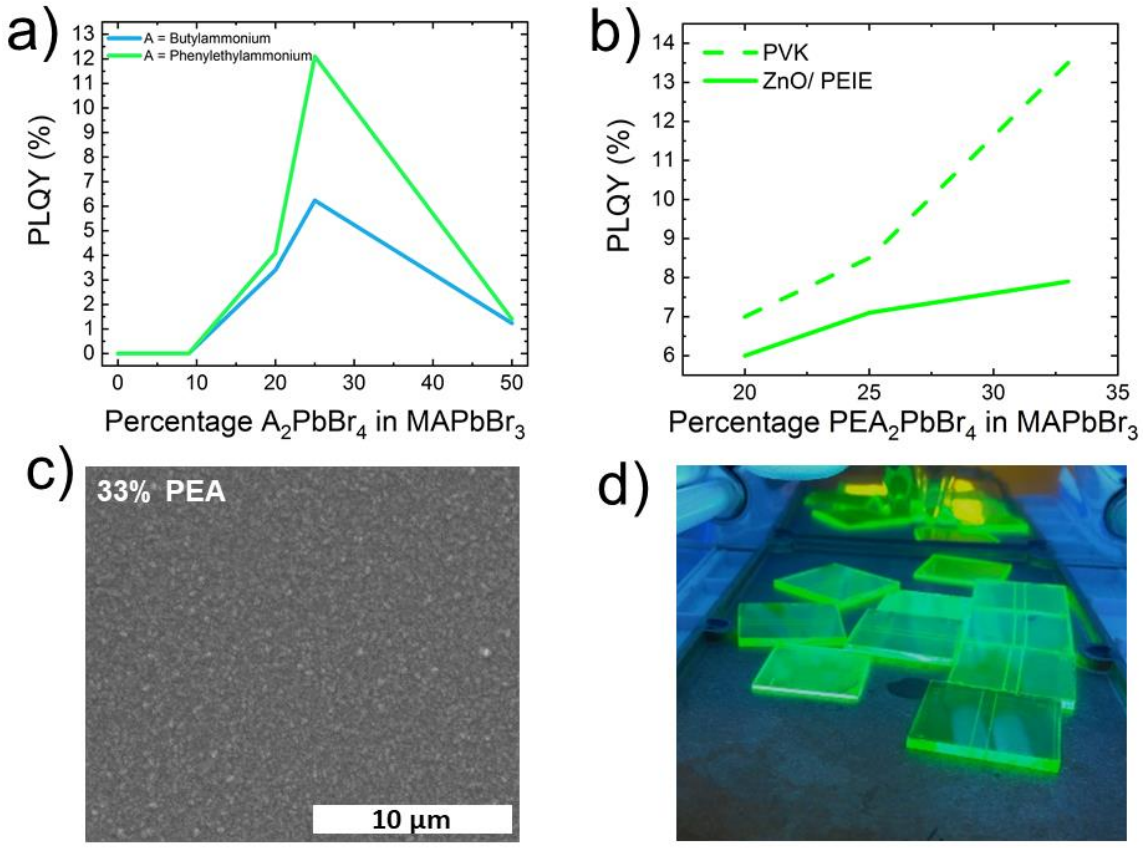


Figure 3.7 a) PLQY (fluence 120 mW cm^{-2}) vs molar percentage of A_2PbBr_4 in $MAPbBr_3$ for A=PEA and A=BA ; b) PLQY vs molar percentage of PEA_2PbBr_4 in $MAPbBr_3$ on PVK and ZnO/PEIE; c) SEM of 33 mol % PEA_2PbBr_4 in $MAPbBr_3$.; d) Photographs of films of PEA_2PbBr_4 in $MAPbBr_3$, substrate size 28 x 28 mm

Upon incorporation of the optimised emitter into LEDs we observed that despite a reasonable PLQY the EQE_{EL} was too low to measure. Further scrutiny of the device under operation showed that as the voltage was increased in a stepwise fashion EL would occur at each step above turn-on, but only for a very short period of time. When we performed a second JV sweep of the LED, no EL was observed. This was an indication of a major degradation in the device and we moved on to explore formamidinium as an alternative A-site cation. We were able to obtain EL from $FAPbBr_3$ without intermixing of a 2D perovskite (Figure 3.8.b.), unfortunately it was very inefficient and therefore it was not possible to measure an EQE_{EL}.

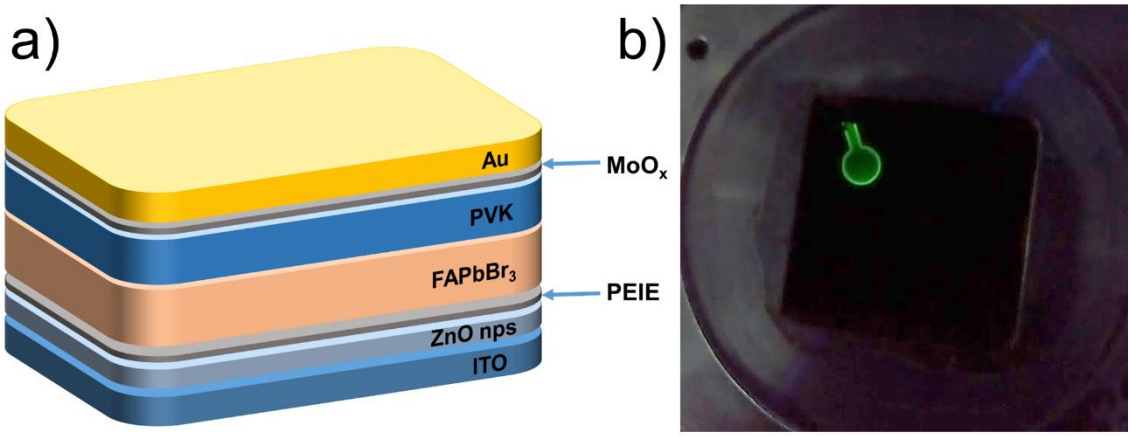


Figure 3.8 a) Device structure of successful green *nip* perovskite LED; b) Photograph of its EL.

3.2.6 Discussion and Conclusions

In Section 3.2 we have implemented a *nip* LED device structure and investigated its applicability to green emitting perovskite LEDs. Initial difficulties with a high pinhole density and rough morphology in the ZnO electron transport layer were rectified by synthesising a colloidal dispersion of ZnO nanoparticles. This led to the fabrication of efficient NIR perovskite LEDs which showed a low leakage current below turn-on voltage.

We then investigated the use of $CsPbBr_3$ as a green perovskite emitter to incorporate into this structure. We find that the fabrication of continuous films of neat $CsPbBr_3$ *via* spincoating is difficult and incorporate the 2D perovskite BA_2PbBr_4 into the precursor solution which allowed us to obtain continuous films. Despite good continuity of the films we did not observe visible emission which we attribute to low PLQY. We then explored different perovskite green emitters where we were able to achieve higher PLQY (up to 15%) with a continuous morphology, however, this did not lead to efficient EL. Finally, we were able to achieve visible EL using the emitter $FAPbBr_3$, however it had too low of an EQE_{EL} to be measured by our system.

It is clear from our results that fabrication of, i) a high quality layer of ZnO , ii) continuous perovskite films, and, iii) obtaining a PLQY of >7% on this transport layer are not sufficient to obtain efficient EL. As we were able to reduce the leakage current through continuity of the layers we posit that either i) charge imbalance, or, ii) reduction of the PLQY of the emitter under operation are the reason for the poor EL efficiency. Given that we observed a major and rapid irreversible degradation of the EL at each voltage step it is likely that the reduction of PLQY was a major contribution. Interestingly, we did not

observe this degradation with $FAPbBr_3$, indicating that the degradation process is not universal for all green emitting perovskites in this device structure.

Recently, Sim *et al.* reported high efficiency $CsPbBr_3$ LEDs in a *nip* configuration.[16] The researchers measured the conduction band minimum (E_{CBM}) of $CsPbBr_3$ (3.3 eV) and found it was significantly closer to vacuum than ZnO (4.5 eV). They modified the electron injection layer from ZnO to an amorphous zinc silicon oxide (a- ZSO). Through varying the Si content they were able to shift the E_{CBM} of a-ZSO to match the conduction band minimum of $CsPbBr_3$ and drastically improve their EL efficiency. They attribute this improvement to reduction in electron hole pair dissociation at the interface through the formation of a type-I heterojunction. It is apparent that this may be a contributing factor to why we were unable to optimise the *nip* configuration and why groups rarely report green *nip* perovskite LEDs. The E_{CBM} of $FAPbI_3$ (~4.0 eV)[17] is closer to ZnO and we did not measure the E_{CBM} of our own ZnO system which may have a shallower E_{CBM} than Sin *et al.* reported. Given that we achieved good performance from our NIR emitter (which should have a similar E_{CBM} to $FAPbI_3$) , and other research groups have,[8,18] we posit that there is a superior energetic alignment between these two materials.

To conclude, we find that ZnO is not a suitable material for the fabrication of efficient green perovskite LEDs and move forward to attempt a *pin* device stack. At the time reports in literature on efficient green perovskite LEDs[19,20] used a *pin* device structure which was an encouraging indication that it might be a more fruitful strategy.

3.3 Fabrication of *pin* F8BT + green-emitting perovskite LEDs and passivation of $APbBr_3$ perovskites for improved PLQY

3.3.1 Introduction

In this phase of the project we optimise a new LED structure which has a *pin* layout in order to test its applicability for making efficient, green emitting perovskite LEDs. When changing structure, the intricacies of efficient charge injection must be addressed, which is what we tackle initially. After this is optimised, we strive to improve the PLQY and subsequently the EQE_{EL} of the perovskite through different means of chemical passivation.

3.3.2 Implementation of a *pin* device structure and first green perovskite LEDs

Several reports of efficient green perovskite LEDs with a *pin* device structure had emerged and therefore we use F8BT as a control emitter to implement this structure in the lab. In order to have a reproducible structure the deposition of three new layers needed to be optimised:

i) The electron injection layer TPBi. Attempts were made to solution process this layer *via* spincoating but this led to a discontinuous film. Therefore, we choose to evaporate the layer using our glovebox evaporation system using new shadow masks designed for the purpose.

ii) The aluminium electrode. Initial attempts to evaporate aluminium using a molybdenum or tungsten boat were unsuccessful. It was apparent that the aluminium is reacting with the boats to form an alloy which increased the resistance of the boat and eventually causing it to break. Therefore, it was only possible to evaporate approximately 30 nm of Al at a time which was insufficient. After some research it was found the most common method for thermal evaporation of Al was using a basket heater and an alumina crucible; however, this proved to generate too much heat in our small chamber evaporator and thus damaged the devices. Eventually, we found that using molybdenum boats coated in alumina were an appropriate evaporation source where a stable rate could be achieved and >100 nm be deposited at a time without damage to the substrate.

iii) The LiF interlayer. LiF is used as an interlayer to increase electron injection into materials with a LUMO energy closer to vacuum that the work function of Al and has been commonly implemented in OLED research.[21,22] The role of LiF is still not clear although it has been suggested that it works either as i) a protective layer for the organic,[21] or, ii) a surface dipole modification.[22] We choose to optimise this interlayer using our prototype emitter F8BT with the structure below (Figure 3.9.a.). We kept the thickness of all other layers the same and looked at the difference in current density flowing through the device assuming that we were limited by the TPBi/Al interface. In Figure 3.9.b. + c. one can see the dramatic effect that LiF thickness has on the current density and device performance. As we increase the thickness, we observe an order of magnitude increase in the injected current at the maximum voltage. Additionally, we see a decrease in the turn-on voltage and an increase in the

EQE_{EL}. We continued to optimise this further (Figure 3.9.d.) and found a saturation of the effect at 1.4 nm thickness. This resulted in bright polymer LEDs with homogenous, visible emission (Figure 3.9.e.). The implementation of this layer was a crucial step towards efficient perovskite LEDs.

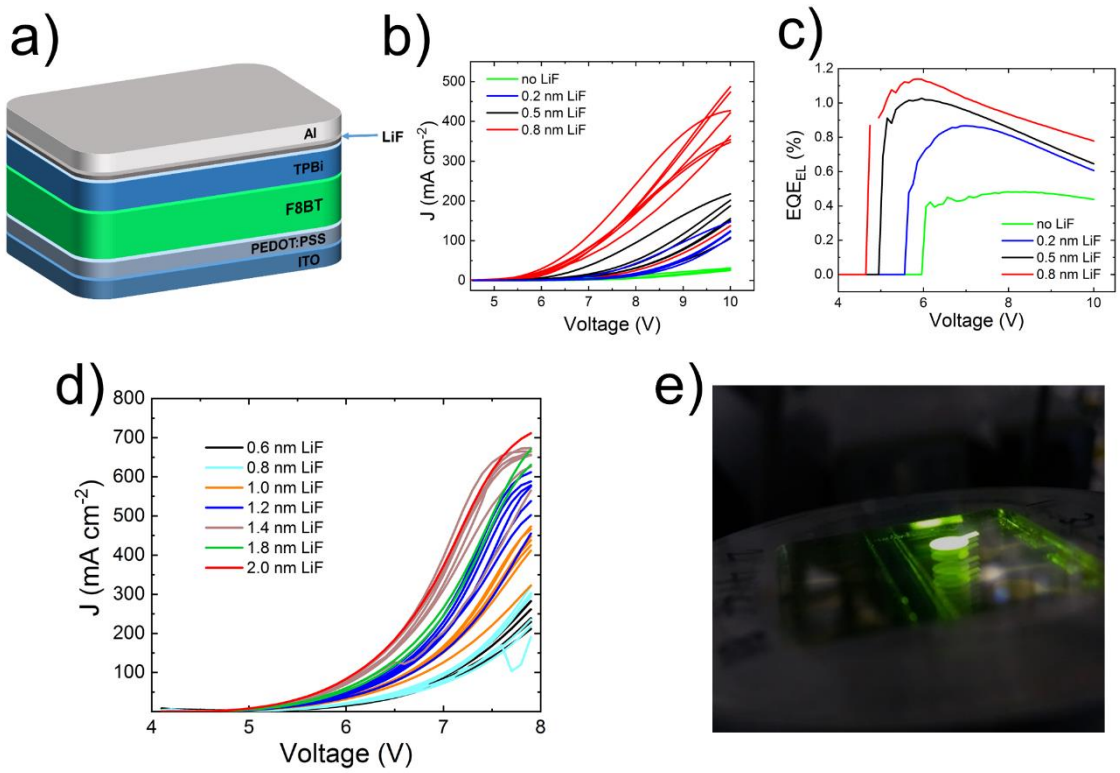


Figure 3.9 a) Device structure of *pin* F8BT LED; b) JV of first LiF optimisation showing improved electron injection; c) Corresponding EQE_{EL} v V; d) JV of further optimisation of LiF thickness; e) Photograph of optimised LED in operation.

Now that we have improved charge injection and achieved relatively efficient emission from this device structure we proceed to try and reproduce a report from Lee *et al.* of efficient perovskite LEDs.[23] The researchers had a baseline device using $MAPbBr_3$ fabricated through a solvent quench procedure which they dramatically improve through the addition of a small volume of the alkylamine benzylamine (BzA) into the antisolvent (chlorobenzene). As can be seen in Figure 3.10.b-d. we are able to successfully produce working perovskite LEDs whose emission could be detected through our integrating sphere measurement system! This was a Eureka moment of this project. We achieve a maximum EQE_{EL} of 0.3% and move forward to improve this performance through the addition of BzA to the antisolvent.

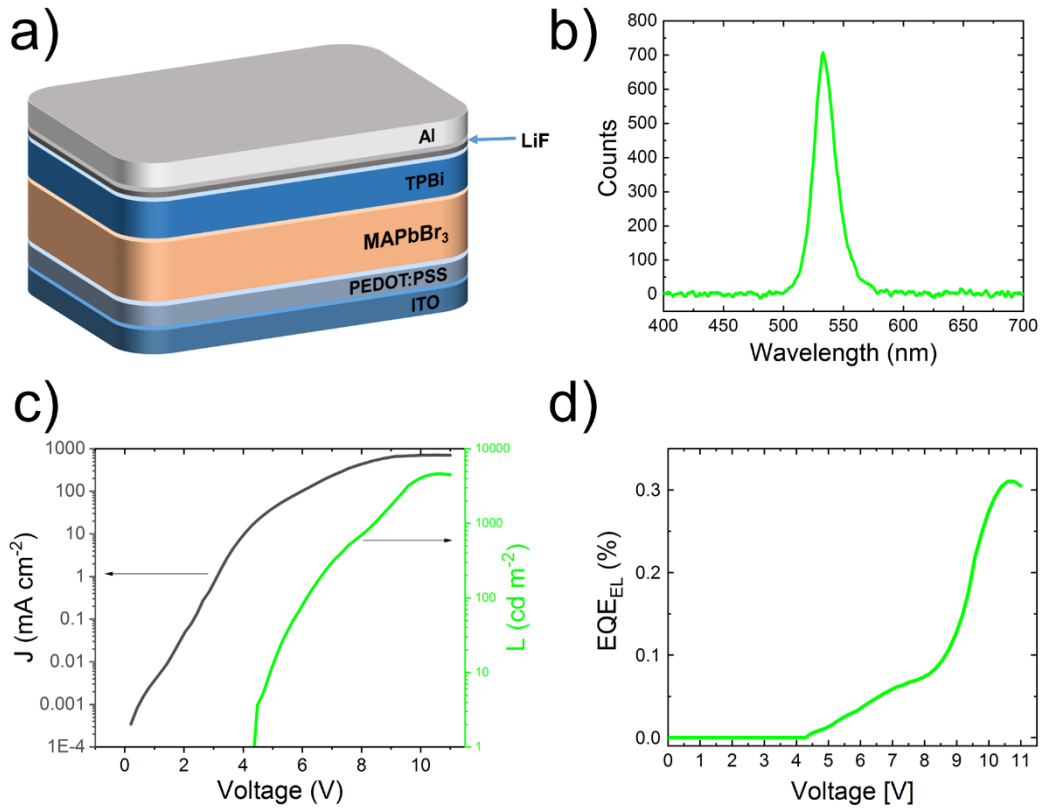


Figure 3.10 First measurable visible perovskite LED in the Snaith group: a) Device structure; b) EL spectrum; c) JVL characteristics; d) EQE_{EL} v V.

3.3.3 Investigation into the effect of benzylamine in the antisolvent

Figure 3.11.a. shows the normalised photoluminescence of the films prepared through the BzA procedure. One can see that there is a slight blueshift in the peak emission wavelength with increasing BzA content which we posit is due to quantum confinement of the photoexcited carriers. Further, in Figure 3.11.b. which shows the un-normalised photoluminescence that there is also a significant increase in total PL intensity with increasing BzA content. Additionally we note that there are two small peaks in the PL of the 0.5 vol% BzA sample, which are likely due to the formation of a small amount of n=2 and n=3 Ruddlesden-Popper phases.[24]

The increase in PL is corroborated by the immediate PLQY which was measured on the films which also increases with BzA content (Figure 3.11.c.). Additionally, in Figure 3.11.c. we show the stabilised PLQY; this represents the measured value after approximately 60 s once the PLQY had decreased drastically. These samples were measured in ambient conditions without encapsulation which was a poor practice and is discussed later in this thesis. The films that are eventually put into devices are kept and tested in nitrogen and thus encapsulated films would have been more appropriate. Finally,

we observe in the UV-Vis (Figure 3.11.d.) that there is no clear shift in the absorption onset, however there is an increase in extinction below the bandgap as we increase the BzA content (indicative of increased scattering) which is coupled with a broadening of the excitonic absorption.[25] We also see a bump in the absorption for the 1 vol% sample which is likely due to the exciton of the n=1 2D phase.[24]

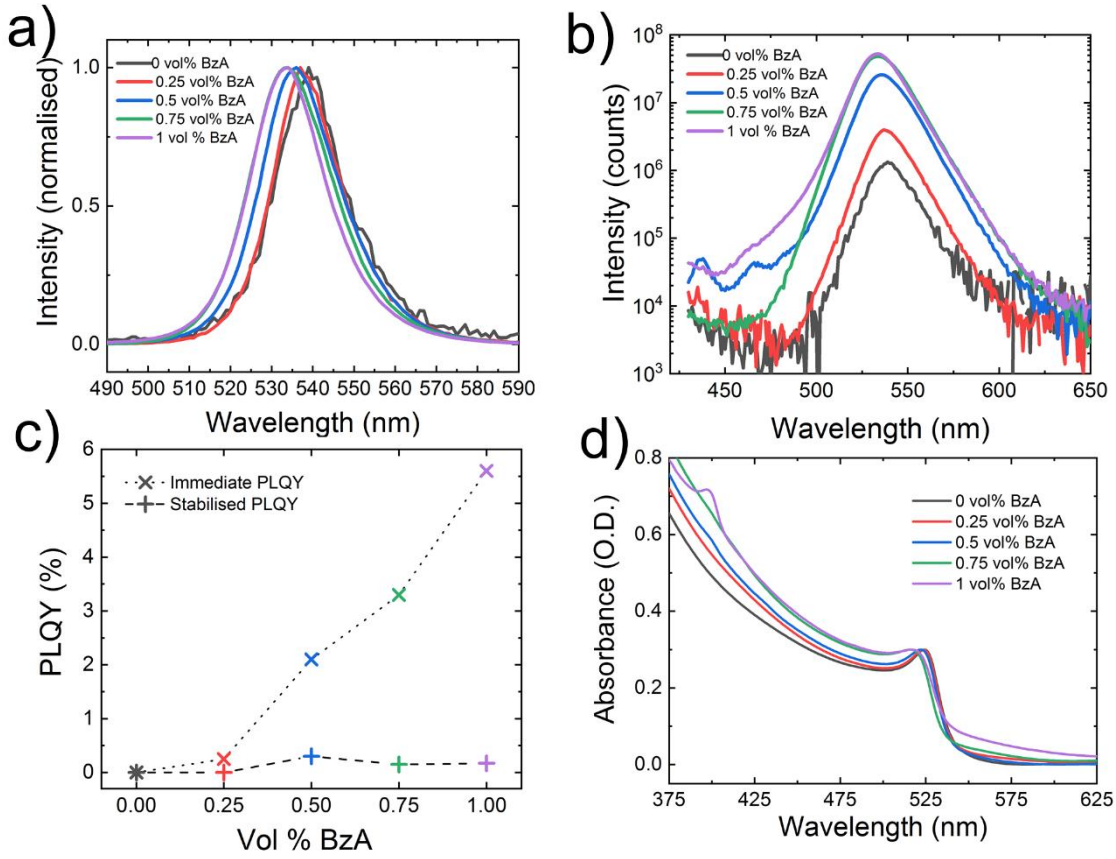


Figure 3.11 Photophysical characterisation of benzylamine modified $MAPbBr_3$ films: a) normalised PL; b) Unnormalised PL; c) Stabilised and unstabilised PLQY; d) UV-Vis absorbance.

Next, we inspected the perovskite films through SEM on an ITO/ PEDOT:PSS substrate (Figure 3.12). We see that as we increase the BzA content there is: i) the evolution of an unusual cubic morphology (more clearly visible in Figure 3.13) and ii) a decrease in grain size. We see that for the 0.75 vol% BzA sample, the morphology has become textured and porous with a high pinhole density, it should be noted that the textured morphology will increase light outcoupling, making it difficult to make absolute comparisons of the PLQY.

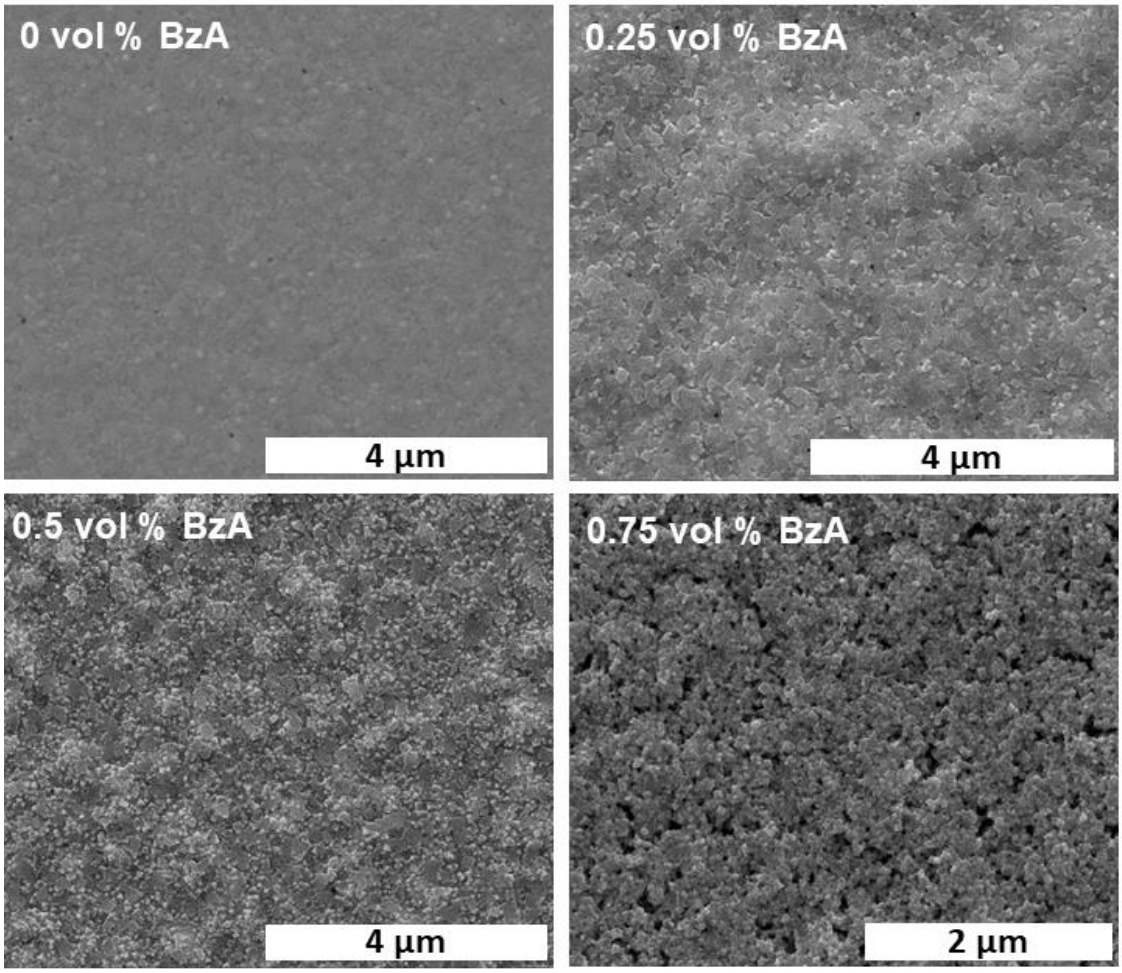


Figure 3.12 SEM characterisation of benzylamine treated $MAPbBr_3$

Considering the photophysical and morphological characterisations as a whole we conclude that the blueshift that we observe is due to the reduction of the size of the emissive domains below the quantum confinement regime. The single grains in our 0.75 vol% BzA sample are ~50 nm in size, however they are not clearly of a size which we would expect quantum confinement for (approx.. 15 nm for $CsPbBr_3$)[26]. The evidence of the formation of Ruddlesden-Popper phases in samples with higher BzA content indicates that the emissive domains could be smaller than the grain size. High n value nanoplatelets could be within the grains causing the observed blueshift.[27] Further, it is clear that the increased extinction below bandgap for the 0.75 and 1 vol% BzA samples is due to the rough morphology which is increasing scattering in the sample. While we have no absolute statement to make on the unusual cubic morphology, we note the similarities in the shape of the grains to single crystals of $MAPbBr_3$ which can be grown through an inverse solubility methods.[28] Our group has shown the importance of methylamine and dimethyamine in this process,[29] both of which are alkylamines like BzA. Their role in single crystal formation is the dissolution of colloids and thus supersaturation of the

solution, resulting in the rapid formation of single crystals. We posit that a similar supersaturation process is occurring here through interaction of BzA with colloids in the still wet film during spincoating.

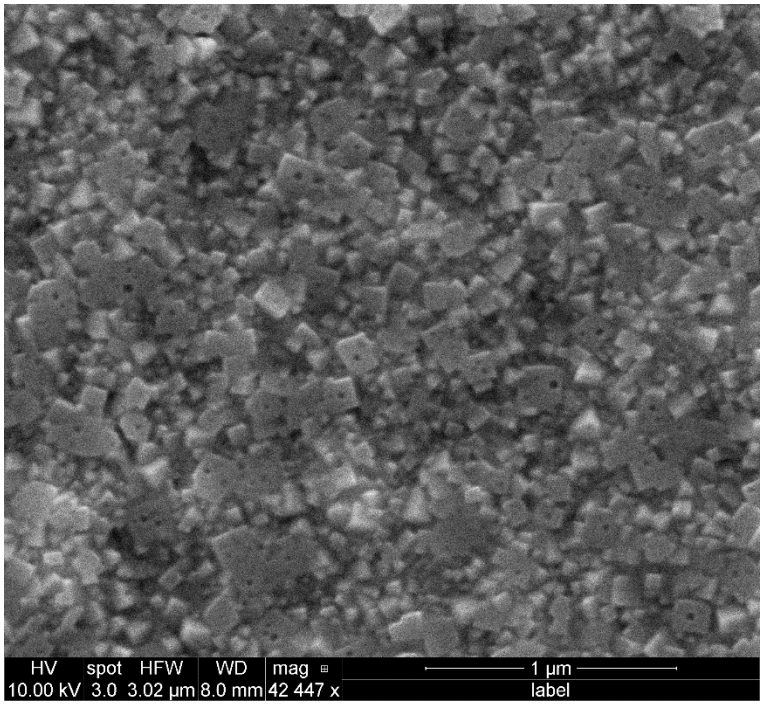


Figure 3.13 SEM of 0.5 vol% Benzylamine treated $MAPbBr_3$ film showing unusual cubic morphology.

Next we fabricated LEDs using the BzA addition to the antisolvent in the same device structure as presented in Figure 3.10.a.. We observe that there is a moderate increase in the EQE_{EL} with increasing BzA content with 0.5 vol% BzA being the optimum with a peak EQE_{EL} of approximately 0.4% (Figure 3.14.c.). We also see a decrease in the current density required to reach peak EQE_{EL} as we go from 0 → 0.5 vol % BzA (Figure 3.14.a.). We posit that this is due to a lowering of the trap state density which is indicated by the increase in immediate PLQY (Figure 3.11.c.); the effect is the same as in steady state PL where increasing carrier density fills the traps and thus enables efficient bimolecular recombination. Perhaps surprisingly, we see that this trend does not continue for our 0.75 vol% and 1 vol% samples where we observe a much lower peak EQE_{EL} at higher current densities even though they demonstrated higher PLQY.

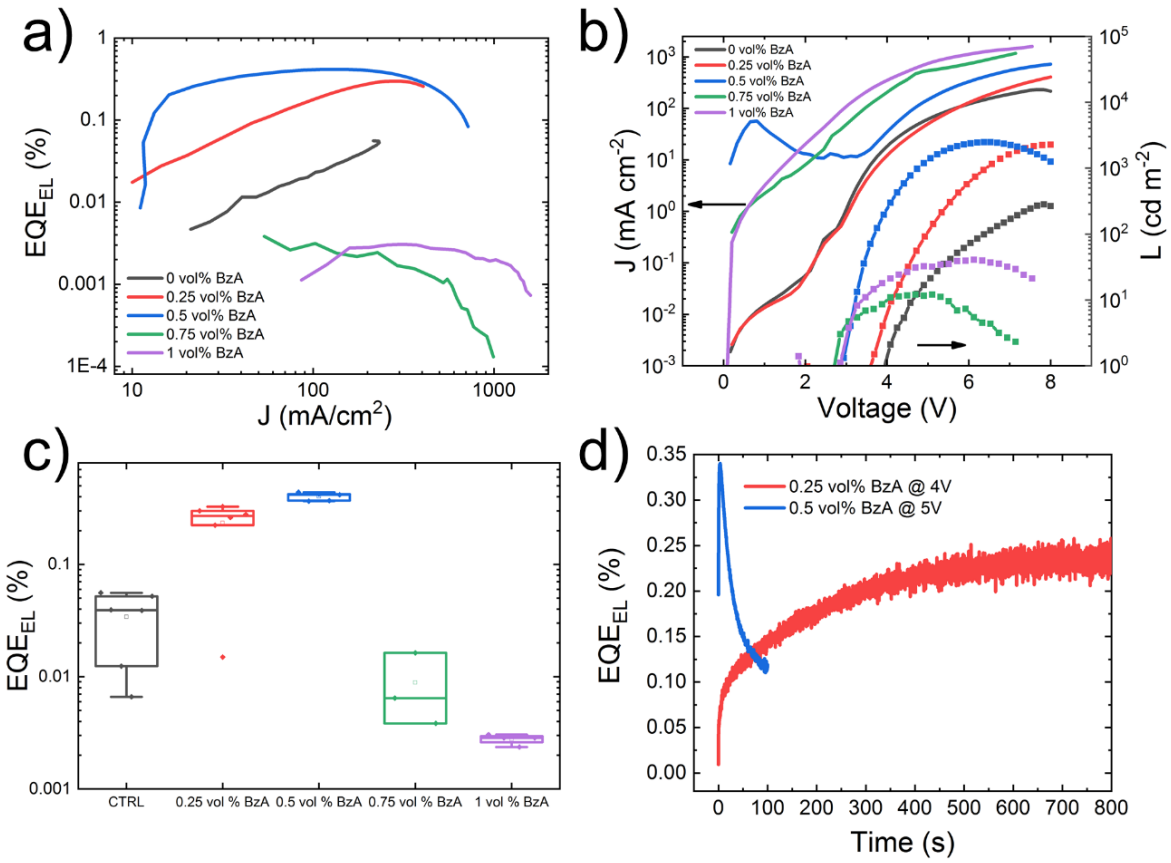


Figure 3.14 Device characterisation of benzylamine modified $MAPbBr_3$ LEDs: a) EQE_{EL} v J; b) JVL characteristics; c) Boxplot of EQE_{EL} as a function of composition; d) Operational stability of 0.25 vol% BzA at 4V and 0.5 vol% BzA at 5V.

Figure 3.14.b. shows the JVL characteristics of the samples, we observed an increase in the current density flowing through the device both above and below turn-on voltage with increasing BzA content which does not agree with the report from literature.[23] BzA is an insulating molecule and thus we would expect increased incorporation to decrease the conductivity of the perovskite film and consequentially the injected current (assuming the conductivity of the rest of the stack remains the same). There is a degree of additional complication as it has been shown that the formation of Ruddlesden-Popper phases can significantly modify the conduction and valence band positions relative to vacuum[24] (which is expected given the change in optical bandgap as observed in the PL (Figure 3.11.a.)). This in turn could affect the alignment of the bands with the transport materials and change the injection efficiency across the heterojunctions.

However, the increase in current density below turn-on voltage indicates the presence of shunts through the sample, which is in agreement with the porous morphology we observe for our 0.75 vol% sample. The significant shunt we observe for our 0.5 vol% sample was typical for most pixels which may be due to the small pinholes which can be observed in

Figure 3.13. The parasitic shunt will negatively affect the EQE_{EL} since carriers pass through the circuit without being injected into the perovskite where they can recombine radiatively; this explains why the 0.75 and 1 vol% samples have a peak EQE_{EL} at higher current densities.

Additionally, we observe a significantly worse operational stability for the 0.5 vol% sample compared with the 0.25 vol% sample. No absolute comparison can be made as the operational conditions are different (5V and 4V respectively) which resulted in different current densities (approx. 100 mA cm^{-2} and 20 mA cm^{-2} respectively) and a rigorous stability study wasn't conducted. Despite this, we found the stability difference striking and we will explore this further in the third experimental chapter of this thesis.

In conclusion, we were able to significantly modify the morphology and improve the PLQY of $MAPbBr_3$ by incorporating benzylamine into the antisolvent. We present evidence that the emissive domains become quantum confined through this addition which may be playing a part in this improvement. When translating the passivated films to devices we do not see significant improvement in the peak EQE_{EL} but do observe changes significant changes in the JVL characteristics. We attribute these changes to, i) reduction in trap state morphology, and, ii) changes in film morphology and continuity. Comparing our results with the report from literature, they achieved an EQE_{EL} of 12% and a PLQY of 60% using this methodology. In hindsight, more time investment in this procedure could have yielded higher efficiencies. Briefly:

i) The literature report focussed on controlling the crystallisation temperature, reducing it from 25 °C →10 °C. This decreased the rate of grain growth and thus allowed more nucleation to occur, resulting in a decreased grain size and a higher PLQY. An exploration of this variable would have been judicious given the importance emphasised in the manuscript.

ii) Further efforts to decrease shunts through control of the processing would likely have increased the EQE_{EL} of at least the 0.5 vol% BzA sample.

iii) A study of the effect of experimental variables on the PLQY of encapsulated films on ITO/PEDOT:PSS would have been a good course of action to take in an attempt to improve the EQE_{EL}.

3.3.4 The effect of choline as a passivating agent

We now move on from the study of BzA in the antisolvent to try and achieve a higher EQE_{EL} green perovskite LED. At this juncture we strove to improve both the PLQY and the photostability of the emitter in an attempt to achieve stable and efficient emission.

We chose a target perovskite where a mixture of FA and Cs is used as the A site cation (we will refer to this as FACs). Previously our group has shown that FACs iodide-rich perovskites afford improved operational stability[30] over MA containing perovskites. We were curious to see if the higher thermal stability of this cation composition would equally improve the stability of perovskite LEDs

First, we optimised the morphology of our FACs perovskite (with the specific composition of $(FA_{0.9}Cs_{0.1})_{1.1}PbBr_3$. We used a 10 mol % excess of A-site cations as this has been shown to improve PLQY in several cases. We first optimised the antisolvent quench procedure until we achieved specular films and inspected the film with SEM (Figure 3.15, 0 vol% FAH), we observe a relatively rough morphology with visible pinholes. We chose to use formic acid (FAH) as an additive to the precursor solution as this has been shown to improve crystallisation, morphology and PLQY.[31] We found an concentration of 5 vol% FAH was optimal for morphology(Figure 3.15) where we do not observe any pinholes and thus proceed with this precursor solution.

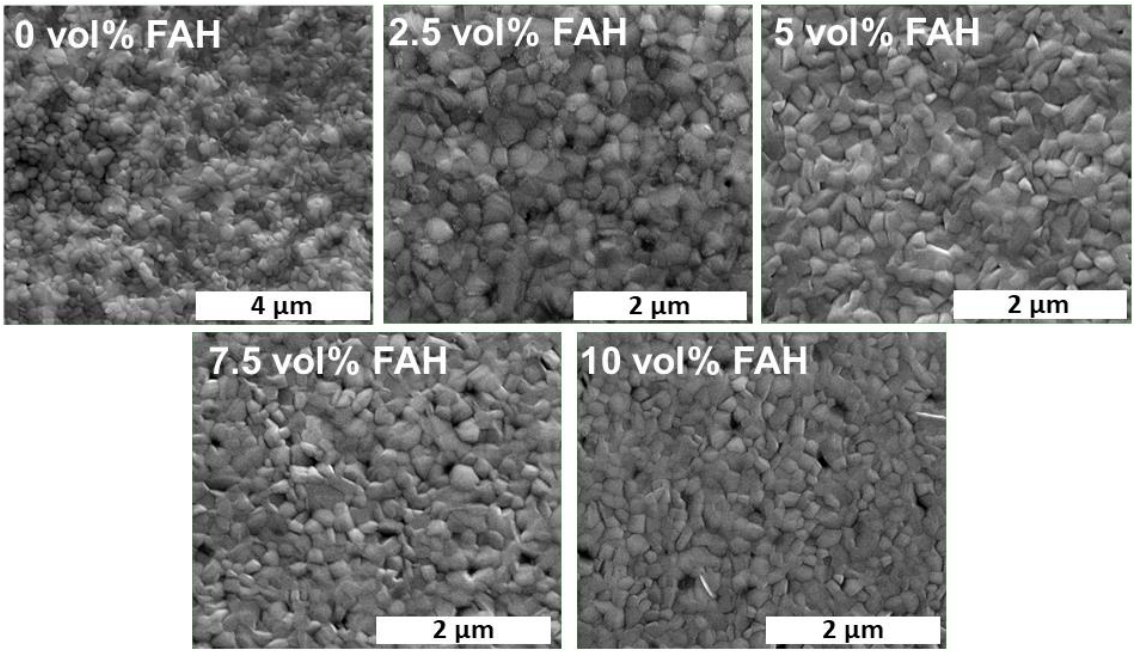


Figure 3.15 SEM characterisation of $(FA_{0.9}Cs_{0.1})_{1.1}PbBr_3$ films with different vol% additions of formic acid to the precursor solvent.

We measured the PLQY of the pristine film in air and found it had a good baseline value of 4.6%. Considering that in the previous BzA study we had achieved similar PLQY (Figure 3.11.c.) and had not achieved good EQE_{EL}, we investigated the effect of choline chloride (ChCl) and choline bromide (ChBr) as passivation agents. We chose the choline halide as a post treatment as this had been shown to improve the PLQY of $MAPbBr_3$[32] and also improve the voltage of lower bandgap perovskite solar cells.[33] Surprisingly, the

PLQY was made worse by both of these treatments except for the ChCl 10 mg mL^{-1} sample which saw a moderate improvement up to 5.2 % (Figure 3.16).

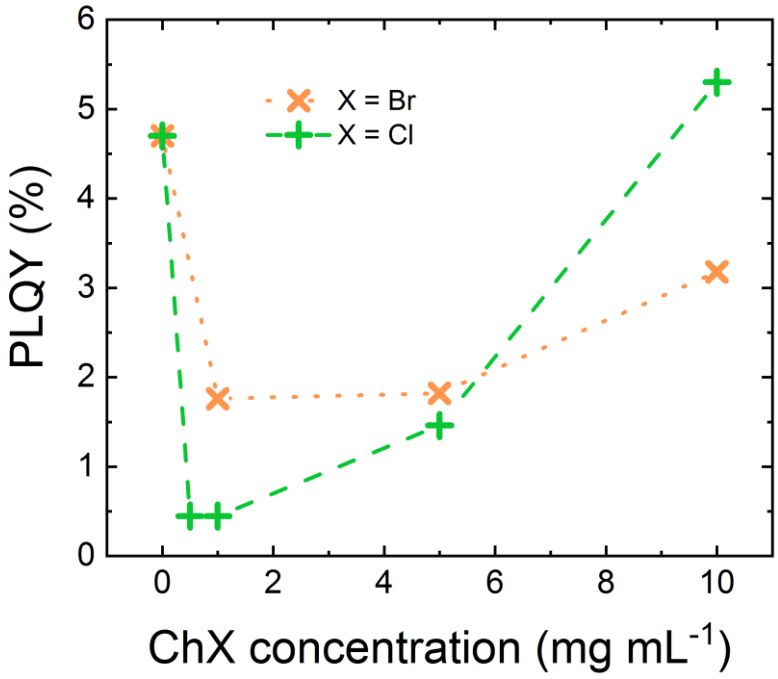


Figure 3.16 PLQY of FACs perovskite as a function of ChX post-treatment; optical intensity 93 mW cm^{-2} , λ_{exc} = 405 nm.

Considering that the passivation method from our previous study had worked by incorporation of BzA into the antisolvent we thought to try dissolving ChBr and ChCl into the antisolvent however it wasn't soluble in any appreciable amount in any of the common antisolvents we tried. Therefore, we developed a procedure where immediately after the antisolvent quench we dispensed the ChX solution dissolved in isopropanol, prior to annealing. Inspecting these films under a UV torch gave a visibly very high PL which was quenched somewhat during an annealing process. Thus we compared the PLQY of annealed and unannealed samples (Table 3.1) and found i) the PLQY of all samples is greatly improved over the control, demonstrating that the new approach is effective, and, ii) annealing the perovskite is detrimental to the PLQY.

Perovskite	PLQY (%)
Control – $(FA_{0.9}Cs_{0.1})_{1.1}PbBr3$	4.6
With ChCl 10 mg mL^{-1} unannealed	26.5
With ChBr 10 mg mL^{-1} unannealed	35.0
With ChCl 10 mg mL^{-1} annealed	18.3

Table 3.1 PLQY improvement with immediate dispense of ChX solution after antisolvent quench; optical intensity 93 mW cm^{-2} , λ_{exc} = 405 nm.

Despite the high PLQY we chose to anneal the samples to encourage complete crystallisation and remove any excess solvent as the improvement over the control is still excellent.

We now study the effect of the encapsulation on the photostability and PLQY of the samples. Figure 3.17.a + b. show the integrated PL intensity of samples measured inside an integrating sphere with a fixed excitation fluence as a function of time, the intensity on the y axis is a measure of PLQY. The excitation fluence was fixed at a value of 93 mW cm^{-2} during this study, so assuming no change in absorbance (which should be minimal from sample to sample) the intensity is comparable from graph to graph as a measure of PLQY.

Figure 3.17.a. shows the evolution of the PL intensity over time for unencapsulated samples. We see similar behaviour from all samples where; i) the ChBr treatment greatly improves the PLQY, ii) the initial value decreases rapidly, and, iii) the PL slowly recovers to a degree, never reaching its initial value. We find that the ChBr 5 mg mL^{-1} sample gives the optimum peak value but decreases as the others continue to improve. Figure 3.17.b. shows data from encapsulated samples from the same fabrication run. We find that; i) The intensity of the PL (and thus the PLQY) has dropped approximately an order of magnitude, ii) there is still an initial, rapid decrease in intensity, and, iii) the PL no longer recovers significantly.

The recovery of the PL in air is reminiscent of reports on other halide perovskites like $MAPbI_3$ where a 'photohealing' effect has been widely reported.[34] This effect has been attributed to oxidative passivation of the surface of the perovskite.[35,36] The mechanism in brief is; i) photogenerated holes can oxidise halide ions which combine to form volatile halogen gasses (e.g. I_2 or Br_2), ii) the resultant halide vacancies can trap electrons which in turn reduce Pb(II) → Pb(0), iii) physisorbed superoxide anions can generate hydroperoxy radicals through abstraction of a proton from the A site cation or water, and, iv) various oxidative reactions can happen on the surface of the perovskite eventually

forming PbO, which passivates the surface. We posit that this mechanism is occurring in these samples as we do not see such recovery kinetics in the films encapsulated in nitrogen.

Despite the much lower PL intensity of the encapsulated samples, there is still a significant improvement over the control for all passivated samples and after the initial drop in intensity the PL remains stable over the course of 5 minutes. There is no clear trend in PLQY and concentration at this stage so we proceeded to make control FACs LEDs.

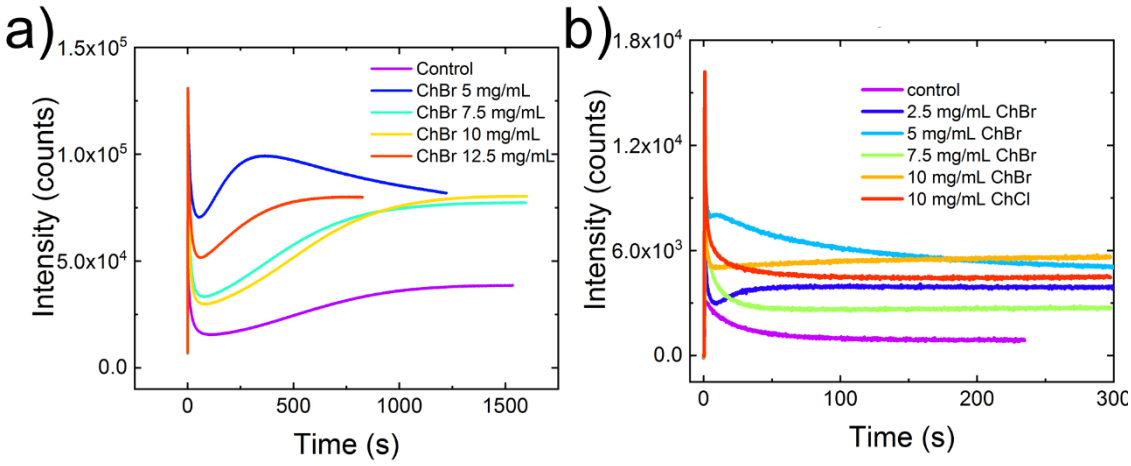


Figure 3.17 Integrated PL intensity vs T at a fixed fluence of 93 mW cm^{-2} of; a) unencapsulated, and, b) encapsulated ChBr treated samples of FACs.

Unfortunately, despite numerous attempts to implement a control FACs LED we were unsuccessful in being able to make devices which were efficient enough to measure. At this point we decide to change perovskite to $FAPbBr_3$ as it is phase stable in the perovskite phase and is still more thermally stable than $MAPbBr_3$.[37] With this change we were able to successfully fabricate control devices with an EQE_{EL} up to 1% (Figure 3.18.a.). We note that the operational stability (at a constant current of 10 mA cm^{-2}) was quite poor and has similar decay kinetics to the encapsulated PLQY. Next, we proceeded to see whether we coul obtain similar improvement of the PLQY of the $FAPbBr_3$ perovskite

using choline as a passivation agent.

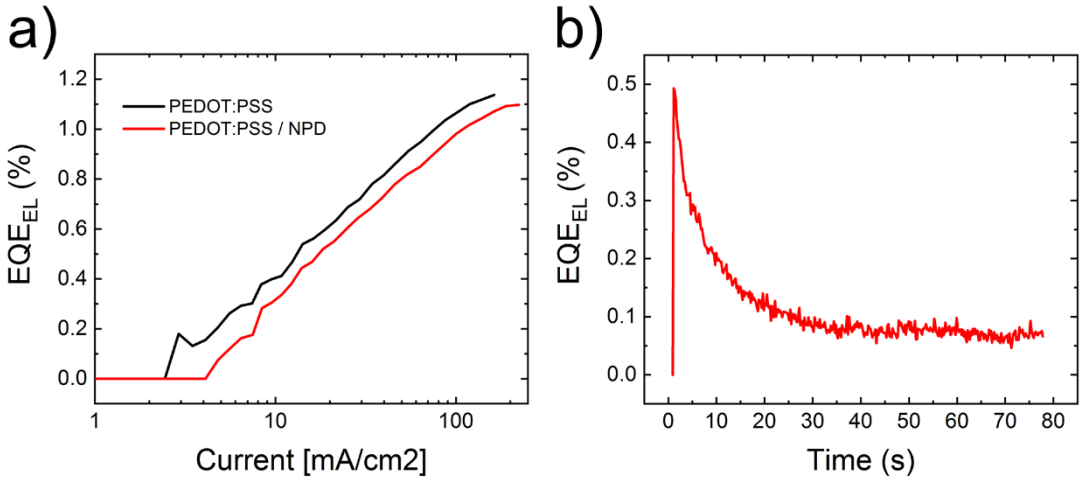


Figure 3.18 a) EQE_{EL} vs J for $FAPbBr_3$ LEDs on PEDOT:PSS and PEDOT:PSS/NPD hole injection layers; b) Operational stability of PEDOT:PSS/NPD $FAPbBr_3$ LED at 10 mA cm^{-2}.

Figure 3.19.a + b. show the unencapsulated and encapsulated samples respectively where we observe quite different behaviour to the FACs samples; i) the photostability in air is much worse (except for the ChCl sample), ii) there is no clear recovery of the PL in air, and, iii) there is not the same level in improvement in the PL for the encapsulated samples with ChBr passivation. Intriguingly, ChCl now has a much stronger effect improving the PL of both the encapsulated and unencapsulated sample both of which show better photostability and PLQY *cf.* $FAPbBr_3$ (Figure 3.19.c.).

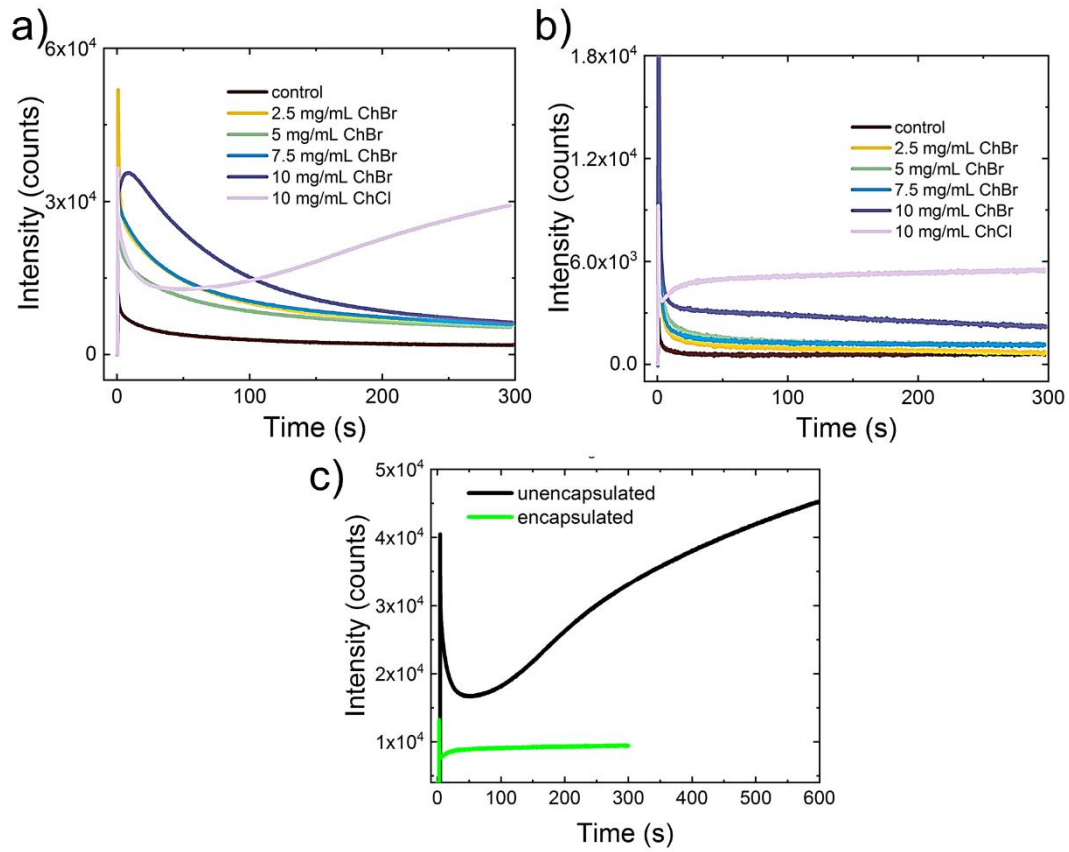


Figure 3.19 Integrated PL intensity vs T at a fixed fluence of 93 mW cm^{-2} of; a) unencapsulated, and, b) encapsulated ChBr treated samples of $FAPbBr_3$; c) comparison of encapsulated and unencapsulated ChCl treated $FAPbBr_3$ films.

When repeating the passivation of $FAPbBr_3$ with ChCl we struggled with reproducibility and investigated experimental variables surrounding fabrication. We investigated the elapsed time between solvent quenching and passivation. Figure 3.20.a. shows the measured PL intensity of this experiment on the day of fabrication, we observe no clear trend and no photohealing effect as we saw in Figure 3.19.c.. However, when these materials were tested on the following day a clear trend was observed that early passivation after the solvent quench results in; i) a higher final PLQY and ii) faster photohealing kinetics.

Figure 3.20.c. shows the PL spectra of the samples after they have reached peak intensity as well as a control $FAPbBr_3$ sample for comparison. We observe that the samples with a passivation time greater than 3 s show PL spectra which are i) skewed to bluer wavelengths, and, ii) broader (indicating a wider distribution of states). The 3 s sample has a PL peak at 537 nm which is blueshifted from the PL peak of untreated $FAPbBr_3$ (548 nm) but at lower energy than the later treated samples (531 nm). Due to the narrower spectrum with a normal distribution of the 3 s sample, we posit that the earlier treatment time causes a more homogenous distribution of choline and chloride. The samples

passivated at 10 s and beyond may have more chloride at the surface of the perovskite resulting in the skewed distribution of the PL.

We then coated the optimised ChCl 3s sample onto different hole injection layers to study the quenching of the PLQY. We find that devices with NPD quench the least and thus proceed to integrate the films into devices with a PEDOT:PSS/ NPD transport layer as had been used successfully to make $FAPbBr_3$ LEDs previously (Figure 3.18.a.).

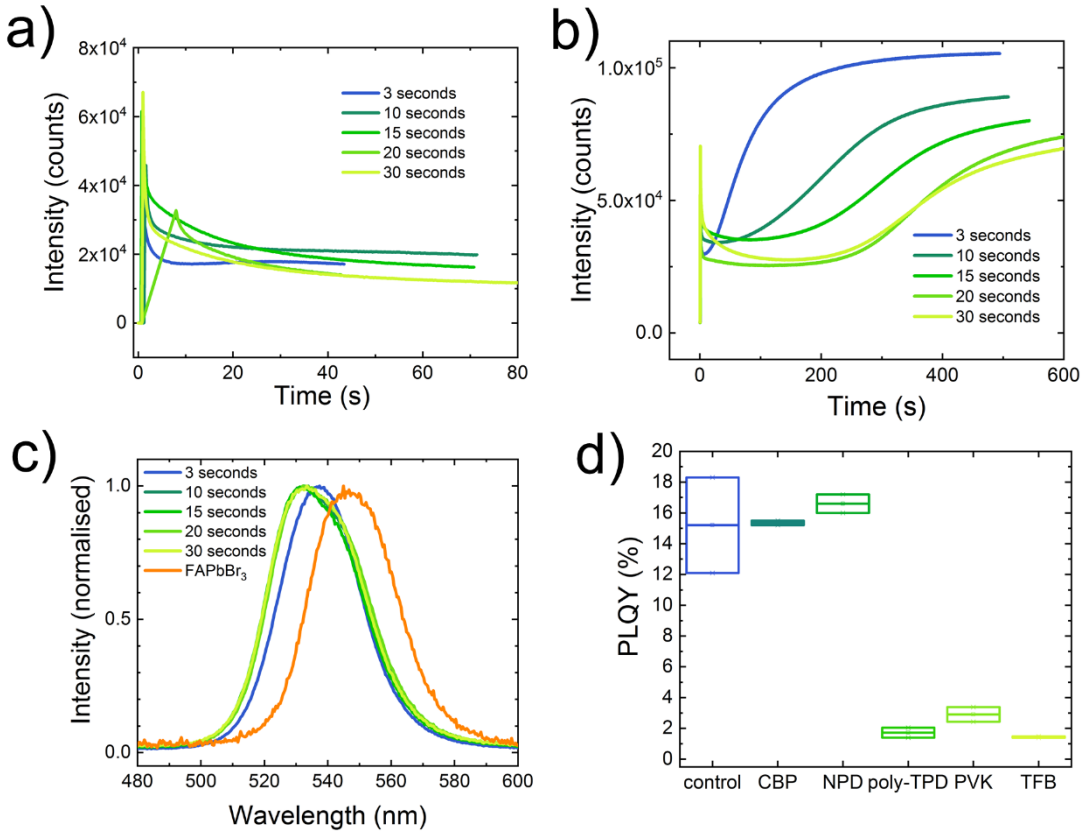


Figure 3.20 Integrated PL intensity vs T at a fixed fluence of 93 mW cm^{-2} of ChCl treated $FAPbBr_3$ films with different treatment times tested on, a) the day of fabrication, and, b) 24 h after fabrication; c) PL spectra of films from b); d) PLQY of optimised films on different hole injection layers.

Unfortunately, we were not able to fabricate LEDs from these high PLQY samples; those with 10 mg mL^{-1} ChCl were extremely resistive. Attempts to get functional devices with lower concentrations of ChCl were also unsuccessful. Figure 3.21.a + b. shows the XRD and UV-Vis of a 10 mg mL^{-1} ChCl sample which was passivated after 3s. We observe two peaks in the XRD at 10.5° and 24.3° which we are not able to assign to the $FAPbBr_3$ structure and also two excitonic absorption peaks in the UV-Vis at 380 and 410 nm. The excitonic absorption peaks are indicative of lower dimensional phases (presumably forming with choline acting as a 2D forming cation). We did not investigate the XRD further but we posit that these unknown peaks also originate from this lower dimensional

phase. We are unaware of the charge transport properties of the unassigned phases however 2D perovskites generally have much lower conductivity.[38] Therefore, we assume that these lower dimensional phases are hampering injection into the $FAPbBr_3$ thus preventing efficient EL.

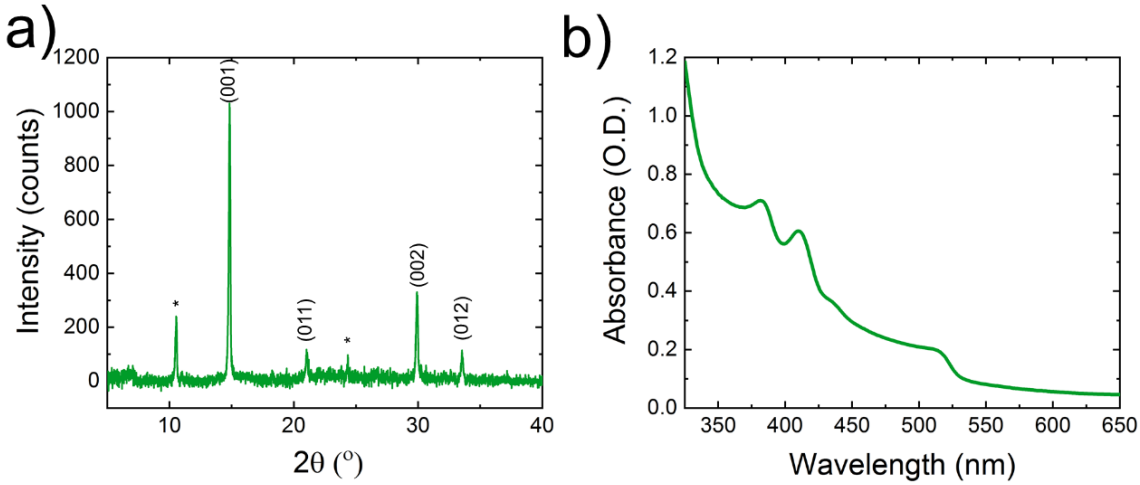


Figure 3.21 a) Powder X-Ray diffraction, and, b) UV-Vis of optimised ChCl treated $FAPbBr_3$

3.3.5 Conclusion

In conclusion, we are able to greatly improve the PLQY of both FACs and $FAPbBr_3$ perovskites using ChBr and ChCl as passivation agents respectively. We found that FACs was not suitable for making efficient perovskite LEDs and thus utilised $FAPbBr_3$ where we achieve an EQE_{EL} of 1%. We find that the time of passivation during fabrication is critical to achieve a reproducibly high PLQY. However, when we try and incorporate these materials into LEDs they are very poor emitters which we attribute to the resistive behaviour of ChCl in the concentrations necessary to achieve high PLQY. However, we have greatly improved the photostability of $FAPbBr_3$ in air which could be of use for applications such as phosphors.

3.4 Chapter Conclusion

Over the course of the chapter we have explored the suitability of a *nip* and a *pin* device structure for perovskite LEDs. We find that we are more reliably able to produce perovskite LEDs using the *pin* device structure. A crucial step towards this realisation was the optimisation of a LiF interlayer. This proved crucial in enhancing electron injection from an aluminium electrode into shallow LUMO organics, which agrees with literature reports.[21,22]

When we were able to successfully reproduce perovskite LEDs of measurable efficiency we attempted to significantly enhance the EQE_{EL} through means of chemical passivation. Our strategy was centralised on the optimisation of the PLQY of the emitter followed by incorporation into our *pin* structure. Our strategy of using BzA in the antisolvent was moderately successful as we increased our maximum EQE_{EL} from 0.3% to 0.4% and saw more efficient operation across a wider range of current densities. Interestingly the optimal condition for EQE_{EL} (Figure 3.14) was not the optimal condition for PLQY (Figure 3.11). An alternative passivation strategy using ChX was explored, where high PLQY of up to 35% were achieved, matched with a significant increase in photostability. In this instance, improvement of PLQY resulted in a reduction of EQE_{EL} to unmeasurable values.

Considering these results as a whole we can conclude that optimisation of a perovskite emitter for PLQY must be concurrently checked for suitability for EL in a LED. Metal halide perovskites can form multiple lower dimensional phases when using passivation strategies with different charge transport properties and stabilities. Additionally many of these passivation agents are insulators and will modify charge injection even if they do not affect the phase behaviour of the perovskite itself. As such an initial trial of a passivation agent for improvement in PLQY must immediately be followed by a trial in LEDs.

3.5 References

1. Hoke, E. T. *et al.* Reversible photo-induced trap formation in mixed-halide hybrid perovskites for photovoltaics. *Chem. Sci.* **6,** 613–617 (2015).
2. Wang, N. *et al.* Perovskite light-emitting diodes based on solution-processed self-organized multiple quantum wells. *Nat. Photonics* **10,** 699–704 (2016).
3. Jiang, Q. *et al.* Surface passivation of perovskite film for efficient solar cells. *Nat. Photonics* **13,** 460–466 (2019).
4. Kabra, D., Lu, L. P., Song, M. H., Snaith, H. J. & Friend, R. H. Efficient Single-Layer Polymer Light-Emitting Diodes. *Adv. Mater.* **22,** 3194–3198 (2010).
5. Si, J. *et al.* Efficient and High-Color-Purity Light-Emitting Diodes Based on in Situ Grown Films of $CsPbX_3$ (X = Br, I) Nanoplates with Controlled Thicknesses. *ACS Nano* **11,** 11100–11107 (2017).
6. Cao, Y. *et al.* Perovskite light-emitting diodes based on spontaneously formed submicrometre-scale structures. *Nature* **562,** 249–253 (2018).

7. Schutt, K. *et al.* Overcoming Zinc Oxide Interface Instability with a Methylammonium-Free Perovskite for High-Performance Solar Cells. *Adv. Funct. Mater.* **29,** 1900466 (2019).
8. Zou, W. *et al.* Minimising efficiency roll-off in high-brightness perovskite light-emitting diodes. *Nat. Commun.* **9,** 1–7 (2018).
9. Kulbak, M. *et al.* Cesium Enhances Long-Term Stability of Lead Bromide Perovskite-Based Solar Cells. *J. Phys. Chem. Lett.* **7,** 167–172 (2016).
10. Xiao, M. *et al.* A Fast Deposition-Crystallization Procedure for Highly Efficient Lead Iodide Perovskite Thin-Film Solar Cells. *Angew. Chemie* **126,** 10056–10061 (2014).
11. Wu, C. *et al.* Improved Performance and Stability of All-Inorganic Perovskite Light-Emitting Diodes by Antisolvent Vapor Treatment. *Adv. Funct. Mater.* **27,** 1–7 (2017).
12. Zohar, A. *et al.* What Limits the Open-Circuit Voltage of Bromide Perovskite-Based Solar Cells? *ACS Energy Lett.* **4,** 1–7 (2019).
13. Ban, M. *et al.* Solution-processed perovskite light emitting diodes with efficiency exceeding 15% through additive-controlled nanostructure tailoring. *Nat. Commun.* **9,** 3892 (2018).
14. Goff, C. M., Matchette, M. A., Shabestary, N. & Khazaeli, S. Complexation of caesium and rubidium cations with crown ethers in N,N-dimethylformamide. *Polyhedron* **15,** 3897–3903 (1996).
15. Kerner, R. A., Zhao, L., Xiao, Z. & Rand, B. P. Ultrasmooth metal halide perovskite thin films: Via sol-gel processing. *J. Mater. Chem. A* **4,** 8308–8315 (2016).
16. Sim, K. *et al.* Performance boosting strategy for perovskite light-emitting diodes. *Appl. Phys. Rev.* **6,** 31402 (2019).
17. Jeong, J. *et al.* Formamidinium-based planar heterojunction perovskite solar cells with alkali carbonate-doped zinc oxide layer †. (2018). doi:10.1039/c8ra02637h
18. Miao, Y. *et al.* Stable and bright formamidinium-based perovskite light-emitting diodes with high energy conversion efficiency. *Nat. Commun.* **10,** 1–7 (2019).
19. Quan, L. N. *et al.* Tailoring the Energy Landscape in Quasi-2D Halide Perovskites Enables Efficient Green-Light Emission. *Nano Lett.* **17,** 3701–3709 (2017).
20. Xiao, Z. *et al.* Efficient perovskite light-emitting diodes featuring nanometre-sized crystallites. *Nat. Photonics* **11,** 108–115 (2017).
21. Chen, H. *et al.* Blue organic light-emitting diode based on 1,2,3,4,5-pentaphenyl-

1(8- phenyl-1,7-octadiynyl)silole. *IEEE J. Sel. Top. Quantum Electron.* **10,** 10–15 (2004).

22. Chen, Y. H., Cheng, Y. J., Lee, G. R., Wu, C. I. & Pi, T. W. Improvements of electron injection efficiency using subphthalocyanine mixed with lithium fluoride in cathode structures of organic light emitting diodes. *Org. Electron.* **12,** 562–565 (2011).
23. Lee, S. *et al.* Growth of Nanosized Single Crystals for Efficient Perovskite Light-Emitting Diodes. *ACS Nano* **12,** 3417–3423 (2018).
24. Xing, J. *et al.* Color-stable highly luminescent sky-blue perovskite light-emitting diodes. *Nat. Commun.* **9,** 1–8 (2018).
25. Ulatowski, A. M. *et al.* Charge-Carrier Trapping Dynamics in Bismuth-Doped Thin Films of $MAPbBr_3$ Perovskite. *J. Phys. Chem. Lett.* **11,** 3681–3688 (2020).
26. Protesescu, L. *et al.* Nanocrystals of Cesium Lead Halide Perovskites ($CsPbX_3$, X = Cl, Br, and I): Novel Optoelectronic Materials Showing Bright Emission with Wide Color Gamut. *Nano Lett.* **15,** 3692–3696 (2015).
27. Shamsi, J. *et al.* Colloidal Synthesis of Quantum Confined Single Crystal $CsPbBr_3$ Nanosheets with Lateral Size Control up to the Micrometer Range. *J. Am. Chem. Soc.* **138,** 7240–7243 (2016).
28. Saidaminov, M. I. *et al.* High-quality bulk hybrid perovskite single crystals within minutes by inverse temperature crystallization. *Nat. Commun.* **6,** 23955 (2015).
29. Nayak, P. K. *et al.* Mechanism for rapid growth of organic-inorganic halide perovskite crystals. *Nat. Commun.* **7,** 1–8 (2016).
30. McMeekin, D. P. *et al.* A mixed-cation lead mixed-halide perovskite absorber for tandem solar cells. *Science (80-.).* **351,** 151–155 (2016).
31. Noel, N. K. *et al.* Unveiling the Influence of pH on the Crystallization of Hybrid Perovskites, Delivering Low Voltage Loss Photovoltaics. *Joule* **1,** 328–343 (2017).
32. Noel, N. K. *et al.* Highly Crystalline Methylammonium Lead Tribromide Perovskite Films for Efficient Photovoltaic Devices. *ACS Energy Lett.* **3,** 1233–1240 (2018).
33. Zheng, X. *et al.* Defect passivation in hybrid perovskite solar cells using quaternary ammonium halide anions and cations. *Nat. Energy* **2,** 1–9 (2017).
34. DeQuilettes, D. W. *et al.* Photo-induced halide redistribution in organic-inorganic perovskite films. *Nat. Commun.* **7,** 1–9 (2016).
35. Godding, J. S. W. *et al.* Oxidative Passivation of Metal Halide Perovskites. *Joule* **3,** 2716–2731 (2019).

36. Anaya, M., Galisteo-López, J. F., Calvo, M. E., Espinós, J. P. & Míguez, H. Origin of Light-Induced Photophysical Effects in Organic Metal Halide Perovskites in the Presence of Oxygen. *J. Phys. Chem. Lett.* **9,** 3891–3896 (2018).

37. Lee, S. *et al.* Control of Interface Defects for Efficient and Stable Quasi-2D Perovskite Light-Emitting Diodes Using Nickel Oxide Hole Injection Layer. *Adv. Sci.* **5,** 1801350 (2018).

38. Liang, D. *et al.* Color-Pure Violet-Light-Emitting Diodes Based on Layered Lead Halide Perovskite Nanoplates. *ACS Nano* **10,** 6897–6904 (2016).

4 Optimisation of High Efficiency 2D/3D Perovskite LEDs

4.1 Introduction

In the previous experimental chapter we have established protocols to reproducibly fabricate a functional perovskite LED and studied different methods for passivation of green emitting perovskites. The LEDs produced in the previous chapter had a low efficiency so we are compelled to continue our investigation into the parameters which govern the fabrication of an efficient perovskite LED. Reports had emerged of high efficiency green emitting perovskite LEDs using 2D/3D heterostructures,[1,2] which demonstrated efficiency improvements through energy funnelling (as detailed in the introductory chapter) and improved light extraction. Quan *et al.* successfully achieved an EQE_{EL} of 7.4% in mid-2017 using a 2D/3D composition of $PEA_2(MA)_4Pb_5Br_{16}$ (n=5) through an antisolvent deposition method.[3] This initial report was followed in February 2018 by a report from Yang *et al.* of an EQE_{EL} of 14.4% using the composition $PEA_2FA_2Pb_3Br_{10}$ (n=3).[4] Both of these reports used the ITO/PEDOT:PSS/Perovskite/TPBi/LiF/Al architecture which we had implemented in the previous chapter. We were compelled to investigate this class of materials further to gain insight on its potential to improve device efficiency.

In this chapter, we first realise high efficiency perovskite LEDs through the use of 2D/3D heterostructures and perform a brief spectroscopic study on a series of different 2D/3D compositions. Once we achieve high efficiency, we then focus on varying the ratio of 2D to 3D perovskite in our solution in order to study the effect of composition on optoelectronic properties, efficiency and importantly stability.

We then address reproducibility issues through modification of device structure, crystallisation conditions and process parameters. Eventually, we uncover important aspects in being able to produce a reproducible compositional series in combination with

high efficiency which will lead us to the final chapter of the thesis where an in depth study of the link between composition and stability is conducted.

4.2 2D/3D LEDs

4.2.1 $PEA_2FA_2Pb_3Br_{10}$ LEDs

We prepared films of $PEA_2FA_2Pb_3Br_{10}$ following the experimental protocols outlined by Yang *et al.*[1] and fabricated LEDs using this material as the emitter, Figure 4.1 shows a summary of the device results. We screen different thicknesses of both the electron and hole transport layers in an attempt to balance the charges and improve device efficiency. One can see in Figure 4.1.c. the boxplot of EQE_{EL} under different transport layer thicknesses. For the 'thick' PEDOT:PSS (using a slower spin speed of 3500 rpm) we don't see any clear trend in the efficiency, however for the 'thin' PEDOT:PSS (spin speed 6000 rpm) we see that increasing the thickness of the TPBi causes an increase in the EQE_{EL} with values in excess of 5% for the 90 nm thick TPBi samples.

Interestingly, we were able to get a high EQE_{EL} of 8% for one substrate with thick PEDOT:PSS and 70 nm thick TPBi(EQE_{EL} v J Figure 4.1.a., JVL Figure 4.1.b). During the fabrication of this sample we noted we left the perovskite precursor solution (solvent DMSO) on top of the PEDOT:PSS for approximately 30 seconds and there was a visible change in the appearance of the substrate where the solution was left. It has been previously reported, that an increase in the conductivity of PEDOT:PSS by up to 2 orders of magnitude through soaking a film of PEDOT:PSS in a DMSO bath.[5] This was attributed to a structural reordering of the film where segregation into more conductive PEDOT:PSS domains and an insulating PSS matrix occurs. Thus, we presume that the DMSO soak is increasing the conductivity of the film and improving hole injection into the perovskite.

This theory is in line with the trend that we observe for the thin PEDOT:PSS samples where increasing the thickness of the TPBi layer improves the EQE_{EL}. This could either be attributed to i) an optical effect where the change of thickness of the TPBi increases the outcoupled mode of the emission from the perovskite layer, or, ii) an improvement of charge balance, through the reduction of the electron current. Given that we observe such a large increase in EQE_{EL} with the DMSO soaked PEDOT:PSS which we presume is due to improved charge balance, we argue that both improvements in EQE_{EL} are due to this.

Figure 4.2.b. shows the operational stability of a 70 nm TPBi device held at a constant current density of10 mA cm^{-2}, we observe a T_{50} of 250 s which is relatively modest but considered to be sufficient to investigate device properties in further detail.

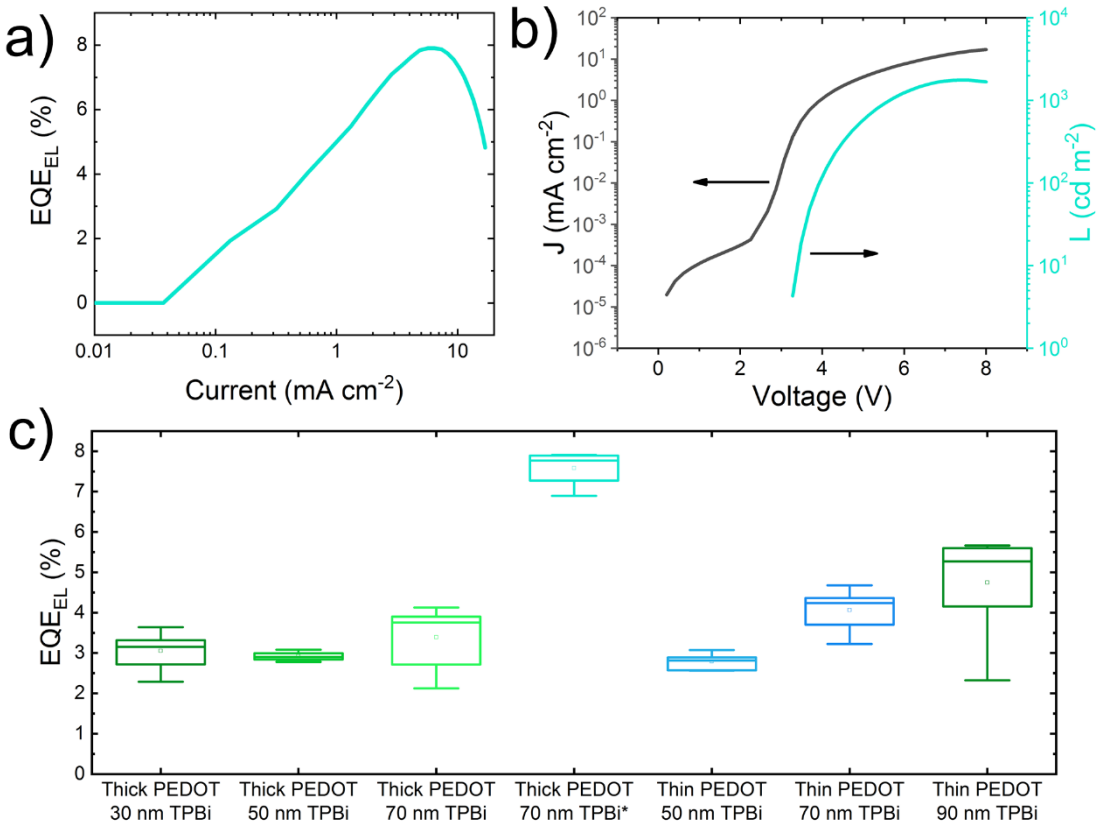


Figure 4.1 a) EQE_{EL} v J for champion device (thick PEDOT device with DMSO soaking, 70 nm TPBi); b) JVL characteristics of champion device; c) Boxplot of efficiencies showing effect of transport layer thickness.

Next, we characterised the UV-Vis, PL (Figure 4.2.c.) on glass and measured the PLQY of films of this 2D/3D material deposited directly on quartz or on top of a PEDOT:PSS film (Figure 4.2.a., note that this measurement was conducted without encapsulation). We observe an absorption onset at approximately 530 nm followed by 2 further excitonic peaks at 470 nm and 435 nm. We attribute these two peaks to the n=3 and n=2 Ruddlesden- Popper phases respectively.[6] The absorbance spectra illustrate that we do not obtain a phase pure n=3 Ruddlesden-Popper perovskite through the solution processing method that we use, instead we find a mixture of low n phase (i.e n=2 and n=3) and high n phase (i.e. those which have similar absorption and emission to $FAPbBr_3$ ~ n > 5). The PL spectrum, however, doesn't closely follow the absorption spectrum, instead we observe a single peak which has a very small Stokes shift from the absorption onset at 530 nm. This has been previously reported in literature and demonstrated through transient absorption spectroscopy to be due to 'funnelling' of photoexcited carriers from

high bandgap low n phases the lower bandgap higher n phases where they can recombine radiatively.[7]

We find that the PLQY peaks at a low optical intensity of 2 mW cm^{-2} on quartz and an even lower value of 0.25 mW cm^{-2} on PEDOT:PSS (Figure 4.2.a.). Zou *et al.* performed simultaneous PL and EL measurements on 2D/3D perovskite films and attribute the 'roll-off' in the PLQY and EQE_{EL} to Auger recombination.[8] It is certainly possible that the funnelling of carrier from wide gap to low gap phases could increase the carrier density in the emissive regions greatly (i.e. the carriers are heavily concentrated in a small portion of the film) which would cause an earlier onset of Auger recombination. In this case however, we attribute the rapid decrease to photoinstability of the films which we observed while performing the measurements. The PL became unstable over the time of the measurement after 2 mW cm^{-2} for the quartz sample and 0.25 mW cm^{-2} for the PEDOT:PSS sample.

Using the relation of transmittance (T) to absorbance (A); $T = 10^{-A}$ and taking the absorbance of our n=3 material at the laser excitation wavelength of λ = 405 nm being approximately A = 0.5 (Figure 4.2.c.) we find the fraction of photons being absorbed by our sample $f = 68\%$. We then can calculate the photon flux Φ (i.e. photons per second per area) at an irradiance of E_e = 2 mW cm^{-2} and convert this to an equivalent electrical current density $J = qf\Phi$, where $\Phi = \frac{E_e\lambda}{hc}$, q is the elementary charge, *h* Planck's constant and *c* the speed of light. This results in an equivalent current density of 0.44 mA cm^{-2} at 2 mW cm^{-2} and 0.055 mA cm^{-2} at 0.25 mW cm^{-2}. If we refer to Figure 4.1.a. we see that our peak EQE_{EL} occurs at a current density of approximately 5 mA cm^{-2}, a much higher current density, which indicates that there is a degradation process occurring during the PLQY measurements which is not occurring in the EQE_{EL} measurements and is thus not likely due to Auger.

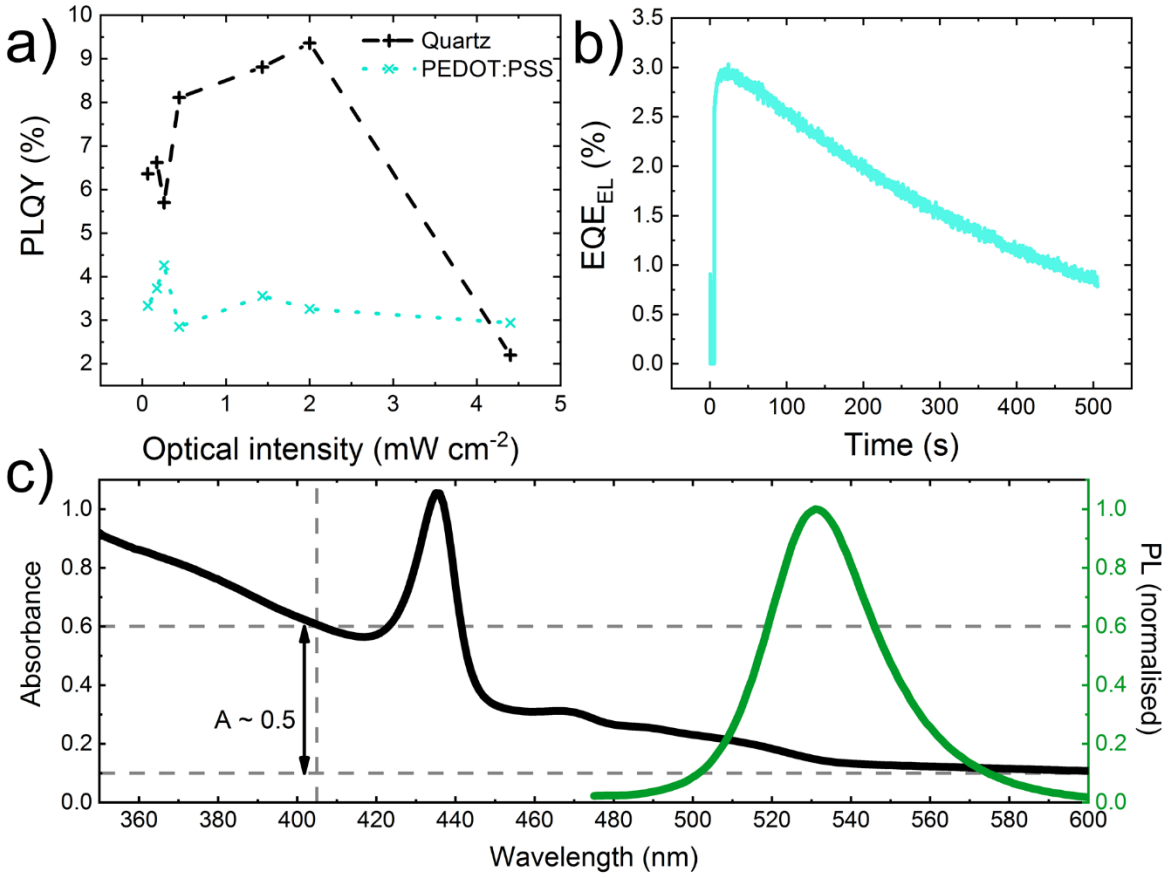


Figure 4.2 a) Intensity dependent PLQY of n=3 films on quartz and PEDOT:PSS λ_{exc} = 405 nm; b) EQE_{EL} v T of n=3, 70 nm TPBi device at 10 mA cm^{-2}; c) UV-Vis and PL of n=3 films.

We find that the maximum PLQY of the perovskite measured on PEDOT:PSS is only 4.5% which is lower than our maximum EQE_{EL}, which has additional layers which will reduce light extraction. This is further indication that there is an unaccounted discrepancy between the EQE_{EL} and the PLQY.

Due to the poor reproducibility of the soaking process (with DMSO) and the presence of quenching of the PLQY by PEDOT:PSS, we chose explore other hole injection layers (HIL) . We measure the PLQY of our n = 3 perovskite on poly (9-vinylcarbazole) (PVK) ; the deposition of the perovskite onto the PVK (which is hydrophobic) required depositing 50 µL of DMSO onto the pre-spinning substrate, followed by dispense of the perovskite precursor solution (details in experimental section under PVK – DMSO treated). At 2 mW cm^{-2} and found a PLQY of 9 %, which is similar to the reference sample on quartz indicating negligible quenching by PVK. Therefore, we proceed to fabricate devices with a PVK HIL (Figure 4.3).

We observe an EQE_{EL} of 9% which peaks at a similar current density to that of our PEDOT:PSS samples (Figure 4.3.c.). We then proceed to vary the composition of the

perovskite precursor solution with the goal to investigate differences in optoelectronic properties and importantly, device stability.

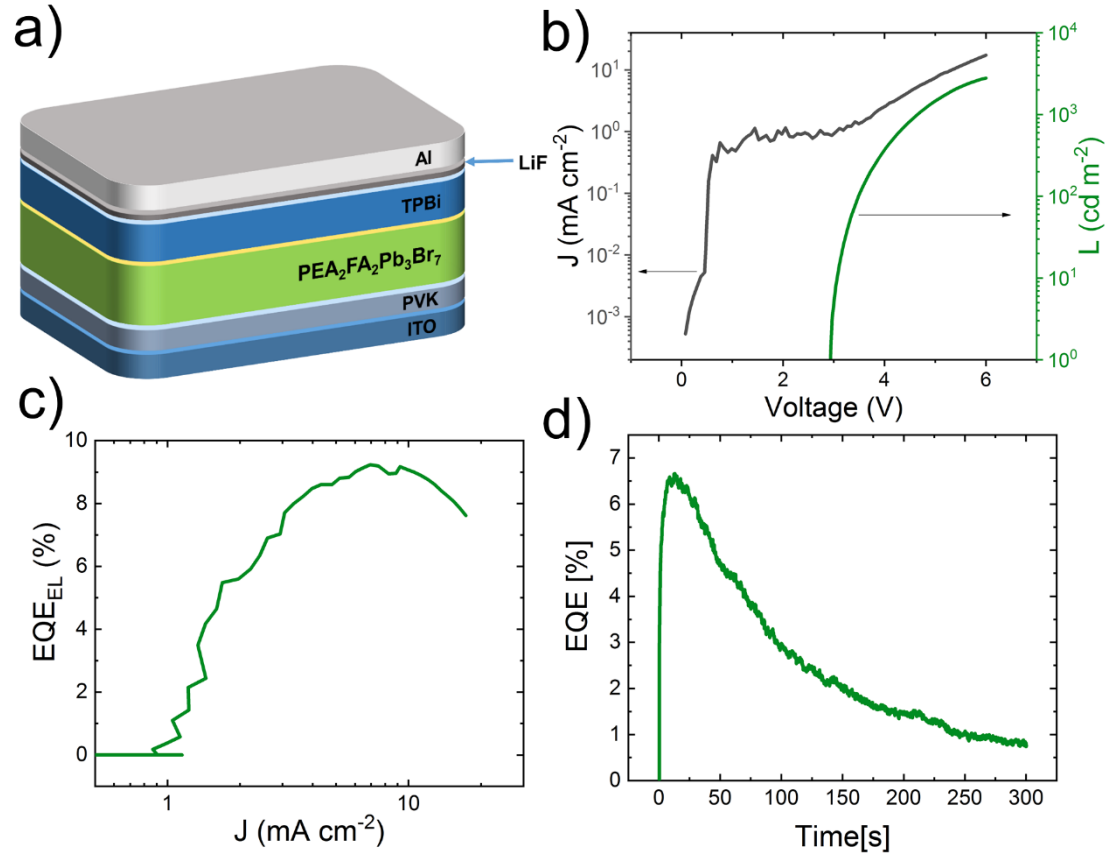


Figure 4.3 a) Device structure of PVK HIL, n = 3 LED; b) JVL characteristics of champion device; c) EQE_{EL} v current density of champion device; d) EQE_{EL} v Temperature at 10 mA cm^{-2} of a representative device.

4.2.2 Further optical properties of $PEA_2FA_{n-1}Pb_nBr_{3n+1}$ films

We continue our investigation into this materials system by varying the ratio of 2D to 3D content by making precursor solutions with stoichiometries for nominal compositions of n=2, 3, 6, 10 and $FAPbBr_3$. Additionally all samples are passivated with the molecule triphenylphosphine oxide (TPPO) as a post treatment unless mentioned otherwise.[9]

We begin by measuring XRD of our films to further investigate the distribution of different phases. We observe the peaks that are present in our n=4 → n= 10 samples can all be found in the $FAPbBr_3$ sample. In the n=2 sample we observe clear evidence of the formation of PEA_2PbBr_4 in the film (e.g. peak at 5°)

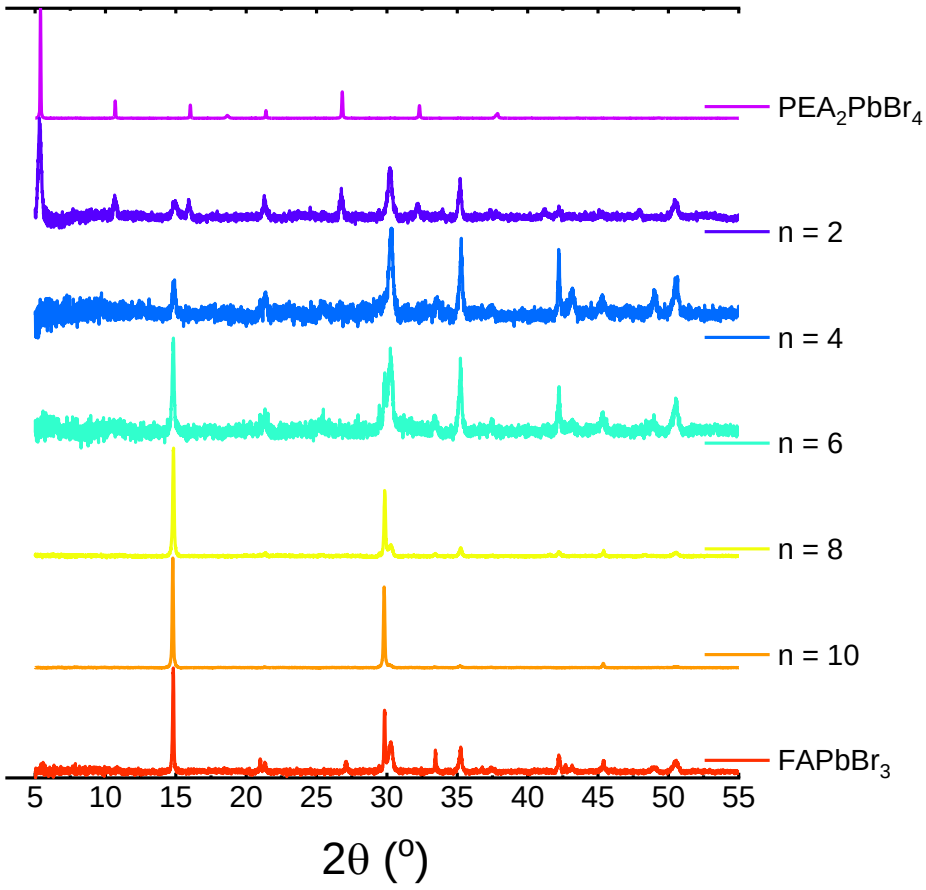


Figure 4.4 XRD of 2D/3D films. One can see clear evidence of PEA_2PbBr_4 in the n=2 sample.

First, we address the poor photostability that we observed when measuring the PLQY in air. We initially tried a polybutyl rubber type encapsulation and measure the photostability of 2D/3D films under a constant laser fluence of 127 mW cm^{-2} (Figure 4.5.a.), as this allowed us to measure all samples with a good signal to noise ratio. We find that as we go from a n=10 → n=2 precursor solution we get a decrease in the photostability. Additionally, we observe a photo-healing effect for our n = 10 sample which was unexpected as we had previously found such photohealing behaviour in the previous chapter for unencapsulated samples. As such, we posit that the poly butyl rubber encapsulation could be permeable to oxygen and we investigate a UV-epoxy as an alternative encapsulant (Figure 4.5.b.). We find that, i) the previously observed trend does not hold, and our n = 3 sample has the best photostability, and ii) there is a general improvement in photostability across samples when encapsulated with UV epoxy.

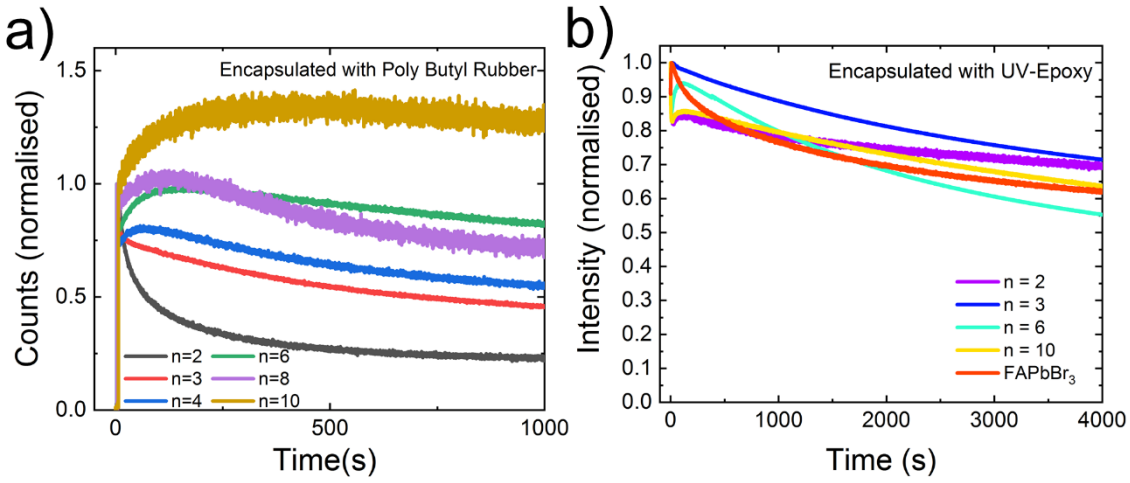


Figure 4.5 Photostability of 2D/3D films (λ_{exc} = 405 nm, fluence = 97 mW cm^{-2}) encapsulated with; a) poly butyl rubber, and, b) UV-epoxy

We present the UV-Vis and PL of our compositional series Figure 4.6.a. and corresponding photographs of the films in Figure 4.6.b.. One can see that all films show significant difference to the control $FAPbBr_3$ sample and do not crystallise in a single phase as indicated by the multiple peaks in the absorption spectrum. In the UV-Vis the n = 10 sample has a shallower absorption onset *cf.* $FAPbBr_3$ but does not show any absorption features from low n phases, as we proceed to n = 6 the absorption onset becomes even shallower and we see excitonic peaks at 435 nm and 405 nm which we attribute to the n =2 and n = 1 phases respectively. Interestingly the n = 2 film appears to form a pure phase in the UV-Vis which is different behaviour to all previous samples. The photograph presented in Figure 4.6.b. nicely demonstrates the general blueshift of the absorption as we see a colour change from orange to yellow.

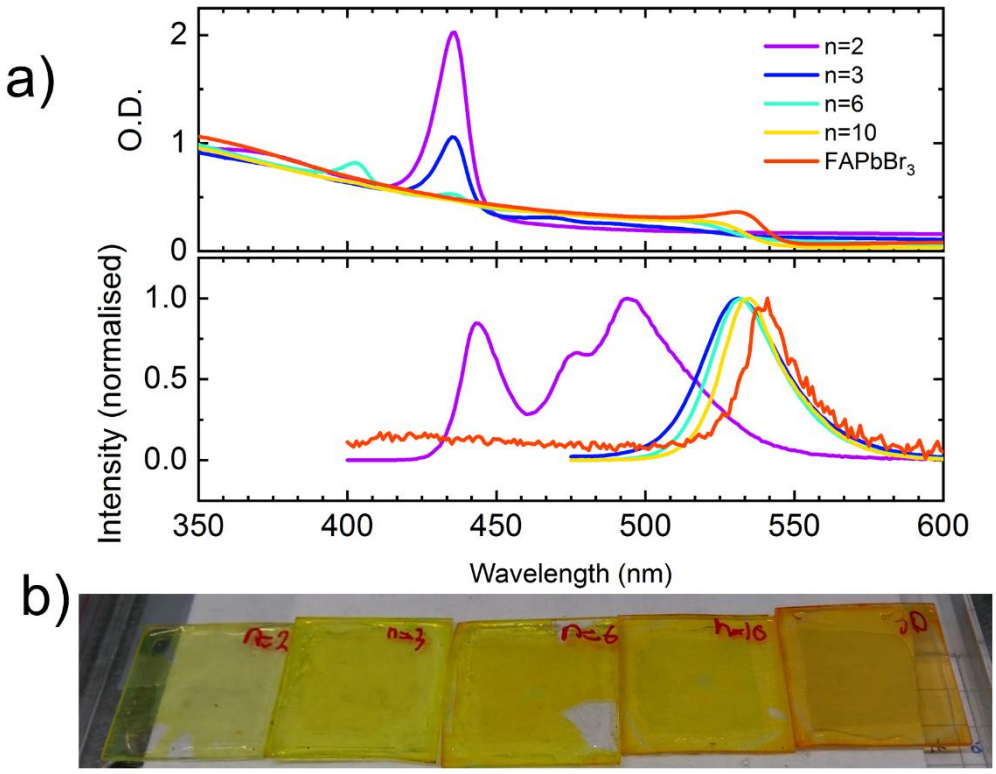


Figure 4.6 a) UV-Vis (top) and normalised PL (bottom) for 2D/3D films; b) photograph of corresponding films.

However, if we observe the PL we can see that the n = 2 sample exhibits PL from multiple phases (most likely the n= 2, 3 and 4). This demonstrates that although the UV-Vis indicates a pure phase there are low bandgap (high n) impurity phases in the film. The PL of the n = 3 → $FAPbBr_3$ samples demonstrate similar behaviour to that which we observed for the benzylamine passivated $MAPbBr_3$ in the first experimental chapter. That is, as we decrease the n value we see a broadening of the PL spectra and a blue-shift of the PL peak which is indicative of some degree of emission from quantum confined regions. We present the unnormalised PL on a log scale in Figure 4.7. We can see that the n = 2 sample is unique in its multiple emission peaks; which indicates efficient transfer of carriers into the low n phases for all samples apart from n = 2.

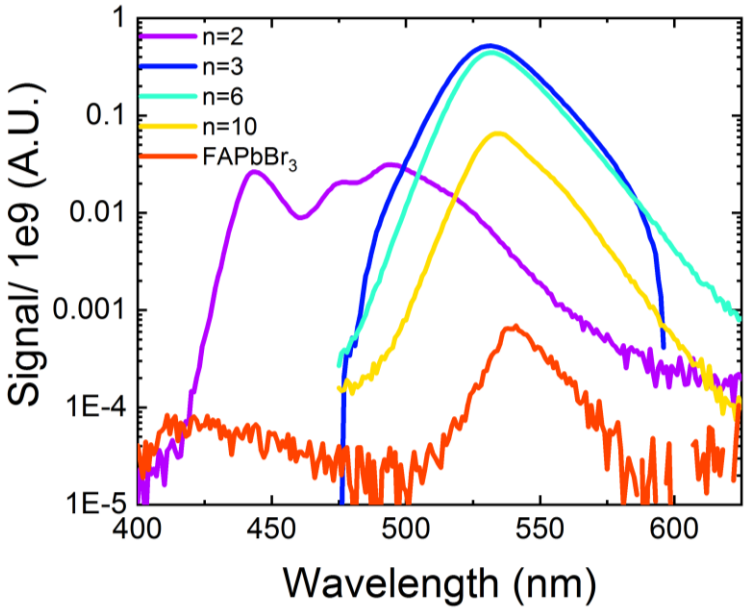


Figure 4.7 Unnormalised PL of 2D/3D samples showing lack of emission from lower dimensional phases (except for n=2).

We present the intensity dependence of the PLQY of our samples in Figure 4.8. We observe a very high PLQY value of 41% for our n = 3 sample at an optical intensity of 0.27 mW cm^{-2}, which is over 4 fold higher than our original measurement on the unpassivated sample in air (Figure 4.2.a.),. Additionally, we see a roll off in the PLQY as we did for the measurement in Figure 4.2.a. but it is not as severe. We didn't observe significant photoinstability until we reached optical intensities in excess of 100 mW cm^{-2} and even then the decrease in intensity over the course of a measurement (which takes 2-3 seconds) was small *cf.* Figure 4.5.b.. This indicates that the previously described concentrating of carriers into high n regions increasing Auger recombination may be occurring. We also observe this roll off behaviour in our n =2 and n = 6 samples, aside from the first data point for the n = 6 sample the roll off is less severe which agrees with decreased Auger recombination due to reduced energy funnelling. Perhaps most interestingly, the n=10 sample shows a high PLQY of ~15% which is independent of optical intensity across the range measured.

We also observe a trend of increasing PLQY from $FAPbBr_3$ → n = 3 followed by a decrease again for the n = 2 sample. This decrease correlates with a reduction of emission from high n value regions, and indeed the PLQY of pure 2D perovskite films is generally much lower (we were unable to measure the PLQY of n = 1 samples when we attempted), this has been attributed to increased phonon mediated recombination due to phonon modes from the 2D forming ligands.[10] Finally, we observe the very poor PLQY of $FAPbBr_3$, which we are only able to measure above 100 mW cm^{-2}, additionally the sample

is showing normal trap filling behaviour with the PLQY increasing with increasing optical intensity.

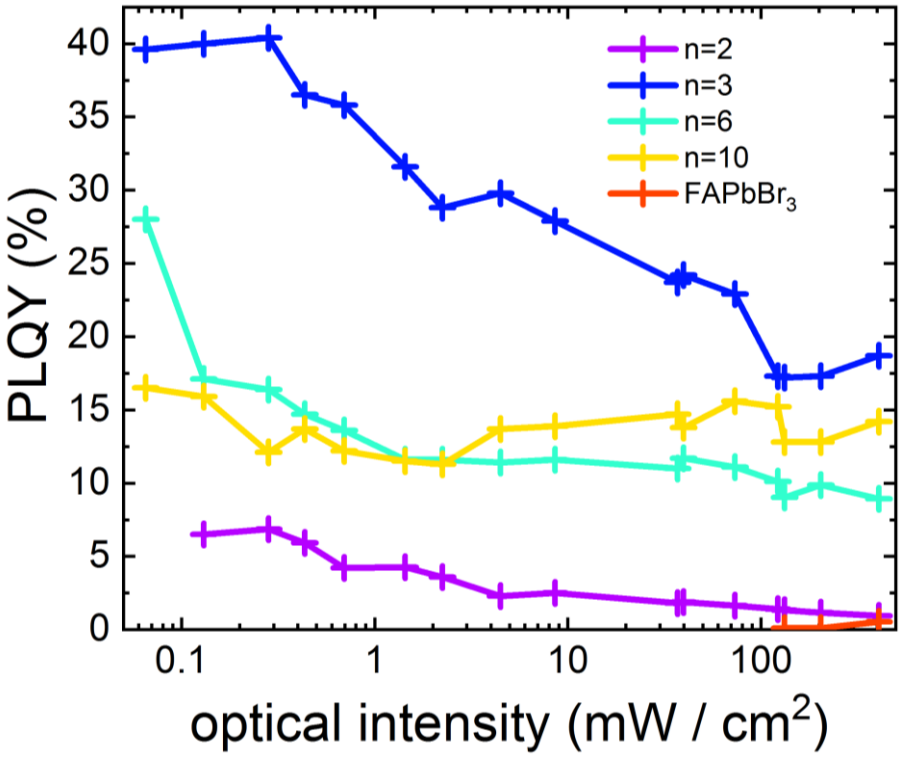


Figure 4.8 Intensity dependent PLQY of 2D/3D films. (λ_{exc} = 405 nm).

Intrigued by the multi-phase nature of our films and wanting to understand the emission process more deeply we perform time resolved photoluminescence (TRPL) measurements on our films (Figure 4.9.a). We choose the wavelength 510 nm as this allows us to excite high n regions alone where little funnelling will occur which could complicate the analysis. We attempted to fit the curves using different models but could not find one which adequately described all of the systems. As such we simply take the time that the intensity falls to 1/e of its initial value as a means for comparison between the films. We observe that the decay of the $FAPbBr_3$ sample occurs very quickly in 8.5 ns. The n=10 sample exhibits a much longer lived decay with 1/e = 69.3 ns. This large increase in lifetime is matched by an increase in PLQY when going from $FAPbBr_3$ to n=10 – this correlates well with a semiconductor where bimolecular recombination is the dominant radiative pathway.

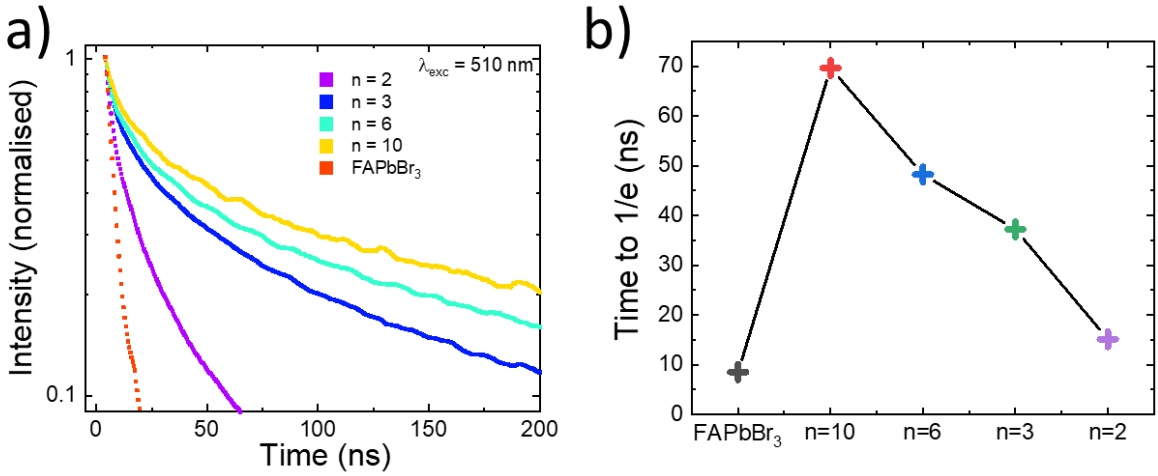


Figure 4.9 a) TRPL of 2D/3D films (λ_{exc} = 510 nm, optical intensity 43 mW cm^{-2}); b) Analysis of time for decay to fall to 1/e of its initial value.

However, our n=6 and n=3 samples both exhibit shorter decay times but high PLQY, which both exceed n=10 at low optical intensities. We posit this is due to a transition in the mechanism of recombination from bimolecular to excitonic, which has been demonstrated to occur in 2D/3D films in literature.[7] Excitonic recombination will occur much more rapidly and still contribute radiative recombination, thus, attempting to fit the monoexponential decay to extract $k_{1\text{-}SRH}$ will be unsuccessful. It is interesting to note that this faster recombination results in a higher PLQY and indicates that exciton mediated recombination is beneficial to the construction of high efficiency perovskite LEDs

4.2.3 Addressing reproducibility issues

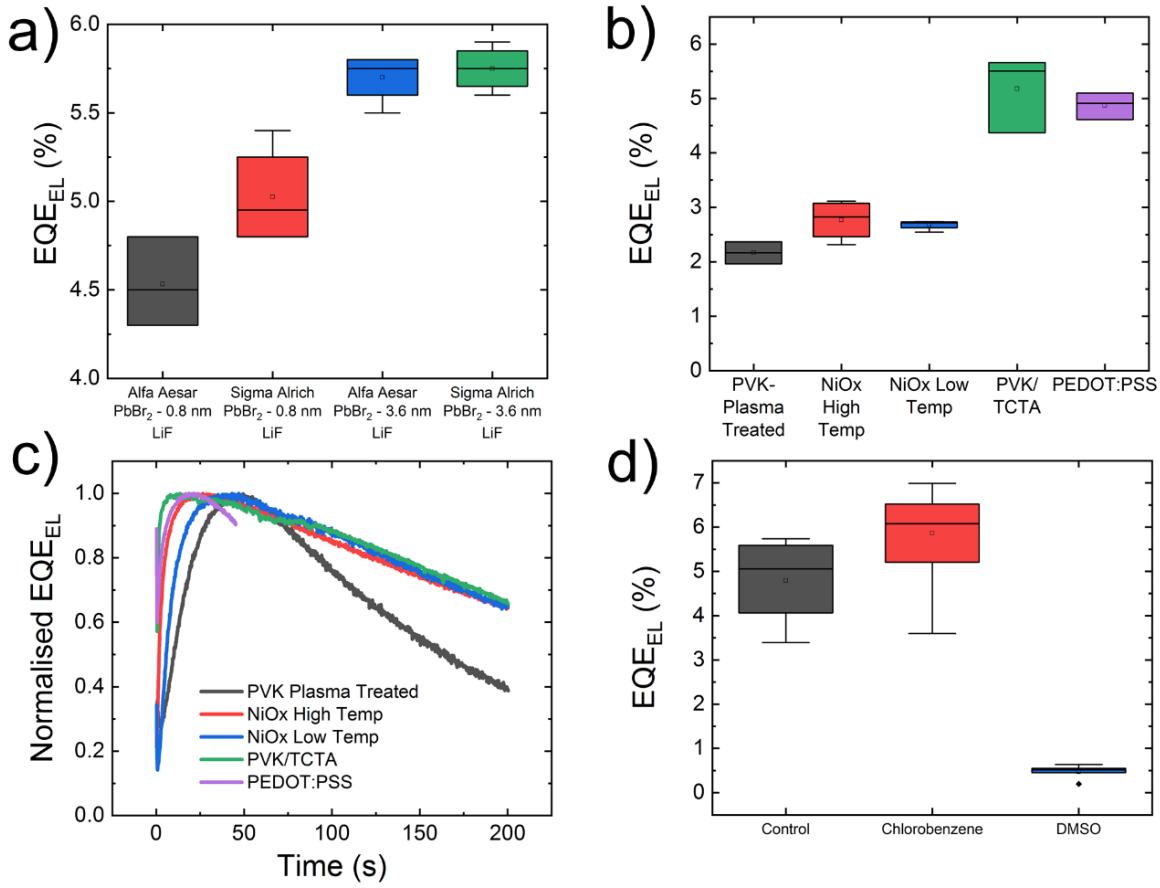


Figure 4.10 a) Boxplot of EQE$_{EL}$ comparing PbBr$_2$ suppliers and LiF thickness; b) Boxplot of EQE$_{EL}$ comparing different HILs; c) Device stability at 10 mA cm^{-2} corresponding to b); d) Boxplot of EQE$_{EL}$ comparing glovebox environment.

We now return to try and reproduce the 9 % LED on PVK and we were unable to wet the perovskite solution on the substrate and obtained low EQE$_{EL}$. Therefore, we try to reoptimise the device from the beginning returning to a PEDOT:PSS HIL as this has good wettability.

Figure 4.10.a. shows the variation of both the supplier we used for PbBr$_2$ and the thickness of LiF we used on the top layer (note that since the first experimental chapter we had increased the rate of Al evaporation to 3 A s^{-1} in an attempt to improve the quality of the deposited film). We observe that 3.6 nm thick LiF was optimal and there was a slight improvement with Sigma Aldrich PbBr$_2$ at this thickness of LiF.

With continuing issues with reproducibility we investigate different HILs to see if PEDOT:PSS was introducing uncontrolled variables (Figure 4.10.b). We find that a dual layer of PVK/ TCTA allows us to improve the wetting of the perovskite precursor solution onto the substrate and achieve a slightly superior EQE$_{EL}$ to PEDOT:PSS. Further, we saw a similar but slightly improved stability compared with PEDOT:PSS (Figure 4.10.b.)

making it a viable HIL for a stability study. This result was repeated and was chosen as the new HIL for the study.

However, further reproducibility issues were encountered, thus we investigated the crystallisation environment during spincoating. We considered that during fabrication, a large amount of DMSO and chlorobenzene vapour was building up in the vicinity of the spincoater. Therefore, we fabricated samples in different atmospheres by soaking a wipe in the respective solvents and placing this saturated wipe around the substrate for the duration of the spincoating process (Figure 4.10.d.). Interestingly we observe that the DMSO samples gives a very low EQE_{EL} and the chlorobenzene sample gives the highest $EQE_{EL.}$ We posit that recrystallisation of the perovskite destroys the very emissive high n domains that are present in the film after the antisolvent quench. Indeed the DMSO films had an orange appearance much more similar to $FAPbBr_3$ than our typical n = 3 films which is indicative of the formation of 3D domains through recrystallisation and a concurrent redshift in absorption onset. The chlorobenzene samples may give higher EQE_{EL} due to reducing the vapour pressure of the DMSO from the precursor solution after the solvent quench, before it is removed from the spincoater. It is not practical nor safe to use such a large amount of chlorobenzene for every substrate so we proceeded by changing the cleanroom wipe which surrounds the spincoater after every substrate in an effort to reduce the DMSO vapour pressure and improve reproducibility.

Another factor affecting reproducibility was that we have an HIL which is soluble in the antisolvent we use for quenching and we are unable to get consistent results with orthogonally soluble HILs (e.g. NiOx, PEDOT:PSS). Therefore we explore the possibility of green 2D/3D perovskite LEDs which do not use an antisolvent to assist crystallisation.

4.3 PEABr:$CsPbBr_3$ Hybrids

We identify a particular report in literature where Ban *et al.* use the molecular additive 1,4,7,10,13,16-hexaoxacyclooctadecane (i.e. 18-crown-6 shown in Figure 4.11) to a solution of $CsPbBr_3$ to modify the colloidal distribution and crystallisation kinetics.[12] By adding 40 mol % (relative to Pb^{2+}) of PEABr to this solution, they are able to obtain films with a PLQY in excess of 60%. Further they are able to incorporate these films into LEDs and achieve an EQE_{EL} of 15.5%. The authors attribute the phenomenon of colloid reduction to the chelate effect, where, a colloid or ionic species which is coordinated by several solvent molecules (e.g. 6 H_2O, Figure 4.11) is coordinated by 18-crown-6 which has 6 coordinating oxygen atoms but is only one molecule. The coordination of the 18-

crown-6 expels the 6 water molecules from the coordination sphere and increases the entropy of the system thus making it thermodynamically favourable.[13] This is known as the "chelate effect". This class of 'crown' molecules can be used to aid the solvation of cesium and ammonium salts in many different organic solvents through this effect.[13,14]

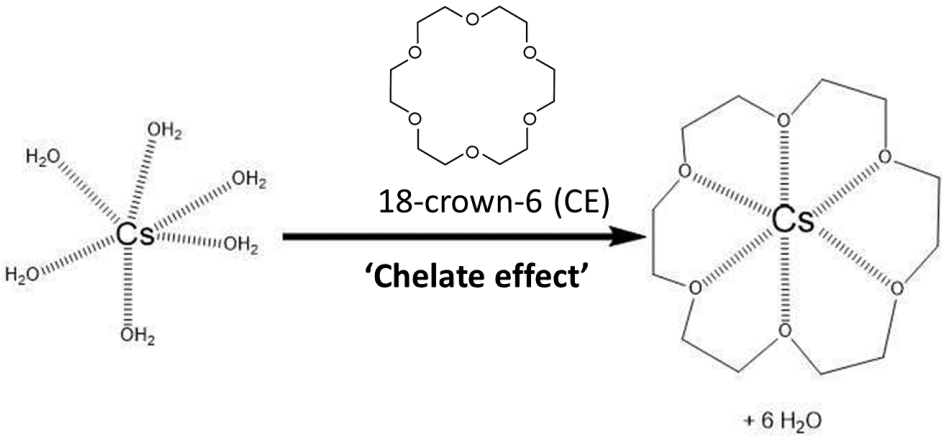


Figure 4.11 Schematic showing how 18-crown-6 increases the entropy of a system using the chelate effect.

4.3.1 18-crown-6: $CsPbBr_3$ films and LEDs

We investigate this effect by preparing a 0.2 M solution of $CsPbBr_3$ in DMSO and adding varying concentrations of 18-crown-6 to the solution, we then spincoat the films under the same conditions with no antisolvent quench. We present the SEM of these films in Figure 4.12, one can clearly see that increasing the concentration of 18-crown-6, i) decreases the grain size where consistent reduction can be observed up until 10-12 mg mL^{-1}, and, ii) improvement in film coverage, the large grains of the untreated film have large pinholes and aside from the 6 mg mL^{-1} 18-crown-6 sample all others have almost complete coverage.

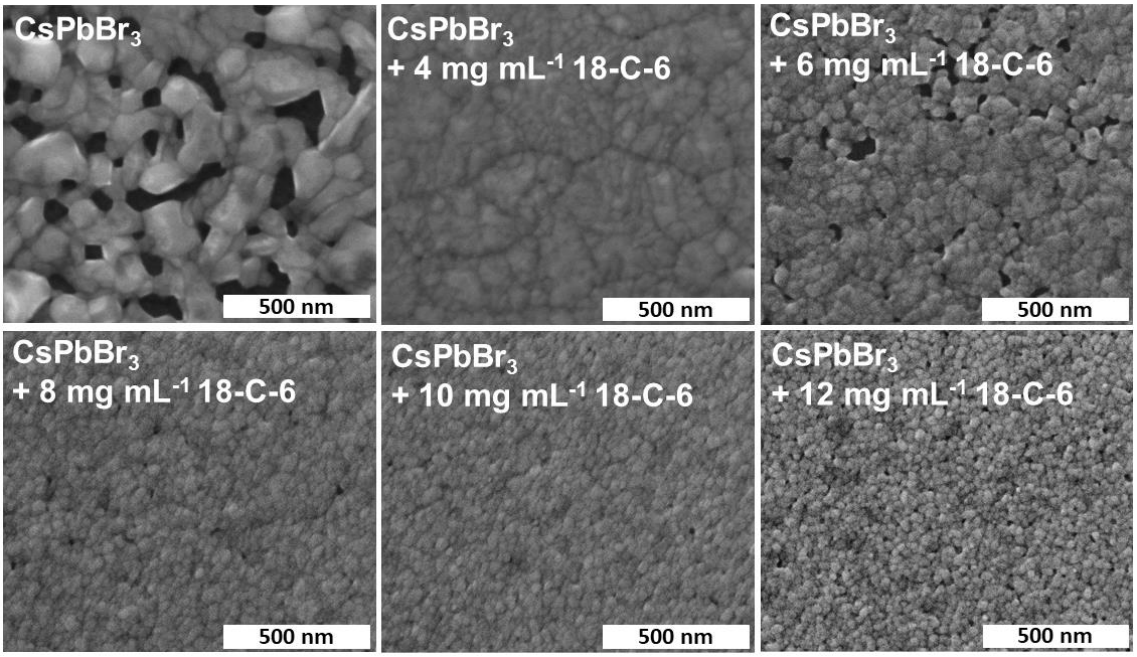


Figure 4.12 SEM of films of $CsPbBr_3$ with various concentrations of 18-crown-6

We now proceed to incorporate these films into an LED stack with PVK as the HIL as we have experience with the material and a recent report of the 40% PEABr material achieved 11% EQE_{EL}.[15] In order to improve the wetting of the perovskite solution onto the PVK we use 2 seconds of oxygen plasma treatment (detailed in experimental section – PVK- Plasma treated). Figure 4.13 summarises the stability and performance of our $CsPbBr_3$ LEDs. We observe an increase in average EQE_{EL} as we increase the concentration of 18-crown-6. Further we observe that all samples with 18-crown-6 have similar stability. The neat $CsPbBr_3$ sample has superior stability but an order of magnitude lower EQE_{EL}

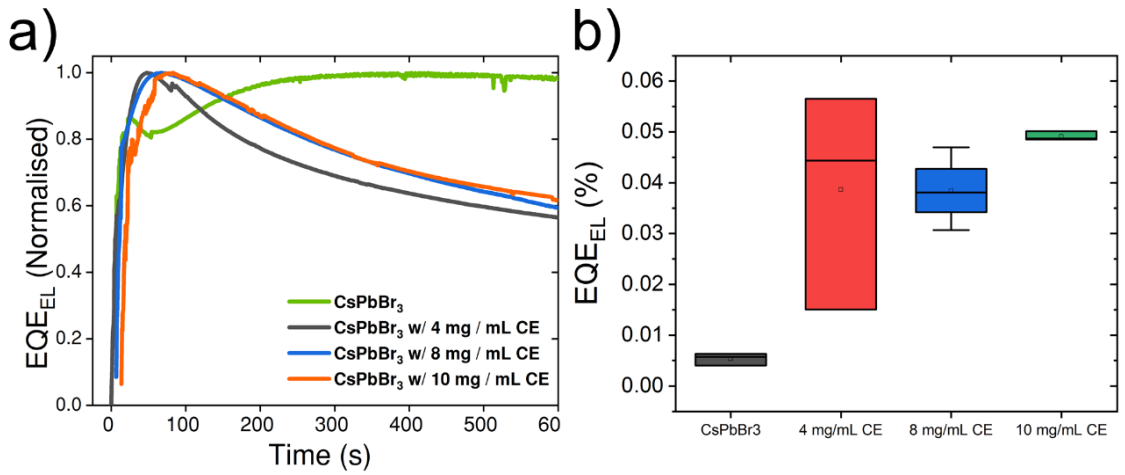


Figure 4.13 a) EQE_{EL} v T for $CsPbBr_3$ LEDs with different concentrations of 18-crown-6; b) Boxplot of EQE_{EL} for those LEDs

4.3.2 Reproducible 2D/3D LEDs (at last)

We now proceed to fabricate devices using the 40% molar excess of PEABr with 4 mg mL^{-1} 18-crown-6 as this was the optimal composition in the literature report.[12] We present a summary of our champion device in Figure 4.14.. Encouragingly we achieve a maximum EQE_{EL} of 4.2 % (Figure 4.14.a.). Further, we note that the current below turn-on voltage is approximately 10^{-6} mA cm^{-2} which is orders of magnitude lower than we were able to achieve with the n = 3 recipe (Figure 4.14.b.) which indicates the presence of less shorts in the device. Further, we see a blue shifted EL spectrum with a peak of ~510 nm (Figure 4.14.c.) compared with ~530 nm for the $FAPbBr_3$ based perovskite, which is consistent with the smaller lattice volume of $CsPbBr_3$ *vs.* $FAPbBr_3$.[16] Finally we observe that the stability is worse than the n =3 LED on PVK/TCTA but stable enough to compare across compositional variations.

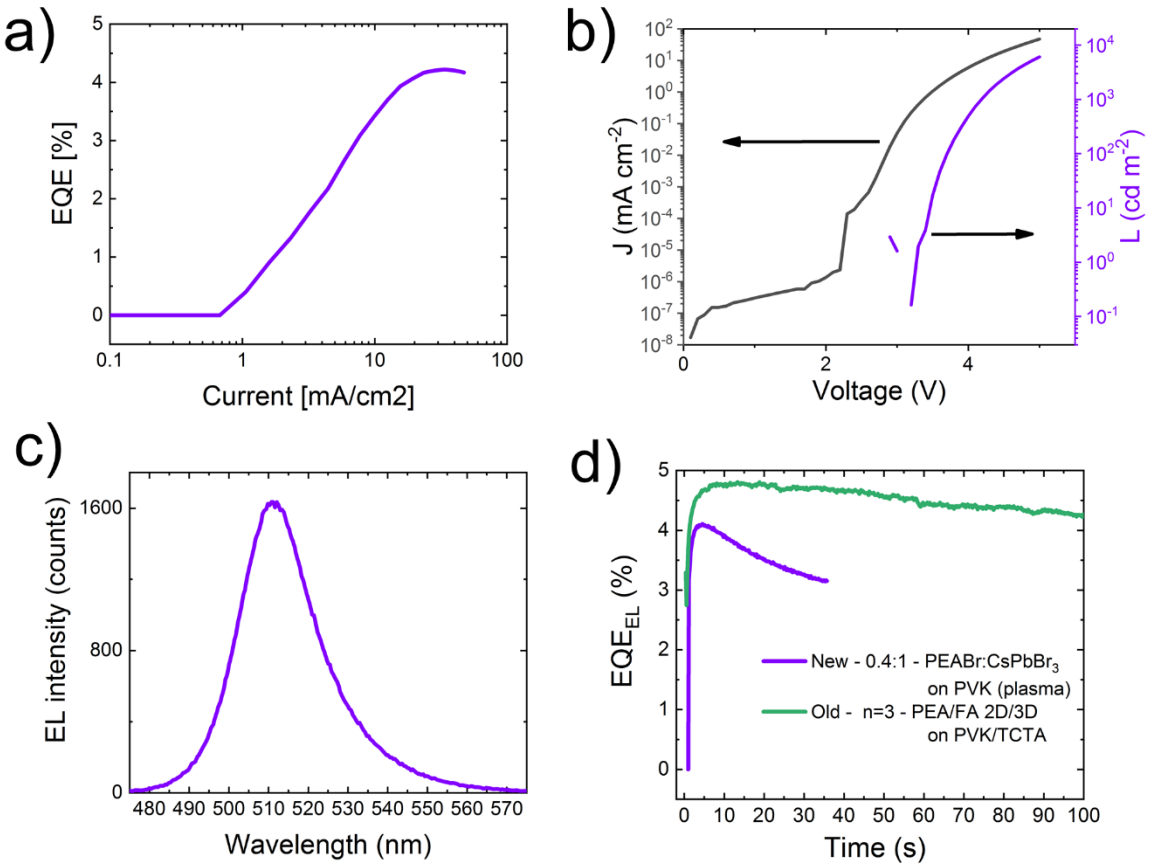


Figure 4.14 Characterisation of $CsPbBr_3$ LED with 40 mol% PEABr and 4 mg mL^{-1} 18-C-6: a) EQE_{EL} v I; b) JVL characteristics; c) EL spectrum; d) Comparison of operational stability at 10 mA cm^{-2} with previous 2D/3D composition.

Most importantly, we find that the removal of antisolvent quench from our fabrication procedure significantly improves reproducibility. We present a boxplot of our control device from 4 consecutive experiments in Figure 4.15. We observe some drift in the baseline but it is more consistent than we have ever been able to achieve. Therefore, *finally* we are able to make a reproducible perovskite LED with high EQE_{EL} such that we can make meaningful conclusions about perturbation of the system.

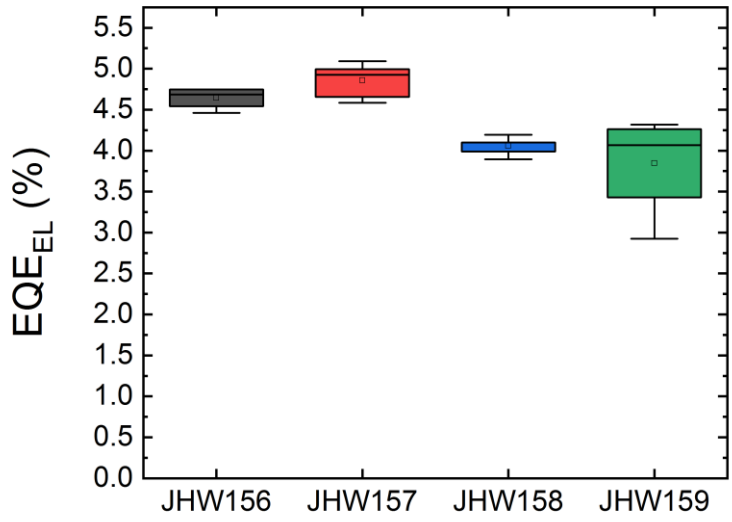


Figure 4.15 Boxplot of $CsPbBr_3$ LED with 40 mol% PEABr and 4 mg mL^{-1} 18-C-6 control device across a series of experiments, showing improved reproducibility.

4.3.3 The effect of PEABr content and testing environment on stability

As such, we proceed to systematically vary the molar ratio of PEABr: $CsPbBr_3$ in our precursor solution and prepare LEDs which we drive at a constant current density of 10 mA cm^{-2} (Figure 4.16.a.). Interestingly, we observe that increasing the PEABr content greatly reduces the operational stability.

We find a striking similarity between the trend of operational stability of these LEDs and the photostability of our poorly encapsulated 2D/3D $FAPbBr_3$ films (Figure 4.4.a.) and consider that our current testing methodology may expose our LEDs to small quantities of air. Currently, we load an LED into an aluminium holder with a glass window in the glovebox, this is sealed by clamping down onto a rubber O-ring. We then interface the holder with a calibrated integrating sphere outside the glovebox (GB) and perform our measurements. We had in the past noticed small spikes in O_2 when reopening this holder when returning the holder to the GB thus we wonder whether exposure to atmosphere is affecting the measurement and strive to measure the LEDs in a completely air free environment. This in addition to; i) the inability to use the integrating sphere for extended periods for long term stability measurements, and, ii) impracticalities of having to load and unload individual samples in the GB and move them to the integrating sphere, motivates us to design and build a GB LED testing rig.

In order to build a reliable testing station we choose a design which has a photodiode (PD) held in reverse bias by a source measure unit (Keithley 2400) at a fixed distance

from the LED, when the PD is illuminated a photocurrent (which is linearly proportional to the number of incident photons) is generated, which is measured by the Keithley (scheme Figure 4.16.d.). If we know that; i) the LED is a Lambertian emitter (which is where the intensity of light in an amount solid angle decreases with cos(θ) of the angle from the normal plane to the emitter, Figure 4.16.c.), ii) the EL spectrum of the LED, and, iii) use a calibrated PD with a known EQE_{PV}, we can calculate the EQE_{EL}. This is because i) we can calculate the solid angle between the LED and the PD and thus the fraction of the total emitted photons which are hitting the PD, and, ii) by integrating the product of the LED spectrum and the EQE_{PV} of the PD we can calculate the ratio of photocurrent to incident photons. Typically when performing these types of measurements one places the PD at a large distance from the LED so that one can use the Lambertian assumption. This is because the Lambertian assumption as described is only valid for a point source. However the LED is not a point source but an emissive surface. In order to maximise the proportion of photons which fall on the PD to increase sensitivity and to decrease the size of the setup, we wanted to minimise the distance between the PD and the LED. We therefore kept the LED and PD 10 mm apart and calculated the radiation view factor between the LED and PD.

A radiation view factor (e.g. $F_{LED \rightarrow PD}$) is the proportion of radiation that leaves the surface of the LED which strikes the PD. Assuming the LED is a Lambertian surface (i.e. every point on the LED surface can be described as a Lambertian emitter) we can use the analytical expression of the radiation view factor of two coaxial square plates (the LED and PD) to calculate the precise percentage of the emitted light which falls on the PD. The details of this calculation can be found here under - unequal coaxial square plates.[17]

After we build this setup, we compare the calculated EQE_{EL} from the new setup and the integrating sphere setup and find them to be the same. We retest the operational stability of the LEDs and find that there are slight differences in the stability, but the trend is the same (Figure 4.16.b.), indicating that the atmosphere is not the main driver of the instabilities.

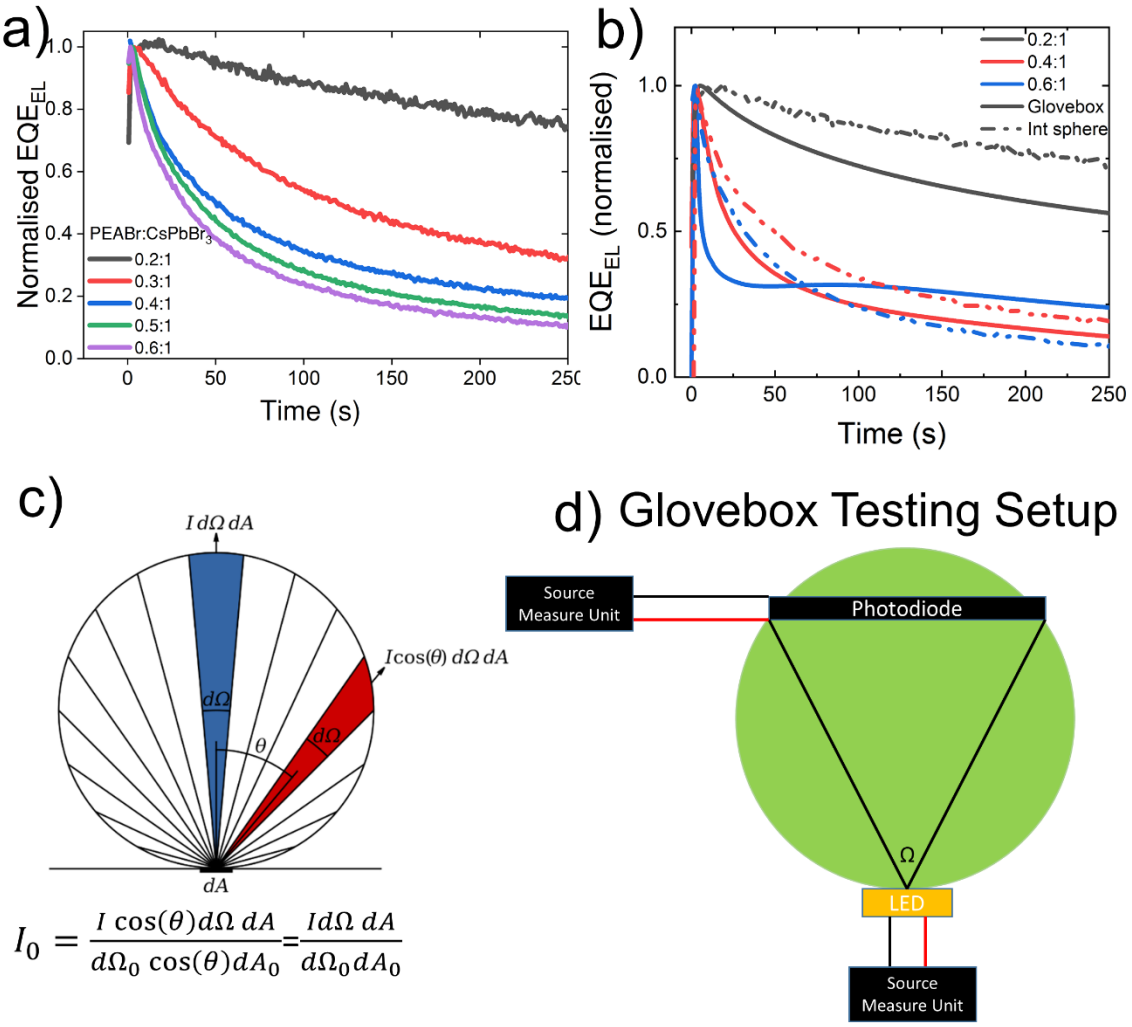


Figure 4.16 a) operational stability of $CsPbBr_3$ LEDs as a function of PEABr content (measured in integrating sphere); b) Comparison of operational stability measured in integrating sphere (ambient) and glovebox testing rig (pure N_2); c) Schematic showing emission pattern of a Lambertian emitter; d) Schematic showing glovebox testing setup.

4.3.4 Characterisation of PEABr:$CsPbBr_3$ hybrids

We now briefly describe the characterisation of the materials used in these devices. The in depth study of these materials and generally this perovskite LED system will be the subject of the third experimental chapter of this thesis so we will not go into great detail. Figure 4.17.a. shows the operational stability of devices held at 10 mA cm^{-2} measured in the GB. We observe that the trend we have previously discovered also holds for $CsPbBr_3$, with the best operational stability observed for the sample with no PEABr. Figure 4.17.b. shows the box plot of EQE_{EL} as a function of composition where we observer that the 0.4:1 PEABr:$CsPbBr_3$ sample is the optimum where the EQE_{EL} falls off quite steeply either side of this composition. Figure 4.17.c. shows the PL spectra of encapsulated films on glass where we observe a similar trend to our benzylamine/$MAPbBr_3$ and 2D/3D

$FAPbBr_3$ films; there is a blueshift of the PL peak and a broadening of the spectrum as we add more PEABr. Finally, Figure 4.17.d. shows the PLQY of the encapsulated films on glass. We observe an excellent PLQY of 63% for our 0.4:1 film which is very encouraging.

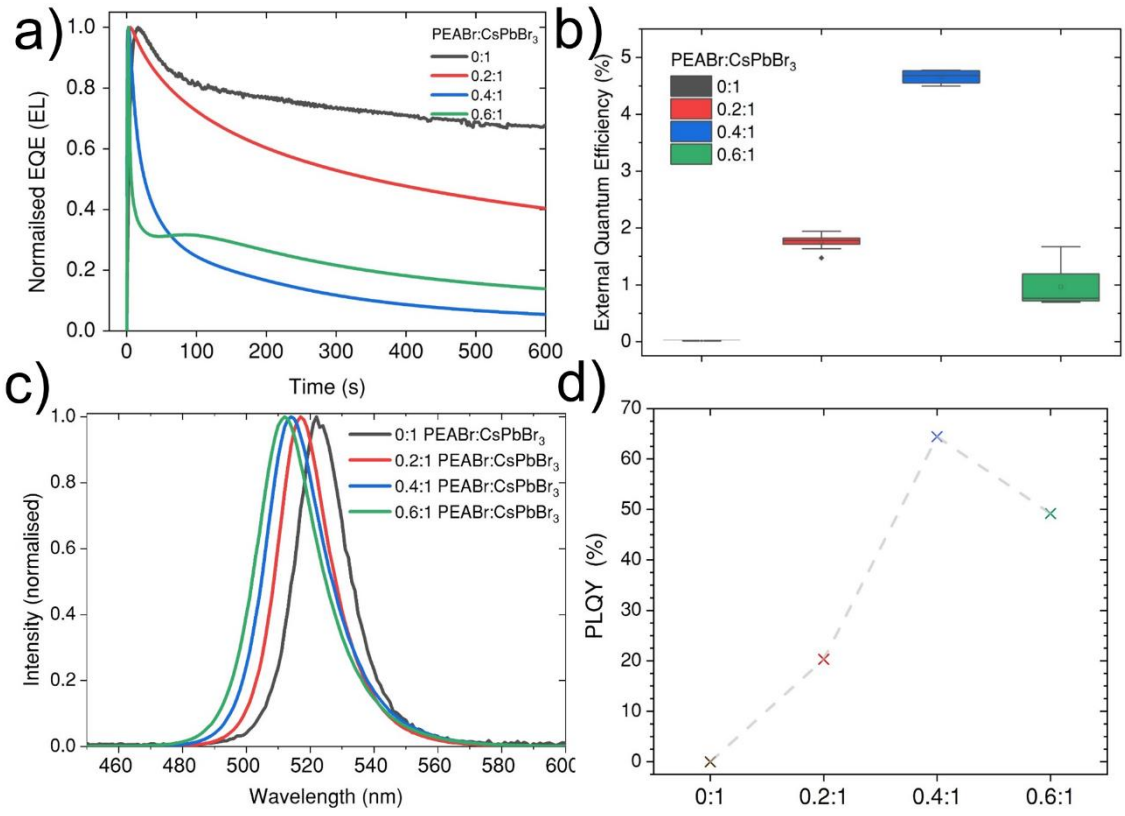


Figure 4.17 Characterisation of PEABr:$CsPbBr_3$ hybrids: a) Operational stability at 10 mA cm^{-2} measured in glovebox; b) Boxplot of EQE_{EL}; c) PL showing blueshift and broadening; d) PLQY of encapsulated films on glass.

4.3.5 Investigation into effect of hole injection layer for high EQE_{EL}

Given the extremely high value of the PLQY and its similarity to the reported value of 60% for this material, we are curious if modification of the device structure can improve the EQE_{EL}. Ban *et al.* use a dual layered HIL of poly-TPD and PFN (which is used as a wetting layer) in the original report to achieve 15.5% EQE_{EL}[12] but we were unable to reproduce their results using PFN.

Therefore, we begin exploring different wetting agents for poly-TPD to see if they will afford, higher efficiencies. We try several different wetting agents but in the first instance we only find that ethoxylated-polyethylenimine (PEIE) is successful in wetting poly-TPD while maintaining a good morphology. Figure 4.18.a. shows a boxplot of an experiment comparing poly-TPD/PEIE with our plasma treated PVK HIL, we observe an

improvement over the control which is encouraging, however, the maximum EQE_{EL} is only 5.5 %. When attempting to modify the charge balance in the poly-TPD/PEIE by decreasing the thickness of the poly-TPD we encounter the unusual phenomenon that once we decrease the concentration of our poly-TPD solution below 10 mg mL^{-1} we are unable to wet the perovskite precursor any more.

As such we continue our search for an improved wetting layer and attempt to use a thin evaporated layer of LiF, Figure 4.18.b. + c. shows the boxplot of EQE_{EL} and operational stability of these devices respectively. We observe that i) 2 nm of LiF gives improved performance vs PEIE with 10 mg mL^{-1} poly-TPD, ii) we are able to wet the perovskite solution on lower concentrations of poly-TPD (with 4 mg mL^{-1} being the optimum), and, iii) the LiF wetting layer gives an improved stability over PEIE. It thus appears that the thickness of the poly-TPD film (Table 4.1) was a crucial condition to optimise.

Poly-TPD solution concentration (mg mL^{-1})	**Poly-TPD film thickness (nm)**
10	32
6	20
4	13

Table 4.1 Thicknesses of spincoated poly-TPD films measured by Dektak profilometry. We were unable to measure the thicnkness of the 2 mg mL^{-1} film.

This may be due to improved charge balance and/or improved light outcoupling. We observe that the total current density injected increases with decreasing poly-TPD thicknesses (Figure 4.19) which correlates well with the increase in EQE_{EL}. This corroborates well with our hypothesis that the charge balance has improved. Further, we find that these devices improve with time (Figure 4.18.d.) giving us an average EQE_{EL} of the optimal composition in excess of 9% one week,

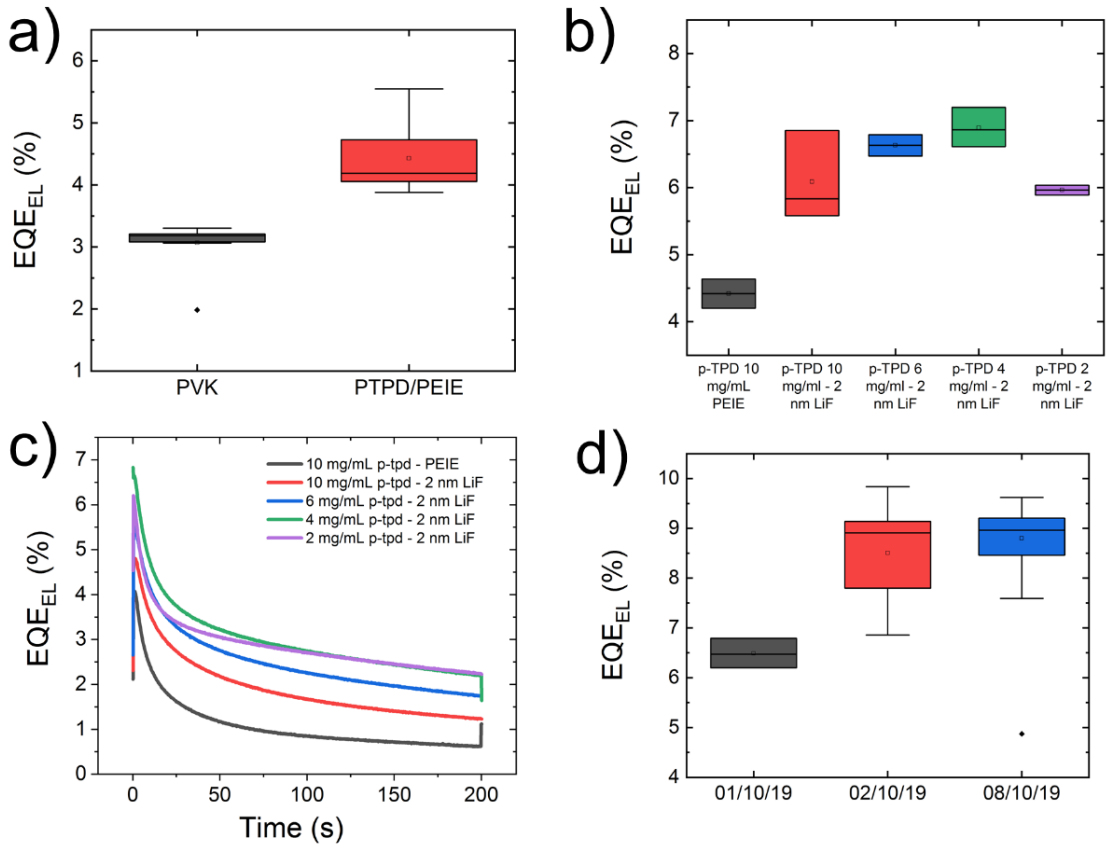


Figure 4.18 a) Boxplot of EQE_{EL} comparing PVK with poly-TPD/PEIE HIL; b) Boxplot of EQE_{EL} v J with different thicknesses of poly-TPD and 2 nm LiF wetting layer; c) Operational stability at 10 mA cm^{-2} for devices shown in b); d) Boxplot of EQE_{EL} showing improved performance of devices after retesting.

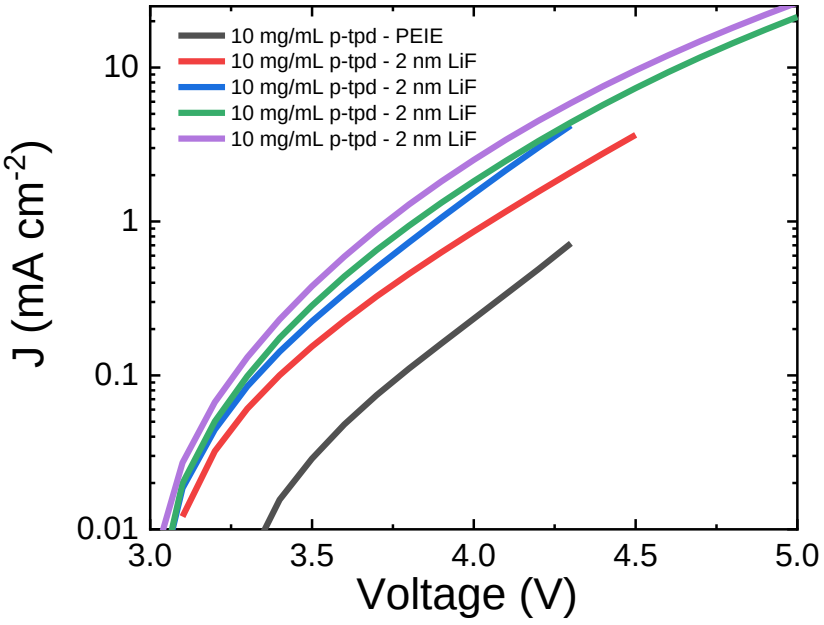


Figure 4.19 Differences in JV characteristics between samples with different thicknesses of poly- TPD. An increase in injected current is observed with decreasing thickness of poly-TPD

As a final step of optimisation we tried tuning the thickness of LiF on our 4 mg mL^{-1} poly-TPD and find that the original condition of 2 nm is optimal (Figure 4.20.a.). Interestingly when we observe that as we increase the thickness of LiF, the degradation characteristics of the LED change quite dramatically and we see an improvement in absolute stability (e.g. 1.5 nm vs 3 nm). This is not studied further during this thesis but is the subject of ongoing work.

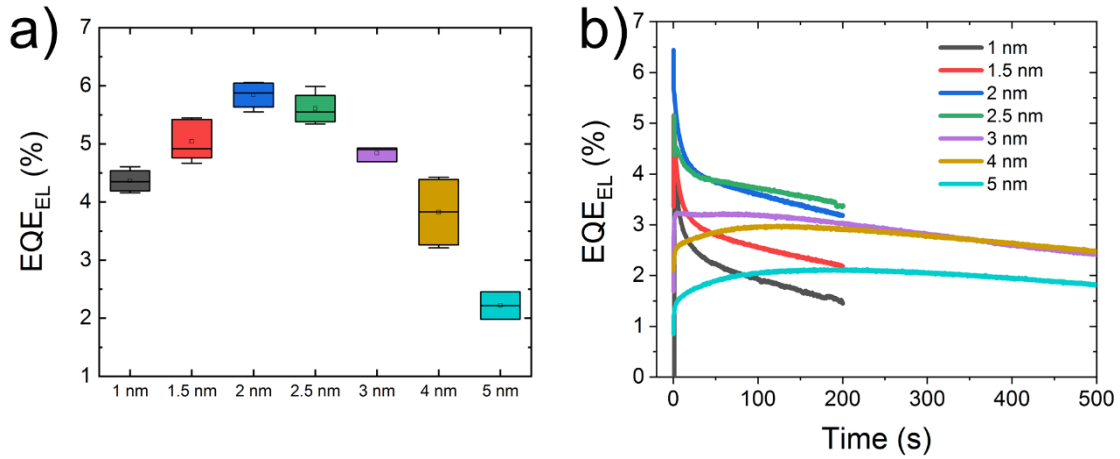


Figure 4.20 a) Boxplot of EQE_{EL} for different thicknesses of LiF on poly-TPD; b) operation stability for devices presented in a).

After a brief further optimisation of changing the concentration of poly-TPD to 5 mg mL^{-1} and retesting several batches of devices, we are able to achieve a champion EQE_{EL} of 12% (Figure 4.21). It took slightly over 2 years of investigation to get from the first attempts at LEDs to this point and as such one should celebrate good results when they finally arrive!

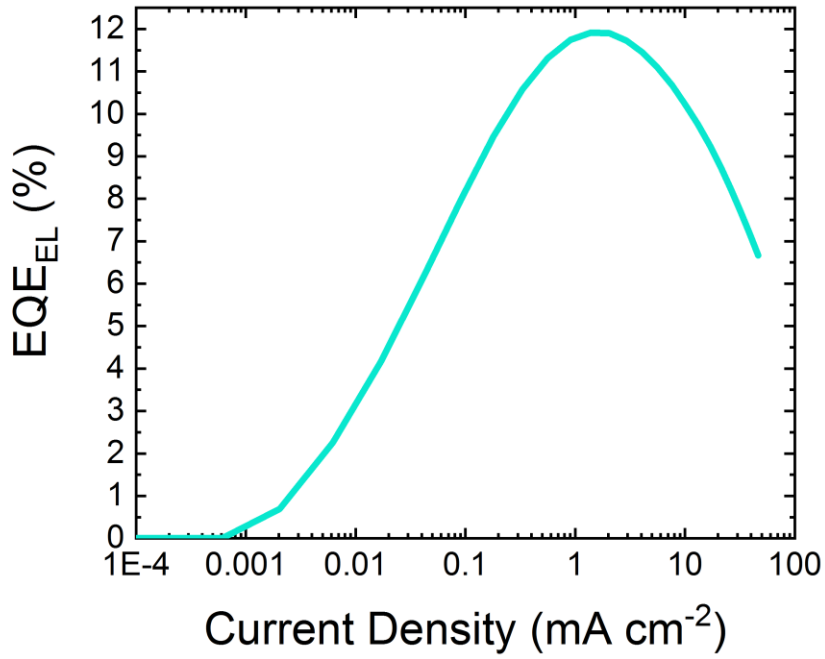


Figure 4.21 EQE$_{EL}$ v I of champion device showing a maximum value of 12%

4.4 Conclusion

Over the course of this chapter we fabricated highly efficient 2D/3D perovskite LEDs and investigated their recombination in films. After performing a brief spectroscopic investigation, we addressed issues for fabricating reproducible LEDs from these films. Despite gaining understanding of several of the variables that were affecting the reproducibility, we were still unable to obtain consistent results. We then changed fabrication procedure such that the molecular additive 18-crown-6 was used to remove the need for an antisolvent quench procedure. This change of methodology proved crucial in improving experimental consistency which we attribute to the solubility of the underlying HIL in the antisolvent. This solubility may have caused issues such as; i) partial and/ or non-uniform washing away of the HIL, or , ii) partial intermixing of the HIL with the perovskite layer.

We then systematically vary the composition of the perovskite, where we find the trend that increasing PEABr content in $CsPbBr_3$ LEDs is deleterious to operational stability. Following this we investigated the HIL and methods to improve its wettability where we develop a novel p-TPD/LiF HIL to achieve an EQE$_{EL}$ of 12%. Through the investigation of the HIL we found that modification of the thickness of poly-TPD was critical which we attribute to improved charge balance and/or light outcoupling. The devices optimised

in this chapter will form the basis of a stability study performed in the following and final experimental chapter of this thesis.

4.5 References

1. Yang, X. *et al.* Efficient green light-emitting diodes based on quasi-two-dimensional composition and phase engineered perovskite with surface passivation. *Nat. Commun.* **9,** 1–8 (2018).
2. Quan, L. N. *et al.* Tailoring the energy landscape in quasi-2D halide perovskites enables efficient green light emission. *Nano Lett.* acs.nanolett.7b00976 (2017). doi:10.1021/acs.nanolett.7b00976
3. Wu, T. *et al.* High-Performance Perovskite Light-Emitting Diode with Enhanced Operational Stability Using Lithium Halide Passivation. *Angew. Chemie Int. Ed.* **59,** 4099–4105 (2020).
4. Yang, X. *et al.* Efficient green light-emitting diodes based on quasi-two-dimensional composition and phase engineered perovskite with surface passivation. *Nat. Commun.* **9,** 570 (2018).
5. Lingstedt, L. V. *et al.* Effect of DMSO Solvent Treatments on the Performance of PEDOT:PSS Based Organic Electrochemical Transistors. *Adv. Electron. Mater.* **5,** 1800804 (2019).
6. Jiang, Y. *et al.* Spectra stable blue perovskite light-emitting diodes. *Nat. Commun.* **10,** 1–9 (2019).
7. Xing, G. *et al.* Transcending the slow bimolecular recombination in lead-halide perovskites for electroluminescence. *Nat. Commun.* **8,** 14558 (2017).
8. Zou, W. *et al.* Minimising efficiency roll-off in high-brightness perovskite light-emitting diodes. *Nat. Commun.* **9,** 1–7 (2018).
9. Na Quan, L. *et al.* Edge stabilization in reduced-dimensional perovskites. *Nat. Commun.* **11,** 1–9 (2020).
10. Gong, X. *et al.* Electron-phonon interaction in efficient perovskite blue emitters. *Nat. Mater.* **17,** 550–556 (2018).
11. Kirchartz, T., Márquez, J. A., Stolterfoht, M. & Unold, T. Photoluminescence-Based Characterization of Halide Perovskites for Photovoltaics. *Adv. Energy Mater.* **10,** 1904134 (2020).
12. Ban, M. *et al.* Solution-processed perovskite light emitting diodes with efficiency exceeding 15% through additive-controlled nanostructure tailoring. *Nat. Commun.*

9, 3892 (2018).

13. Rüdiger, V., Schneider, H.-J., Solov'ev, V. P., Kazachenko, V. P. & Raevsky, O. A. Crown Ether–Ammonium Complexes: Binding Mechanisms and Solvent Effects. *European J. Org. Chem.* **1999,** 1847–1856 (1999).
14. Goff, C. M., Matchette, M. A., Shabestary, N. & Khazaeli, S. Complexation of caesium and rubidium cations with crown ethers in N,N-dimethylformamide. *Polyhedron* **15,** 3897–3903 (1996).
15. Zou, Y. *et al.* Boosting Perovskite Light-Emitting Diode Performance via Tailoring Interfacial Contact. *ACS Appl. Mater. Interfaces* **10,** 24320–24326 (2018).
16. Mannino, G. *et al.* Temperature-Dependent Optical Band Gap in $CsPbBr_3$, $MAPbBr_3$, and $FAPbBr_3$ Single Crystals. *J. Phys. Chem. Lett.* **11,** 2490–2496 (2020).
17. Radiation View Factors. Available at: http://webserver.dmt.upm.es/~isidoro/tc3/Radiation View factors.pdf. (Accessed: 10th October 2020)

5 Revealing Factors Influencing the Operational Stability of Perovskite Light-Emitting Diodes

The work in this chapter is adapted from the publication; Warby, J. H., Wenger, B., Ramadan, A. J., Oliver, R. D. J., Sansom, H. C., Marshall. A. R. and Snaith, H. J. Revealing Factors Influencing the Operational Stability of Perovskite Light-Emitting Diodes *ACS Nano* , 14, 7, 8855–8865, (2020)

I conceived the idea, collected and analysed all data in this project unless stated otherwise, All authors on this publication made excellent contributions to the work. B. Wenger helped develop the LED testing system, conceive some of the optical experiments and provided useful insights when interpreting and analysing data. A. J . Ramadan collected, analysed and helped interpret X-Ray photoelectron spectroscopy data. R. D. J. Oliver collected and help analyse and interpret Fourier transform photocurrent spectroscopy data. H. C. Sansom helped analyse and interpret X-Ray diffraction data. A. R. Marshall and H. J. Snaith helped conceive experiments and provided useful insight into data analysis.

5.1 Introduction

Since the first reports of perovskite light-emitting diodes (LEDs) in 2014,[1] there has been a rapid improvement in the initially modest efficiencies with several groups reporting external electroluminescent quantum efficiencies (EQE_{EL}) in excess of 20%. [2–5] This high efficiency which is comparable with state of the art organic LEDs (OLEDs) is moderated by the currently poor stability. Reported LEDs have a time to reach 50% of their initial EQE_{EL} (T_{50}) which range from seconds, [6,7] to 250 hours in the best case. [8,9] These lifetimes are orders of magnitude worse than those of OLEDs which can operate for tens

of thousands of hours which is preventing perovskite LEDs from making the jump from the lab to commercial applications. It is apparent that the stability of these devices needs to be more critically assessed as this short falling is the technologically gaiting aspect.

Recently, the most widely reported strategy for achieving high efficiency in perovskite LEDs has been to incorporate ammonium cations with large lipophilic tails that are known to form two-dimensional Ruddlesden- Popper perovskite phases (described in section 1.2.2)[10–13] into the precursor solution to form so called "2D/3D" compositions. This greatly improves the optoelectronic properties of the emitter layer through: i) direct chemical passivation, ii) increased dielectric confinement, iii) funnelling of carriers into the lowest energy states, thus increasing carrier concentration and bimolecular radiative recombination, and iv) reduction of grain size which further confines the carriers.[10,13,14] The most widely used cation to form "2D/3D" compositions is phenylethylammonium (PEA). There have been few reports investigating the effect of the composition of the emitter layer in perovskite LEDs[15,16] and none which systematically investigate the effect of phenylethylammonium.

In this chapter we investigate the effect of composition of the emissive layer on the operational stability of perovskite LEDs. We vary the amount of the alkyl-ammonium salt phenylethylammonium bromide (PEABr) which we add to a precursor solution of cesium lead tribromide ($CsPbBr_3$). We find that the addition of PEABr is highly beneficial for the goal of high efficiency, where we see an improvement of EQE_{EL} from 0.24 % for our control $CsPbBr_3$ device to 12.1% for our optimal composition. However, we also find a strong inverse correlation of the amount of phenylethylammonium in the emitter and the operational stability, which is a cause for significant concern. We investigate the drivers behind this instability and find two main contributing factors, i) a significant loss in the radiative efficiency of the emitter, and, ii) most significantly, the emergence of a charge injection barrier in the LED which we postulate leads to significant charge imbalance in the device.

5.2 Fabrication and characterisation of PEABr:$CsPbBr_3$ hybrids

In this section we fabricate and characterise a series of films which represent a broad range of compositions of the PEABr:$CsPbBr_3$ hybrid system. We investigate structural and optoelectronic properties to understand the nature of this system and the effects of phenylethylammonium prior to incorporation into devices.

5.2.1 Morphological tailoring and characterisation

In order to have a fair comparison between the different hybrids once they are incorporated into our LED structure, we deem it necessary to have continuous films of the emitter across the entire compositional series. If there are pinholes in the film there will be direct contact between our electron and hole injection layers which would result in a shunt which is a parasitic loss for EQE_{EL}. If we fabricate films of neat $CsPbBr_3$ *via* spincoating, we obtain a film with a high pinhole density (Figure 5.1), therefore, we add the molecule 18-crown-6 (CE) into the precursor solution to modify the crystallisation. This methodology was introduced by Ban *et al.* [11] where they reported continuous films of $CsPbBr_3$ by adding CE (which is a member of the crown ether family of molecules) to a 0.2 M solution at a concentration of 4 mg mL^{-1}. Crown ethers are widely used to improve the solubility of metal and ammonium salts in a wide variety of solvents.[17,18] The underlying mechanism of their action can be explained through the chelate effect.[19] Ban *et al.* present dynamic light scattering data which demonstrates that the average colloid size in the $CsPbBr_3$ precursor solution is reduced through the addition of CE which reveals the improved solubility. Further, they show a decrease in absorption and diffraction intensity for $CsPbBr_3$ films with CE which indicates that it supresses crystallisation. These two effects modify the crystallisation such that one can obtain continuous films *via* spincoating.

We fabricate a series of films of $CsPbBr_3$ with increasing concentration of CE and measure SEM to assess the morphology (Figure 5.1. a.). We find that at a concentration of 4 mg/mL CE we obtain continuous films of $CsPbBr_3$ coupled with a significant decrease in grain size, at a concentration of 8 mg/mL we still obtain continuous films and the grain size is further reduced. These observations are consistent with the findings of Ban *et al.*

Now that we have obtained continuous films of $CsPbBr_3$ we proceed to incorporate PEABr into the precursor solution. From this point forward in the chapter all perovskite films contain CE at a concentration of 4 mg/mL unless mentioned otherwise.

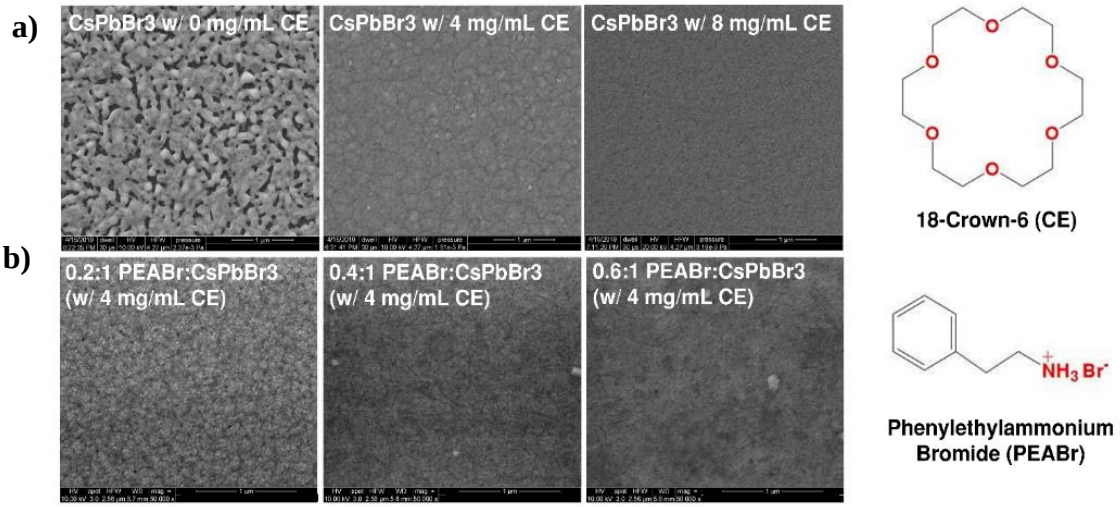


Figure 5.1. a) The effect of increasing 18-crown-6 concentration on film morphology and its structure. Addition of 18-crown-6 has a marked impact on the film morphology.; b) The effect of PEABr on film morphology and the chemical structure of PEABr, all of the films have 4 mg/mL of 18-crown-6 in the precursor solution. Additon of PEABr has a strong effect on the film morphology causing even further decrease in grain size until we cannot easily resolve it by SEM.

We find that the incorporation of PEABr into the precursor solution affects the morphology further still. As the ratio of PEABr:$CsPbBr_3$ is increased from 0.2:1 to 0.6:1 one observes that there is a decrease in grain size to the point where it is not possible to individually resolve the grains in the 0.4:1 and 0.6:1 samples (Figure 5.1. b.). Further, all films are continuous which allows us to proceed in our characterisation.

5.2.2 Optical absorption and emission

Next, we investigate the optoelectronic properties of our films. We fabricate a wider series of films which we denote with the nomenclature $(PEABr)_xCsPbBr_3$ (x = 0-1.0) We present images of the films in ambient light (Figure 5.2. a.), and under UV excitation (Figure 5.2. b.). We wish to state that the nomenclature does not refer to the crystal phase of the film but the stoichiometry of the precursor solution.

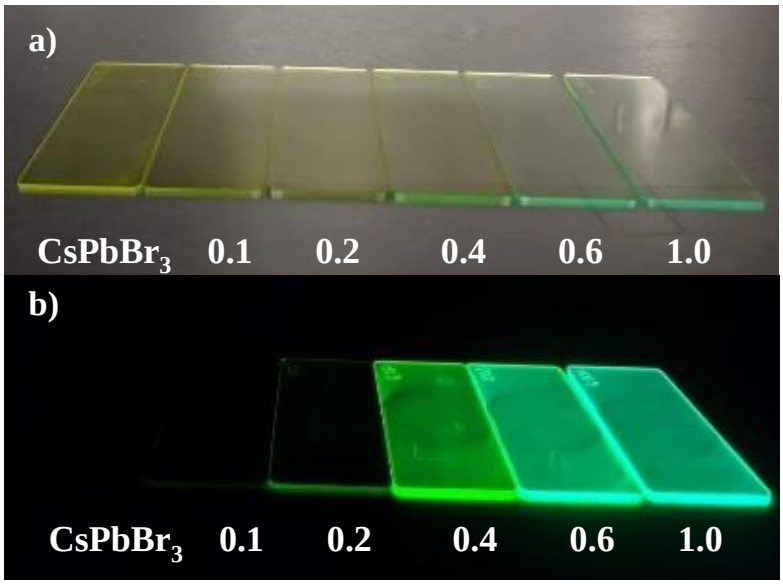


Figure 5.2. a) Photograph of films used for characterisation under ambient lighting in glovebox, numbers indicate molar fraction i.e. 0.1 = (PEABr)0.1CsPbBr3, b) photograph of corresponding films under 365 nm UV light in glovebox.

We begin by characterising the UV-Visible absorption (UV-Vis) (Figure 5.3.a.). and photoluminescence spectra (PL) of the films (Figure 5.3.b.). For our control films of pristine $CsPbBr_3$ we observe an excitonic absorption peak centred at 515 nm and an emission spectrum with one peak centred at 525 nm. As we incorporate PEABr into the precursor solution we observe:

i) A diminishing of the total absorption intensity which can be readily explained as we have adjusted the precursor solution such that the total weight percent of salts remains constant (details are found in Experimental methods), which results in a decrease in the molarity of $CsPbBr_3$ as we increase the relative amount of PEABr.

ii) A concurrent blueshift in the absorption onset and the emission peak. We posit that this is due to quantum confinement of the generated charge carriers within the emissive domains. This generally occurs in $CsPbBr_3$ crystals which are below 15 nm in size.[20]

iii) A concurrent broadening of the excitonic absorption and an increase in the FWHM of the emission peak. These two features are generally attributed to an increase in disorder in the system,[21] which generally results in a deterioration in optoelectronic properties. We will discuss this further in section 5.2.3.

iv) The formation of excitonic peaks at approximately 430 and 460 nm for the $PEABr_{1.0}CsPbBr_3$ sample. These can be attributed to lower dimensional

phases in the film, likely the n = 2 and n= 3 phase. [22] It is interesting to note that we do not observe significant absorption from these features in the other samples, despite a high loading concentration of PEABr.

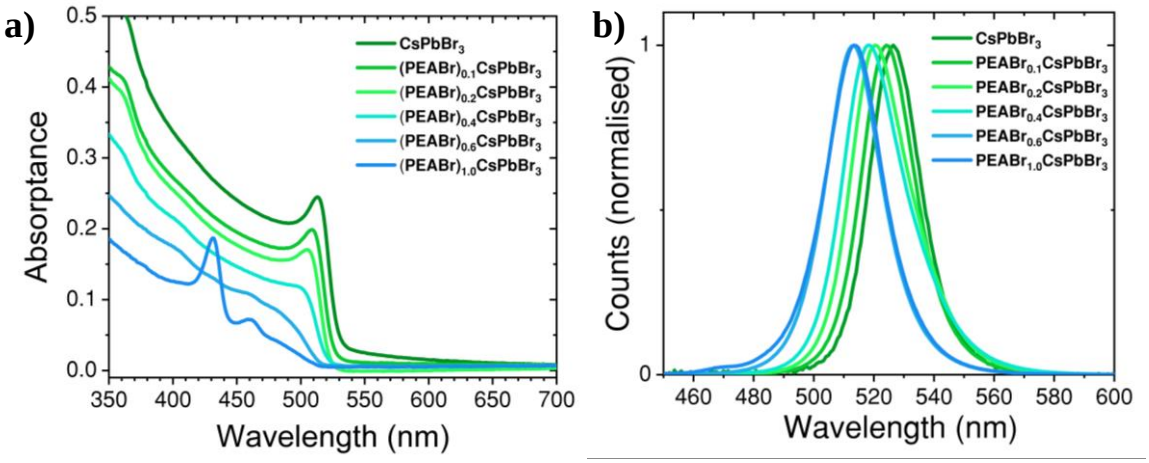


Figure 5.3. a) Absorptance data of $CsPbBr_3$ with increasing molar excess of PEABr; b) Normalised photoluminescence spectra of $CsPbBr_3$ with increasing molar excess of PEABr;

5.2.3 Photoluminescent quantum yield

Now, we determine the photoluminescent quantum yield (PLQY) of the films (Table 5.1, Figure 5.4). PLQY is defined as the ratio between the number of photons emitted to the number of photons absorbed. This value is critical when assessing an emitter for an LED as it represents the maximum possible value for the EQE_{EL} if all other losses in the device can be accounted for.[23,24] We find that the introduction of PEABr into the precursor solution causes a large increase in the PLQY. The introduction of only 10 mol % excess boosts the PLQY from 0.4%, up to 16.4%. When we increase this to 100 mol % excess we obtain a PLQY of 71.8% which is among the highest values reported for a continuous perovskite thin film.[25] Indeed when one considers the ray-optical limit of $1/n^2$ and assume $n = 2$[26] we would expect a maximum PLQY of 13%, therefore we believe that there is significant photon recycling occurring in these films which has been recently highlighted by Cho *et al.* [24]

We wish to highlight that the concomitant increase in PLQY with a broadening of both the excitonic absorption and the emission spectrum (FWHM, Table 5.1) presents an unusual trend. As we previously stated, broadening of these spectra indicates an increase in disorder in the system which should result in a decrease in PLQY. We believe that this is because the emissive domains are in the quantum confinement regime and have a high polydispersity (which is a form of disorder). This is consistent with our fabrication

process which is not optimised to control polydispersity. The polydispersity of the system should not be deleterious to the optoelectronic properties of the system and PEABr is clearly improving it, thus giving rise to this peculiar effect.

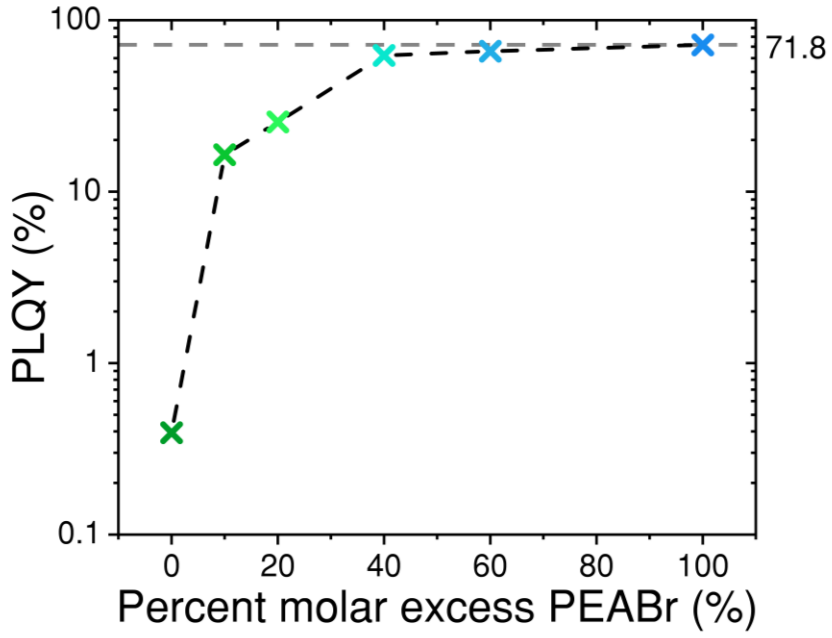


Figure 5.4. Photoluminescent quantum yield of $CsPbBr_3$ with increasing molar excess of PEABr

Perovskite Composition	PL Peak (nm)	PLQY (%)	FWHM (nm)	PL Stability – I/I_0 after 300 s
$CsPbBr_3$	526	0.4	21.2	1.26
$(PEABr)_{0.1}CsPbBr_3$	524	16.4	22.4	0.76
$(PEABr)_{0.2}CsPbBr_3$	520	25.5	25.3	0.58
$(PEABr)_{0.4}CsPbBr_3$	518	62.3	26.8	0.84
$(PEABr)_{0.6}CsPbBr_3$	512	66.0	23.9	0.90
$(PEABr)_{1.0}CsPbBr_3$	513	71.8	25.1	0.92

Table 5.1. PL Peak, PLQY, FWHM of PL and PL stability of the different compositions of (PEABr)xCsPbBr3 used in this study. All films were on glass and encapsulated in an N_2 filled glovebox.

5.2.4 X-Ray Diffraction

Next, we investigate the crystal structure of our $CsPbBr_3$ and $(PEABr)_{0.4}CsPbBr_3$ films on ITO. We are able to fit all peaks in the diffractograms to the crystal structures of $CsPbBr_3$ and ITO (Figure 5.5, Table 5.2). This further supports our hypothesis that we are not forming any 2D phases (e.g PEA_2PbBr_4) in our films with PEABr until we reach the critical point of $(PEABr)_{1.0}CsPbBr_3$ where we observe exitonic absorption from 2D phases in the UV-Vis. This leads us to hypothesise that we are forming nanocrystalline domains of $CsPbBr_3$ in a matrix of PEABr.

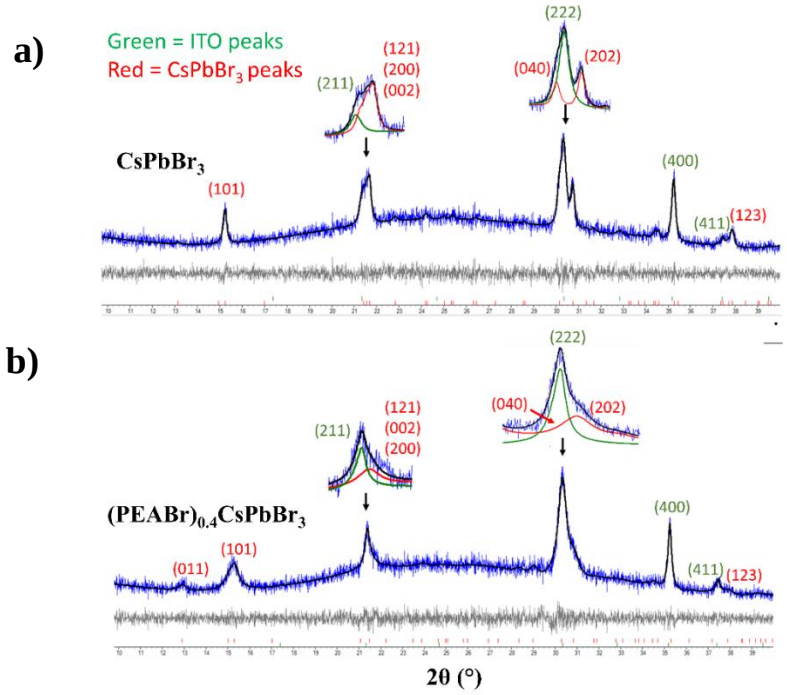


Figure 5.5. a) Peak fitting of $CsPbBr_3$ sample to $CsPbBr_3$ and ITO peaks; b) Peak fitting of $(PEABr)_{0.4}CsPbBr_3$ sample to $CsPbBr_3$ and ITO peaks

$CsPbBr_3$ Bragg reflection (h k l)	**$CsPbBr_3$ 2θ peak positions (°)**	**$(PEABr)_{0.4}CsPbBr_3$ 2θ peak positions (°)**
0 1 1	N/A	12.90
1 0 1	15.25	15.24
1 2 1	21.41	21.08
2 0 0	21.56	22.23
0 0 2	21.69	21.47
0 4 0	30.16	30.27
2 0 2	30.77	30.83
1 2 3	37.88	37.88

Table 5.2. Peak assignments for $CsPbBr_3$ peaks in diffractograms presented in Figure 5.5

We find further support for this hypothesis when we analyse the peaks associated with Bragg reflections from the 1 0 1 plane and find that there is significant broadening of the peak (Figure 5.6). Our $CsPbBr_3$ sample has a FWHM of 0.195°, whereas our $(PEABr)_{0.4}CsPbBr_3$ sample has a FWHM of 0.646°. This represents a threefold broadening and is consistent with a large reduction in coherent scattering length and thus particle size. If we assume that the scattering domains are spherical and perform a Scherrer broadening analysis we find that this corresponds to an average domain diameter of 47 nm for our $CsPbBr_3$ film and 15 nm for our $(PEABr)_{0.4}CsPbBr_3$ film.

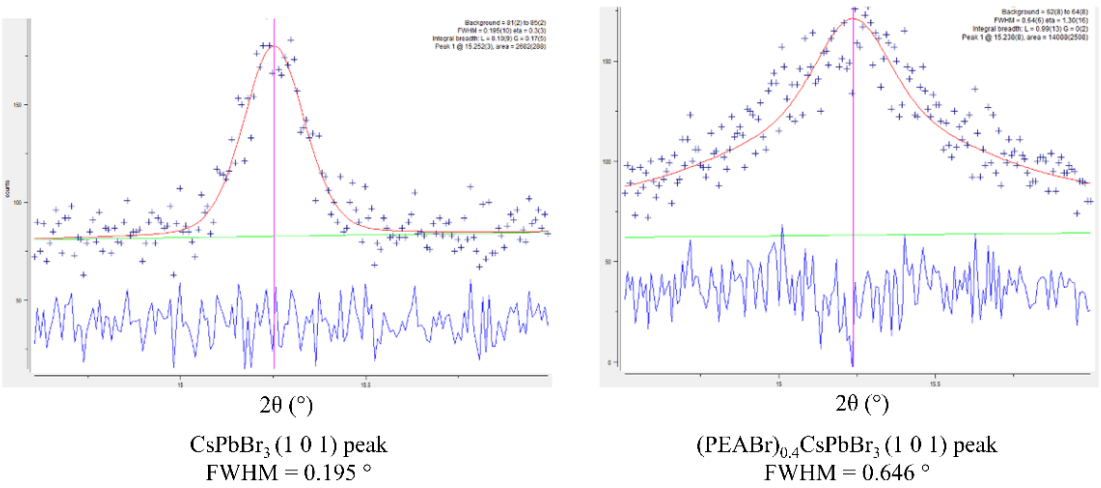


Figure 5.6. comparison of the FWHM of $(PEABr)_{0.4}CsPbBr_3$ and $CsPbBr_3$ (101) peaks, $(PEABr)_{0.4}CsPbBr_3$ has a FWHM 3 x larger than $CsPbBr_3$.

5.3 Incorporation of films into devices

5.3.1 Device Structure

We incorporate our series of films into a typical *pin* heterojunction device structure used in literature for perovskite LEDs [12] with some adjustments to allow for facile processing. We will then track changes in device performance and critically operational stability. The device stack (ITO/poly-TPD/LiF/$(PEABr)_xCsPbBr_3$/TPBi/LiF/Al) is illustrated in Figure 5.7. Poly-TPD and TPBi are the hole and electron injection layers respectively. We deposit a 2 nm layer of LiF onto the poly-TPD as it allows us to wet the precursor solution onto the substrate. Due to the shallow LUMO of TPBi (2.7 eV)[27] a thin layer of LiF is evaporated in between the Al as this has been shown to facilitate electron injection.[28]

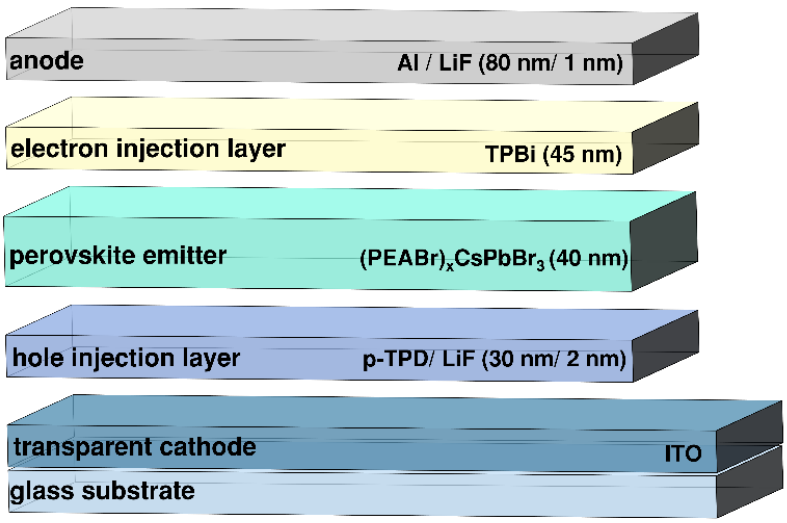


Figure 5.7 LED device structure used in this study including layer thicknesses

5.3.2 Device Performance

We now characterise the fabricated LEDs for their performance. We present the current density (J) v EQE_{EL}(Figure 5.8), box plots of maximum EQE_{EL} for one batch of devices (Figure 5.9) and current density-voltage-luminance characteristics (J-V-L, Figure 5.10). We achieve an excellent EQE_{EL} of 12.1% for our champion $(PEABr)_{0.4}CsPbBr_3$ LED which demonstrates a large improvement over the control $CsPbBr_3$ device with a maximum EQE_{EL} of only 0.24%.

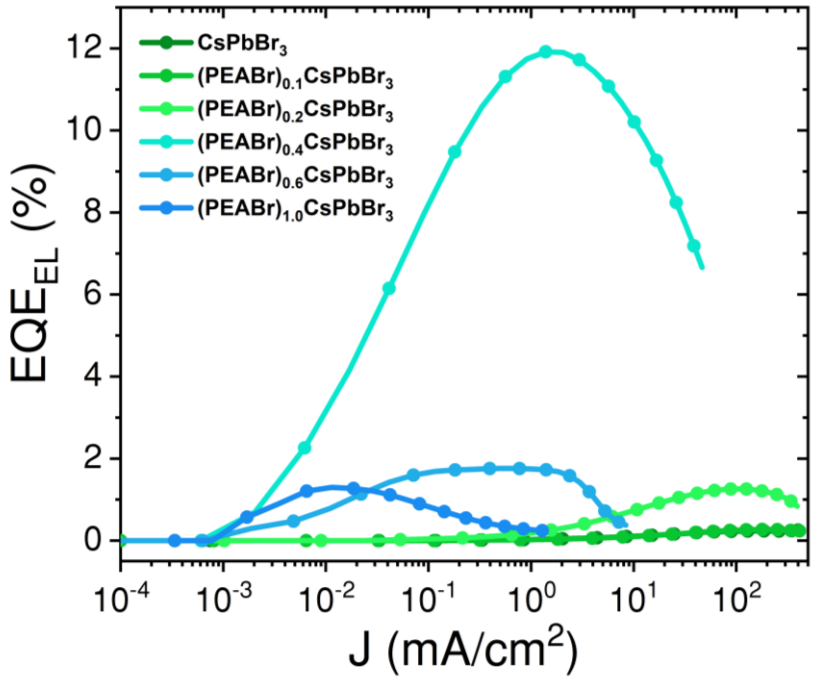


Figure 5.8. Typical J v EQE_{EL} for all $(PEABr)_xCsPbBr_3$ compositions in this study

It is interesting to note that the trend of PLQY does not closely follow the trend of EQE_{EL}. For $(PEABr)_{0.1}CsPbBr_3$ and $(PEABr)_{0.2}CsPbBr_3$ we saw significant improvement in PLQY, but the EQE_{EL} shows no improvement for $(PEABr)_{0.1}CsPbBr3$ and only moderate improvement for $(PEABr)_{0.2}CsPbBr3$, in comparison to the neat $CsPbBr_3$ LEDs. A reduction in EQE_{EL} can arise from a reduction in the emission efficiency (PLQY) of the isolated emitter layer, luminescence quenching *via* the presence of charge injection contacts, or unfavourable charge balance. If we specifically compare $(PEABr)_{0.4}CsPbBr_3$ to $(PEABr)_{1.0}CsPbBr_3$, we observe a sizable increase in PLQY of the isolated thin films (Table 5.1), but a substantial drop in EQE_{EL}. This tells us that either the luminescence quenching from the charge extraction contacts is sensitive to the emission layer composition or the charge balance has become less favourable. We will return to this point when investigating the operational stability of the devices later on.

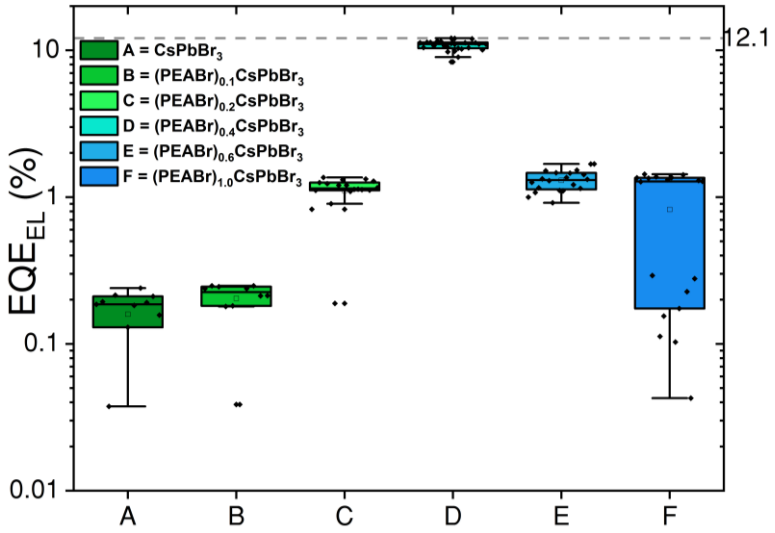


Figure 5.9. Box plots of measured EQE_{EL} for one batch of devices sweeping through all $(PEABr)_xCsPbBr_3$ compositions during this study.

Interestingly, although they are relatively high efficiency we observe that as we increase the proportion of PEABr the 'roll off' of the EQE_{EL} moves to lower current densities (Figure 5.8). This manifests in a very low maximum luminance for the $(PEABr)_{0.6}CsPbBr_3$ and $(PEABr)_{1.0}CsPbBr_3$ LEDs of 145 and 11 cd/ m^2 respectively (Figure 5.10), which is too low to be commercially useful (typically OLEDs will operate up 1000 cd/ m^2).

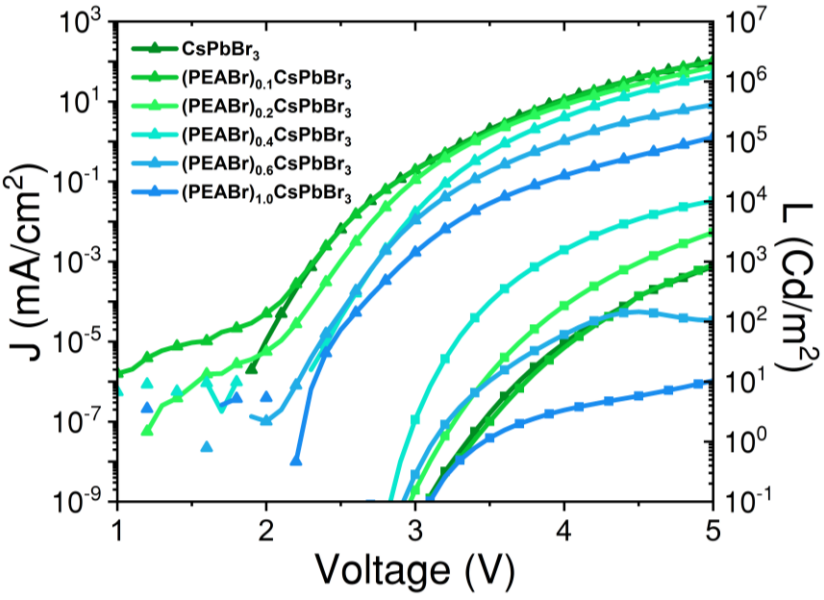


Figure 5.10. JVL characterisation of all $(PEABr)_xCsPbBr_3$ compositions in this study. The data here generated from the same sweeps of J v EQE_{EL} in Figure 5.8

In Figure 5.10 we observe that as we increase the proportion of PEABr there is a decrease in the current density at a given voltage. This is expected as PEABr is an insulating molecule and should therefore decrease the conductivity of the perovskite film. This

further explains the decreased luminance of our high PEABr LEDs. For a hybrid insulator/ semiconductor material it is logical that there will be an optimal ratio for high efficiency LEDs where a balance between electronic conductivity and high PLQY of the film on injecting contacts is obtained.

5.3.3 Device Stability

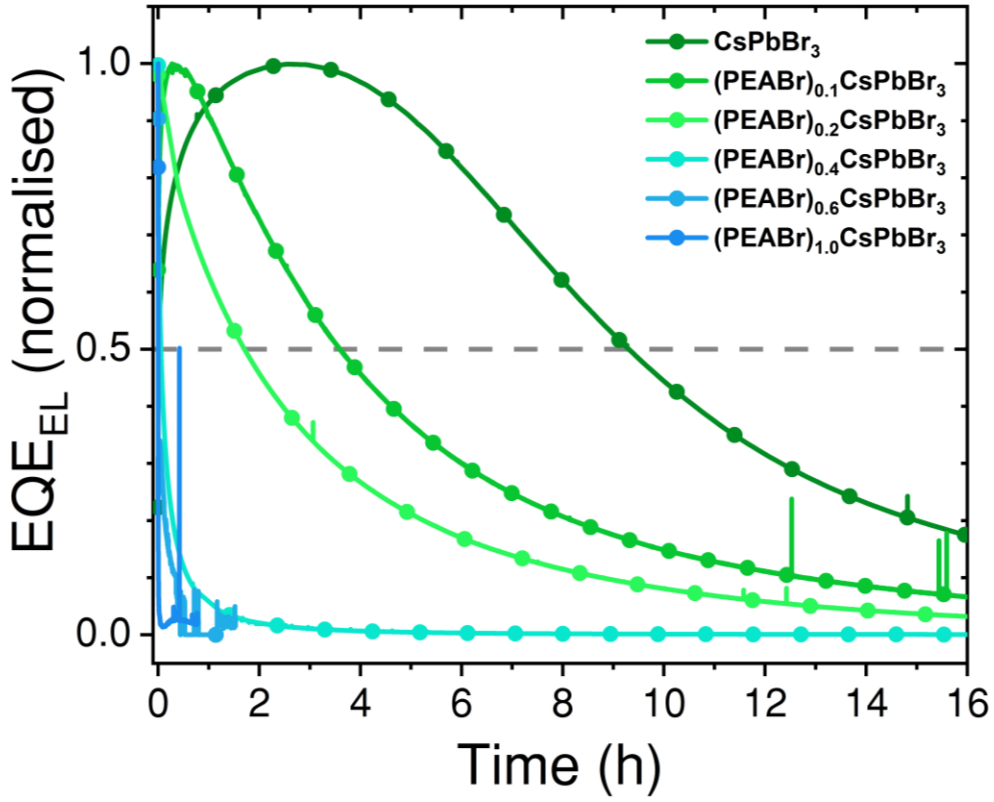


Figure 5.11 Normalised EQE_{EL} v Time data for perovskite LEDs operated at 10 mA cm^{-2} showing the remarkable drop off in stability with increasing PEABr content

Now we investigate the operational stability of our devices at a fixed current density of 10 mA cm^{-2}, the measurement is performed in a nitrogen filled glovebox to remove the effects of oxygen and water on stability. We present the EQE_{EL} vs time of this measurement on a normalised (Figure 5.11) and absolute scale (Figure 5.12). Further, we present the T_{50} in both tabulated (Table 5.3) and graphical form (Figure 5.13). Strikingly, we observe that as we increase the proportion of PEABr to $CsPbBr_3$ there is a strong negative correlation with stability. We determine that the T_{50} decreases from 9.3 hours for our $CsPbBr_3$ LED to only a few seconds for $(PEABr)_{0.6}CsPbBr_3$ and $(PEABr)_{1.0}CsPbBr_3$. Most concerning is that the T_{50} for our highly efficient LED is only 203 seconds which is more than 150 times shorter than our control device. Upon closer inspection of Figure 5.12 one can see that our efficient $(PEABr)_{0.4}CsPbBr_3$ sample

becomes less efficient that our control, in absolute terms after only 2.5 hours. This is highly concerning when considering PEABr as a strategy for highly efficient perovskite LEDs.

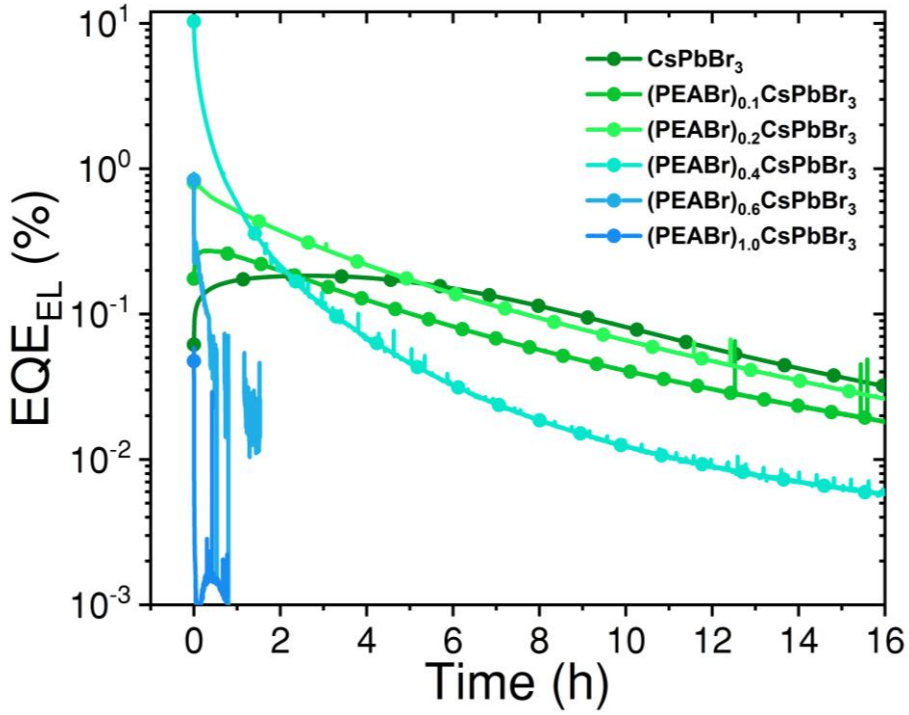


Figure 5.12 Absolute EQE_{EL} v Time data for perovskite LEDs operated at 10 mA cm^{-2} showing the remarkable drop off in stability with increasing PEABr content. Further our most efficient composition becomes worse than our control after only 2.5 hours

Having unveiled this remarkable trend, we conduct a literature review of the operational stability of $CsPbBr_3$ LEDs (Table 5.4) to see if there is consistency with our findings. We categorise the different LEDs by the strategies used to tailor the emitter material. These are, i) bulk polycrystalline $CsPbBr_3$ with modification through either small molecules, metal salts or polymers (i.e. cesium trifluoroacetate or poly ethylene oxide), ii) $CsPbBr_3$ with bulky ammonium cations such as PEABr and iii) colloidal nanocrystals of $CsPbBr_3$, which employ a range of ligands for passivation. It is not possible to make a decisive conclusion from this review as there are a variety of operational conditions and device structures, however we do see a general trend. This is that bulk $CsPbBr_3$ generally has a longer T_{50} than both colloidal nanocrystals and $CsPbBr_3$ with bulky ammonium cations. Further, we note that the best reported stabilities for $CsPbBr_3$ both fall into category i) where they achieve impressive T_{82} = 80 h and T_{50} = 250 h while maintaining a decent EQE_{EL} of 4.8% and 10.5% respectively. [8,9] The literature is therefore consistent

with our findings that ammonium cations are detrimental to the stability of $CsPbBr_3$ LEDs.

Perovskite Composition	**Max EQE_{EL} (%)**	**T_{50} @ 10 mA cm^{-2}**
$CsPbBr_3$	0.24	9.3 hours
$(PEABr)_{0.1}CsPbBr_3$	0.25	3.6 hours
$(PEABr)_{0.2}CsPbBr_3$	1.38	1.7 hours
$(PEABr)_{0.4}CsPbBr_3$	12.1	203 seconds
$(PEABr)_{0.6}CsPbBr_3$	1.68	3 seconds
$(PEABr)_{1.0}CsPbBr_3$	1.43	6 seconds

Table 5.3. Max EQE_{EL} achieved and T_{50} at 10 mA cm^{-2} for all $(PEABr)_xCsPbBr_3$ LEDs measured in this study.

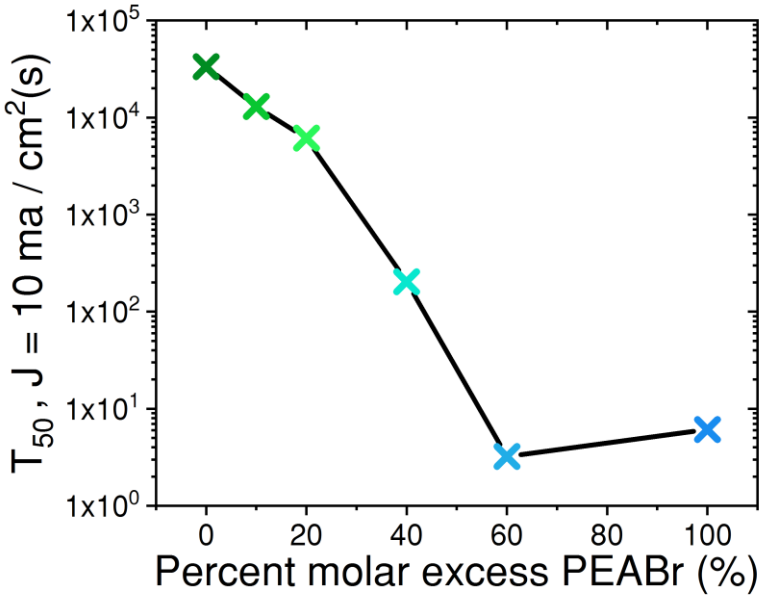


Figure 5.13. Graphical plot of T_{50} vs PEABr amount showing the strong decrease in stability when PEABr is added.

Emitter material	*Device structure*	*Max EQE_{EL}*	*Operational Stability*	*Operating conditions*
$CsPbBr_3$ from CsTFA[8]	ITO/PEDOT:PSS/Perov/TPBi/LiF/Al	10.50%	t50 > 250 h	L_0 = 100 cd m^{-2}
$CsPbBr_3$ (evaporated)[30]	ITO/PEDOT:PSS/Perov/TmPyPB/Liq/ Al	1.55%	t50 = 38 min	L_0 = 200 cd cm^{-2}
$CsPb_2Br_5$/ $CsPbBr_3$[31]	ITO/PEDOT:PSS/Perov/TPBi/LiF/Al	1.10%	t50 = ~6 hours	10 mA cm^{-2}
$CsPbBr_3$: LiBr[32]	ITO/NiOx/TFB/PVK/Perov/TPBi/LiF/ Al	16.2%	t50 = 21 hours	L_0 = 100 cd m^{-2}
$CsPbBr_3$: PEO[9]	ITO/PEDOT:PSS/Perov/TPBi/LiF/Al	4.76%	t82 = 80 h	L_0 = 1000 cd m^{-2}
$CsPbBr_3$[33]	ITO/BufHIL/Perov/TPBi/LiF/Al	1.37%	L50≈ 34 min	50 cd cm^{-2}
$CsPbBr_3$:CsBr[34]	ITO/PEDOT:PSS/MHP/ B3PYMPM/Cs2CO3 /Al	0.15%	L>L0 @ 15 h	66.67 mA cm^{-2}
$CsPbBr_3$:PEO[35]	ITO/NiOx/$CsPbBr_3$/TPBi/LiF/Al	2.94%	L>L_0 after 30 mins	3.1 V
$CsPbBr_3$:KBr[36]	ITO/p-TPD/PVK/Perov/TPBi/LiF/Al	7.7%	T_{50} = 3.5 hours	L_0 = 100 cd m^{-2}
BABr:$CsPbBr_3$[37]	ITO/PEDOT:PSS/PVK/Perov/TPBi/LiF /Al	10.10%	t75 = 45 mins	~26 mA cm^{-2}
NMABr:$CsPbBr_3$[38]	ITO/TFB/PVK/Perov/TPBi/LiF/Al	4.70%	t70 = 120s	0.2 mA cm^{-2}
PEABr:$CsPbBr_3$[11]	ITO/poly-TPD/PFN/MHP/ TPBi/LiF/Al	15.50%	t50 = 90 min	2 mA cm^{-2}
BABr:$CsPbBr_3$[39]	ITO/PEDOT:PSS/TFB/Perov/TPBi/Ca/ Al	8.42%	t50 = 45 mins	3.4 V
PEABr:$CsPbBr_3$[36]	ITO/p-TPD/PVK/Perov/TPBi/LiF/Al	16 %	T_{50}= 0.8 hours	L_0 = 100 cd m^{-2}
PEABr+NaBr:$CsPbBr_3$[40]	ITO/NiOx/PVK/Perov/TPBi/LiF/Al	12%	T_{50} = 40 mins	0.33 mA cm^{-2}
$CsPbBr_3$ NPs[41]	poly-TPD/PFI/Perov/TPBi/Li F/Al	0.06%	L50≈10 min	5 V
$CsPbBr_3$ NPs[42]	PEDOT:PSS/PTAA/MHP/TPBi/LiF/Al	16.5%	L50 =136 mins	0.6 mA cm^{-2}

Table 5.4 Literature review of Stability and efficiency of state of the art $CsPbBr_3$ perovskite LEDs. The results are in three categories: Blue = Bulk $CsPbBr_3$ with polymer or small molecule additives; Yellow = Alkylammonium additives with $CsPbBr_3$ spincoated together; Green = colloidal $CsPbBr_3$ nanocrystals which are coordinated with ammonium salts.

5.4 Investigation into mechanism of efficiency loss

We now turn our investigation to ascertaining why PEABr containing $CsPbBr_3$ LEDs have worse operational stability.

5.4.1 Thermal and photo- stability

We begin by investigating the thermal stability for our $(PEABr)_{0.4}CsPbBr_3$ LEDs. Previous reports of LEDs made with our $(PEABr)_{0.4}CsPbBr_3$ composition have demonstrated deterioration of the optoelectronic properties after annealing for times greater than 10 minutes.[43] Further, a recent report by Jiang *et al.* of high efficiency perovskite solar cells (>23% PCE) uses phenylethylammonium iodide as a surface treatment to achieve high open circuit voltage, which they show to be unstable at 85 °C.[44] We anneal the LED at 50 °C and check the EQE_{EL} of all pixels on the substrate periodically throughout an hour (box plot, Figure 5.14.a.). We choose this temperature since Zhao *et al.* measured the junction temperature of perovskite LEDs (which have a very similar emitter and device structure to ours) to be approximately 40 °C while in operation.[45] We see no decrease in the EQE_{EL} over the course of one hour, which rules out a solely thermal degradation process.

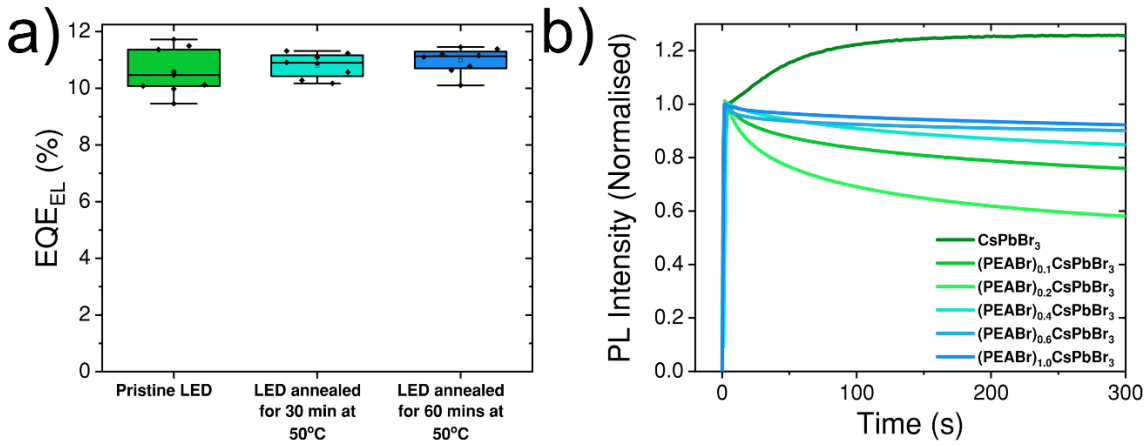


Figure 5.14. a) EQE_{EL} statistics for all 8 pixels on one $(PEABr)_{0.4}CsPbBr_3$ substrate after annealing for different periods of time at 50 °C; b) Photostability as a function of composition at an irradiance of 93 mW/ cm^2 ; λ_{exc} = 405 nm. All samples were encapsulated to remove the effects of atmosphere on the measurement.

We continue by assessing the photostability of our series of films on glass (Figure 5.14.b). We measure the integrated emission of our films over the course of 300 s at a constant irradiance of 93 mW cm^{-2} (λ_{exc} = 405 nm). We find that i) all of the films have higher photostability than the operational stability of our $(PEABr)_{0.4}CsPbBr_3$ LED, and, ii) the

trend in photostability does not closely follow the trend operational stability; the $(PEABr)_{0.2}CsPbBr_3$ sample has the lowest photostability.

5.4.2 Changes in structural and electronic properties

Now, we turn our attention to characterising $CsPbBr_3$ and $(PEABr)_{0.4}CsPbBr_3$ LEDs before and after operation to unveil the driving forces in efficiency loss. We fabricate devices with a 1 cm^2 (device in operation Figure 5.15) active area to maximise signal and operate them at 20 mA/cm^2 for 1 hour to incur significant degradation.

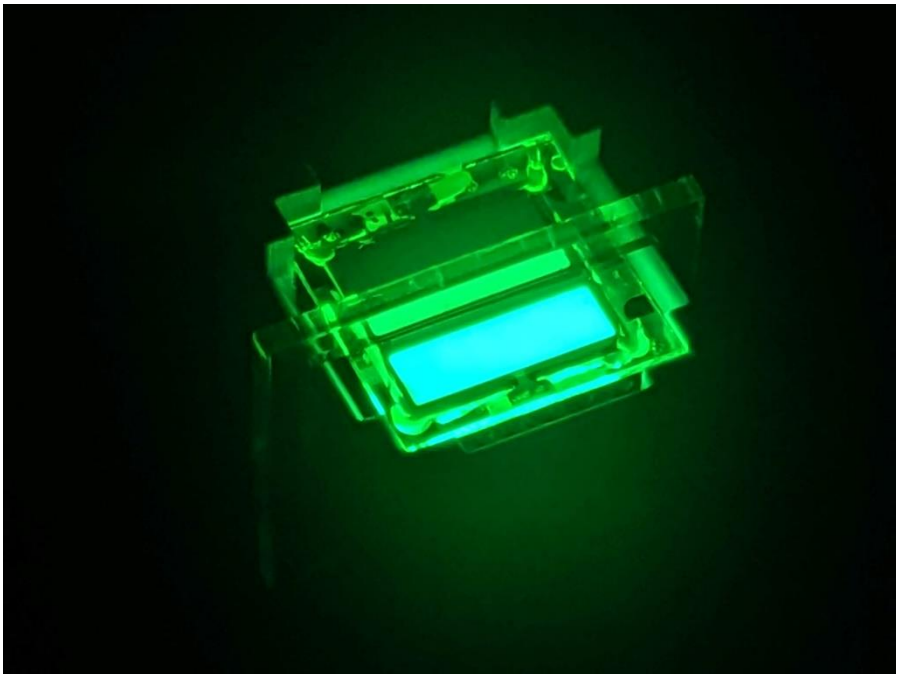


Figure 5.15. A 1 cm^2 $(PEABr)_{0.4}CsPbBr_3$ LED in operation such as those used for structural degradation studies.

5.4.2.1 UV-Vis and PL

We begin by characterising the UV-Vis absorption (Figure 5.16.a). Perhaps surprisingly, we see no significant changes in either the UV-Vis for our $(PEABr)_{0.4}CsPbBr_3$ LED despite orders of magnitude drop in the EQE_{EL}. We see the same lack of change or our $CsPbBr_3$ LED which is less surprising as the EQE_{EL} has not degraded significantly at this point. Further we measure the PL of our $(PEABr)_{0.4}CsPbBr_3$ LEDs and find that there are no changes in the spectra after operation (Figure 5.16.b).

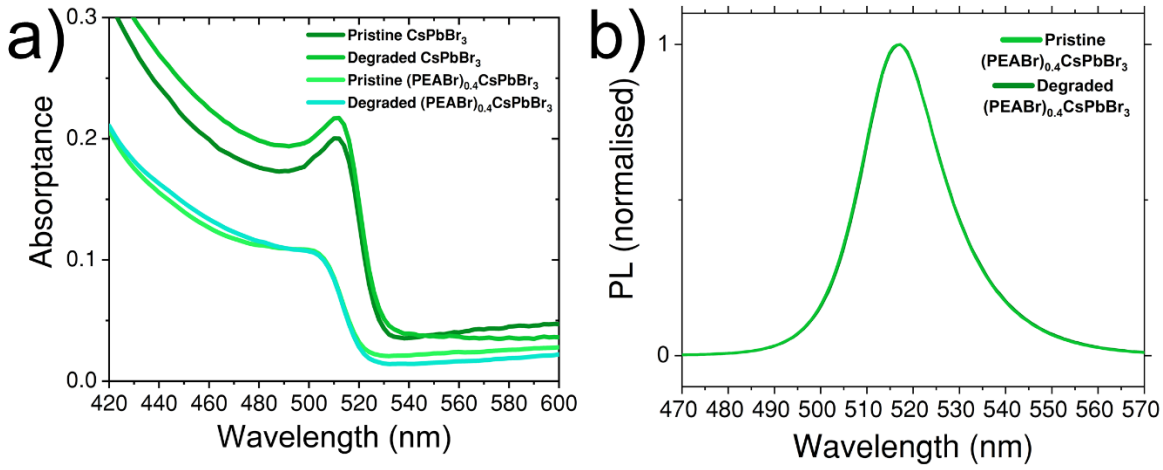


Figure 5.16. a) UV-Visible absorptance data for pristine and degraded LEDs, typically two 1 cm^2 electrodes were evaporated on a substrate, one was electrically degraded and both the electrodes were delaminated for further characterisation; b) PL spectra for a pristine and degraded (PEABr)$_{0.4}$CsPbBr$_3$ LED. The degraded samples in this figure were operated for 1 h at 10 mA/cm^2.

We continue by assessing the absorption and PL of samples with higher PEABr content. We present the PL of a (PEABr)$_{1.0}$CsPbBr$_3$ device (Figure 5.17.a) and the UV-Vis of a (PEABr)$_{0.9}$CsPbBr$_3$ device (Figure 5.17.b). In the PL we see a slight redshift in the maximum once the device has degraded, this is in agreement with the UV-Vis where we also see a slight redshift.

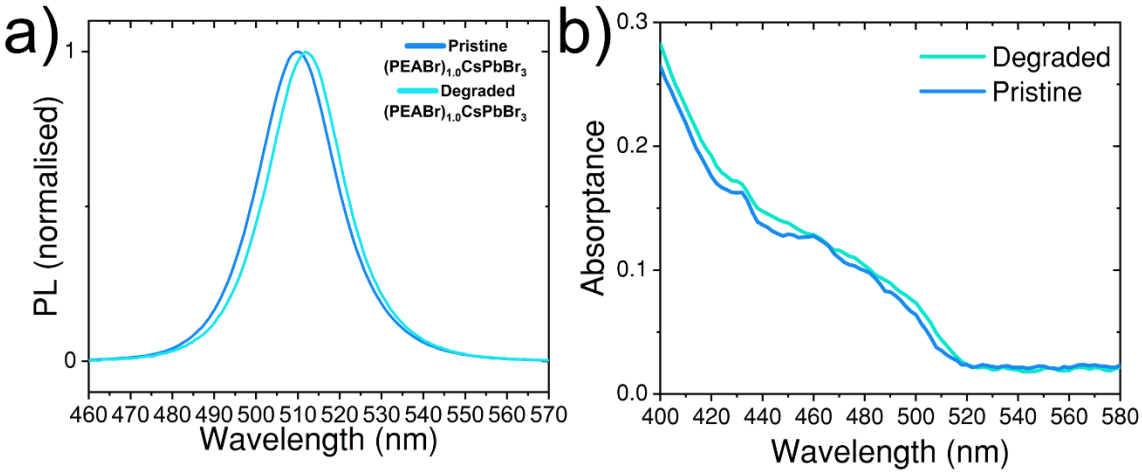


Figure 5.17. a) PL of (PEABr)$_{1.0}$CsPbBr$_3$ LED before and after operation for 1 h at 10 mA/cm^2; b) UV-Vis data of (PEAr)$_{0.9}$CsPbBr$_3$ LED before and after operation for 1 h at 10 mA/cm^2.

These two observations are consistent with a reduction in confinement of the charge carriers. This reduction in confinement should be the result an increase in the size of the emissive domains in the film i.e. an increase in the grain size. We propose that the increase

in grain size is due to phenylethylammonium decomposing in our high PEA samples via the reaction:

$$R\text{-}NH_3^+X^- \rightarrow R\text{-}NH_3 + HX$$

Equation 1.1: Proposed decomposition pathway for PEABr where R = C_6H_5-CH_2-CH_2 and X = Br^- which is analogous to the well know decomposition reaction of methylammonium iodide where R = CH_3 and X = I^-

Where R = C_6H_5-CH_2-CH_2 and X = Br^-. The proposed decomposition pathway is analogous to the decomposition of methylammonium iodide ((R = CH_3 and X = I^-) which is well known in the field of perovskite photovoltaics. It has been shown to occur under environmental stresses such as oxygen, humidity and elevated temperature.[46]

Indeed, Prakasam *et al.* recently investigated the degradation of methylammonium lead bromide perovskite LEDs, and report the formation of $PbBr_2$ under operation, and show compelling evidence for the formation of methylamine, consistent with methylammonium deprotonating under electrical injection.[15] Watanabe et al. studied the degradation of $PEA_2FA_2Pb_3Br_{10}$ and showed degradation of their 2D phases into 3D $FAPbBr_3$.[16] They do not provide a mechanism but we postulate that they are also observing the decomposition of phenylethylammonium into phenylethylamine. Further, Fang *et al.* showed the photodecomposition of the layered perovskite PEA_2PbI_4 into PEA, HI and PbI_2 which indicates that these materials may not be stable when full of charge under electrical bias. [47]

5.4.2.2 Fourier transform photocurrent spectroscopy

Considering that we observed changes in the UV-Vis for $(PEABr)_{0.9}CsPbBr_3$ we turn our attention to characterising the Fourier transform photocurrent spectra (FTPS) for our $(PEABr)_{0.4}CsPbBr_3$ LEDs before and after various stages of operation (Figure 5.18). FTPS affords orders of magnitude in increased sensitivity which would allow us to detect small red-shifted minority phases or sub bandgap states which could contribute to photocurrent. However we don't see any significant changes in the shape FTPS spectra even after 1 h of operation. It is interesting to note that although there are no changes in the shape of the spectra, there is a decrease in the collected photocurrent once the LED has been operated for times greater than 10 minutes. This is an indication that changes occurring in the device which reduce the carrier collection efficiency, potentially at the interfaces of the perovskite and carrier selective contacts

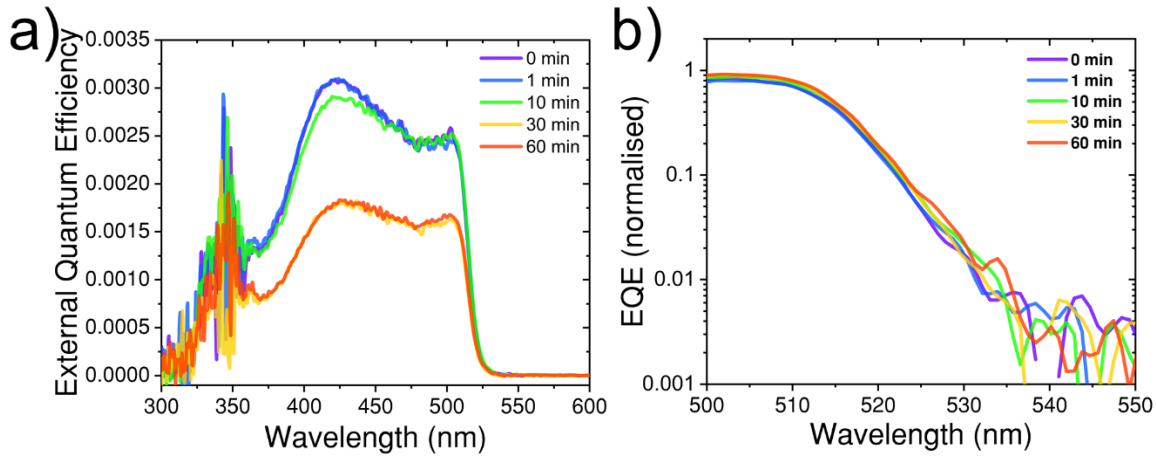


Figure 5.18. a) FTPS spectra for $(PEABr)_{0.4}CsPbBr_3$ LED after operation at 10 mA/cm^2 for various amounts of time; b) The same spectra presented on a normalised scale, showing no significant changes in the low energy tail.

5.4.2.3 XRD and XPS

We characterise our $CsPbBr_3$ and $(PEABr)_{0.4}CsPbBr_3$ LEDs before and after operation with X-ray photoelectron spectroscopy and find there are no significant changes in the Pb 4*f*, Al *2p* or Br 3*d* core level spectra. This rules out the formation of Pb(0) at the surface which is a known defect in lead halide perovskites.[48] We present the overlaid spectra in Figure 5.19.

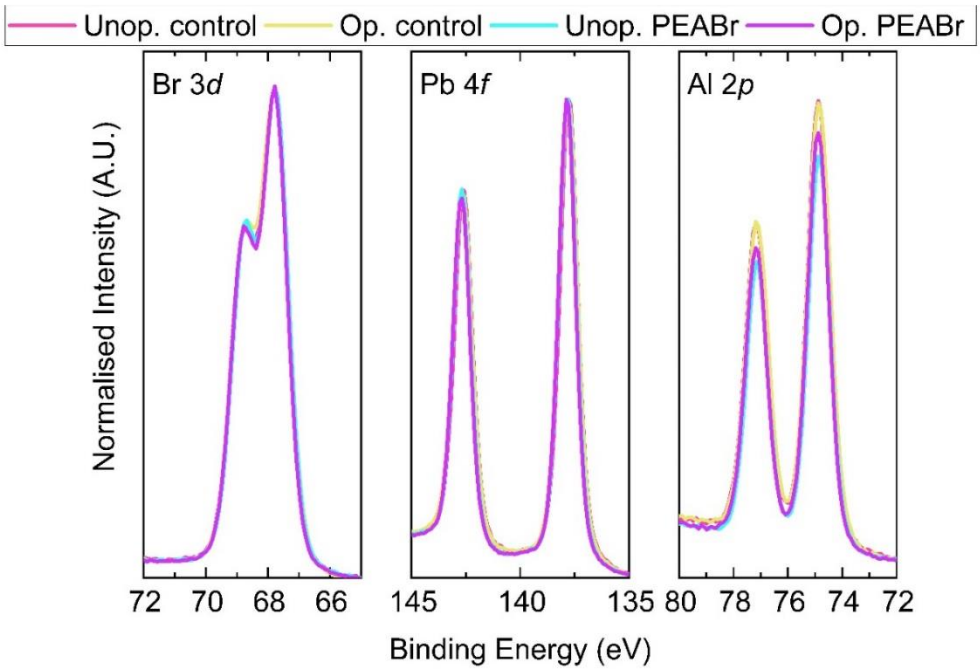


Figure 5.19. Overlapped high resolution XPS spectra of Pb 4f, Br 3d and Al 2p for unoperated (unop.) and operated (op.) LED devices. PEABr concentration in the relevant devices is 40% molar excess. The figure shows shows no significant shift in peak positions between control and PEABr devices and those which have been operated vs. unoperated.

We now measure the XRD for the same samples to assess any potential structural changes that may have occurred during operation. We do not observe any significant changes in the indicating that no structural changes have occurred during operation. This is in agreement with the UV-Vis, PL and XPS characterisation for these samples where we also didn't observe any significant changes

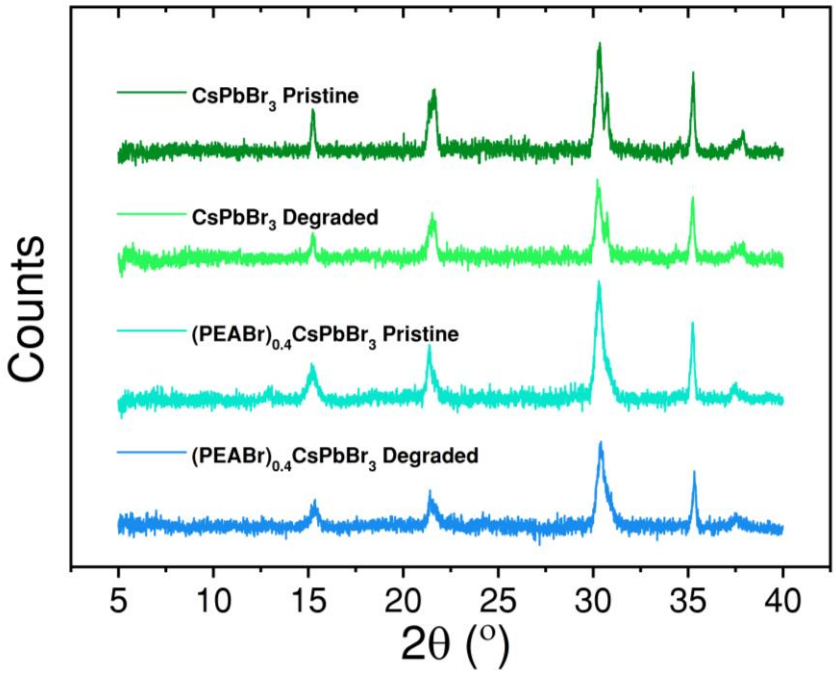


Figure 5.20. XRD data for pristine and degraded LEDs, typically 2 x 1 cm^2 electrodes were evaporated on a substrate, one was electrically degraded and both the electrodes were delaminated for further characterization.

5.4.2.4 Morphology

We now consider whether changes in morphology are occurring during operation, which may influence the loss in EQE_{EL}. We operate the LEDs for 1 hour at 20 mA cm^{-2}, delaminate the Al electrode and then wash off the TPBi top contact with chlorobenzene to reveal the perovskite film below. We also prepare pristine LEDs which have gone through the same delamination and washing procedure for fair comparison. These samples are then characterised and compared with scanning electron microscopy (SEM) (Figure 5.21). We do not see any obvious changes in the morphology of the perovskite films which motivates us to look further for potential sources of degradation.

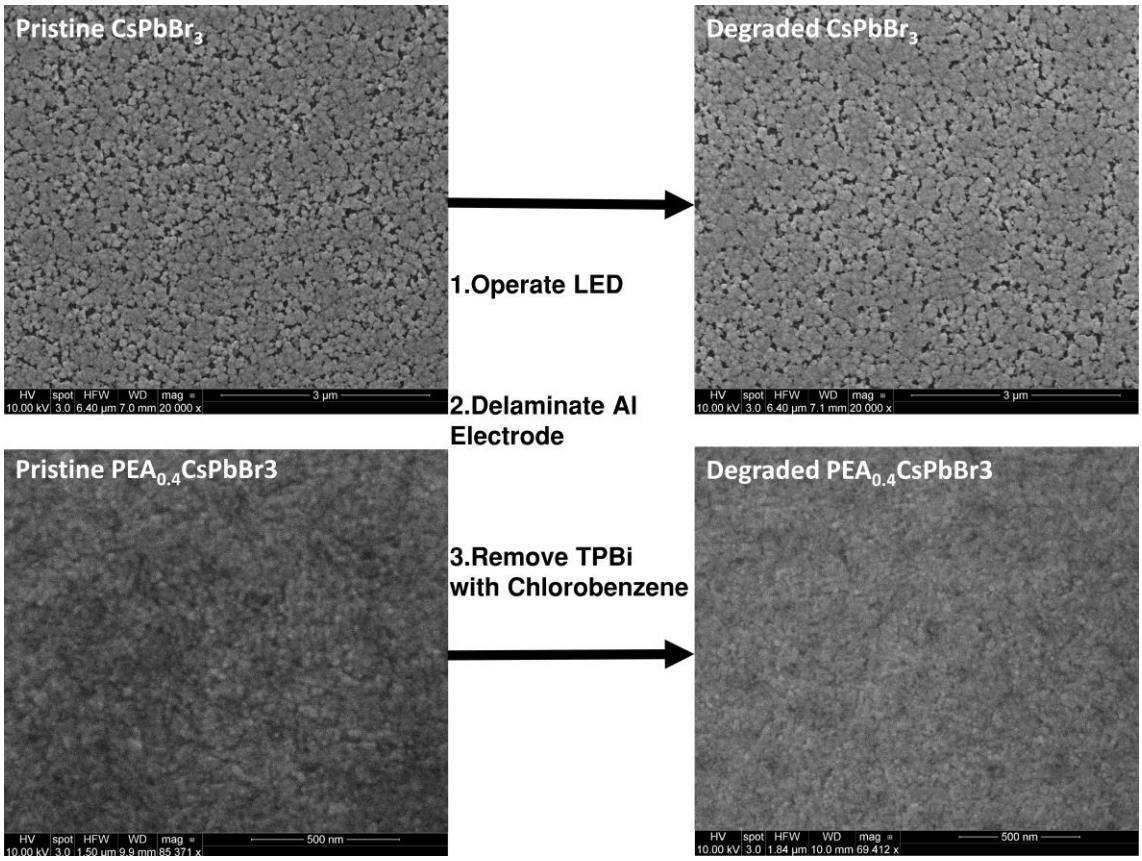


Figure 5.21. SEM characterisation of our control films and our most efficient composition $(PEABr)_{0.4}CsPbBr_3$ before and after operation. The samples were operated and then the Al electrode was delaminated and the TPBi electron injection layer was washed off with chlorobenzene

5.4.2.5 Electroluminescence spectra

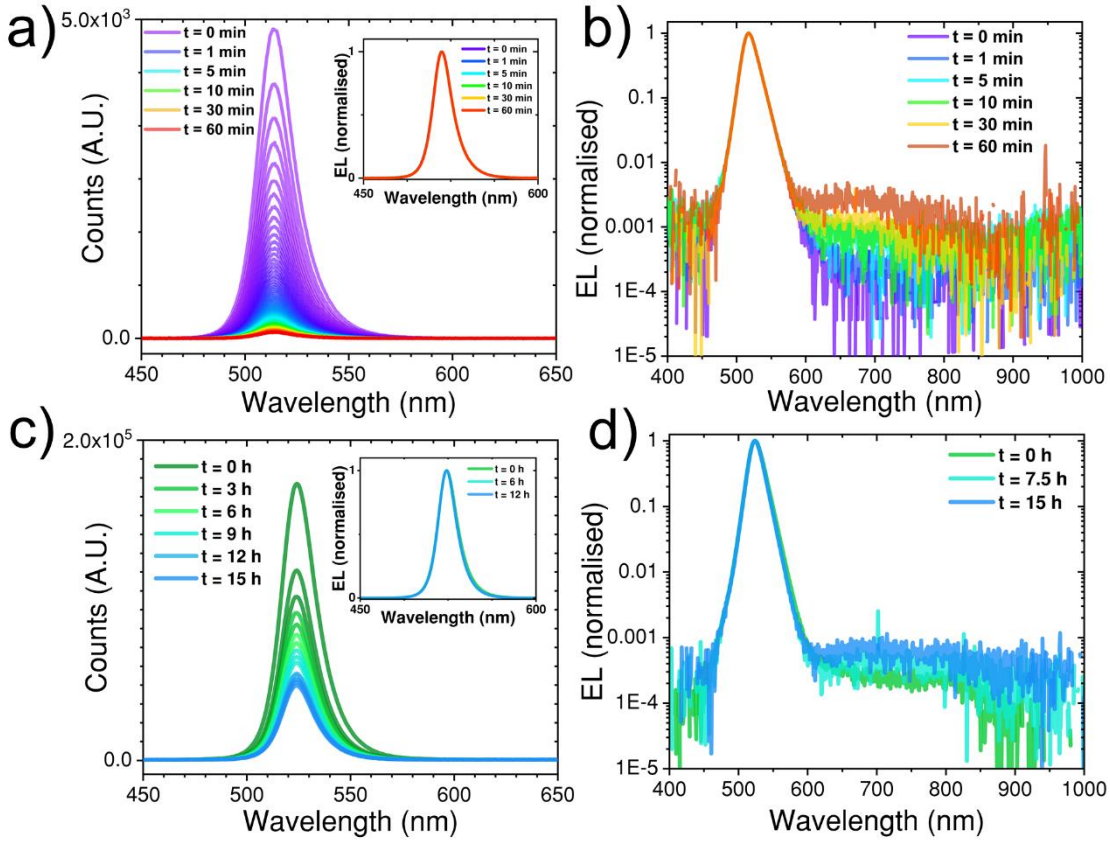


Figure 5.22 a) Decay of intensity of EL for $(PEABr)_{0.4}CsPbBr_3$ LEDs operated at 20 mA/cm^2 on an absolute scale (inset: The same data on a normalised scale); b) Normalised EL spectra of $(PEABr)_{0.4}CsPbBr_3$ LEDs operated at 20 mA/cm^2 on a log scale showing the growth of a broad shoulder in the emission; c) Decay of intensity of EL $CsPbBr_3$ LEDs operated at 20 mA/cm^{2}on an absolute scale (inset: The same data on a normalised scale), note the remarkably superior stability compared with $(PEABr)_{0.4}CsPbBr_3$; b) Normalised EL spectra of $CsPbBr_3$ LEDs operated at 20 mA/cm^2 on a log scale showing the growth of a broad shoulder in the emission, note that the shoulder is present in the pristine device whereas it is not in $(PEABr)_{0.4}CsPbBr_3$.

Looking further for an indication of decomposition we closely inspect the spectral features of the electroluminescence (EL) of $(PEABr)_{0.4}CsPbBr_3$ LEDs over the course of degradation. Figure 5.22.a shows the decrease of EL intensity over the course of the measurement with the normalised spectra shown in the inset. First, it appears that there was no significant change in the spectrum. However, when shown on a log scale, we find a broad shoulder spanning from 600-900 nm growing relative to the 520 nm emission over the course of time (Figure 5.22.b). Intrigued by the presence of this shoulder we look at the same region for $CsPbBr_3$ LEDs (Figure 5.22.d), and observe that even the pristine LED has a broad shoulder between 600-900 nm. Interestingly, this shoulder grows at a much slower rate than in the $(PEABr)_{0.4}CsPbBr_3$ LEDs, which correlates with our

observations for stability. This type of broad emission in $CsPbBr_3$ was first reported by Motti *et al.* under PL excitation in vacuum which they attributed to photo-emissive trap states.[49] As far as we are aware this is the first report of such emissive trap states in EL, and may provide a compelling signature of the degradation of our films.

A recent report by Park *et al.* reported a broad shoulder in the PL of the layered perovskite $(C_4H_9NH_3)_2PbBr_4$ upon its degradation in the same region we observe.[50] Through the use of IR nanoscopy, they show that this is correlated with photogenerated A-site vacancies which occur via decomposition of butylammonium into butylamine and HBr. Considering this, we believe the growth of the shoulder in our emission is consistent with the hypothesis that phenylethylammonium is converting into phenylethylamine under electrical operation. As we see no evidence of 2D structures in our characterisation of $PEABr_{0.4}CsPbBr_3$ we believe that phenylethylammonium is occupying A-sites on the surface of nanocrystalline domains of $CsPbBr_3$. Once phenylethylammonium has decomposed and lost its positive charge it no longer tightly binds to the A-site of the perovskite lattice which generates an A-site vacancy. We hypothesise that this vacancy is a highly detrimental defect for efficient radiative recombination. It is further ratification that this defect is detrimental as $CsPbBr_3$ has a similar broad shoulder in its EL spectrum in its pristine state and is poorly emissive.

5.4.2.6 Changes in Current Voltage Characteristics

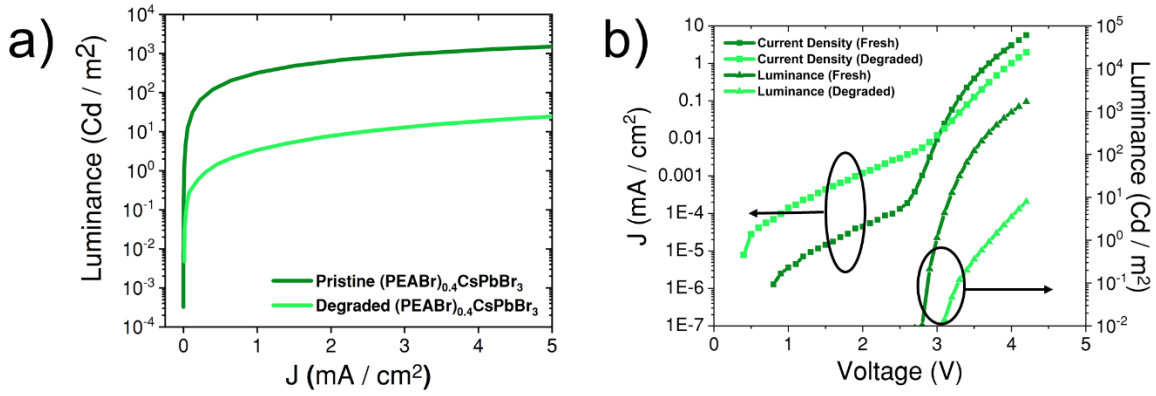


Figure 5.23. a) J v L of pristine and degraded $(PEABr)_{0.4}CsPbBr_3$ LED after 1 h of operation at 10 mA cm^{-2}; b) changes in J-V-L characteristics before and after 1 h of operation at 10 mA cm^{-2} .

We continue our investigation by probing the electrical characteristics of our $(PEABr)_{0.4}CsPbBr_3$ LED before and after significant amounts of degradation (1 h operation at 10 mA cm^{-2}). We find that for a given current density the luminance is approximately 2 orders of magnitude lower for the degraded device (Figure 5.23.a). We

observe that there is an increase in current density at low bias (Figure 5.23.b), indicating either i) a reduction in the shunt resistance (leakage current), ii) an increase in the background carrier density in the perovskite films, or, iii) doping of the injection layers. However, when we reach the turn on voltage for the LED (~2.5 V) less current is flowing through the device. The increased resistance under operating conditions could result from either a reduction in charge carrier mobility in the perovskite emitter layer or in the charge injection layers, or an increased barrier to charge injection at one or both of the contacts. This change to the resistance and current flow through the LED is likely to have a negative impact on efficiency. If the charge injection is primarily limited for one carrier type (electron or holes), then there may exist a unipolar current of the opposite carrier type, where the charges then drift right through the device and back into the external circuit.[51] A significant charge injection barrier can also lead to the opposite carrier accumulation at that interface, leading to increased non-radiative recombination in the electrodes, transport materials or at this interface.

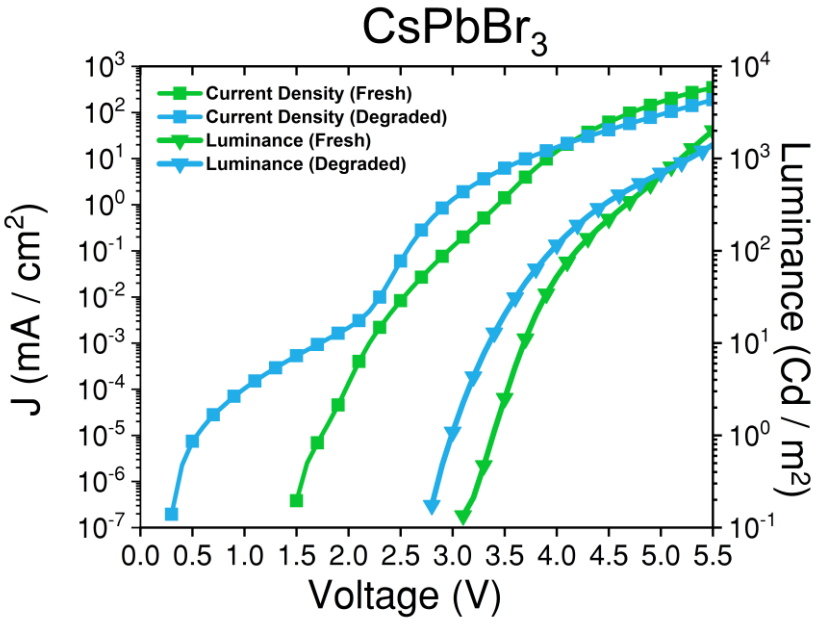


Figure 5.24. Changes in J-V-L characteristics of $CsPbBr_3$ LED before and after 1 h of operation at 10 mA cm^{-2}.

Intrigued by this discovery we characterise the pristine and operated (1 h, 10 ma cm^{-2}) JV curves for our control $CsPbBr_3$ LED (Figure 5.24) and also observe significant changes. We find that there is i) an increase in current density at low bias, ii) the evolution of a kink in the JV curve and iii) the formation of a barrier to injection at higher biases. We do not observe a significant decrease in luminance and it in fact increases at some biases. Figure 5.11 shows that after 1 hour the EQE_{EL} of the $CsPbBr_3$ LED is still increasing so

the observed changes in JV are actually beneficial to the performance of this device. We posit that similar degradation mechanisms are occurring in $CsPbBr_3$ LEDs but at different rates.

5.4.2.7 Photoluminescent quantum efficiency of the device

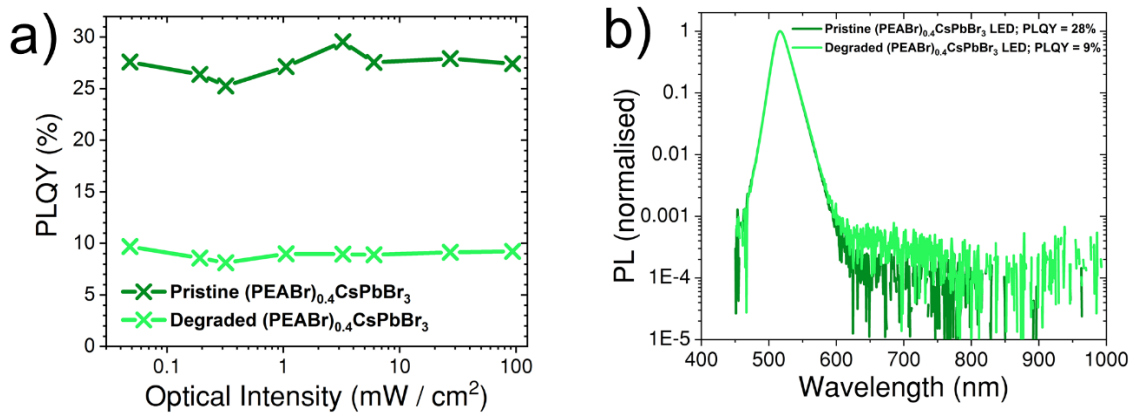


Figure 5.25. a) Intensity dependence of PLQY of full LED before and after operation for 1 h at 10 mA cm^{-2} ; b) changes in the PL spectrum of $(PEABr)_{0.4}CsPbBr_3$ LED after operation for 1 hour at 10 mA cm^{-2}

Next we measure the PLQY of our full device stack for the same $(PEABr)_{0.4}CsPbBr_3$ LED for which we have just presented the JVL data, before and after operation. We find that the PLQY decreases from ~28% down to ~9% across a wide range of optical excitation intensities (Figure 5.25.a.). In addition to the decrease in PLQY, we also observe the previously mentioned tail in the emission of degraded $(PEABr)_{0.4}CsPbBr_3$ (Fig. 4 d). Interestingly, the PLQY of the degraded devices is much higher than the degraded EQE_{EL} and experiences much less of a relative decrease, only dropping to ~30% of its initial value whereas the EQE_{EL} is ~1.5% of its initial value. It therefore appears that although a certain fraction of the degradation in EQE_{EL} is originating from trap site generation in the perovskite emission layer, the majority of the degradation is arising from an electronic consequence of the increased resistance under driving voltages.

We also note that even before degradation, the PLQY of the complete device (metal electrodes included) is much higher than the EQE_{EL} that we determine. This shows that there are electronic losses under operation which are not present under light illumination. This indicates that the charge injection layers are not perfect charge blocking when an electric field is applied, or that there is an imbalance in the charge injection rate for electrons and holes, and clearly indicates significant scope for improvement of the LEDs. Further, we note that the PLQY does not vary with optical excitation intensity even for the degraded LED we present. If we are creating traps in the bulk of the emission layer in

the degraded devices, we would expect lower PLQY at low excitation intensities, due to trap filling with increasing excitation intensity. Since we do not observe this, we postulate that the non-radiative recombination is happening mostly at the interfaces.

5.5 Discussion and Conclusions

In this work we show that the addition of PEABr to $CsPbBr_3$ perovskite LEDs significantly decreases the operational stability. The T_{50} = 9 h for $CsPbBr_3$, which we report is over 2 orders of magnitude longer than our high-efficiency $(PEABr)_{0.4}CsPbBr_3$ LEDs. However, we do not find any significant changes to the electronic or crystal structure of the material after degradation. We do observe that the PLQY of our optimized device decreases from ~28% to ~9% after 1 h of operation at 10 mA cm^{-2} (32% its initial value), but this does not fully explain the drop in EQE , which drops from 10.3% to 0.16% during this time (1.5% its initial value). Additionally, we observe significant changes in the J−V characteristics of the device over this time. Namely, we observe an increase in current density below the LED turn-on voltage and a reduction in the current density, hence an increase in resistance, above the turn-on voltage.

It is apparent that the primary cause for the rapid degradation are changes to the electronic operating characteristics of the devices, rather than changes to the emission efficiency of the emitter layer. Metal halide perovskites are known to contain mobile ions, which can have significant effects on the electronic characteristics of devices.[52,53] We postulate that the changes we observe are a result of an alteration of the charge injection contacts as a consequence of mobile ions migrating from the perovskite emitting layer into the charge injection layers, or accumulating at one of the interfaces in the device. Due to the direction of the electric field under operation, we would expect diffusive cations to be driven into the *n*-type charge injection interface and layer (cathode), and anions to be driven into the *p*-type charge injection layer and interfaces (anode). Depending upon the precise nature of the ions, this accumulation of ions could result in increased *n*- or *p*-doping of the respective injection layers, in an analogous fashion to a light emitting electrochemical cell.[54] Further, a significant shift in the energetic alignment could occur at these interfaces due to dipole layer formation or the accumulation of a solid-state ionic double layer. Both these processes could significantly influence the charge injection and recombination at these interfaces.

The clear trend of decreasing operational stability with increasing concentration of PEABr, points towards it being a likely source of these mobile ions. As we previously highlighted (Equation 1.1), there is evidence in the literature for generation of HBr in operating devices via decomposition of alkylammonium halides. We postulate that the H^+ and Br^- ions formed are the previously mentioned mobile ions. $CsPbBr_3$ does not contain any alkylammonium cations so cannot undergo the same decomposition pathway, which can explain the relative increase in stability. However, it does contain mobile ions (mainly interstitials and vacancies)[53] which may still play a role on the long term stability. Analysis of changes in ion distributions before and after operation of perovskite LEDs should be critical in further elucidating degradation processes and identifying means to circumvent such degradation. There is evidence in the literature of ion migration through the device; a recent analysis on degraded $FAPbI_3$ LEDs through time-of flight- secondary ion mass spectrometry shows accumulation of $^{I-}$ at the polymeric p-type (TFB, Poly(9,9-dioctylfluorene-altN-sec-butylphenyl)-diphenylamine)/Au interface.[55]

The finding that the JV characteristics of our more stable $CsPbBr_3$ LED also change over the course of 1 hour indicates that the degradation mechanism of all of our LEDs may be linked. We posit that the rate of their degradation (in term of JV characteristics) is governed by mobile ions and the rate at which they can move through the LED stack.

In light of the degradation that we have unveiled, we believe that the effect of phenylethylammonium on morphology could also be detrimental to stability. We have shown that phenylethylammonium greatly decreases grain size, as evidenced by i) SEM, ii) increased Scherrer broadening in XRD, and, iii) blueshift in the UV-Vis, PL and EL, which greatly increases the surface area to volume ratio in our films. As ion transport is known to happen more rapidly at grain boundaries,[56] it is logical that larger grains of $CsPbBr_3$ will yield more stable LEDs. This is ratified by a report by Wu et. al where they grow micron sized grains of polyethylene oxide passivated $CsPbBr_3$ and achieve an excellent T_{80}= 80 hours at 1000 cd/m^2 which is the best reported $CsPbBr_3$ LED stability we are aware of.[9]

The decreased PLQY in the devices indicated enhanced non-radiative recombination. This could be explained by i) the decomposition of PEABr reducing chemical passivation in the film, ii) doping of the contact layers by mobile ions increasing interfacial non-radiative recombination, or iii) the formation of other unidentified traps during operation. We wish to stress that it is not clear from our characterisation which one of these contributes to the loss in PLQY, therefore we believe that further research is required to determine if this loss can be prevented in these hybrid materials.

We consider that the capability of perovskite LEDs has been well demonstrated by the field and now stability should be more critically assessed. In light of our findings we propose that future research into the stability of perovskite LEDs should focus on i) the development of new charge injection layers and device architectures which are impervious to the diffusion of mobile ions, and ii) the development of perovskite materials which have less diffusive ions while maintaining high luminescence efficiency.

5.6 References

1. Tan, Z.-K. *et al.* Bright light-emitting diodes based on organometal halide perovskite. *Nat. Nanotechnol.* **9,** 687–692 (2014).
2. Cao, Y. *et al.* Perovskite light-emitting diodes based on spontaneously formed submicrometre-scale structures. *Nature* **562,** 249–253 (2018).
3. Lin, K. *et al.* Perovskite light-emitting diodes with external quantum efficiency exceeding 20 per cent. *Nature* **562,** 245–248 (2018).
4. Zhao, B. *et al.* High-efficiency perovskite–polymer bulk heterostructure light-emitting diodes. *Nat. Photonics* **12,** 783–789 (2018).
5. Xu, W. *et al.* Rational molecular passivation for high-performance perovskite light-emitting diodes. *Nat. Photonics* (2019). doi:10.1038/s41566-019-0390-x
6. Liu, Y. *et al.* Efficient blue light-emitting diodes based on quantum-confined bromide perovskite nanostructures. *Nat. Photonics* **13,** 760–764 (2019).
7. Gangishetty, M. K., Hou, S., Quan, Q. & Congreve, D. N. Reducing Architecture Limitations for Efficient Blue Perovskite Light-Emitting Diodes. *Adv. Mater.* 1706226 (2018). doi:10.1002/adma.201706226
8. Wang, H. *et al.* Trifluoroacetate induced small-grained CsPbBr3 perovskite films result in efficient and stable light-emitting devices. *Nat. Commun.* **10,** 665 (2019).
9. Wu, C. *et al.* Improved Performance and Stability of All-Inorganic Perovskite Light-Emitting Diodes by Antisolvent Vapor Treatment. *Adv. Funct. Mater.* **27,** 1–7 (2017).
10. Quan, L. N. *et al.* Tailoring the energy landscape in quasi-2D halide perovskites enables efficient green light emission. *Nano Lett.* acs.nanolett.7b00976 (2017). doi:10.1021/acs.nanolett.7b00976
11. Ban, M. *et al.* Solution-processed perovskite light emitting diodes with efficiency exceeding 15% through additive-controlled nanostructure tailoring. *Nat. Commun.* **9,** 3892 (2018).

12. Xiao, Z. *et al.* Efficient perovskite light-emitting diodes featuring nanometre-sized crystallites. *Nat. Photonics* **11,** 108–115 (2017).
13. Yang, X. *et al.* Efficient green light-emitting diodes based on quasi-two-dimensional composition and phase engineered perovskite with surface passivation. *Nat. Commun.* **9,** 570 (2018).
14. Xing, G. *et al.* Transcending the slow bimolecular recombination in lead-halide perovskites for electroluminescence. *Nat. Commun.* **8,** 14558 (2017).
15. Prakasam, V., Tordera, D., Bolink, H. J. & Gelinck, G. Degradation Mechanisms in Organic Lead Halide Perovskite Light-Emitting Diodes. *Adv. Opt. Mater.* **7,** 1900902 (2019).
16. Watanabe, S. *et al.* Excited-state stability of quasi-two-dimensional metal halide perovskite films under optical and electrical excitations. *Appl. Phys. Lett.* **115,** 233502 (2019).
17. Goff, C. M., Matchette, M. A., Shabestary, N. & Khazaeli, S. Complexation of caesium and rubidium cations with crown ethers in N,N-dimethylformamide. *Polyhedron* **15,** 3897–3903 (1996).
18. Rüdiger, V., Schneider, H.-J., Solov'ev, V. P., Kazachenko, V. P. & Raevsky, O. A. Crown Ether–Ammonium Complexes: Binding Mechanisms and Solvent Effects. *European J. Org. Chem.* **1999,** 1847–1856 (1999).
19. Hancock, R. D. & Martell, A. E. The Chelate, Cryptate and Macrocyclic Effects. *Comments Inorg. Chem.* **6,** 237–284 (1988).
20. Protesescu, L. *et al.* Nanocrystals of Cesium Lead Halide Perovskites ($CsPbX_3$, X = Cl, Br, and I): Novel Optoelectronic Materials Showing Bright Emission with Wide Color Gamut. *Nano Lett.* **15,** 3692–3696 (2015).
21. Nayak, P. K. *et al.* Impact of Bi^{3+} Heterovalent Doping in Organic-Inorganic Metal Halide Perovskite Crystals. *J. Am. Chem. Soc.* **140,** 574–577 (2018).
22. Spanopoulos, I. *et al.* Uniaxial Expansion of the 2D Ruddlesden−Popper Perovskite Family for Improved Environmental Stability. (2019). doi:10.1021/jacs.9b01327
23. Braly, I. L. *et al.* Hybrid perovskite films approaching the radiative limit with over 90% photoluminescence quantum efficiency. *Nat. Photonics* **12,** 355–361 (2018).
24. Cho, C. *et al.* The role of photon recycling in perovskite light-emitting diodes. *Nat. Commun.* **11,** 611 (2020).
25. Richter, J. M. *et al.* Enhancing photoluminescence yields in lead halide perovskites by photon recycling and light out-coupling. *Nat. Commun.* **7,** 13941 (2016).

26. Shi, X.-B. *et al.* Optical Energy Losses in Organic-Inorganic Hybrid Perovskite Light-Emitting Diodes. *Adv. Opt. Mater.* **6,** 1800667 (2018).
27. Anthopoulos, T. D. *et al.* Highly efficient single-layer dendrimer light-emitting diodes with balanced charge transport. *Appl. Phys. Lett.* **82,** 4824–4826 (2003).
28. Chen, H. *et al.* Blue organic light-emitting diode based on 1,2,3,4,5-pentaphenyl-1(8- phenyl-1,7-octadiynyl)silole. *IEEE J. Sel. Top. Quantum Electron.* **10,** 10–15 (2004).
29. Zhao, L. *et al.* Electrical Stress Influences the Efficiency of CH3NH3PbI3 Perovskite Light Emitting Devices. *Adv. Mater.* **29,** 1605317 (2017).
30. Hu, Y. *et al.* Vacuum-evaporated all-inorganic cesium lead bromine perovskites for high-performance light-emitting diodes. *J. Mater. Chem. C* **5,** 8144–8149 (2017).
31. Qin, C., Matsushima, T., Sandanayaka, A. S. D., Tsuchiya, Y. & Adachi, C. Centrifugal-Coated Quasi-Two-Dimensional Perovskite $CsPb_2Br_5$ Films for Efficient and Stable Light-Emitting Diodes. *J. Phys. Chem. Lett.* **8,** 5415–5421 (2017).
32. Wu, T. *et al.* High-Performance Perovskite Light-Emitting Diode with Enhanced Operational Stability Using Lithium Halide Passivation. *Angew. Chemie Int. Ed.* (2020). doi:10.1002/anie.201914000
33. Cho, H. *et al.* High-Efficiency Solution-Processed Inorganic Metal Halide Perovskite Light-Emitting Diodes. *Adv. Mater.* **29,** 1700579 (2017).
34. Wei, Z. *et al.* Solution-processed highly bright and durable cesium lead halide perovskite light-emitting diodes. *Nanoscale* **8,** 18021–18026 (2016).
35. Wang, Z. *et al.* Efficient and Stable Pure Green All-Inorganic Perovskite CsPbBr3 Light-Emitting Diodes with a Solution-Processed NiOx Interlayer. *J. Phys. Chem. C* **121,** 28132–28138 (2017).
36. Zou, C., Liu, Y., Ginger, D. S. & Lin, L. Y. Suppressing Efficiency Roll-Off at High Current Densities for Ultra-Bright Green Perovskite Light-Emitting Diodes. *ACS Nano* **14,** 6076–6086 (2020).
37. Vashishtha, P., Ng, M., Shivarudraiah, S. B. & Halpert, J. E. High Efficiency Blue and Green Light-Emitting Diodes Using Ruddlesden–Popper Inorganic Mixed Halide Perovskites with Butylammonium Interlayers. *Chem. Mater.* **31,** 83–89 (2019).
38. Wu, T. *et al.* Nanoplatelet modulation in 2D/3D perovskite targeting efficient light-emitting diodes. *Nanoscale* **10,** 19322–19329 (2018).

39. Wang, Z. *et al.* Manipulating the Trade-off Between Quantum Yield and Electrical Conductivity for High-Brightness Quasi-2D Perovskite Light-Emitting Diodes. *Adv. Funct. Mater.* **28,** 1804187 (2018).
40. Chen, H. *et al.* Sodium Ion Modifying In Situ Fabricated $CsPbBr_3$ Nanoparticles for Efficient Perovskite Light Emitting Diodes. *Adv. Opt. Mater.* **7,** 1900747 (2019).
41. Zhang, X. *et al.* Enhancing the Brightness of Cesium Lead Halide Perovskite Nanocrystal Based Green Light-Emitting Devices through the Interface Engineering with Perfluorinated Ionomer. *Nano Lett.* **16,** 1415–1420 (2016).
42. Song, J. *et al.* Organic–Inorganic Hybrid Passivation Enables Perovskite QLEDs with an EQE of 16.48%. *Adv. Mater.* **30,** 1805409 (2018).
43. Zou, Y. *et al.* Efficient Perovskite Light-Emitting Diodes via Tuning Nanoplatelet Distribution and Crystallinity Orientation. *Adv. Mater. Interfaces* 1801030 (2018). doi:10.1002/admi.201801030
44. Jiang, Q. *et al.* Surface passivation of perovskite film for efficient solar cells. *Nat. Photonics* **13,** 460–466 (2019).
45. Zhao, L., Lee, K. M., Roh, K., Khan, S. U. Z. & Rand, B. P. Improved Outcoupling Efficiency and Stability of Perovskite Light-Emitting Diodes using Thin Emitting Layers. *Adv. Mater.* **31,** 1805836 (2019).
46. Grancini, G. *et al.* One-Year stable perovskite solar cells by 2D/3D interface engineering. *Nat. Commun.* **8,** 15684 (2017).
47. Fang, H.-H. *et al.* Unravelling Light-Induced Degradation of Layered Perovskite Crystals and Design of Efficient Encapsulation for Improved Photostability. *Adv. Funct. Mater.* **28,** 1800305 (2018).
48. Birkhold, S. T. *et al.* Interplay of Mobile Ions and Injected Carriers Creates Recombination Centers in Metal Halide Perovskites under Bias. *ACS Energy Lett.* **3,** 1279–1286 (2018).
49. Motti, S. G. *et al.* Photoinduced Emissive Trap States in Lead Halide Perovskite Semiconductors. *ACS Energy Lett.* **1,** 726–730 (2016).
50. Park, D. Y. *et al.* Investigation of Chemical Origin of White-Light Emission in Two-Dimensional $(C_4H_9NH_3)_2PbBr_4$ via Infrared Nanoscopy. *J. Phys. Chem. Lett.* **10,** 7942–7948 (2019).
51. Murata, K., Cinà, S. & Greenham, N. C. Barriers to electron extraction in polymer light-emitting diodes. *Appl. Phys. Lett.* **79,** 1193–1195 (2001).
52. Snaith, H. J. *et al.* Anomalous Hysteresis in Perovskite Solar Cells. *J. Phys. Chem.*

Lett. **5,** 1511–1515 (2014).

53. Kim, G. Y. *et al.* Large tunable photoeffect on ion conduction in halide perovskites and implications for photodecomposition. *Nat. Mater.* **17,** 445–449 (2018).
54. Dzwilewski, A. *et al.* A Unifying Model for the Operation of Light-Emitting Electrochemical Cells. *J. Am. Chem. Soc.* **132,** 13776–13781 (2010).
55. Li, N. *et al.* Stabilizing Perovskite Light-Emitting Diodes by Incorporation of Binary Alkali Cations. *Adv. Mater.* **32,** 1907786 (2020).
56. Shao, Y. *et al.* Grain boundary dominated ion migration in polycrystalline organic-inorganic halide perovskite films. *Energy Environ. Sci.* **9,** 1752–1759 (2016).

6 Conclusion

In this thesis I investigate factors that influence efficiency, reproducibility and stability in perovskite light-emitting diodes. In chapter 3, I investigate the suitability of different device architectures for green-emitting perovskite LEDs where I conclude that ZnO is not a suitable electron injection material without significant modification. After this the suitability of a *pin* device architecture is demonstrated. Finally, I investigate different passivation strategies for green-emitting metal halide perovskites and test their suitability in this *pin* device structure. Through this, I demonstrate that optimisation of PLQY must be done in concurrence with device testing due to the multiphase behaviour of metal halide perovskites and the insulating nature of the passivation agents.

In chapter 4, I investigate 2D/3D perovskite emitters and their suitability in perovskite LEDs. I discover that they are a good strategy for making efficient perovskite LEDs where an EQE_{EL} of 12.1% is demonstrated. I also highlight different factors which affect reproducibility when fabricating these materials and identify solvent atmosphere and antisolvent quench procedures as two variables which must be controlled or removed to afford a reproducible device. Further I develop a novel poly-TPD/LiF hole injection layer which allows the fabrication of highly efficient, reproducible perovskite LEDs. After making reproducible devices, I discover that incorporation of phenylethylammonium bromide into $CsPbBr_3$ LEDs negatively affects their stability.

In chapter 5, I investigate the origins of this instability where I demonstrate very few changes to the bulk properties of the hybrid semiconductor occur upon device degradation. I do however, show the evolution of an emissive trap state which is indicative of changes to the electronic structure of the material. This is corroborated with significant changes to the radiative efficiency of the emitter in degraded LEDs. Further, I identify significant changes in the JV characteristics of the LED after operation which points towards mobile ions in the material causing significant changes to the injection characteristics of the device.

The research which has been presented in this thesis provides the basis of discovery of underlying mechanisms which govern the instability of perovskite light-emitting diodes. Previously unidentified degradation pathways have been shown and investigated. Further, the critical parameters which change throughout degradation have been identified. This

will allow for more targeted and relevant research into how to further improve their stability. It provides a significant contribution to the field in unveiling these mechanisms and begins to disentangle ways to solve these underlying degradation mechanisms. This should accelerate the field to more stable perovskite LEDs; which is currently the most significant hurdle to their commercialisation.